Doctoral Thesis

Influence of physical and chemical factors on evolution of cells

Kinga Matuła

Doctoral thesis

Influence of physical and chemical factors on evolution of cells

Kinga Matuła

Supervisor: Professor Robert Hołyst
Auxiliary supervisor: Jan Paczesny, Ph.D.

The presented dissertation was prepared within
the International Doctoral Studies at the Institute of Physical Chemistry of
the Polish Academy of Sciences,
Department of Soft Condensed Matter,
44/52 Kasprzaka, 01-224 Warsaw, Poland

Warsaw, October 2019

Supervisor: Professor Robert Hołyst
Co-supervisor: Jan Paczesny, PhD

Reviewers:
D. Sc. Eng. Michał Chudy, Associate Prof. (Warsaw University of Technology)
D. Sc. Renata Gadzała-Kopciuch, Associate Prof. (Nicolas Copernicus University in Toruń)

Doctoral Thesis Committee:
Professor Piotr Garstecki (chair, IPC PAS)
D. Sc. Robert Nowakowski, Associate Prof. (vice-chair, IPC PAS)
Professor Jerzy Górecki (IPC PAS)
Professor Andrzej Poniewierski (IPC PAS)

Financial support

This work was supported by

the National Science Centre within the Maestro Grant 2011/02/A/ST3/00143

NATIONAL SCIENCE CENTRE
POLAND

and

the Foundation for Polish Science within the INTER Grant 75/UD/SKILLS/2014

FNP
Foundation for Polish Science

Rodzicom

"If you can dream it, you can do it"

-Walt Disney-

Contents

List of abbreviations, symbols, and notations

Abbreviation	Description
N-D	N=0, 1, 2 or 3, refers to dimensionality of the system
A	Surface area of a particle
A431	Human epidermoid carcinoma
A549	Adenocarcinomic human alveolar basal epithelial cells
AFM	Atomic force microscopy
CFU	Colony forming unit
C. glutamicum	*Corynebacterium glutamicum*
Cryo-SEM	Cryo scanning electron microscopy
d	Radius of a tip of ZnO nanorod
d_b	Size of bacterium
D	Diffusion coefficient of a solute molecule
DEG(s)	Differenitally expressed gene(s)
DNA-seq	DNA sequencing
E_b	Young modulus of ZnO nanorods
Enr	Young modulus of bacterium
EDS	Energy-dispersive X-ray spectroscopy
E. coli	*Escherichia coli*
F	Force
η	Viscosity
h	Thickness of diffusion layer of nanopartcile
HaCaT	Immortalized human keratinocytes
$HepG_2$	Human liver cancer cell line
HeLa	Human cervical cancer cell line
k	Dissolution rate constant
L	Diameter of flask
m_b	Mass of bacterium
MIC	Minimum inhibitory concentration
MCNs	Multicomponent nanoparticles
padj	Benjamini-Hochberg adjusted p-value
PBMC	Peripheral blood mononuclear cells
PFU	Plaque forming units
QD	Quantum dot
r	Distance of a moving fluid from the axis of rotation
p	Pressure exerted at the surface of bacterium
ρ	Density
R_e	Reynolds number
RNA-seq	RNA sequencing
ROS	Reactive oxygen species
S. cerevisiae	*Saccharomyces cerevisiae*
SEM	Scanning electron microscopy
s.e.m.	Standard error of the mean
S. epidermidis	*Staphylococcus epidermidis*
SNP(s)	Single nucleotide polymorphism(s)
Stk	Stokes number
TCA	Tricarboxylic acid cycle
TEM	Transmission electron microscopy
v	Relative velocity
v	Linear velocity of a medium
V_s	Volume of a solution
ω	Angular viscosity
ZnO	Zinc oxide
ZnO NP	Rounded ZnO nanoparticles
ZnO NR	ZnO nanorods
UV	Ultraviolet radiation

Theses

- The shape of nanostructures, with matching active surface area, is an important factor influencing cell viability and behavior.

- Under dynamic conditions, that enable collisions between nanostructures and cells, ZnO nanorods appear to be more damaging compared to rounded ZnO nanoparticles. This is due to the increased probability of mechanical damage caused by ZnO nanorods as a result of the piercing of the cell wall and/or membrane.

- Gram-positive bacteria appear to be more resistant to mechanical stress induced by nanostructures due to their thicker cell walls. Gram-negative bacteria that possess thin cell walls or eukaryotic cells with soft membranes are more vulnerable to mechanical stress exerted by ZnO nanorods.

- *Escherichia coli* can adapt to mechanical stress induced by ZnO nanorods by changing phenotype and genotype.

- Mechanical stress induced by sharp ZnO nanorods causes changes in the phenotype of *Escherichia coli*. Mechanical resistance of bacteria appears as a change of the cell shape into more spherical, an increase of density of periplasm and the average thickness of the cell wall, and change of elemental composition of periplasm and cytoplasm.

- Mechanical stress induces changes at the genome and transcriptome level in *E. coli* such as: single nucleotide polymorphisms and down-regulation of expression of genes encoding proteins involved in key metabolic pathways like glycolysis, β-oxidation of fatty acids, the citric acid cycle, as well as uptake of amino acids and enzyme cofactors.

Chapter 1

General introduction and thesis outline

This chapter provides a general introduction to nanotechnology, nanostructures, and interactions between nanoparticles and cells. This chapter is useful for both novice researchers in the field, but also for experienced scientists who wish to explore upcoming possibilities related to the application of nanoparticles. The final section presents the main goal of the research and the thesis outline.

1.1. Nanotechnology and nanoparticles

Richard Feynman during his presentation in 1959 entitled "There's Plenty of Room at the Bottom" given to the American Physical Society at Caltech, seeded the concept of "*manipulating and controlling things on a small scale, thereby entering a new field of physics which was bottomless, like low-temperature physics*"[1]. This new study, introduced by Feynman, is called nanotechnology. The prefix "nano-" derives from the Greek ("*nanos*" meaning "dwarf"), and refers to one billionth of a meter (10^{-9} m). To put this number into a broader perspective (see Fig. 1.1.), one would need to split a human hair around 70,000 – 80,000 times to reach 1 nanometer (nm). In fact, nanotechnology is defined as the study that deals with the manipulation, control, and integration of atoms or molecules, sized between 1-100 nm in at least one dimension[1,2].

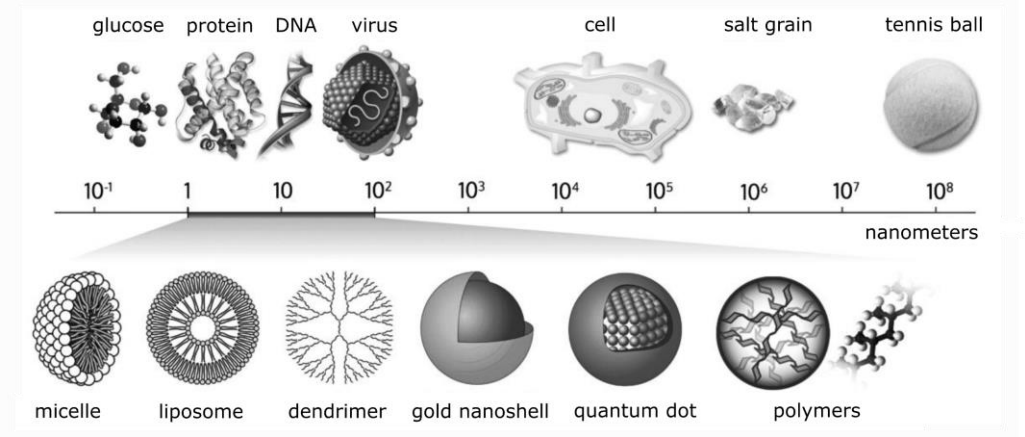

Fig.1.1. The nanoscale comparison of different objects with the illustration of exemplary nanostructure (picture adapted)[3].

Nanotechnology is a relatively young branch of science, however, non-engineered nanoparticles have always existed naturally in form of dust or smoke (volcanos eruption, forest fires, erosion, cosmic dust, photochemical reactions in high layers of Earth's atmosphere, etc.)[4]. Incidental sources of nanoparticles also include industrial processes, combustion, vehicles or construction. From a more biological perspective, nanoparticles comprise proteins, polysaccharides, DNA, viruses, and nanobacteria[5,6]. Interestingly, scattered examples of the production and utilization of nanoparticles date even to the pre-Christian era. For instance, gold and silver nanoparticles were used in glass-making, painting or sculptures, since artisans were attracted by the unusual optical properties of nanostructures. First notes about the discovery of soluble gold are estimated at 1200-1300 BC (Egypt, China)[7,8]. However, the most recognized example of early nano-based art is the Romans Lycurgus cup (from the 4th century AD), which contains tiny metal crystals of Au and Ag (~70 nm) in molar ratio 14:1. This type of glass is known as dichroic glass since it displays green color when is illuminated externally, or red when the light source is placed inside[9,10].

Undoubtedly, in the beginning, there were optical properties of nanoparticles that have been appreciated the most. Interestingly, spherical gold nanoparticles sized

around 3.2 to 5.2 nm possess characteristic red color[11], while spherical silver nanostructures (~30 nm in diameter) have yellow color[12,13], in contrast to reddish-yellow bulk gold or greyish silver. Apparent color depends on size and shape of the nanomaterial, also surface functionalization and environment. Gold nanoparticles can be red but also yellow, green, blue or violet (see Fig. 1.2.). Optical properties can be easily tuned according to a phenomenon called plasmon resonance[14,15]. When metal nanoparticles are exposed to electromagnetic radiation, only a distinct wavelength of the visible light, that causes polarization of the conduction electrons, is adsorbed. As a result, s-p free electrons can develop resonant character that involves collective oscillation of the electron cloud at the surface of the nanoparticle. The frequency of the oscillation is determined by the size and shape, meaning that change in dimension of the nanoparticle shifts the plasmon resonance. Hence, relatively large nanostructures absorbing in the red region reflect blue-green color, whereas small nanoparticles yield red apparent color as a result of absorption in blue region[14,16,17].

Fig. 1.2. Gold nanoparticles of different diameters obtained by Martin synthesis prepared by the author. The wine color suspension (first from the right) contains the most stable gold nanoparticles of the size of around 3.5 nm.

There are several visible examples of the utilization of nanostructures in stained-glass windows, pigments, jewelry or construction materials over the centuries, well before physical and chemical properties of nanostructures were revealed and understood[7,18]. However, here I would like to stop here for a moment and ask a more fundamental question: what makes nanoparticles so unique in comparison to bulk materials, besides already mentioned optical properties? Nano-sized objects possess two characteristic features that clearly distinguish them from micro- or macroparticles. First, every object smaller than 50 nm is no longer subjected to the laws of classical physics – this is quantum physics that becomes valid[19,20]. Consequently, nanoparticles that are made from the same material as macroparticles exhibit different magnetic, optical or electronic properties that are usually hard to predict[21,22,23]. The second characteristic feature is that nanostructures possess a high ratio of surface to volume[2,24]. To visualize this one can image 500 ml beaker, where normally two tennis balls can be placed, which surface area is around a half page of A4 format (~300 cm^2). If the same beaker is filled up with nanostructures, their total surface area can be estimated to equal three areas of National Stadium in Warsaw (~600 000 m^2). The large surface area, and what it follows a large number of surface atoms in comparison to a small volume, results in different reactivity

with the surrounding environment. Such surface atoms are more weakly bonded than those in the interior of the nanoparticle. They are more unstable and willing to react, which is advantageous in catalysis, and provides flexibility in the further surface modifications. On the other hand, high reactivity causes a serious health threat. The harmful effect is intensified especially in the case of nanostructures of up to few nm that can easily cross cell-barrier[25,26,27,28]. Summarizing, smaller matter correlates with higher reactivity and different properties in comparison to bulk materials.

The last decade brought spectacular progress in nanotechnology, and currently, there is a lot of discussions about what should be exactly termed nanotechnology. Researchers classified the following fields, but it should be stressed that this is only an exemplary classification:

- the study of nanostructures using electron microscopy[29,30];
- the growth and characterization of thin films[31,32,33,34,35];
- the bottom-up approach in the synthesis and fabrication of materials[36,37];
- drug delivery systems[38,39,40];
- lab-on-a-chip techniques[41,42,43,44];
- micro-electrochemical systems (MEMS)[45,46,47,48];
- smart and self-replicating systems/nanorobots[49,50,51], nanosystems monitoring different environments e.g., living organisms or space elevators[52,53,54].

This reflects that nanotechnology covers a very broad spectrum of disciplines, also revealing the interdisciplinary character. Therefore, in the broader context, nanotechnology can be understood as a technology of design, fabrication, and application of different nanostructures and materials that includes the study of fundamental properties and phenomena of materials in the nanometer scale. Nanotechnology was recognized as one of four main technological fronts of 21st century[55]. Together with information technologies, biotechnology/synthetic biology and new energy technologies it promises to revolutionize the world[56]. In 2004 UN Task Force on Science, Technology and Innovation highlighted advantages related to nanotechnology that comprise high productivity using little labor and land, low cost and a relatively modest requirement for materials and energy[57].

1.1.1. Types of nanoparticles

Metal nanoparticles are certainly the most well-known and studied class of nano-systems due to flexibility in synthetic control, tunability of size, shape, optical properties, structure, composition, encapsulation, as well as assembly and wide application[58]. Nevertheless, nanotechnology compromises a wide range of nano-sized objects that can be classified based on their composition, morphology or dimensionality. Taking into consideration composition, nanostructures can be dived into four main groups: organic, inorganic, hybrid structures and carbon-based[7] (see Fig. 1.3).

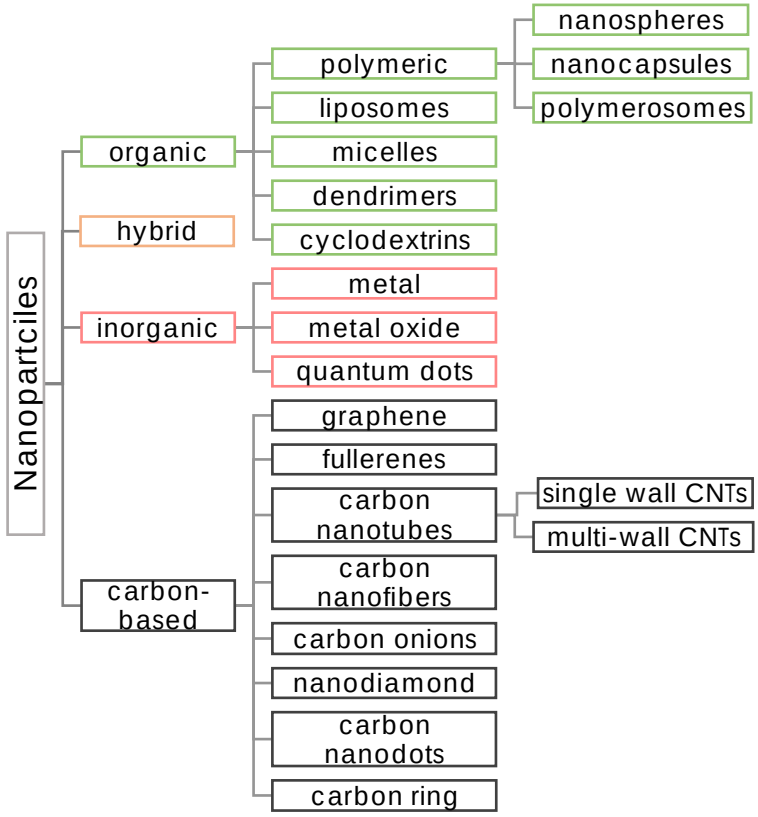

Fig. 1.3. Classification of nanoparticles based on the composition. CNTs denotes carbon nanotubes.

Organic nanostructures are particles, composed of polymeric, lipid, protein or carbohydrate components, that exist naturally (e.g., viruses, protein aggregates, lipid bodies) or can be fabricated in various forms[59,40]:

- liposomes – phospholipid vesicles usually sized between 50-100 nm[60];
- micelles – colloidal aggregates of small surfactant molecules of block amphiphilic copolymers, size around 10-100 nm[40];
- dendrimers – highly branched, monodispersed polymer systems of size up to 10 nm, that consist of core and surface[61];
- cyclodextrins – cyclic oligosaccharides of size up ~1.8 nm, with lipophilic cavity and hydrophilic surface[62];
- polymeric nanocapsules – vesicles structures with reservoir inside surrounded by copolymer unimers or membrane, size around 100-300 nm[40];
- polymeric nanospheres – matrix-type, solid nanoparticles, with a tunable size (even up to 450 nm)[40,63];
- polymersomes – artificial vesicles made using amphiphilic block copolymers assembled in bilayer spheres of diameter from 5 nm (even up to 5 μm), more stable than liposomes[64].

The usage of organic components makes organic nanoparticles perfect candidates for application in controlled drug delivery systems[65,66], bioimaging[67,68], biosensing[69], tissue regeneration[70], antibacterial applications[71]. Besides the convenience in non-covalent encapsulation of active substances, such systems exhibit also biodegradability, non-

toxicity, stability in circulation in the bloodstream, and ability to effectively permeate cell membranes[72]. Recently, next to standard organic carriers utilized for entrapping of agents, also "polymer therapeutics" used as multicomponent constructs appeared. They constitute type of drugs, or prodrugs, that encompass conjugates of polymer, drugs, proteins, aptamers and non-viral vectors with block copolymer micelles[73].

Inorganic nanoparticles constitute the second large group of nano-sized objects which includes metal, metal oxide nanoparticles and quantum dots. Gold (Au NPs) and silver nanoparticles (Ag NPs) are the most prevalent types of metal nanoparticles with numerous applications, for instance in imaging (as contrast agents)[74,75,76], and SERS technique - a sensitive analytical platform based on surface-enhanced Raman spectroscopy[77]. Biomedicine successfully utilizes Au NPs also in drug delivery systems[78,79]. Platinum (Pt), nickel (Ni), palladium (Pa), Ag and Au nanoparticles that possess catalytic properties[80,81,82] create new perspectives for various chemical reactions in a catalytic branch of industry. Enormous progress occurred in electronics[2,83], photochemistry[84], and material sciences[1,85] thanks to silicon (Si), copper (Cu), iron (Fe), cobalt (Co), zinc (Zn), lead (Pb), Ag and Au nanoparticles.
Among metal oxide nanoparticles, zinc oxide (ZnO), silicon dioxide (SiO_2), aluminum oxide (Al_2O_3), tin dioxide (SnO_2), titanium dioxide (TiO_2), MnO_2 (manganese dioxide), zirconium dioxide (ZrO_2), CeO_2 (cerium dioxide), Fe_2O_3 (iron oxide), magnetite (Fe_3O_4), nickel oxide (NiO), are currently the most widely used types of nanostructures since they possess biocompatible, catalytic properties or exhibit good mechanical characteristics. Catalytic reactions are usually based on the utilization of TiO_2, Fe_2O_3, NiO or ZnO[86,87]. Biocompatibility of TiO_2, ZnO, CeO_2 has contributed to the development of implantology and prostetics[88]. Magnetic alloy nanoparticles (Fe-Co, Fe-Ni, Fe-Pt, Co-Pt, Co-Ni) or magnetic oxide nanostructures (Fe_3O_4, Fe_2O_3, $NiFe_2O_4$, $MnFe_2O_4$, $CoFe_2O_4$, NiO, Co_3O_4) possess various application, for instance in water purification[89], magnetic resonance imaging, magnetofection (highly efficient gene delivery system), radioimmunotherapy, tissue engineering, cell separation and cell sensing[90].
Quantum dots (QDs) are semiconductor nanocrystals sized between 2 and 20 nm that constitute the third group of inorganic nanoparticles. The single QD is composed of hundreds up to thousands of atoms of groups: II–VI elements (e.g., CdSe, ZnS); III–V elements (e.g., InAs, InP); I–III– VI_2 elements (e.g., $CuInS_2$), IV–VI elements (e.g., PbS, PbSe), IV elements (e.g., Ge, Si)[91]. The main feature of QDs it that they emit light upon excitation. QDs exhibit size-dependent optical properties and therefore are widely used in: biophotonics (including optical and photoacoustic imaging, biosensing, photothermal therapy)[92,93,94], nanomedicine (drug, gene and protein delivery systems, imaging guiding surgeries), QDs-based light-emitting diodes[95], QD luminescent solar concentrators[96], and in carrier multiplication (boosting the photocurrent of devices)[97].

Carbon-based nanomaterials are based on carbon as the starting material which is the most widely used natural material and the most stable form of carbon under standard conditions[98,99,100]. Carbon-based nanostructures represent an individual group due to the large variety of structures with an exceptional impact in different branches of nanotechnology. A few forms of carbon-based structures can be distinguished:

- graphene - atomically thin film (obtained by exfoliation) composed of hexagonally arranged carbon atoms, possesses unique electrical properties and high flexibility[101,102,103];
- fullerenes - the C_{60} molecule that is a highly symmetrical sphere of size around 0.7 nm, synthesized by heat or laser-induced evaporation[102,104];

- carbon nanotubes – a cylindrical carbon structure (1-30 nm in diameter) that can be synthesized by chemical vapor deposition of graphite or arc discharge[103];
- carbon nanofibers – a cylindrical structure made from graphene layers stacked one on the top of other (50-200 nm in diameter)[105,106];
- carbon onion – a fullerene-like member of the carbon-based family of size below 10 nm, consist of multiple concentric carbon shells that are defective[107,108];
- nanodiamond – nanomaterial that consists of sp^3 carbon atoms (in contrast to other types of carbon-based nanomaterials) sized between 2-10 nm, obtained by the detonation of explosives with negative oxygen balance[102,109];
- carbon nanodots – also known as carbon QDs, carbonaceous, graphitic nanoparticles with size between 2-10 nm that can be obtained by oxidation of the arc-discharged soot, laser ablation, oxidative acid treatment[102,110,111].
- carbon black – spherical, amorphous nanomaterial (20-50 nm in diameter) that aggregates resembling a bunch of grapes, obtained by thermal decomposition or partial combustion[18,112].
- carbon ring - carbon allotrope built from rings of two-coordinate atoms; recently, carbon ring was obtained for the first time in history (cyclo[18]carbon (C18)) and recently reported in *Science* magazine[113].

Due to high biocompatibility, catalytic activity, intriguing electronic properties, and good mechanical stability, they are used in drug delivery systems (drug, gene delivery)[102], photothermal therapy[102], bioimaging[102,114], tissue scaffolds[103,115], bio-sensing[102,116], electronics[117] and optoelectronics[114], and fuel cells[118,119].

Hybrid nanostructures are based on a combination of organic and inorganic components, where two classes can be distinguished[2]:

- class I hybrids – components are linked through weak hydrogen bonds or Van der Waals forces (e.g., nanocomposites where oligomers, organic molecules are physically trapped in an inorganic matrix);
- class II hybrids – components are linked through covalent bonds (e.g., molecules of inorganic and organic components are chemically bonded).

Typically, the polymeric matrix provides structural properties, allowing for mechanical characteristics or processability (that can be easily tuned). Inorganic part yields in functional properties (magnetic, catalytic, luminescent, etc.), can reinforce the thermal or mechanical properties of the polymer.

Recent advancements in unconventional synthetic methods make it possible to obtain multicomponent nanoparticles (MCNs) that have multiple domains of distinct materials within one nanoparticle. Two configurations of MCNs can be distinguished: symmetric (e.g., core–shell) or asymmetric (e.g., dumbbell, coaxial, oligomer)[120].

In general, the core/shell type nanoparticles can be broadly defined as materials composed of a core (inner material) and a shell (outer layer material), which are composed of two or more materials. These can comprise a wide range of various combinations in close interaction, including inorganic/organic, inorganic/inorganic, organic/organic, and organic/inorganic materials. Different classes of core/shell nanoparticles have been distinguished: i) concentric spherical (the most common), ii) hexagonal, iii) nanomatryushka material, iv) multiple small core materials coated by single shell material, v) movable core within hollow shell material[121].

Recently, also MCNs with the asymmetric spatial distribution of domains have gained in increased importance since that they may outperform their symmetric counterparts in certain applications[122,123124]. Currently, conventional strategies for breaking symmetry for the preparation of MCNs are being replaced by nonconventional approaches (e.g., interface-guided synthesis, surface-protected growth, welding-induced synthesis) that overcome several limitations connected with poor reproducibility or sensitivity to small variations in synthetic conditions[120].

It is worth mentioning that the final properties of core/shell nanoparticles or asymmetric MCNs are the result of the synergistic effect of the combination of organic and inorganic components[125]. Biomedicine that is widely understood as single or combinatorial drug delivery systems and diagnosis including fluorescent imaging and phototherapy[126,127], is one the leading fields in the development, and application of hybrid nanostructures. Such nanosystems are also extensively used in sensing applications (molecularly imprinted polymers, high-performance liquid chromatography-based analysis, SERS-based detection)[128], catalysis (organic transformations, photocatalysis, electrocatalysis)[129,130,131] and nanoelectronics[132].

Besides classification based on the composition, all types of nanoparticles can be categorized taking into consideration the number of dimensions (Fig. 1.4), where 100 nm is taken as the upper limit of the nanoscale. According to this assumption, the following structures can be distinguished[102,119]:

- zero-dimensional (0-D), where all the dimensions are measured within nanoscale: quantum dots, fullerenes, nanolenses, nano-onions, hollow nanospheres,
- one-dimensional (1-D), where two dimensions are confined to the nanometer scale: nanotubes, nanowires, nanobelts, nanorods, nanotubes, nanoribbons;
- two-dimensional (2-D), where two dimensions are outside the nanoscale: graphene, nanoprisms, nanowalls, nanosheets, nanodiscs, junctions (branched, continuous islands);
- three-dimensional (3-D), where three dimensions are not confined to the nanoscale (arbitrary dimensions above 100 nm): nanoballs, nanocoils, nanocones, nanopillars, nanoflowers.

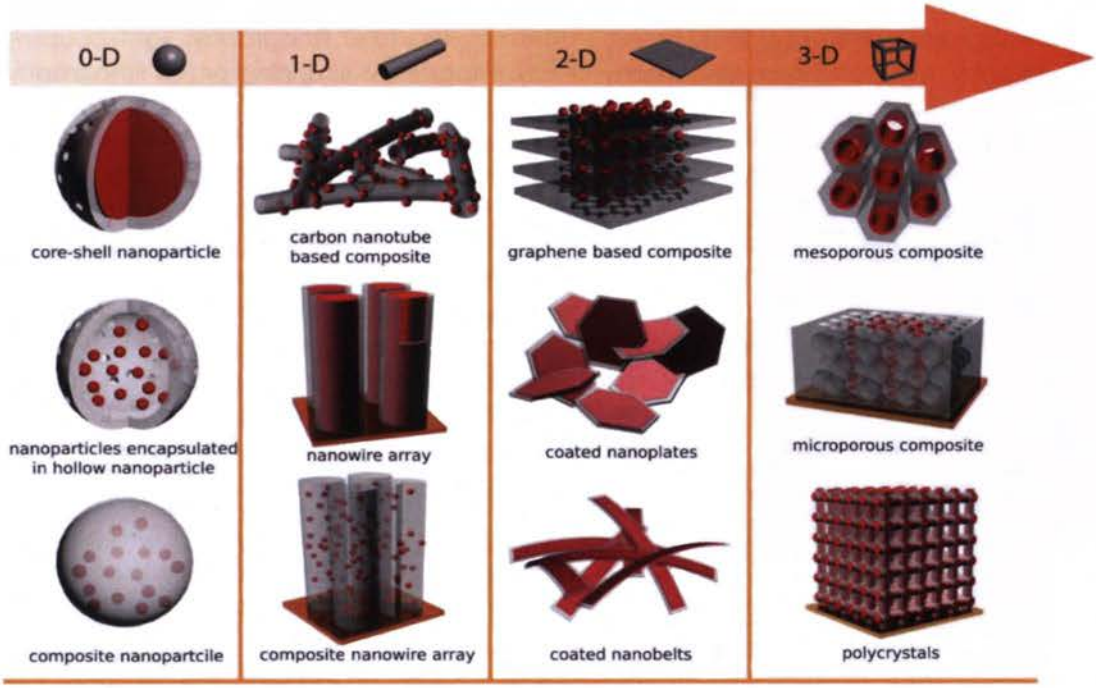

Fig. 1.4. Illustration of exemplary 0-D, 1-D, 2-D, 3-D nanomaterials with heterogeneous morphology. Picture adapted from reference[133].

Classifications of nano-objects based on the composition and dimensionality are the most fundamental ones. However, in literature, various divisions are presented that distinguish nano-objects regarding chemical ordering (mixed, core-shell, layered)[134], shape (nanospheres, nanorods, nanocubes, nanopyramids, branched nanostructures, rectangular nanoplates, triangular nanoplate, etc.)[135,136] or morphology (solid, mesoporous/hollow)[137]. Nanoparticles can be also divided into two main groups taking into account the production methods that will be the subject of the next chapter.

1.1.2. How to obtain nanoparticles?

There are two main approaches used in the preparation of nanoparticles: top-down and bottom-up. **Fig. 1.5** summarizes commonly used methods in the synthesis of nanomaterials and the fabrication of nanostructures[2,7].

The top-down (breakdown) approach refers to all methods in which external force is applied to a given bulk material that leads to its rapture into nanometer-scale particles. For instance, dry grinding is a typical example of the top-down approach that utilizes jet mills, shearing mills, hammer mills, shock shearing mills, roller mills, tumbling mills or ball mills in order to ground solid material. Currently, the most attractive top-down approach is lithography that is utilized to produce computer chips and nano-electronic devices. Nanolithography uses photons, electrons or charged ions to transfer a pattern from a photomask to a photoresist layer, that covers a bulk substrate or a thin film of material. The method comprises a series of posttreatment steps that allow to chemically engrave the pattern in or deposit onto the target material. Various nanolithographic

approaches can be distinguished, basing on the type of used radiation: photolithography (UV lithography or optical lithography), extreme ultraviolet lithography, light coupling lithography, electron beam lithography, X-Ray lithography, scanning probe lithography, dip-pen lithography, nanoimprint lithography, and soft lithography[138,139,140]. It should be stressed that top-down methods are energy-consuming, waste-heavy and lavish regarding the quantity of material spent on the process[25]. At the same time, nanostructures obtained by the top-down approach are rich in surface imperfections like crystallographic damages or structural defects. Such imperfections often influence physical properties and chemical character of the surface of nanoparticle or nanofilms, e.g., reduced conductivity can be observed as a result of inelastic surface scattering that causes excessive heat generation[2]. Nevertheless, the top-down approach is still attractive and sufficient for the fabrication of nanoparticles for some of the applications. Different, more biological example of the top-down approach is the construction of artificial cell by stripping down genome and decreasing its size to the lowest number of genes that are necessary to survive and maintain basic cellular processes[141].

The second approach is the bottom-up (build-up) manufacturing, which entails the production of larger structures, thanks to self-assembly. Self-assembly is a unifying concept in nature. It governs the formation of complex structures with spatial correlations across multiple length-scales. There are two main modes of self-assembly: equilibrium, where spontaneous integration of components is driven by the reduction of Gibbs free energy[2,7,25] and dynamic, where the energy is continuously pumped into the system and dissipated to sustain the structure[142].

Atomic transformation or molecular condensations of gaseous or liquid phase result in the production of nanostructures that are chemically homogeneous, with fewer defects or impurities, and with better ordering[2].

Commonly used chemical vapor deposition employs chemical reaction between substrate exposed to the volatile precursor, in contrast to physical vapor deposition that utilizes a cooling process of vapor phase into the condensed phase. Nanotechnology also comprises liquid phase methods that can be divided into two groups: liquid/liquid methods (e.g., chemical reduction of metal ions) and sedimentation (e.g., sol-gel method used for the production of metal oxide nanostructures)[7]. Generally, nanoparticles obtained by liquid-phase methods possess high dispersity, compared to dry techniques[7]. Biological methods, using bacteria, yeast, fungi, algae or even plants to obtain nanostructures with well-defined chemical composition, morphology and size are also noteworthy[143,144]. Such "green" route eliminates the usage of expensive chemicals or energy and moreover is environment-friendly. From a more biological perspective, cells can be considered as perfect "nanofactories" – proteins, protein aggregates, DNA, RNAs, ribosomes, lysosomes, etc., are produced from the simplest building blocks operated at nanoscale machinery[36]. The bottom-up approach is also applied in the construction of life-inspired systems in order to understand how living systems work[,145,146,147,148], or in building synthetic cells from scratch, that mimic their natural equivalents[149,150].

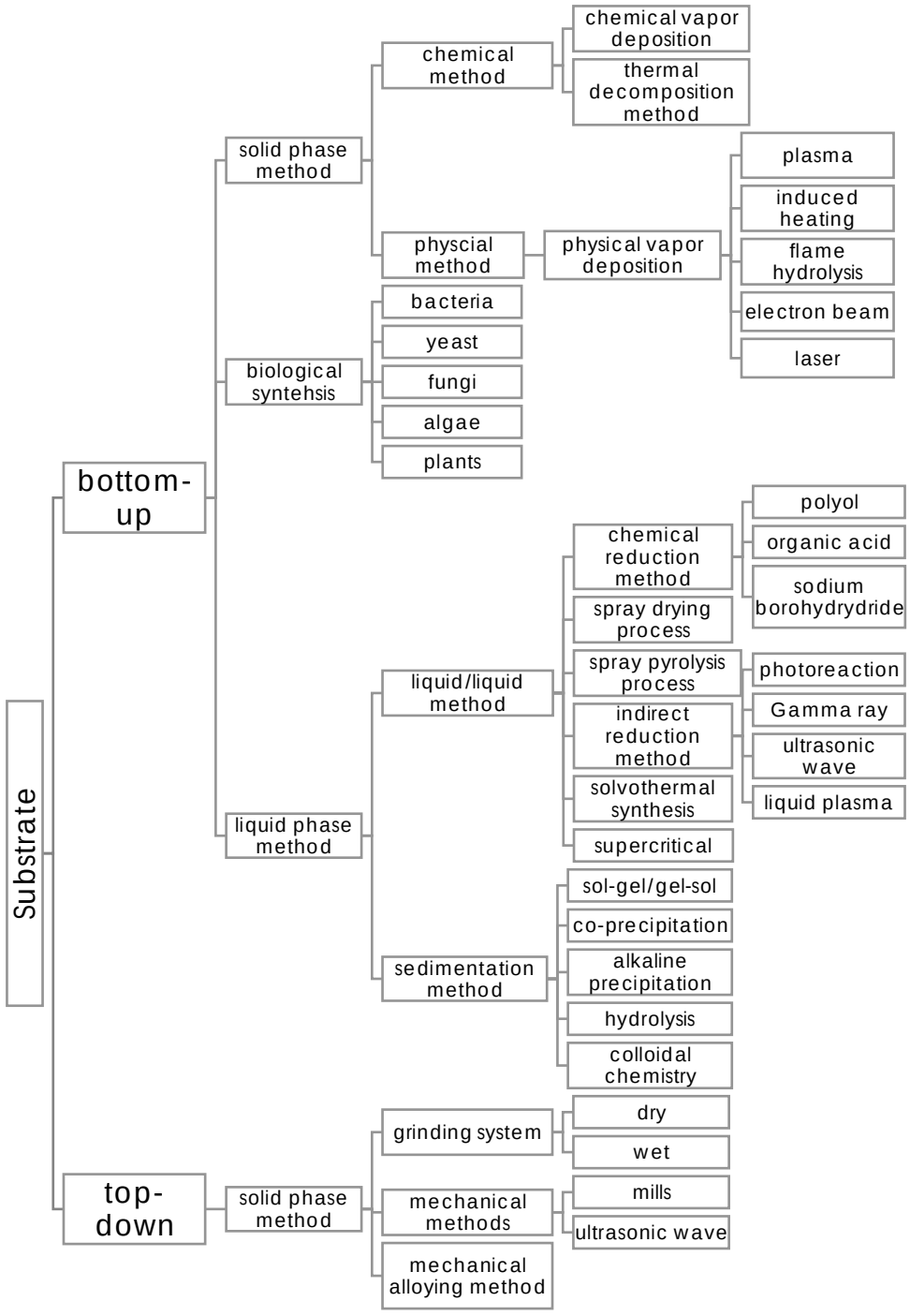

Fig. 1.5. The roadmap of top-down and bottom approaches used in the preparation of nanoparticles[2,7,119,143].

Although various fabrication methods of nanoparticles are available, there are a few conditions that are common for all methods and should be considered[7]:

- size control, size distribution, shape of nanoparticles;
- crystal structure, composition, purity of nanoparticles;
- control of aggregation;
- high reproducibility;
- stabilization of physical and chemical properties;
- high reproducibility, mass production, scale-up process (especially in the case of industrial processes);
- low costs.

1.1.3. Characterization of nanoparticles

Although early examples of the utilization of the nano-based approach are dated to the pre-Christian era, nanotechnology has vigorously evolved only at the end of the 20th century. This milestone was achieved thanks to the development of microscopic methods and other characterization techniques, that allow currently for the analysis of nano-sized objects with extreme sensitivity, accuracy, and atomic-level resolution. In this chapter, the main techniques utilized in the characterization of nanomaterials and nanoparticles will be discussed regarding both the physical and chemical properties of nanostructures (see Fig. 1.6).

The size is one of the most important characteristics, that determines the classification of the object into nano-, micro- or macro- category[58]. Typically, the size determination is followed by the size distribution measurements in order to acquire information about the population variability. Depending on the type of the material, e.g., organic vs inorganic, fluorescent vs nonfluorescent, conductive vs nonconductive, various techniques can be utilized (see Table 1.1). Imaging techniques, like scanning microscopies, additionally allow for examination of the morphology, and subsequently the classification of nanostructures as high-aspect-ratio particles (e.g., nanowires, nanotubes, nanobelts, nanozigzags) or low-aspect-ratio particles (e.g., spheres, prisms, ovals, cubes)[151]. From the biological point of view, the surface area, that influences the interaction with the surrounding environment, i.e., cell - nanoparticle interaction is relevant. The surface area offers also room for various catalytic[152] or biological applications[153] and is often used to predict dissolution rate and bioavailability of particles[154]. Composition and surface functionality, regarding the exact bonding nature, can provide essential information about the bulk and surface properties of the material. Chemical or elemental composition constitutes a crucial indicator of the purity of nanoparticles and the performance of the synthesis[155].
Surface charge is the second characteristic that determines the particle-target interaction, i.e., with proteins, cells or other small molecules, and stable conditions of nanosized objects in a solution[156,157]. From a practical point of view, zeta potential is more often evaluated since it allows for examination of the behavior of nanoparticle in a solution. A net charge of the particle in a solution is determined by electric potential created at the interface of solvent molecules adhering to the surface of the nanoparticle, and mobile molecules in a bulk[59,158].

The crystallinity plays also an important role, especially in controlling other properties e.g., mechanical, electronic, catalytic or magnetic properties of nanoparticles[159,160] since it provides information about the spatial arrangement of atoms or molecules.
The concentration of nanoparticles is usually measured for airborne nanoparticles or in the case of synthesis of nanostructures performed in liquid phase[161].

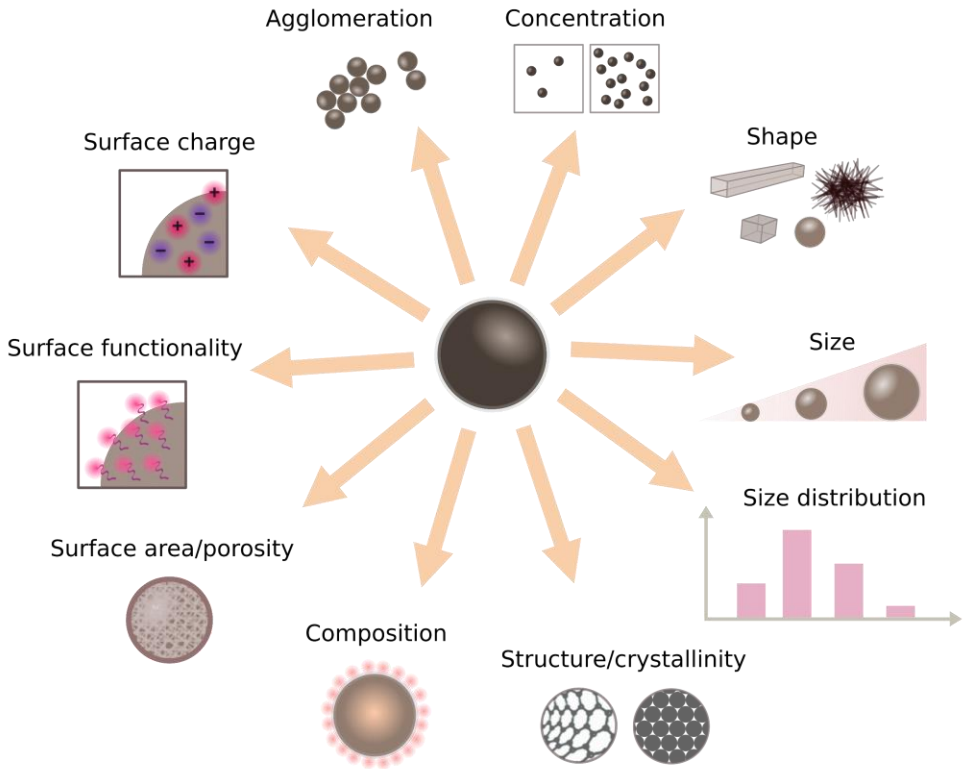

Fig. 1.6. Illustration of commonly examined physical and chemical characteristics of nanostructures.

Table 1.1. The most popular techniques used in the characterization of nanoparticles.

Technique	Principle of the technique	Remarks
Size/Shape/Surface morphology/Agglomeration		
Scanning electron microscopy (SEM) [2,162,163]	Electron probe technique using a precisely focused beam of electrons that penetrates the sample during scanning. Detection of electrons scattered or emitted from the sample and optionally also X-rays enables acquisition: 1) secondary electron images, 2) backscattered electron images, 3) elemental X-ray maps. Variations of SEM: • Environmental scanning electron microscopy (ESEM) – used for imaging of natural samples (wet, uncoated); • Low vacuum scanning electron microscopy (LVSEM) – employed in imaging of non-conductive samples (e.g., polymers); • Cryogenic scanning electron microscopy (Cryo-SEM) – dedicated to imaging of delicate samples (e.g.,	3-D images, information about topography, morphology, size and chemical composition.

	hydrogels, cells, foams), requires freezing of the sample; • Field emission scanning electron microscopy (FE-SEM) – utilized in semiconductor devices analysis (cross-section), thickness analysis of coatings; highly focused and the low-energy electron beam is used.	
Transmission electron microscopy (TEM) [2,164,165,166,167,168]	Electron probe technique using a parallel, coherent beam of electrons that passes through a thin specimen (<100 nm). Electrons can be scattered, backscattered, transmitted or diffracted yielding different information about the sample. Variations of TEM: • High-resolution transmission electron microscopy (HRTEM) – used in the characterization of the crystallinity with atomic resolution and analysis of electron diffraction; the high resolution is achieved by phase-contrast; • Scanning transmission electron microscopy (STEM) – a focused beam of electrons that is rastered across the sample is applied to obtain high-contrast images of hard and soft materials with atomic resolution; • Energy-filtered transmission electron microscopy (EFTEM) - applied in the case of materials with small differences in atomic number; uses electrons within a particular energy window to receive the image with better contrast and spatial resolution; • Cryogenic transmission electron microscopy (Cryo-TEM) – applied in studies of size, shape, structure, dispersion and colloidal composition of delicate biological samples, requires freezing step; • High-angle annular dark-field scanning transmission electron microscopy (HAADF-STEM) – used to distinguish materials composed of atoms with large differences of atomic number (e.g., C and Au), requires STEM; • Electron tomography (ET) – used to obtain 3-D image with structural information from 2-D projections (imaging by sections); employed in the case of chemical and biological samples; • Liquid cell electron microscopy – real-time imaging technique using TEM based on the protocol that minimizes electron scattering; gives the possibility to image polymers (and investigate their dynamics) without metal-ion labeling.	2-D (mainly) or 3-D images, higher resolution can be achieved compared to SEM (~0.5 Å), information about size, shape, crystallinity structure.
Atomic force microscopy (AFM) [2,169,170,171,172]	Scanning probe technique using a sharp tip attached to a flexible cantilever that probes force-distance characteristics. A topographic map of nanometer resolution can be obtained. Both, electrically conductive or insulating materials can be analyzed. Three modes are available: • contact – the contact force induces bending of the cantilever that adjusts to changes in topography (repulsive force); • tapping – the tip is vibrating close to the surface in such distance which allows for barely tapping the sample (short-range forces), the oscillation amplitude of the cantilever varies according to tip-to-sample distance; • non-contact – the probe is vibrating near the surface of the sample in distance of tens to hundreds of angstroms (attractive force), changes in the resonant frequency of the cantilever reflect variations in tip-to-	3-D profile, size, shape, surface roughness, periodicity of the analyzed sample can be obtained. Lateral resolution ~5-10 nm, vertical resolution ~0.1 nm.

	sample distance or topography, used in studies of soft and elastic samples.	
Scanning tunneling microscopy (STM) [2,173,174,175]	Scanning probe technique based on quantum tunneling, utilizing a sharp, conducting tip (with applied bias) that scans the surface. Electrons tunnel through the gap between the tip and the sample (~10Å), yielding tunneling current that changes with tip-to-sample spacing, which is used to create an image. Only conductive materials can be analyzed. Two modes are available: • constant-height – tunneling current differs on topography and is measured at each spot to create a topography image; • constant-current – tunneling current is kept constant by adjusting the height of a piezoelectric scanner (the voltage is applied that changes the distance of the scanner).	3-D topography, size, shape, surface roughness, periodicity of the surface can be measured. Lateral resolution ~0.1 nm, vertical resolution ~0.01 nm.
Dynamic Light Scattering (DLS) [176,177,178]	A spectroscopic technique, known also as photon correlation spectroscopy (PCS), that is based on the measurement of the speed of diffusing particles arising from the Brownian motion. The size of particles (hydrodynamic radii) is assessed by measuring the rate at which the intensity of the scattered light fluctuates. Analyte has to be dispersed/dissolved in liquid. Fluorescence of the particles is not required and sometimes can even complicate measurements.	Size distribution for the whole population, relaxation in complex fluids (e.g., polymers) can be measured.
Fluorescence correlation spectroscopy (FCS) [179,180,181,182]	A spectroscopic technique based on the observation of diffusion of single particles, moving in femtoliter confocal volume. Autocorrelation analysis of the amplitude and the speed of fluctuations of fluorescence intensity, followed by the application of the proper model, allows for the extraction of the size (hydrodynamic radii) of the particles from diffusion coefficient. The technique requires fluorescent or fluorescently labeled particles.	Size distribution for the whole population, diffusion coefficient, kinetics of chemical reaction rates, single-triplet dynamics, can be obtained.
Raster image correlation spectroscopy (RICS) [183,184,185,186]	A spectroscopic technique based on a spatial autocorrelation analysis of a series of images obtained by laser-scanning microscopy. 2-D spatial autocorrelation analysis of data allows obtaining diffusion coefficient, (in microseconds to seconds timescales) from which particle size can be calculated. A slower or immobile fraction of structures can be filtered out. The technique requires the usage of fluorescent or fluorescently labeled objects.	Diffusion, size for the filtered population can be obtained.
Single particle tracking, (SPT) [187,188,189]	A spectroscopic technique based on the observation of single particles (fluorescent or labeled with a fluorophore). It allows recording different forms of the mobility of the particle in a heterogenic environment (e.g., cytoplasm). The generated trajectory is used to extract information about diffusion coefficient and hydrodynamic radii of the object. SPT is widely used in tracking proteins, lipids in cytoplasm or within the cell membrane.	Size of single particles can be obtained. Widely used in biological applications.
Nanoparticle tracking analysis (NTA) [190,191,192]	A spectroscopic technique utilizing light scattered by particles suspended in a liquid that are moving due to Brownian motion. The camera captures the movement of each and every particle simultaneously. A laser beam passes through the chamber with suspended nanoparticles on which the beam light is scattered. The scattering is visualized by microscope with a camera. Specially designed software tracks many particles and calculates the hydrodynamic diameter of nanostructures. using the Stokes-Einstein equation. Both, fluorescent and nonfluorescent objects can be measured.	Size of single particles (10-2000 nm), size distribution and concentration can be obtained.

Localized Surface Plasmon Resonance (LSPR) [12,193,194]	Spectroscopic technique based on the interaction of light with the surface electrons of metal nanoparticles. Collective oscillation of the cloud of electrons is induced only when a specific wavelength of the electromagnetic field is absorbed. This depends on the size, shape, and composition of nanoparticles and dielectric environment. Only conductive nanoparticles can be measured.	Size for the whole population can be determined.
Sedimentation velocity analytical-ultracentrifugation (SV-AUC) [195,196,197]	Analytical technique based on ultracentrifugation, that determines the rate at which molecules move in response to generated centrifugal force. The concentration gradients are measured by the optical system at various times along the cell for all particles that are depleted from the central part of the centrifuge. SV-AUC is frequently used in the case of analysis of proteins or protein aggregates.	Size, shape, and interactions between macromolecules can be measured.
Mobility particle size spectrometry (MPSS) [198,199]	Electrical mobility technique based on the mobility of charged particles that are separated by differential mobility analyzer. Objects passing through the chamber are counted by condensation particle counter since they scatter laser light. Two types of MPSS are available: • SMPS – fast-scanning technique, the applied voltage is increased continuously; • DMPS – differential mobility technique, the applied voltage is increased in a stepwise manner for each mobility bin.	Size distribution (3-1000 nm) can be obtained. MPSS is widely used in aerosols studies.
Scanning ion occlusion spectroscopy (SIOS) [200,201,202]	A spectroscopic method based on the detection of single particles diffusing through a tunable nanopore membrane. Each particle, traversing the pore, generates a current pulse (blockage events) that is scaling linearly with mean particle volume.	Size of single particles (60-1000 nm), size distribution can be also determined.
Size-exclusion chromatography (SEC) [203,204,205]	A chromatographic technique based on the separation of nanostructures on columns packed with porous particles or polymer. It is based on the exclusion of nanoparticles from pores of the stationary phase or by adsorption. Detection of a fraction of nanoparticles eluted by the liquid phase can employ UV-Vis spectroscopy, fluorescence, differential refractive index or conductivity measurements.	Size, size distribution can be measured. SEC is also used as the separation and purification method.
Small-angle X-ray scattering (SAXS) [206,207,208,209,210]	An analytical technique in which the elastic scattering is recorded (at very low angles 0.1-10°) as a result of the interaction of X-ray beam with electrons within the sample. The scattered pattern (intensity of X-rays scattered as a function of the scattering angle) provides structural information, typically in the range of 1-100 nm. SAXS can be used in the case of solid, powder, liquid solutions (even opaque) and gel samples that comprise spherical, lamellar, rod-like and cylindrical particles.	Particle size, shape, porosity, internal structure, and arrangement can be determined.
Surface area		
Brunauer–Emmett–Teller (BET) [211,212,213]	Physisorption method based on adsorption of gas (e.g., nitrogen) on an external and internal surface of porous nanomaterial or nanoparticles with an uneven surface. The true surface area is calculated on the bases of the BET theory, after determination of the amount of gas adsorbed under a given pressure.	Surface area can be determined only for dry particles.
Nuclear magnetic resonance (NMR) [214,215,216]	A spectroscopic technique based on the absorption of electromagnetic radiation by nuclei of atoms that are placed in the external magnetic field. Solvent relaxation NMR determines spin-spin and spin-lattice relaxation time of solvent molecules attached to the surface of the nanoparticle and those mobile in a bulk.	Surface area, the interaction between molecules and diffusion time can be studied.

Scanning mobility particle spectrometer /Differential mobility particle spectrometer (SMPS/ DMPS)[199,217]	An analytical technique referring to mobility size particle spectrometer that consists of neutralizer, differential mobility analyzer (DMA) and condensation particle counter (CPC). based on the mobility measurement of electrically charged particles in an electric field. Charged particles are separated in DMA, then counted in CPC and the mobility distribution is measured by scanning the voltage continuously (in SMPS) or in the step-wise manner (in DMPS) through the entire range of electrical particle mobility.	Soot particle distribution can be measured. Used in aerosol, combustion, particle nucleation and growth studies.
Composition		
Energy-dispersive X-ray spectroscopy (EDS) [218,219,220]	An Analytical technique, usually combined with SEM, TEM or STEM. The electron beam is sufficient to eject electrons from atomic shells, and consequently, other electrons from higher energy shells can fill the electron whole, releasing X-rays. The emitted energy is characteristic for a given element and the composition can be determined	The entire spectrum is collected in one run, energy-dependent resolution.
Wavelength dispersive X-ray spectroscopy (WDS) [163,221]	An analytical technique that is analogous to EDS. The difference is that X-rays emitted from atoms are diffracted by crystals in order to collect one wavelength at a time, in contrast to EDS that captures all X-rays with broad-spectrum energies.	Better resolution can be gained. Crystal dependent resolution (5 eV).
Electron energy loss spectroscopy (EELS) [222,223]	An analytical technique, that uses a photoelectric beam (usually larger than 50 keV), based on inelastic scattering of some electrons from a specimen that results in energy loses and deflection of their pathway. EELS typically is combined with TEM or STEM and provide information complementary to EDS analysis. RHEELS (reflection high-electron energy loss) that includes reflection and aloof EELS (in which the beam interacts with a sample via the long-ranged Coulomb interaction) are variations of EELS.	Atomic composition, chemical bonding, conduction band properties can be measured.
Auger electron spectroscopy (AES) [224,225]	A spectroscopic and surface-specific analytical technique (probing depth 2-5 nm) that uses a high energy electron beam to excite electrons in atoms. When an atom is bombarded with a high-energy electron beam, a core electron can be ejected leaving behind a hole. To keep its stability, an outer shell electron fills the vacancy, and the second electron is ejected (Auger electron). The energy of ejected Auger electrons has characteristic values (few tens of eV to 2000 eV) and can be correlated with certain elements present at the surface.	Used in the case of solid material, complementary to TEM an
X-ray photo-electron spectroscopy (XPS) [226,227,228]	Surface-sensitive analytical technique based on the photoelectric effect where a surface of a sample is bombarded with X-ray radiation (both monochromatic and non-chromatic) in a vacuum. As a result, photoelectrons are emitted and their characteristic kinetic energies (50–2000 eV) allow for further identification that can be performed in a similar manner to AES. XPS probes the surface to a depth of 10 nm.	Elemental composition, information about chemical bonding can be derived from the measured energies of electron and energy shifts.
Energy-filtered transmission electron microscopy (EFTEM) [229,230,231]	Analytical technique based on illumination of very thin samples with a high-energy electron beam which allows for quantitative mapping of elemental species with a spatial resolution ~1nm. Some of the electrons, interacting with the samples, can be elastically and inelastically scattered. In the case of inelastic scattering, both energy loss and a change in momentum. EFTEM is based on inner-shell ionization that gives rise to signals in energy-loss that	EFTEM is used to obtain spectra in EELS.

	are characteristic and well-defined for elements. In this case of zero-loss images, the contrast of images is improved by the utilization of energy filters that cut off electrons that were inelastically scattered (greater than 5 eV).	
Liquid chromatography- mass spectrometry /Liquid chromatography-tandem mass spectrometry (LC-MS LC-MS/MS) [232,233,234]	An analytical technique that combines physical separation using liquid chromatography (LC) or high-performance liquid chromatography (HPLC), with mass spectrometry that allows for the identification of individual components. In LC, a mixture of components is dissolved in the mobile phase and carried through a stationary phase (column filled up with a fine adsorbent solid). The separation occurs due to a difference in the interactions of the components with the mobile and solid phase – different components of the mixture travel at different speeds. Then, the single constitutes are converted onto gaseous ions in mass spectrometer, sorted and characterized by their mass-to-charge ratio (m/z) and relative abundance as well. The tandem technique (MS/MS) is usually used to analyze more complex biological and environmental samples (that require additional digestion step) composed of organic and inorganic compounds.	Widely used in studies of protein corona (nanoparticle-based delivery systems), studies of the interaction between nanoparticles and biomolecules
Surface charge		
Electro-phoretic light scattering (ELS) [235,236,237]	Spectroscopic techniques based on light scattered by nanoparticles suspended in liquid phase (colloids) that measures zeta potential. This key parameter is defined as the electric potential at the boundary of the double layer (typically from +100 mV to -100 mV), created by a thin layer of ions of the opposite charge to the particle, that travels with the nanostructure in the solution. During measurement, a laser beam passes through a cell that contains conducting electrodes. In the case of ELS oscillating electric field causes the motion of nanoparticles (in DLS it is Brownian motion). The mobility of nanoparticles influences the frequency. The phase shift of the incident beam that is used to calculate electrophoretic mobility and then zeta potential.	Zeta potential influences particle stability (values < +25 mV or > -25 mV indicates high stability), cellular uptake and intracellular trafficking
Laser Doppler Velocimetry (LDA) [238,239,240]	A spectroscopic method based on light scattered by particles suspended in a solution, which is placed in a cuvette with an applied electric field. Charged particles move towards the electrodes with the opposite charge. The scattered light to different angles is compared to light in reference beam when nanoparticles are moving (Doppler shift). Their velocity is used to calculate electrophoretic mobility, and then zeta potential according to Henry's equation.	LDA is also used in flow measurements in aerodynamics, in medical applications to quantify blood flow and clinical otology.
Tandem Differential Mobility Analysis (TDMA) [241,242,243]	Analytical technique based on the separation of charged nanoparticles according to their electrical mobility. The TDMA is built from two differential mobility analyzers (DMAs) and a condensation nucleus counter (CNC). Each differential mobility analyzer consists of a cylindrical capacitor (an inner electrode and an outer electrode). The sample in the form of the polydisperse dry aerosol is introduced to a cylindrical column, becomes charged and is separated according to the migration velocities across sheath flow that depend on their electrical mobility. Charged particles are attracted or repelled by the created potential inside the column. Particles of the desired electric mobility can pass a slit situated at the end of the DMA. The second DMA scans the size distribution of	A large number of particles can be analyzed.

	particles and the CNC counts the particles by growing them through heterogeneous condensation of supersaturated butanol to a size suitable for detection.	
Scanning ion conductance microscopy (SICM) [244,245,246]	Scanning microscopy technique based on a high resolution, topographic imaging of objects using nanopipette. The voltage applied between the two electrodes (a glass scanning nanopipette electrode and the other one is positioned in a bulk solution) causes the ionic current flow in and out of the nanopipette. The flux of ions influences the conductance that is measured between an electrode and can be utilized by software to calculate the charge.	Dedicated to soft surfaces e.g., cells (hopping mode SICM) in studies of surface charge.
Atomic force microscopy (AFM) [247,248,249]	Scanning probe microscopy technique based on the interaction of a tip, mounted on cantilever, with a surface of the sample. The original concept evolved from a different technique called surface force apparatus (SFA). Electrostatic measurements are based on forces induced from overlapping electrical double layers when the AFM probe is approaching a charged surface of the sample. The registered force-distance curve can provide information about surface charge densities. AFM is not recommended in the case of analysis of objects (especially cells) in the isotonic environment due to short Debye length.	Not only the electrostatic force contributes to tip-sample interaction. That introduces substantial uncertainty about surface charge assessed by AFM.
Crystallinity		
X-Ray diffraction (XRD) [250,251]	An analytical, nondestructive technique used for identification of crystallinity, structures, phases, crystal orientations, average grain size, strain, and crystal defects of crystalline materials. X-rays generated by heating a filament in a cathode tube bombard the sample. Interference of a monochromatic X-ray beam that is scattered from each set of lattice at specific angles, generates X-ray diffraction peaks. The distribution of atoms within the lattice determines the peak intensities. Consequently, the X-ray diffractograms constitute the fingerprint of periodic atomic arrangements in the analyzed material.	Powerful and rapid technique. Requires tenths of a gram of the material, homogeneous and single phase preferably.
Electron back-scattered diffraction (EBSD) [252,253,254]	An analytical technique used to determine the crystal orientation and the local crystal structure at the surface of a specimen. Measurements are based on the collection of elastically backscattered electrons (BSEs) which have undergone coherent Bragg scattering. EBSD detector collects the BSEs over a large angle, which generates electron backscatter diffraction patterns consisting of Kikuchi bands. The pattern analysis provides the information on the crystalline structure and orientation of the crystal that the electrons were scattered by.	EBSD is usually combined with SEM, offers significantly better spatial resolution in comparison to XRD.
Concentration		
Conden-sation Particle Counter (CPC) [255,256,257]	A technique based on light scattering by particles that are counted individually when passing through a laser beam of the optical system. CPC uses a condensation technique to enlarge the size of small particles by saturating a workplace with the fluid (e.g., water, isopropyl alcohol), the molecules which condensate onto the surface of nanoparticles and cause their growth. CPC is suitable for aerosol samples, however, the knowledge about the solubility of particles is required. The measured concentration range is between 0 to ~250,000	CPC is widely used in aerosol studies, filter testing, monitoring of nanotechnological processes.

	particles/cm^3, where particle size can vary from 3 nm to 1 μm.	

1.2. Interaction of nanoparticles with cells

From a physical and chemical point of view, the interaction between cells (i.e., cell wall, membranes) and nanoparticles is based on van der Waals forces, electrostatic interactions, hydrogen bonding, and chemical reactions[258]. Once nanoparticles are introduced into a solution (i.e., cell-culture media in which experiment is performed, blood or other body fluids), they acquire different physicochemical properties due to adsorption of different molecules, including proteins that create so-called "protein corona"[259]. Three main factors influence the "identity" of nanoparticles and their interaction with cells are [260,261,262]:

- collective physicochemical properties, like size, shape, surface charge, etc. (aforementioned in section 1.1.3);
- biological factors like protein source (a type of medium in which nanoparticles are suspended) and protein abundance;
- experimental factors including osmolarity, ionic strength, temperature, etc.

Possible mechanisms of interaction between nanostructures and cells include uptake of the nanoparticles[263,264,265,266], contact killing[267,268], the influence that can arise from released species (e.g., ions)[13], and mechanical stress[269,270].

The first type of interaction is uptake that is a transfer of molecules or nanoparticles trough the membranes, both in active and passive manner[263]. Biological systems rely on their natural barrier in contact with the environment but eukaryotes and prokaryotes are very different in specific mechanisms.

The majority of molecules, drugs and small particles (size of up to a few nanometers) enter eukaryotic cells by diffusion as passive transport. Active uptake machinery is needed to transport target nanoparticles across the fluid plasma membrane. Five main endocytic mechanisms can be distinguished: phagocytosis, caveolin-mediated endocytosis, clathrin-mediated endocytosis, clathrin/caveolae-independent endocytosis, and macropinocytosis. Some references consider the last four mechanisms of endocytosis as the broadly defined process of pinocytosis, which is relatively common and occurs in many cell types, in contrast to phagocytosis which emerges in professional phagocytes. The uptake of nanoparticles plays a critical role in the design of drug delivery systems, especially in cancer treatment[271,272,273].

In the case of prokaryotes, nanoparticles have little chance to get through the intact bacterial cell wall, where peptidoglycan is present[263]. This is because the cell wall of bacteria exhibits small permeability; only objects of size below a few nanometers can diffuse through the cell wall[274]. Import of small molecules or peptides can occur, but such objects need to be degraded via extracellular enzymes (e.g., proteases). Then, small pieces can be taken up passively via channels in the membrane, or actively via importing pumps[275]. The entry of bigger particles is not possible without previous damage or destabilization of the cell wall (naturally, e.g., during a horizontal transfer of genes or artificially, e.g., due to electroporation or heat shock). Nonclassical variation of uptake observed in the case of metal- or metal-oxide nanoparticles (e.g., cobalt, iron, manganese oxide) is Trojan-horse-type uptake[276]. Nanostructures sneak inside the cell,

where they are packed into vesicles. Lower pH inside the lysosomes promotes further dissolution and ion release. The rapid increase of osmotic pressure may induce water uptake, swelling, causing eventually the burst of the vesicle with the release of toxic ions[263].

The alternative to active uptake is so-called adhesive interaction, with which nanostructures can penetrate cell membrane passively[277]. Unlike to aforementioned endocytic mechanisms, the nanostructures are not membrane-bound but rather free in the cytoplasm[278]. Interestingly, nanostructures of size up to 200 nm were found in red blood cells. Typical phagocytic receptors at the cell surface and intracellular structures required for the active transport were not identified, which suggests diffusion through membrane pores and passive entering by van der Waals or steric interactions[279]. The passive translocation of nanostructures through the lipid membrane of erythrocytes has been proposed by another group[280].

Contact killing or contact-mediated killing refers to the multistep mechanism of killing microbes. Contact killing comprises a few steps, however, there is no consensus as to the exact sequence of events[281,282,283], mainly due to lack of consistency in applied protocols, used microbial strains, and tested experimental conditions. Many research suggest that the mechanism is initiated by (i) dissolved ions into the medium that are causing (ii) cell damages, followed by cell membrane rupture. Perforated cell wall allows (iii) ions to diffuse inside and (iv) generate toxic radicals which lead to further damages and DNA degradation[281]. It should be stressed that most of the data are related to contact killing effect referring to copper nanoparticles[281,282,284,285,286,287] and silver nanoparticles[283,288,289,290]. However, there are reports suggesting an alternative mechanism of contact killing, namely local destabilization of cell envelope due to interactions with metal atoms. This causes loosening of the envelope structure and rupture of the cell due to internal pressure[291].

Release of chemical species or release mediated killing is related to the release of free ions from the nanoparticle surface or/and assistance of nanostructures in reducing oxygen and generation of free radicals that leads to oxidative stress. The produced reactive oxygen species (ROS) can irreversibly damage cells (e.g., their membrane and their cell wall, DNA, and mitochondria), resulting in cell death. Released ions can diffuse inside the cell and block the active center of enzymes, deactivating the functionality of the protein. There is plenty of recent reviews that focus on the toxic potential of materials at the nanolevel[292,293,294,295,296]. Exposure of the nanomaterial to UV can lead to activation of electron-hole pairs, and in consequence bond splitting and radical formation. Several characteristics of nanoparticles contribute to ROS generation which seems to be the best-known paradigm for nanotoxicity[293].

Mechanical killing is based on the physical killing of cells by mechanical rupture caused by sharp nanostructures. The first example of the nano-based antibacterial surface was discovered at the wings of the clanger cicada[270]. Such an exceptional surface is composed of nano-sized pillars that trap and kill microbes by pulling bacteria apart. This mechanism is of particular interest and will be discussed further in section 2.1.

Chemical reactions might also cause damages to the cell. From the more chemical perspective, a decrease in the size of the particle can lead to perturbation in electronic configuration due to discontinuous crystal planes or structural defects of

nanostructures[293,297]. This, in turn, can give rise to altered electronic properties of the nanoparticle and creation of the specific surface groups that can serve as reactive sites, i.e., electron-donor/acceptor active groups (chemically or physically activated).
Electron capture can contribute to the formation of superoxides, which can generate additional ROS through Fenton chemistry or dismutation. Another possibility is the presence of redox-cycling organic chemicals, especially in the case of particles that contain transition metals.
Surface groups (related to the type of material) can make nanoparticles more hydrophobic or hydrophilic, lipophobic or lipophilic. Hydrophobicity influences the interaction of nanoparticles with cell membranes/cell walls and determines the uptake[262] whereas hydrophilicity determines water suspendability.

1.3. Physical properties of nanoparticles in interaction with cells

The influence of the mechanical properties of the local environment is important in the case of cells. The effect of physical cues on eukaryotic cells has been neglected for a long time, however, two decades ago it became clear that mechanical factors can significantly influence cell behavior[298,299]. Microenvironment and mechanical properties have been recognized to have a great influence on development, differentiation, cell fate decisions, developmental potency, disease and regeneration of cells and tissues[300,301,302,303,304,305]. It was proved that cells respond to the external mechanical signals[306]. For instance, stem cells typically differentiate into osteoblasts when 2D environment is stiff, while lineage selection on soft substrate favors differentiation towards adipocytes[305].

The most important physical property defining the nanomaterial and influencing the interaction with cell (e.g., uptake, diffusion, transport, accumulation) is the size. The first key step of uptake is the physical interaction between nanostructure and the cell membrane. This can induce segregation and clustering of nanoobjects on the surface, which is followed by cell membrane response (lipid segregation, lipid-protein domain formation, the formation of membrane invaginations)[307]. Importantly, there exist scale rules within all biological systems: most membrane bilayers have a thickness of 4-10 nm, while the nuclear pole complex is measuring 80-120 nm in diameter[308]. Such macromolecular assemblies execute their size-restricted barrier function when nanostructures enter and exit the cell. In many nano-based systems (e.g., ZnO, Ag, carbon, TiO_2), smaller nanoparticles were proved to exhibit a higher antimicrobial activity[309]. Obviously, size affects whether a given particle can penetrate through the membrane and into the cell wall. However, it is not clear whether the observed size effect is solely related to increased surface area[309].

Impact of the aspect ratio (defined as the ratio of length to the width) of nanoparticles was recognized as a crucial factor in interaction with cells, especially in the uptake and transport. It was demonstrated that specific silica rod-shaped particles (fluorescently labeled) are preferentially taken up in A549 and HeLa cells. Particles with the aspect ratio of 2.1-2.5 were taken up in larger quantities (80-fold increase of the mean fluorescence intensity for A549 and 40-fold increase for HeLa cells)and faster compared to spherical particles, as well as longer and shorter length rods[310]. However, there were at least a few experimental studies demonstrating that rod-shaped nanoparticles undergo lower cellular uptake than spherical nanoparticles[311,312,313]. For instance, the uptake of spherical Au particles was 5-7 times faster compared to rod-shaped particles[314,311]. In another study, it was shown that Au nanorods of larger aspect ratio (studied aspect ratio

up to 4), were internalized slower than the shorter rods. Although researchers believe that such hindered uptake is due to the prolonged membrane wrapping time required for the longer rod-shaped particles, there are still discrepancies in the literature.
It is not yet fully understood how the physicochemical properties regulate the exocytosis, however, it seems that exocytosis is mainly impacted by size and aspect ratio. It was shown that spherical Au nanoparticles coated with transferrin (Tf-Au) nanoparticles were exocytosed in a linear relationship to size. The classic example is an unfavorable influence of fiber-like asbestos crystals in cells, the clearance of which is hindered[315]. Also in the case of multiwalled carbon nanotubes (with high aspect ratio), clearance proceeded at an extremely slow rate. The inability to efficiently remove the aggregated carbon nanotubes (in form of rigid and fiber-like structures) can lead to nanotoxicity by inducing so-called frustrated phagocytosis (the failure to wrap the nanotubes in phagosomes leads to the release of ROS species and hydrolytic enzymes, initiating chronic granulomatous inflammation)[316].

Also, other interactions with living cells and organisms are affected by the shape of the nanostructures. For instance, PEGylated Au nanorods were proved to achieve longer circulation in blood compared to PEGylated Au nanospheres that were taken up and accumulated to a larger extent[317,312]. Various types of functionalized carbon nanotubes of the cylindrical shape and high aspect ratio have been shown to penetrate cell membranes[318]. It is not yet established whether the shape affects nanotoxicity in bacteria as it does in eukaryotes. Investigation of silver nanoparticles against *Escherichia coli* revealed that nanoplates exhibited the highest antibacterial activity compared to spherical and rod-shaped nanostructures (probably due to high atomic density of facets). The effect of shape was also strongly obscured by cytotoxicity of material itself.
Agglomeration of nanoobjects is known to alter the physical and chemical properties of nanoparticles and in consequence affects the interaction with cells. Although very little is known on the correlation of shape and agglomeration state, reduced bacterial activity is rather attributed to nanostructure agglomeration[319]. Presumably, this may be related to the removal of nanoparticles from the medium. Consequently, such nanoparticle agglomerates may physically contact the cell surfaces in a different manner compared to dispersed nanoparticles[309].

Interestingly, the surface area, dissolvability, and degradability also have a significant impact on cells. Several investigations demonstrated that the biological implications of cell exposure to the insoluble nanostructures scale with the surface area rather than mass[320,321,322]. Moreover, the large surface can dramatically enhance the rate of dissolution, equilibrium solubility, the generation of reactive oxygen species (c.f. Chapter 1.2). Importantly, under certain conditions, the dissolution rate constant (k) of dissolvable nanomaterial is given by the equation: $k = A(D/V_s) \cdot h$, where A is the surface area of the particle, D is diffusion coefficient of a solute molecule, V_s is volume of the solution, and h is a thickness of diffusion layer[323]. Hence, nanoparticles are often expected to dissolve faster and to a greater extent compared to larger particles of the same materials[324]. The released ions can be utilized by the cell as a trace element or they may induce the toxicological effect[325].

Although our knowledge regarding the interaction and influence of nanoparticles on cells has advanced greatly in the past several years, much effort should be concentrated on both understanding and exploiting nanoparticles at the tissue and

subcellular levels. A thorough understanding of cellular behavior and safety lack systematic investigation so far. Besides the aforementioned, the chemical and physical properties of nanomaterials, also (nonobvious) bio-related factors impact the overall effect, i.e., cell-type (the type of cell line)[311,326], cell cycle[327,328], cell state (healthy vs cancer cell)[326]. All these are essential knowledge required for the development of safe nano-based approach in future applications.

1.4. Aim of the research and thesis outline

The main goal of this work was to examine the mechanical stress induced by nanoparticles on living cells. This constitutes a major step towards the understanding of physical interaction between nanostructures and cells. Knowledge on how exactly the physical aspect of nanostructures influence cells still remains elusive and underestimated. This aspect is of importance to further combine nanotechnology with biological systems.

Chapter 1 provides a general introduction to nanotechnology, nanoparticles and possible modes of interaction of nano-sized objects with cells. In Chapter 2, the main focus is on the investigation of the shape of ZnO nanoparticles in direct contact with cells. The first part of the experiments shows a detailed characterization of the nanostructure used further in biological experiments. In order to address the issue of mechanical stress induced by nanoparticles, various types of cells (bacterial, fungal, eukaryotic) were exposed to a large number of collisions with nanostructures of two different shapes: rounded ZnO nanoparticles and sharp ZnO nanorods. In this chapter, also static experiments with the nanoparticles are presented. Chapter 3 provides a broad overview of results collected to unveil phenotypic plasticity of Gram-negative bacteria that acquired mechanical resistance. Several experimental techniques were carefully chosen to reveal differences in viability, morphology and cell behavior of survivor bacteria. Chapter 4 constitutes the first step toward better understanding the genetic origin of changes in bacteria exposed to ZnO nanorods. DNA sequencing was used to investigate the possible emergence of mutations, and RNA sequencing was employed to examine gene expression profiles. Obtained results are discussed in the context of the acquisition of resistance against mechanical stress. Chapter 5 as a continuation of genetic studies, provides a general overview of ongoing projects related to whole transcriptome analysis (RNA-seq) of bacteria during exposure to ZnO nanorods and investigation of the mutation rate (DNA-seq). All findings are summarized in Chapter 6 that indicates the most important future directions of the research in the field of bacterial adaptation and summarizes the collected results presented in this thesis.

Chapter 2

Influence of ZnO nanoparticles on the viability of cells

This chapter describes the influence of the shape of ZnO nanoparticles on different types of cells: bacterial, fungal and eukaryotic. Sharp ZnO nanorods appeared more damaging compared to rounded ZnO nanoparticles in the case of cells with a thin cell wall (Gram-negative bacteria) or soft membranes (cancer cell lines). In contrast, Gram-positive bacteria, which possess a thicker cell wall, appeared more resistant to mechanical stress induced by sharp nanorods.

This chapter has been published as:

Kinga Matuła†, Łukasz Richter†, Witold Adamkiewicz, Bo Åkerström, Jan Paczesny, Robert Hołyst, Influence of nanomechanical stress induced by nanoparticles of different shape on viability of cells. *Soft Matte*r, 2016, 14;12(18).

2.1. Introduction

Evolution of bacteria under chemical pressure is currently in the spotlight due to the alarmingly fast acquisition of resistance to antibiotics and spreading of so-called "superbugs". On 18th of November 2015, the emergence of resistance against colistin was reported in The Lancet Infectious Diseases[329]. Colistin is used as a drug of the last resort – used when other antibiotics fail. Recent studies revealed that only 12 hours is sufficient for *Escherichia coli* to develop four-point functional mutation (in form of single nucleotide polymorphisms), which enable bacteria to survive two hundred higher concentration than the lethal dose of antibiotic[330]. There is also evidence that resistance would spread around the world and raised the spectra of untreatable infections[331].

There is a great need for the development of new antibacterial agents. It was well-recognized that nanoparticles, especially silver nanoparticles (Ag NPs), could have replaced antibiotics in some applications[332,333,334]. However, there are also worrying reports published on resistance against silver nanoparticles. Silver ions released from Ag nanoparticles can act similarly to antibiotics[335,336,337,338]. Nanoparticles can be perceived both, as chemical and physical factors affecting bacteria functioning, depending on the nature of interactions between nanomaterial and cells[263,339]. The possibility of utilization of nanoparticles in the various biological application requires detailed knowledge about the physical and chemical properties of nanostructures that can influence cells. Interestingly, the chemical effect of nanoparticles is deeply investigated in contrast to the physical aspect that is often neglected. We vest our hopes in nanostructures, especially regarding their non-chemical mechanisms of killing bacteria, e.g., contact killing[291,340,341] or mechanical puncturing[269,270,342].

Here, two exemplary nano-based approaches, that originate from the utilization of the physical aspect of nanostructures – shape, are introduced. The first, already mentioned concept, assumes the utilization of nanoparticles to support the development of antibacterial materials. For instance, surfaces can be covered with sharp nanoparticles to induce mechanical piercing of bacteria upon contact with the surface. Such nano-based materials can be applied in hospitals and public places, where sterility is desired. Examination of mechanical interaction of nanoparticles with cells can exclude possible induction of mechanical resistance of bacteria against nanostructures. The second application is related to transplantology, implantology, prosthetics, and cybernetics have started to merge very recently, giving a promise for the development of novel medical technologies. There are new possibilities for reparation or replacement of damaged organs. For instance, external cameras or sound processors can be connected directly to the brain of seeing- and hearing-disabled individuals in order to recover lost abilities or improve other functions of the body. To exploit these upcoming possibilities, there is a need to introduce nanodevices or nano-based products into living organisms and integrate them with tissues. Therefore, the second approach assumes probing physical interaction of nanoparticles with eukaryotic cells to choose the most demanded shape that will reduce the risk of death of cells upon direct contact.

Interestingly, the antibacterial effect of sharp nanostructures was found in nature. The surface of cicada wings is covered with a well-ordered pattern of nanopillars (Fig. 2.1). Ivanova and co-workers showed that the bacteria are mechanically damaged by the movement of the cicada wings and subsequent collisions with nanopillars[269,270]. The

authors claim that Gram-positive bacteria (*Bacillus subtilis*, *Pseudococcus maritimus,* and *Staphylococcus aureus*) have higher resistance in comparison to Gram-negative strains (*Branhamella catarrhalis*, *Escherichia coli*, and *Pseudomonas fluorescens*). The effect is caused by a more rigid cell wall of Gram-positive bacteria compared to Gram-negative strains.

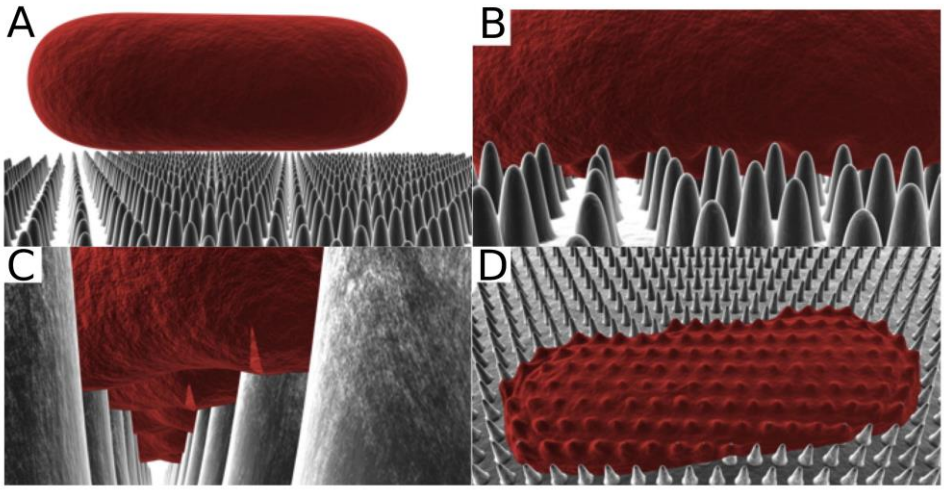

Fig. 2.1. Biophysical model of bacterial cell interactions with nanopatterned cicada wing surfaces. Adapted from reference[270] with permission from Elsevier.

Besides cicada wings, there are also many other examples of nano-based surfaces (Fig. 2.2) that were briefly reviewed by Tripathy et al.[342]. It was emphasized that optimal geometry and density of pattering are not known and still there is room for the development of cost-effective methods for fabrication of large bactericidal surfaces.

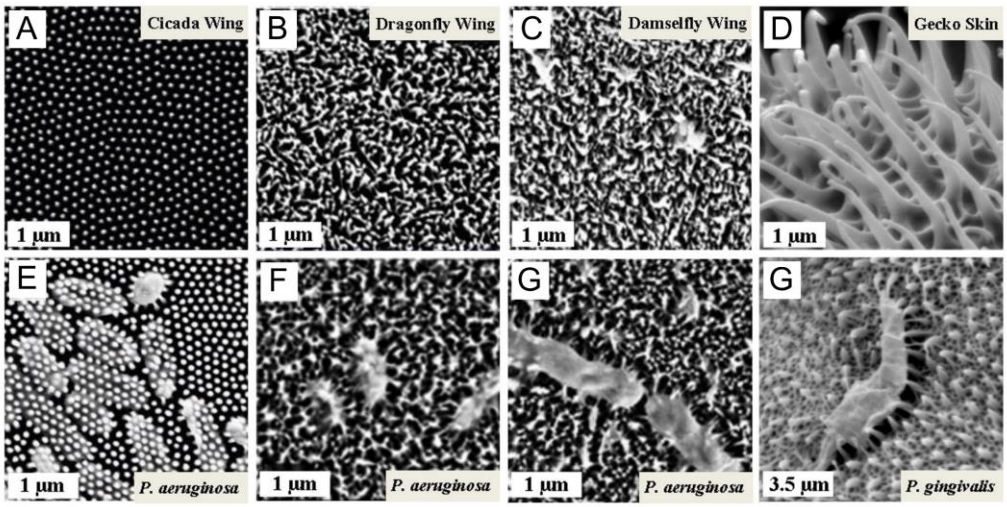

Fig. 2.2. Examples of natural antibacterial surfaces. (A) Cicada Wings (Psaltoda claripennis). (B) Dragonfly Wings (Diplacodes bipunctata). (C) Damselfly Wings (Calopteryx haemorrhoidalis). (D) Gecko Skin (Lucasium steindachneri). Adapted from reference[342] with permission from Elsevier.

In the case of synthesized nanoparticles, the dependence between size and cytotoxicity was investigated for different types of nanostructures[343,344,345,346]. This is a great challenge since the smaller the portion of matter becomes, the higher cytotoxicity is observed. Likewise, material composition, the shape, electronic structure, surface coatings, surface species (*e.g.,* metal-containing), the solubility of the nanoparticles and possible interactions with other environmental stimuli (e.g., UV activation) can trigger cytotoxicity[19,347,267,268,348,349]. Finally, different types of cells react in various ways to chemical and physical factors, thus they can experience different cytotoxicity upon exposure to nanoparticles[350].

The main challenge in the evaluation of the effect of the shape on the cytotoxicity of nanoparticles is that the published data seem inconsistent and they lack a systematic experimental approach. Some studies have shown the higher killing effect of sharp nanorods in comparison to more spherical nanoparticles. Rago *et al.* demonstrated that sharper needles (smaller diameter) have a higher potential for penetration of the bacterial cell wall[351]. Similar results were observed in the case of shape-dependent cytotoxicity on eukaryotic cells. Schaeublin *et al.* showed that gold nanorods have a higher cytotoxic effect on human skin cells in comparison to spherical gold nanoparticles[352]. Bhattacharya *et al.* confirmed the higher cytotoxicity of nanorods over nanospheres in peripheral mononuclear blood cells exposed to ZnO nanostructures[353]. However, Jain *et al.* investigated the impact of the ZnO nanorods on Gram-positive (*Staphylococcus aureus* and *Bacillus subtilis*) and Gram-negative (*Escherichia coli and Aerobacter aerogenes*) bacteria[354] and found that the Gram-positive strains are more sensitive to the ZnO nanorods. Reddy *et al.* observed a much higher influence of the ZnO nanoparticles (size around 13 nm) on *Staphylococcus aureus* (Gram-positive) comparing to *Escherichia coli* (Gram-negative)[355]. In contrast, Wahab *et al.* did not find any differences in the cytotoxicity of the ZnO nanoparticles (20-30 nm, 5-45 μg/mL) between Gram-positive and Gram-negative bacteria[356]. The reported differences in the observed effects of shape of nanoparticles may arise from the different mechanisms of interaction with living cells that are based on size, shape, surface modification, utilization of stabilization reagents and also concentration. For instance, in the studies by Jain *et al.* and by Reddy *et al.*, the main toxic effect was connected with the formation of free radicals at the surface of ZnO nanostructures and release of Zn^{2+} ions[354,355]. Li *et al.* claimed that Gram-negative bacteria are protected against a variety of relatively small molecules, such as antibiotics, detergents, digestive enzymes, dyes, and heavy metals by a lipopolysaccharide (LPS) layer in contrast to Gram-positive strains[17].
Therefore, it is justified to consider mechanical collisions as a factor that influences cell behavior and viability.

The main goal of the presented studies is to examine the mechanical stress induced by nanoparticles on living cells. This constitutes a major step towards the better understanding of the physical interactions between nanostructures and cells. The main focus is on the evaluation of the cell viability upon exposure to nanoparticles of two different shapes. To address this issue, different types of cells (bacterial, fungal, eukaryotic) were exposed in a stirred medium to a large number of collisions with rounded ZnO nanoparticles (NP) or ZnO nanorods (NR). Zinc oxide was chosen for the following reasons:

- ZnO nanoparticles exhibit low cytotoxicity[357,358] and are used as drug carriers, in cosmetics, and fillings in medical materials[359]. Low cytotoxicity of the material

itself gives an opportunity to investigate size-dependent cytotoxicity that is not obscured by other effects.

- ZnO is one of the most attractive materials for the design of nano-based optical device since it has desired optoelectronic properties. ZnO is an n-type semiconductor, which is photoactive under near UV light. The wide bandgap of ZnO of 3.37 eV at room temperature is optimal for short-wavelength optical device applications[360,361]. ZnO has a potential application as photocatalyst[362,363] or nanofilters[364], in photovoltaics[364] and also as a gas sensors[365]. Both, low cytotoxicity and potential application in the fabrication of nanodevices make ZnO a great candidate for the preparation of biocompatible nanosystems[94,366].
- An additional asset is that the synthesis of ZnO nanostructures is relatively simple, easy to scale up and allows to obtain nanoparticles of different sizes.

The possibility of diffusion of nanoparticles through pores in the cell wall of prokaryotes and the uptake by eukaryotic cells during the experiments were minimized by choosing this size range of ZnO nanostructures[12,35,36]. Gram-positive (*Staphylococcus epidermidis*, *Corynebacterium glutamicum*) and Gram-negative (*Escherichia coli*, *Enterobacter aerogenes*) bacteria, as well as eukaryotic cells of various origin, were studied. The latter was represented by yeast (*Saccharomyces cerevisiae*), the human cell lines liver cancer $HepG_2$-cells, lung cancer A594-cells, immortalized human keratinocytes HaCaT and A431-cells, as well as primary human peripheral blood mononuclear cells (PBMC) isolated from human plasma.

2.2. Characterization of ZnO nanostructures

Investigation of mechanical stress induced by ZnO nanostructures required preparation and characterization of the material for the experiments with cells. Two types of ZnO nanostructures were used: sharp nanorods (NR) and shapeless, resembling spherical nanostructures (NP). The ZnO nanopowder that consisted of rounded nanoparticles was purchased (AlfaAesar), and ZnO nanorods were prepared using aqueous chemical growth (ACG) method[367]. According to the ACG synthesis, ZnO crystallizes as the sea-urchin-like structures. The obtained product was subjected to sonication to disrupt claw-like structures and obtain single, separated needles. Crucially, both types of ZnO nanostructures were used without any additional stabilization agents and surface modifications (i.e., coatings). These two aspects are crucial, regarding possible cytotoxic effects that might arise from further modifications of the product and not necessarily from the bare material itself[368]. Crystallographic structure, surface area, size and concentration of ZnO NP and ZnO NR were adjusted to be as similar as possible in order to decrease the potential interference in shape-dependent effect on cells.

The next step comprised a detailed characterization of ZnO NP and ZnO NR. Scanning electron microscopy (SEM) was used as the most direct technique to evaluate the shape of nanostructures (Fig. 2.3B, C). The zeta potential was investigated in order to assess the stability of nanostructures and additionally, dynamic light scattering mode allowed to measure the hydrodynamic diameter. X-ray diffraction enabled an analysis of the crystallographic structure of ZnO NP and ZnO NR. Results obtained by means of SEM are summarized in Tab. 2.1 which proved that ZnO NP and synthesized ZnO NR are comparable regarding the volume and active surface area, with the main difference in shape.

Table 2.1. Parameters evaluated by SEM imaging (length, width, diameter), dynamic light scattering and measured zeta potential for two types of ZnO nanostructures. The shape of ZnO NR was approximated with the spheroid and ZnO NP with the sphere.

Parameter	ZnO nanoparticles (NP)	ZnO nanorods (NR)
Scanning electron microscopy		
Length (nm)	-	312 ± 171
Width (nm)	-	76 ± 21
Diameter (nm)	122 ± 40	-
Calculated volume (μm^3)	$9.51\ 10^{-4} \pm 9.35\ 10^{-4}$	$9.44\ 10^{-4} \pm 7.34\ 10^{-4}$
Calculated active surface area (μm^2)	$4.68\ 10^{-2} \pm 3.07\ 10^{-2}$	$5.99\ 10^{-2} \pm 3.46\ 10^{-2}$
Zeta potential measurements		
Zeta potential (mV)	-5.6 ± 5.0	-12.0 ± 4.3
Dynamic light scattering		
Hydrodynamic diameter (nm)	322 ± 151 nm	732 ± 130 nm.

The hydrodynamic diameter measured for ZnO NP was highly polydisperse, what was in line with SEM observations. However, the most striking is the high value of the hydrodynamic diameter of ZnO NP and NR that arose from the fitting procedure – particles were assumed to be spherical, which made the estimation subjected to error. ZnO NR are nonsymmetrical, and consequently, the rotation along short axis (width) increases the volume occupied by single nanostructures. This is reflected in much larger hydrodynamic diameter compared to SEM results.

Zeta potential is electrostatic potential at the electrical double layer that is surrounding a nanostructure in solution. The zeta potential values between -10 mV and +10 mV are considered as almost neutral, while the values less than -30 mV or greater than +30 mV are regarded as strongly anionic and cationic, respectively. Since most of the cells possess negatively charged membranes, zeta potential can trigger the tendency of nanoparticles to permeate membranes. Importantly, the cationic nanoparticles display a higher ability connected with cell wall disruption[158]. Arakha et al. studied thoroughly the influence of zeta potential on the cytotoxicity. Particles with negative surface potential exhibit an insignificant antimicrobial propensity compared to particles of the same size but positively charge[369]. Similar results were reported for engineered, Gram-selective gold nanoparticles (with mixed-charge) obtained by tuning the balance of surface charge[156].
Obtained zeta potential values –5.6 ± 5.0 mV for ZnO NP and -12.0 ± 4. mV for ZnO NR can be considered as approximately neutral and relatively safe for cells.

X-ray diffraction (XRD) revealed that both ZnO NP and ZnO NR had hexagonal structure: $P6_3mc$ group (see Fig. 2.3A). This was of main concern regarding ZnO NR synthesis since different crystallographic planes of ZnO possess different chemical and photochemical activity, which could significantly influence cytotoxicity[370]. The broadening of X-ray signals observed in the powder diffraction patterns corresponded to the smallest characteristic size of crystallites (around 50 nm) in the case of both ZnO NP and ZnO NR[371,372].

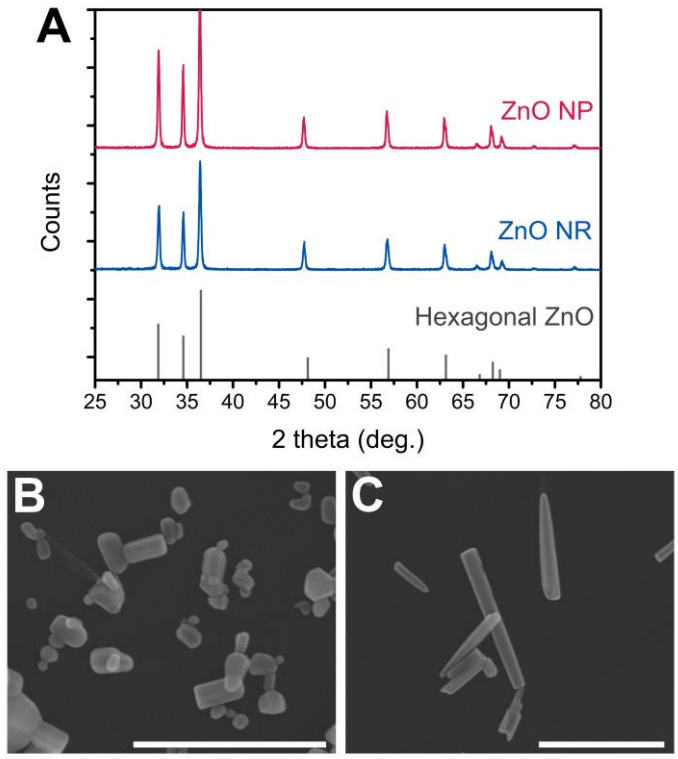

Fig. 2.3. Characterization of ZnO nanostructures used in the experiments with cells. (A) XRD patterns of studied rounded ZnO nanoparticles (NP) and ZnO nanorods (NR). SEM pictures present (B) ZnO NP, and (C) ZnO NR. Scale bars correspond to 500 nm.

The cytotoxicity of the material itself could have obscured the effect of the shape of nanoparticles. Therefore, the large size of nanostructures, negative zeta potential and the absence of coating ligand were beneficial and facilitated the low toxicity of the material.

To conclude, the synthesis of ZnO nanorods was optimized in order to match the surface area of rounded ZnO nanoparticles. XRD revealed that the nanostructures possessed the same crystallographic structure. SEM is a more reliable technique in the evaluation of the size of ZnO NP and ZnO NR.

2.3. Influence of Zn^{2+} released from ZnO nanostructures

The influence of the shape of ZnO nanoparticles on cells could be obscured by the chemical effects of Zn^{2+} ions released from the nanostructures. Therefore, it was crucial to examine: i) the amount of Zn^{2+} ions present in the medium, and ii) their effect on the growth of cells. Before the experimental investigation of the dissolution of ZnO NP and ZnO NR, literature was carefully studied to gain the first estimation of the amount of Zn^{2+}that could be expected in a water-based solution.

There is a number of publications that are focused on the influence of solubility of ZnO and the dissolution of ZnO nanostructures. Reed *et al.* studied the solubility of nano-ZnO in ultrapure water and in cell culture media: RPMI-600 and Dulbecco's modified

Eagle's medium[373]. The highest concentration of Zn^{2+} reported was around 30 µg/mL, however, in most of the cases, it did not exceed 10 µg/mL. Wong *et al.* found that the concentration of dissolved Zn^{2+} from nano ZnO in seawater was smaller than 4 µg/mL[374]. The value of dissolution of oxide particles, reported by Brunner et al., was 4.2 µg/mL of Zn^{2+} due to the dissolution of ZnO in 18°C[276]. Franklin *et al.* investigated the cytotoxic impact of nanoparticulate ZnO, bulk ZnO, and $ZnCl_2$ on freshwater microalga (*Pseudokirchneriella subcapitata*)[375]. In the case of suspension with a final concentration of 100 mg/L of both, bulk and nanoparticulate ZnO, the concentration of Zn^{2+} was around 15 µg/mL in pH around 7.5. David *et al.* demonstrated the first application of the electroanalytical technique AGNES to measure the concentration of Zn^{2+} in aqueous solution with ZnO nanoparticles[376]. Interestingly, the authors highlighted the high sensitivity of the solubility measurements that can be influenced by temperature, pH, medium composition, prior preparation of a sample and procedure performed before the elemental analysis. The dependence between size and dissolution of characterized ZnO nanoparticles at circumneutral pH was investigated by Mudunkotuwa et al[377]. Two crucial observations were reported: i) the smaller the ZnO particles were, the higher amount of Zn^{2+} ions was in solution was measured; ii) the presence of citric acid significantly increased dissolution of ZnO nanostructures of all sizes. The measured concentration of Zn^{2+} after 24-hour incubation of aqueous suspension of ZnO nanostructures with diameter from 47±7 to 130±21 nm at initial pH of 7.5, was in the range of 4.4±0.1to 3.4±0.1 µg/mL, respectively. Bian et al. measured dissolution of ZnO nanoparticles of different sizes, for low and high pH, with and without the addition of humic acid. For nanoparticles with diameters of 15±4 to 241±115 nm, the amount of Zn^{2+} present in solution (without the addition of humic acid) was between 22±1 and 10±1mg/L, respectively[378]. To summarize, the expected concentration of Zn^{2+} released form ZnO nanoparticles should be in the range of 4-30 µg/mL.

The amount of Zn^{2+} ions released from ZnO NP and ZnO NR resuspended in the medium to the final concentration of 1 mg/mL was measured after 24-hour incubation. LB medium (a medium used to culture bacteria) and MiliQ water were used to test the dissolution of nanostructures. The dissolution was tested at 37°C and intensive mixing (200 rpm) due to the fact that culturing of bacteria and eukaryotic cells require a higher temperature. Additionally, in the case of microbes, intensive shaking is necessary to prevent sedimentation. Spectrophotometric titration in the presence of eriochrome black T indicator was used to measure the amount of Zn^{2+} in the supernatant obtained after centrifugation of ZnO NP and ZnO NR. All interfering ions were complexed by CN^- ions, while all Zn^{2+} ions were released from such complexes after addition of formaldehyde. The experimental results are summarized in Table 2.2.

Table 2.2. Amount of Zn^{2+} ions present in suspensions of ZnO NP and ZnO NR (final concentration of 1mg/mL) after 24-hour incubation.

	ZnO NP	ZnO NR
MiliQ water	18.7 ± 0.9 µg/mL	16.6 ± 0.6 µg/mL
LB medium	44.6 ± 1.6 µg/mL	38.0 ± 1.5 µg/mL

The amount of Zn^{2+} ions is higher in the case of LB medium in comparison to MiliQ water. The reason for such a result is that the main component of LB medium is yeast extract that is a source of additional Zn^{2+}contributing to the final concentration measured by spectrophotometric titration.

After investigation of the dissolution of ZnO NP and ZnO NR, the effect of released Zn^{2+} was investigated on living cells. To predict the worst-case scenario, even higher concentration (50 µg/mL) than determined in LB medium was used. Two types of experiments were performed: with a small and large starting amount of inoculum (inoculum refers to a small portion of medium with bacteria that is used to start a new culture) at the beginning of the treatment. The goal was to observe the difference in growth curves between control bacteria and the cells exposed to Zn^{2+}.
During the experiment with the small number of cells, optical density (OD_{600}) at 600 nm was measured. OD_{600} corresponds to the number of bacteria in the medium. The OD measurement is based on the amount of light scattered by the cells in the suspension. Hence, the higher the OD_{600} value, the higher the number of cells is present in the sample. However, it should be stressed that OD measurements are not possible in the case of fully opaque liquids.

In the case of Gram-negative strains (*Escherichia coli*, *Enterobacter aerogenes*), it was possible to start and test the effect of Zn^{2+} with a very small amount of starting inoculum (OD_{600}=0.01). Gram-positive strains (Staphylococcus epidermidis, Corynebacterium glutamicum) are generally more susceptible to the presence of different types of ions, surfactants, antibiotics, digestive enzymes[379]. Therefore, the starting OD was higher (OD_{600}=0.03-0.05) because, in the case of OD_{600}=0.01-0.02, the growth of bacteria was completely inhibited over time. To sum up, zinc ions had a small influence on Gram-negative bacteria, whereas the growth of Gram-positive strains was limited, reflecting a strong chemical influence of Zn^{2+} (Fig. 2.4).

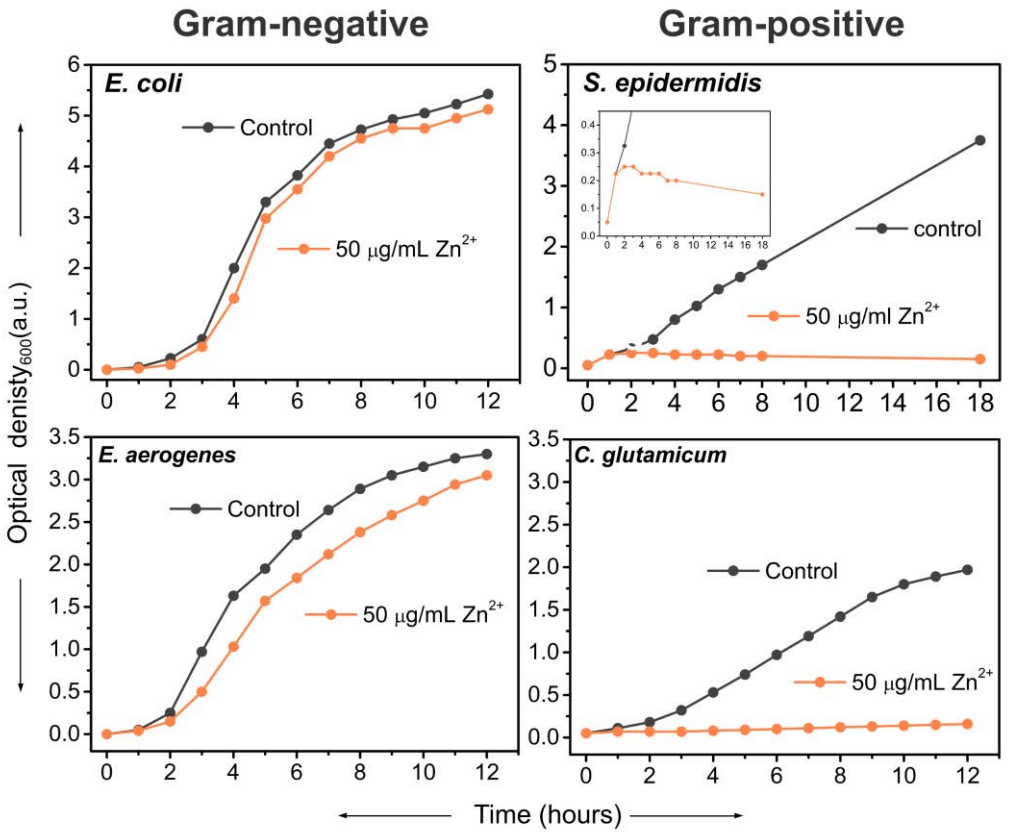

Fig. 2.4. The influence of Zn^{2+} **ions (concentration of 50 μg/mL) on** *E. coli*, *S. epidermidis*, *E. aerogenes,* and *C. glutamicum* depicted as changes of OD_{600} of cultures over time. In the case of Gram-negative strains the initial OD_{600}=0.01, and for Gram-positive strains OD_{600}=0.03-0.05 due to higher susceptibility to zinc ions.

In the next step, the exposure to Zn^{2+} ions was investigated only on two exemplary strains: *E. coli* strain and *S. epidermidis.* Now the starting amount of bacteria was increased. Enumeration of the bacteria was performed using colony plating method. Typically, small aliquots of bacterial suspensions were taken from the batches, diluted and pipetted onto agar plates with a solid medium for further incubation. Then, a single colony forming units (one colony corresponds to one bacterium) were counted. The results are depicted below as the change in the number of colonies in time (Fig. 2.5). In the case of *E. coli*, the supplementation of the medium with Zn^{2+} ions did not harm the cells. The growth of the bacteria was even accelerated after 12 hours (Fig. 2.5A). It can be explained by the fact that zinc plays a key role in different cellular processes like DNA and RNA replication, cellular respiration, protein synthesis, and intracellular signaling. Zinc is crucial for most classes of enzymes as a cofactor, however, a too high level can be potentially cytotoxic[380,381]. In contrast, the presence of Zn^{2+} ions had a bacteriostatic effect on *S. epidermidis*, i.e., the number of CFU was stable over the 48 hours during the experiments (Fig. 2.5B).

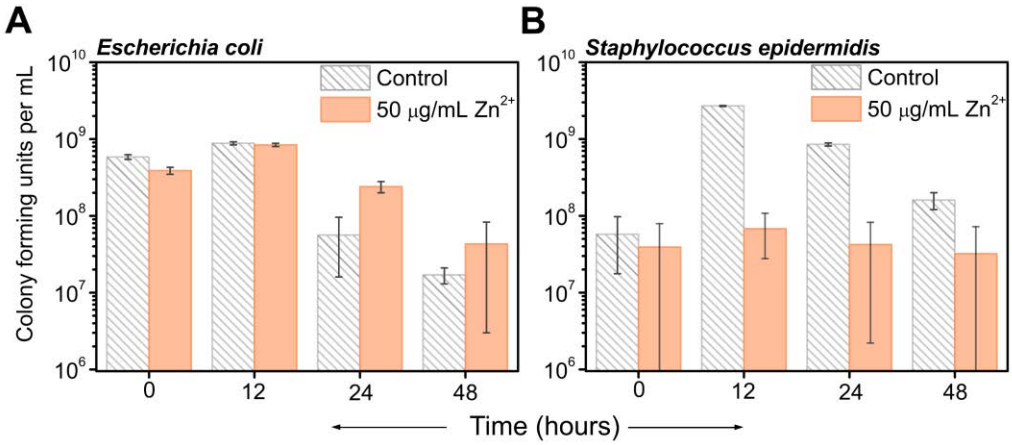

Fig. 2.5. The influence of Zn^{2+} **ions (concentration of 50 μg/mL) on** (A) *E. coli*, (B) *S. epidermidis*, depicted as the change in the number of colonies forming units over time. The starting OD in both cases was OD=1.0.

The viability experiment with the small (Fig. 2.6A) and large starting number of cells (Fig. 2.6B) was also performed for fungi. *Saccharomyces cerevisiae* is considered as a model, eukaryotic cell organism[382]. However, it is also a fungal cell that possesses a cell wall composed of chitin, β-glucans, and mannoproteins[383]. Hence, *S. cerevisiae* constitutes a perfect link between bacteria that possess a cell wall, and eukaryotes that are cell wall-less. *S. cerevisiae* grows in a similar manner to bacteria – it grows in medium, creating a cell suspension and forms colonies when plated on the solid medium. Interestingly, the effect of Zn^{2+} on *S. cerevisiae* was positive, especially in the case of the OD measurements with the small initial number of the cells. Here, should be highlighted that the favorable effect of Zn ions is well known and described in the literature. Supplementation with Zn^{2+} improves yeast growth, viability, resistance to stress and enhance fermentation performance in the brewery and other industrial applications[384].

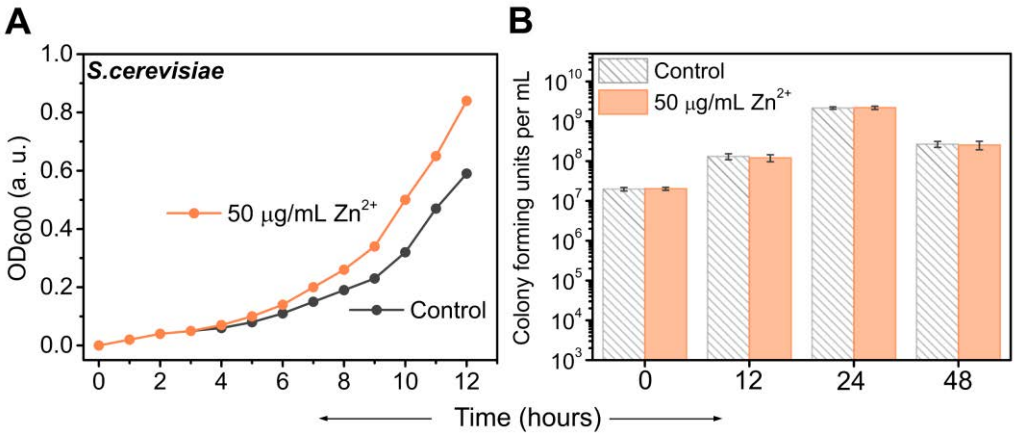

Fig. 2.6. The influence of Zn^{2+} **ions (concentration of 50 μg/mL) on** *S. cerevisiae*. (A) Change of OD_{600} of culture over time for a small starting number of the cell, the initial OD_{600}=0.01. (B) The change in the number of colonies forming units over time. The starting OD was OD_{600}=1.0.

To summarize, the amount of Zn^{2+} released from ZnO NP and ZnO NR was measured in MiliQ water and LB medium. To investigate the influence of the highest possible concentration of Zn^{2+}, the bacteria, and fungal cells were exposed to the concentration of 50 µg/mL. The experiments were performed for both small and large initial numbers of cells. In general, Gram-positive strains exhibited high susceptibility to the presence of Zn^{2+} in the medium. In contrast, Gram-negative strains are less vulnerable to exposure to the ions released. Moreover, for the higher cell number, the growth can be even supported. This is related to the presence of LPS layer present in Gram-negative bacteria, which acts as a scavenger and protects cells from small, harmful species. In contrast, Gram-positive bacteria do not possess LPS layer.

2.4. Influence of ZnO nanostructures on prokaryotes and eukaryotes

In this section, the influence of nanomechanical stress – physical stress induced by nanostructures, is described. ZnO nanoparticles and ZnO nanorods with the matching surface area and the same crystallographic structure are tested against bacteria, fungi, and eukaryotes of various origins. Two Gram-negative bacterial strains (*Escherichia coli, Enterobacter aerogenes*), two Gram-positive bacterial strains (*Staphylococcus epidermidis, Corynebacterium glutamicum*) were chosen. Eukaryotic systems used in the experiments were varying from relatively simple (yeast *Saccharomyces cerevisiae*), to immortalized cell lines: liver cancer $HepG_2$-cells, lung cancer A594-cells, human immortalized keratinocytes HaCaT-cells, human epidermoid carcinoma A431-cells, and peripheral blood mononuclear cells (PBMC) isolated from human plasma. Key questions addressed here are: i) do cells "feel" the difference between the shapes of nanoparticles, ii) how and in which fields the obtained knowledge can be further exploited.

2.4.1. Prokaryotes – exposure in dynamic conditions

The critical issue in the case of the experiments with ZnO nanoparticles was the choice of the concentration. Yamamoto et al. reported that ZnO particles of a size of 100 nm exhibit cytotoxicity to *E. coli* in concentrations of around 0.1 mg/mL, whereas for structures of size of 500 nm the safe concentration is around 10 mg/mL[343]. It was proved by Brayner and coworkers that the concentration higher than 1.3 mM causes damages of *E. coli* exposed to spherical particles of a diameter of around 15 nm[385] which gives 0.1 mg/mL after recalculation.

The size of ZnO nanoparticles prepared for the examination of the influence of the nanomechanical stress was in the range investigated by Yamamoto. Most of the experiments were performed for the concentration of 1 mg/mL for both ZnO nanoparticles and ZnO nanorods. The choice of such concentration assured low cytotoxicity of the material itself and limited uptake in the case of the experiments with eukaryotes. Moreover, Rago et al. reported that for a similar ZnO nanoparticle system, the influence of reactive oxygen species (ROS) was undetectable[351].

The viability of bacteria depends on the structure of a cell envelope that is represented in Fig. 2.7. The cell wall is the first stress-bearing barrier that protects the interior of the bacterial cell from a harsh and unpredictable environment. The cell envelope provides structural integrity and dictates the shape of the bacterium. In 1884 Christian Gram developed a staining method (will be also discussed in section 3.3) that allowed

classifying bacteria into two major groups based on the structure of the cell wall: Gram-negative and Gram-positive bacteria.

The cell envelope of Gram-negative bacteria, for example, *Escherichia coli*, is composed of the phospholipidic inner membrane (also called the cytoplasmic membrane); periplasmic space which is a gel-like structure in with a rigid peptidoglycan layer is located, and an outer membrane formed by phospholipids and lipopolysaccharides. Peptidoglycan (murein) is a mesh-like structure formed by glycan strands of N-acetylmuramic acid and N-acetylglucosamine residues cross-linked by short peptide chains[386,387]. This peptidoglycan that determines stiffness and mechanical resistance. Murein is a minor component of the cell envelope of Gram-negative bacteria (<10%)[388]. In contrast, Gram-positive bacteria, such as *Staphylococcus epidermidis*, possess a cytoplasmic membrane along with a thick layer of peptidoglycan(~30-70%)[387,388,389,390].

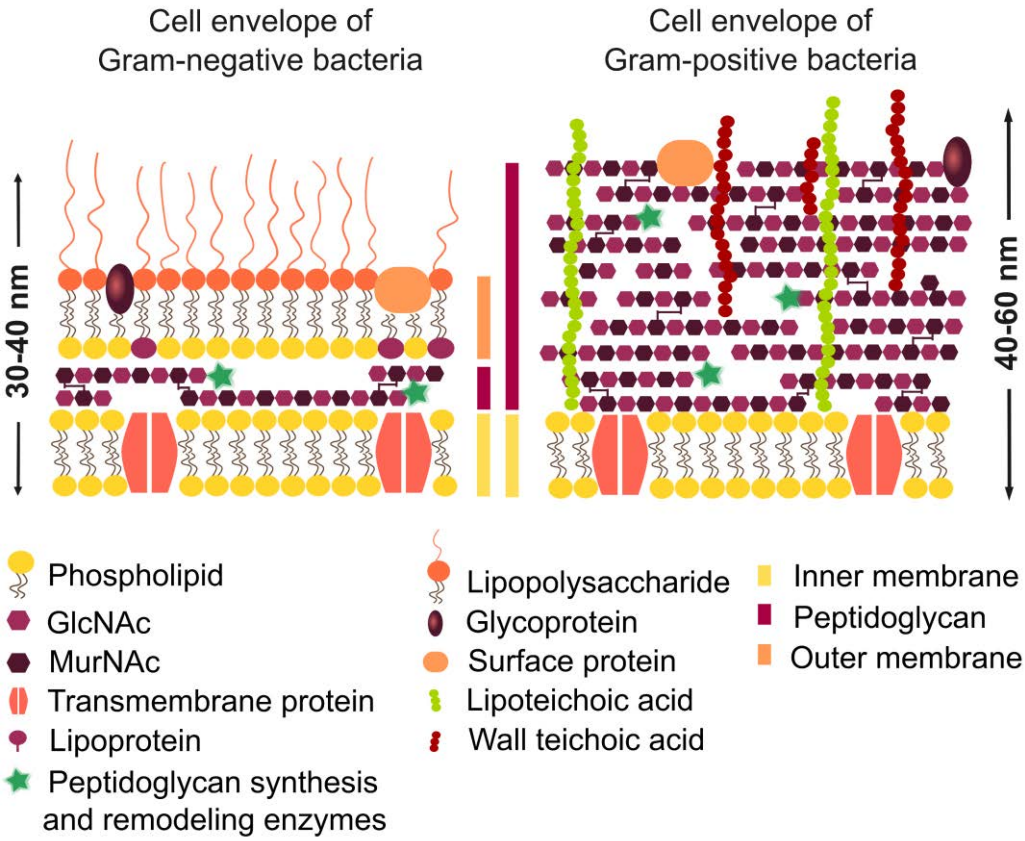

Fig. 2.7. Schematic comparison of the cell wall structure of Gram-negative and Gram-positive bacteria. GlcNAc denotes N-acetyl-glucosamine and MurNAc denotes N-acetyl-muramic.

Since the cell wall is required for bacterial survival, a number of various antibiotics (for example penicillins, cephalosporins, glycopeptides, carbapenems) stop bacterial infections by interfering with proteins involved with the cell wall synthesis, while having no effects on human cells (which do not have the cell wall)[390]. Two main important aspects are taken into experimental consideration i) Gram-negative bacteria possess

lipopolysaccharide (LPS) that provides protection against ions and toxic molecules[379]; ii) Gram-positive bacteria are more mechanically resistant than Gram-negative bacteria, due to a thick layer of murein. The lack of the outer membrane in the case Gram-positive strains leads to higher susceptibility to Zn^{2+} ions. This statement is supported by experiments described in the previous section (Fig. 2.4) where the bacteria were exposed in the medium supplemented with Zn^{2+} ions.

To check the effect of nanomechanical stress induced by ZnO nanostructures, the number of colony forming units (CFU) was monitored during 48 hours of the exposure (Fig. 2.8). The shape of sharp ZnO NR facilitated the mechanical puncturing of the bacteria over time. In the case of *E. coli* and *E. aerogenes*, which are Gram-negative strains, the number of viable cells was significantly lower in the samples exposed to ZnO nanorods compared to rounded ZnO nanoparticles. The cell wall with the thinner layer of peptidoglycan of these bacteria exhibits greater vulnerability to mechanical damages in comparison to Gram-positive bacteria. SEM images presented in Fig. 2.9, revealed many *E. coli* cells impaled onto ZnO NR. SEM analysis of the specimen supports the statement based on killing the bacteria via the nanomechanical puncturing[391].

The effect of ZnO NP and ZnO NR for both Gram-positive strains, *C. glutamicum,* and *S. epidermidis*, was similar. The differences between the number of the bacteria after exposure to ZnO NP and ZnO NR were not statistically significant because of the thicker layer of peptidoglycan within the cell wall, which makes the cells more mechanically resistant. The observed decrease of more than one order of magnitude in the number of CFU for treated bacteria compared to control (without any ZnO) was a result of the presence of Zn^{2+}(c.f. section 2.3). The true effect of the nanomechanical stress on Gram-positive bacteria was obscured by the greater susceptibility to the presence of Zn^{2+} ions[391].

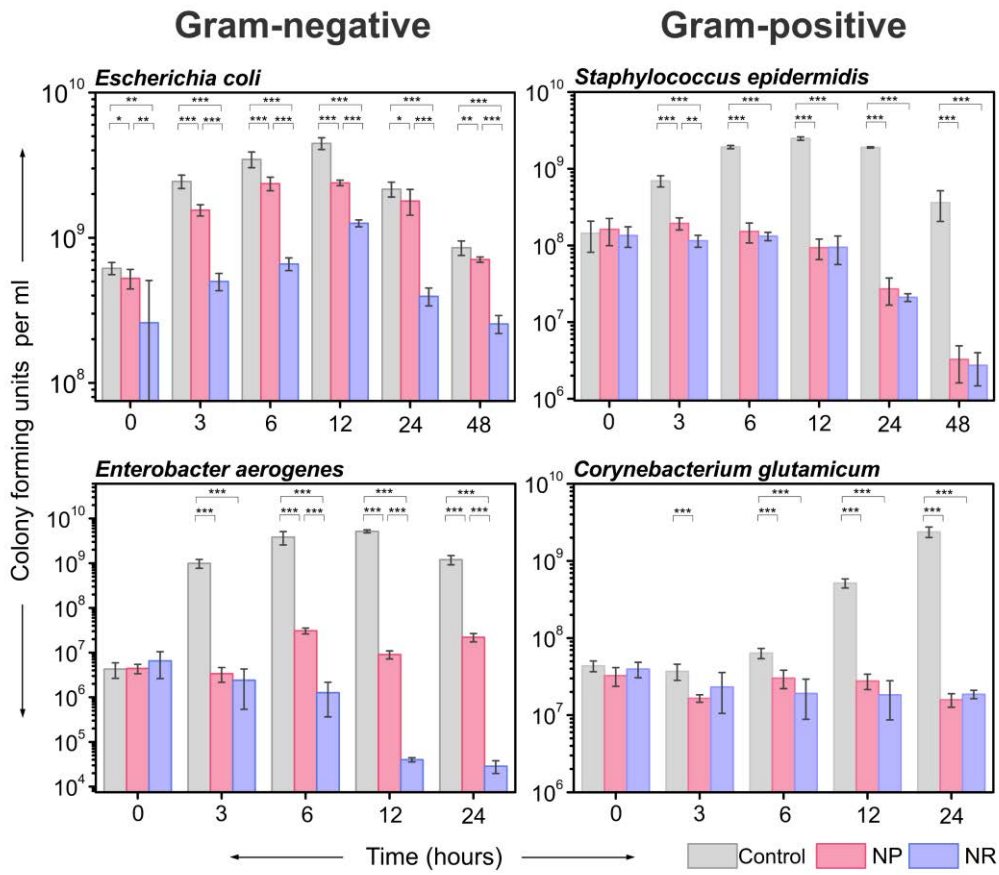

Fig. 2.8. Influence of rounded ZnO nanoparticles (NP) and ZnO nanorods (NR) on Gram-negative bacteria: *E. coli*, *E. aerogenes* and Gram-positive strains *S. epidermidis*, *C. glutamicum* (dynamic exposure, 200 rpm). Plots represent differences expressed in colony forming units per ml over time after the exposure of the bacteria to ZnO NP and NR (the concentration of 1 mg/ml). * $P < 0.05$; ** $P < 0.01$; *** $P < 0.001$.

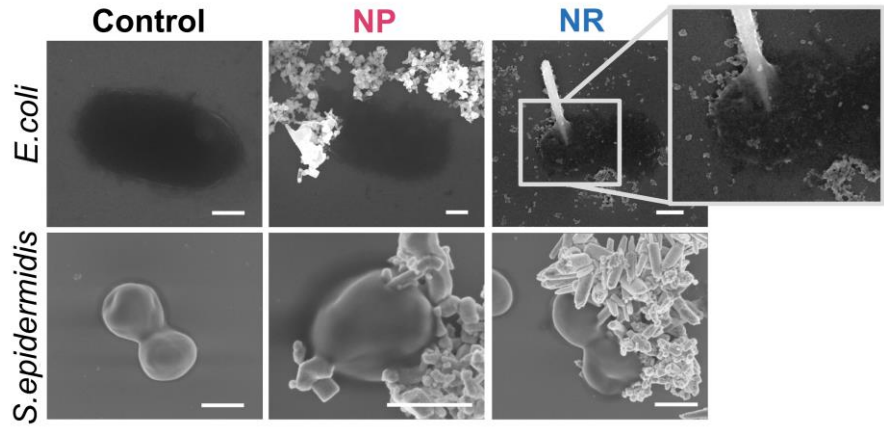

Fig. 2.9. SEM images of *E. coli* and *S. epidermidis* after the exposure to rounded ZnO nanoparticles (NP) and ZnO nanorods (NR). The inset shows a single *E. coli* bacterium pierced by a single ZnO nanorod. Scale bars correspond to 500 nm.

Summarizing this section, ZnO nanorods appeared more damaging compared to spherical particles against bacteria with the thin cell wall. This is due to the increased probability of mechanical damage caused by nanorods upon piercing of the cell wall and membrane. The bacteria with the thicker cell wall do not experience the difference in the shape of the nanostructures due to the stiffer cell wall[391].

2.4.2. Prokaryotes – exposure in static conditions

ZnO nanorods (NR) as more elongated structures are expected to form a less stable suspension. Such nanostructures could deposit on the surface of the bacteria more effectively, causing more damages in comparison to rounded ZnO nanostructures (NP). To prove that mechanical stress induced by nanostructure, and not colloidal instability was, in fact, the reason for the observed decrease in the number of the cells, the experiment in static condition was performed.

The bacterial suspension was spread uniformly on the surface of solid agar medium in order to form separated bacterial colonies (Fig. 2.10A). Subsequently, the suspensions of ZnO NR and ZnO NP in the medium were spray-deposited onto the surface of solid medium with prior seeded bacteria. The coverage of the surface by the nanostructure was examined by SEM imaging (Fig. 2.10C). The amount of ZnO NP and ZnO NR was validated and adjusted to induce static contact between the nanostructures and the bacteria and mimic the effect of colloidal instability. No statistically significant effect was observed after the 24-hour incubation of *E. coli* together with ZnO NP and ZnO NR (Fig. 2.10B). Only in the case of incubation of Gram-positive strain *S. epidermidis* with spray-deposited nanostructures, the decrease in range of 25% in the number of counted colonies was noticed compared to control (without ZnO). The effect can be explained by the higher susceptibility of *S. epidermidis* to the presence of Zn^{2+} ions.
The experiment demonstrated the importance of the damaging impact of the nanostructures induced by dynamic conditions. The additional experiment was performed in order to further clarify the importance of dynamic conditions applied during the experiment. Therefore, the liquid agar medium was mixed with the nanostructures together with the bacteria to embed, both the nanoobjects and microbes in the matrix. The highest concentration reached in the medium was around 1 mg/mL. Even higher concentration was tested, however, the nanostructures were not evenly distributed in agarose matrix and vast majority deposed at the bottom of the Petri dish. No significant differences in the number of colonies were reported for *E. coli* in the case of plates containing 1 mg/mL of the nanostructure in comparison to control plates (Fig. 2.11). *S. epidermidis* again appeared to be more vulnerable to the presence of Zn^{2+} ions within the solid medium. The colonies which grew inside the matrix with embedded ZnO nanoparticles and ZnO nanorods were extremely small. Since they were hardly visible, it appeared impossible to take an informative digital picture. The results were in line with other investigations, which proved that Zn^{2+} ions block the growth of *S. epidermidis.*

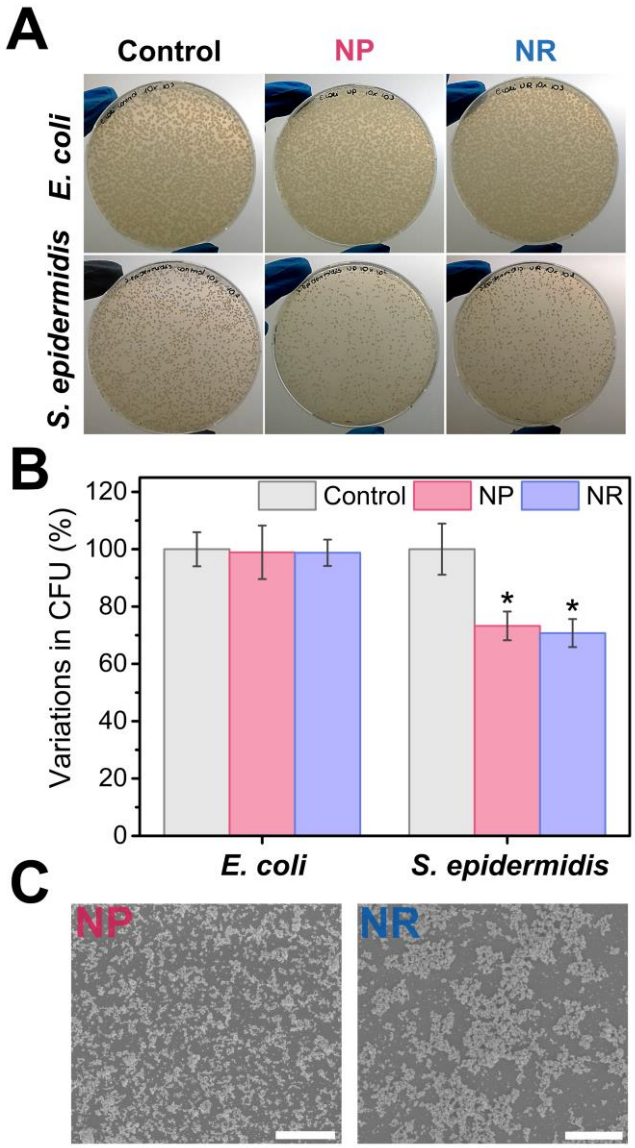

Fig. 2.10. Results of the control experiments in which no dynamic interactions between ZnO nanostructures and the bacteria were applied. (A-B) No effect of shape was observed upon exposure to the nanoparticles in static conditions. Representative pictures of agar plates onto which *E. coli* and *S. epidermidis* were first seeded and directly afterward rounded ZnO nanoparticles (NP) and ZnO nanorods (NR) were spray-deposited, * $P < 0.05$. (C) The amount of deposited ZnO nanostructures on the surface of the agar plates is presented in SEM pictures. Scale bars correspond to 20 μm (left, NP) and 50 μm (right, NR).

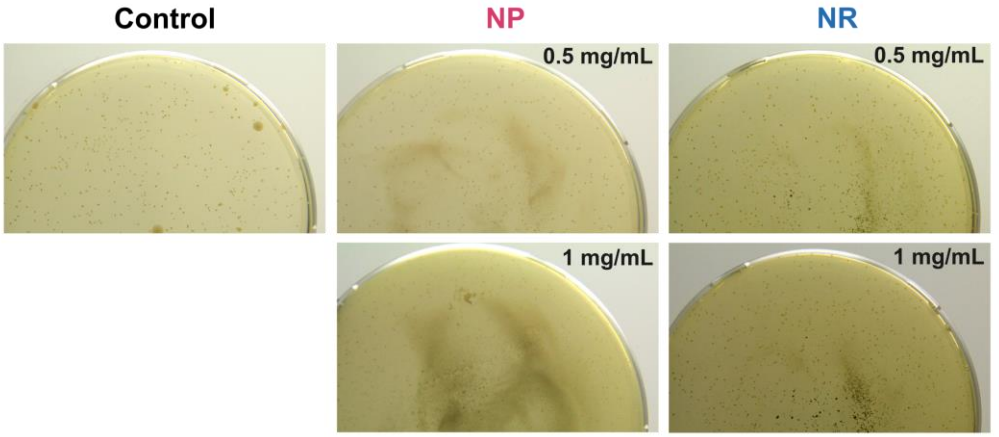

Fig. 2.11. Digital photographs of agar plates. The experiment performed in a motionless manner with the application of ZnO nanoparticles (NP) and ZnO nanorods (NR) (0.5 mg/ml or 1 mg/ml), had a small influence on *E. coli*.

2.5. Influence of ZnO nanostructures on eukaryotic cells

The nanomechanical stress induced by rounded ZnO nanoparticles (NP) and ZnO nanorods (NR) was investigated using eukaryotic model cells/cell lines: *S. cerevisiae*, cancer cells lines and peripheral blood mononuclear cells isolated from the blood of donors (patients).

The viability of yeasts was investigated by a colony count method, this is the method that was used in the case of bacteria. The exposure to physical stress induced by ZnO NP and ZnO NR caused a decrease in the number of the cells, ten times and one hundred times, respectively. SEM analysis confirmed the hypothesis that the disruption of the cells is caused by sharp ZnO NR (Fig. 2.12).

To elucidate the influence of the shape of the nanostructures on the viability of more complex eukaryotic systems, the measurements were firstly performed on adherent cell line $HepG_2$. Lactate dehydrogenase (LDH) was used as a viability marker which is released when the cells are disrupted. Since adherent cell culture is carried out in a motionless manner, the additional control samples were performed where the cells were cultured with ZnO nanostructures without mixing (Fig. 2.13A, curves marked with 0 rpm). Crucially, additional rotation did not affect the release of LDH in the control samples. In the case of the control samples treated in a motionless manner, the effect of ZnO NP and ZnO NR (no increase of LDH) was not observed until around 180 minutes. This confirmed once again that colloidal instability did not play the main role in the investigation of the effect of the shape of the nanostructures. In contrast, when $HepG_2$ cells were exposed to ZnO NP and ZnO NR with stirring, the significant increase of LDH was reported. In time range between 0 and 180 minutes, the main difference between rotated and motionless samples resulted from the mechanical stress induced by collisions with the nanoparticles. As in the previous experiments with the bacteria, ZnO NR appeared to be more damaging compared to ZnO NP, which was also observed in the images obtained using fluorescence microscopy (Fig. 2.13B). The slight increase of LDH level after 180 minutes observed in the motionless samples can be explained by the increasing concentration of

Zn^{2+} that caused disturbance of homeostasis. However, the difference still constituted a low background in comparison to the real effect caused by mechanical stress.

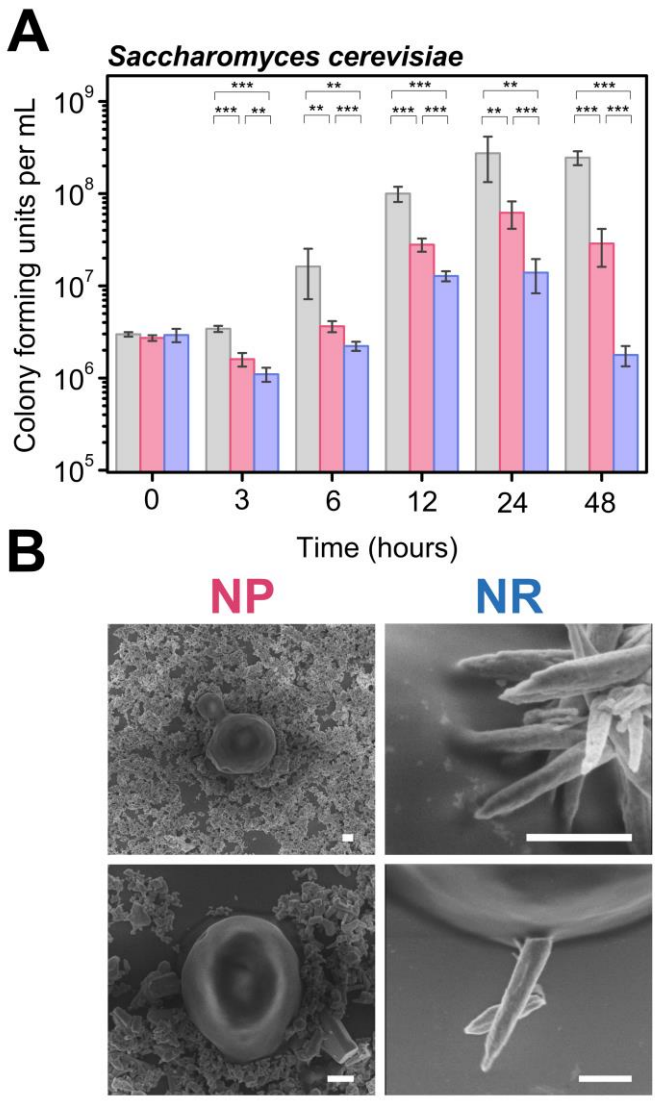

Fig. 2.12. Influence of rounded ZnO nanoparticles (NP) and ZnO nanorods (NR) on *S. cerevisiae*. (A) The viability plot depicts the difference in colony forming units per ml over time upon exposure to ZnO NP and ZnO NR. * $P < 0.05$; ** $P < 0.01$; *** $P < 0.001$. (B) SEM images of *S. cerevisiae* captured after the exposure to the nanoparticles. Yeast cells are mechanically damaged by ZnO NR. Scale bars correspond to 500 nm.

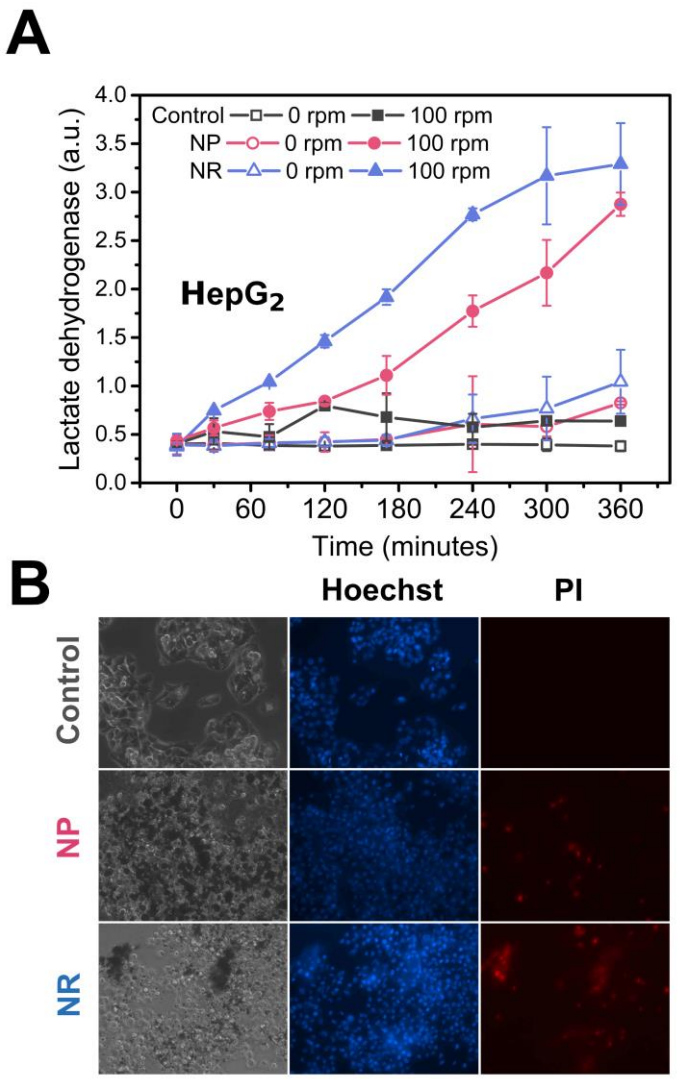

Fig. 2.13. Influence of rounded ZnO nanoparticles (NP) and ZnO nanorods (NR) on $HepG_2$ (human liver cancer cell line). (A) The viability plot depicts the difference in lactate dehydrogenase level. (B) Fluorescence microscopy images of $HepG_2$ cells stirred (100 rpm) for 6 hours with the nanoparticles. Hoechst stains all cells, whereas PI is present only in dead cells. Single experiments with LDH-analysis were performed in triplicates, are presented in the diagrams. Error bars represent the standard deviation of triplicated measurement of LDH multiplied by 4.303 which is Student-Fisher $t_{n,a}$ factor. For n = 3 corresponds to the level of confidence of a = 0.95.

Even more dramatic difference was observed in the case of A594 cell line (human alveolar type II epithelium-like lung carcinoma cell line) when exposed to the mechanical stress induced by nanostructures. In the case of ZnO NR, the LDH level was around five times higher in comparison to ZnO NP (Fig. 2.14).

Next, two skin cancer cell lines were investigated: HaCaT - immortal keratinocyte cell line, and A431 - skin cancer cell line. The results obtained for HaCaT were in line with data presented by Schaeublin *et al*[352], ZnO NR appeared damaging whereas ZnO NP did

not exhibit such effect (Fig. 2.14). The experiments revealed that A531 was rather exceptional and more mechanically resistant to the presence of ZnO NP. In the case of A431 cells, LDH level in samples exposed to ZnO NP and ZnO NR was very similar but elevated in comparison to control (Fig. 2.14). A similar effect was observed only in the case of Gram-positive bacteria, i.e., bacterial cells which were very resistant to mechanical damaging. Different responses to mechanical stress between various cells could arise from the morphological and mechanical properties of cells due to their primary functions. Moreover, the behavior of cytoskeleton elements like actin filaments or microtubules could lead to an increase of stiffness upon exposure to physical stress[392]. Peripheral blood mononuclear cells (PBMC), as white blood cells with a round nucleus (lymphocyte, monocytes, macrophages), constitute a critical component of the immune system. Results obtained for PBMCs were in line with literature data[353], ZnO NR again appeared more damaging compared to ZnO NP (Fig. 2.14).

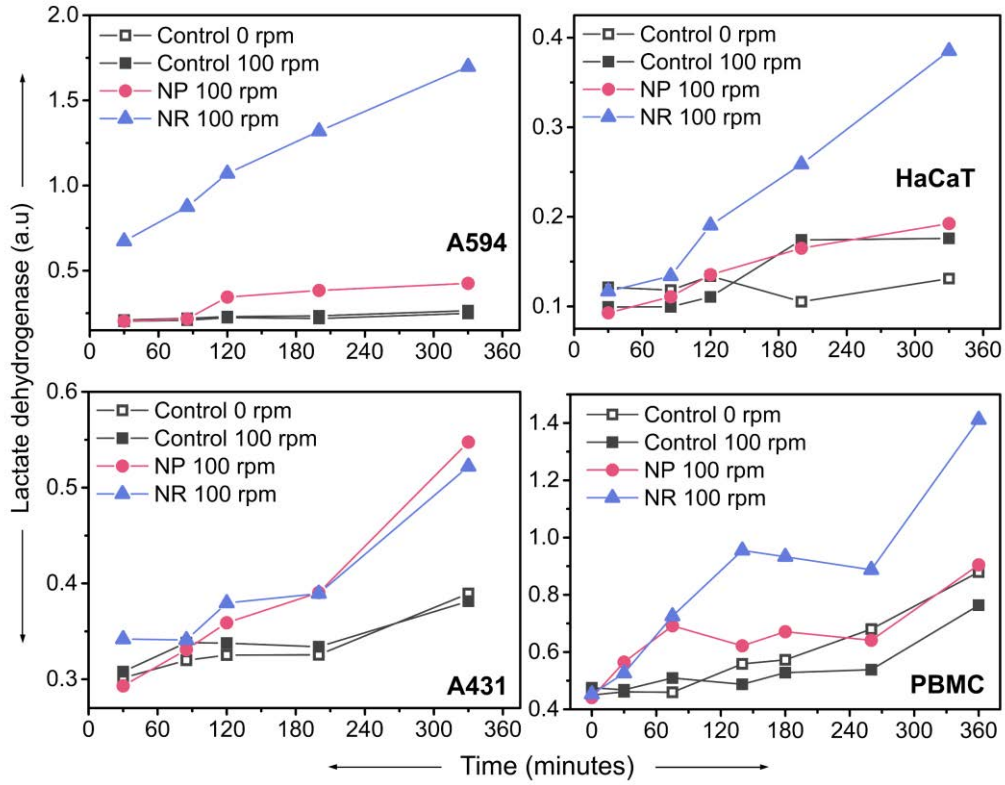

Fig. 2.14. Influence of ZnO NR and NP on eukaryotic cell lines and PBMCs. The particles were added at the concentration of 1 mg/ml to $HepG_2$, A594, HaCaT, A431 cells and peripheral blood mononuclear cells (PBMC) that were stirred (100 rpm). Single experiments, with LDH-analysis (lactate dehydrogenase), run in triplicates. Error bars are too small to be visible.

2.6. Conclusions

There are several publications on the influence of ZnO nanoparticles, which aim to evaluate cytotoxicity and dependence between the size of nanostructures and bactericidal effect[354,355,356,393,394,395]. Typically, the size of nanoparticles used in such experiments is in the order of a few nanometers up to dozens of nanometers, and the

studied concentrations were in the range of μg per milliliter. Moreover, the main focus is on the fate of the nanoparticles inside cells, consequently, the information about the physical interaction between cells and nanoparticles is very limited. The comprehensive information about the influence of mechanical interaction is crucial since nanoparticles are widely used in bio-applications.

In this chapter, systematic studies on the influence of mechanical stress induced by rounded ZnO nanoparticles and sharp ZnO nanorods are presented (size exceeding 300 nm and concentration of 1 mg ml^{-1}). Firstly, the nanostructures were carefully characterized by SEM (size, shape were evaluated), X-Ray diffraction (the crystallographic structure was determined), dynamic light scattering (hydrodynamic diameter), zeta potential and spectrophotometric titration (behavior of the nanostructures in media regarding the release of Zn^{2+}). Next, different types of bacteria and eukaryotes were exposed to mechanical stress induced by rounded ZnO nanoparticles (NP) and ZnO nanorods (NR). *Escherichia coli* and *Enterobacter aerogenes* were studied as examples of Gram-negative bacteria, whereas *Staphylococcus epidermidis* and *Corynebacterium glutamicum* were chosen as Gram-positive representatives. *Saccharomyces cerevisiae* constituted the "bridge" between bacteria and more eukaryotic cells ($HepG_2$, A594, HaCaT, A431, and PBMCs). In general, ZnO NR exhibited higher cell-damaging potential as their shape facilitated mechanical damaging on prokaryotes, fungi, and eukaryotes cultured in motion. The possibility of colloidal instability, as the main factor differentiating ZnO NP and ZnO NR, was excluded. In the case of Gram-negative bacteria, ZnO NR facilitated mechanical damaging of the cells due to sharp shape in comparison to ZnO NP. However, Gram-positive strains appeared more resistant to mechanical stress due to the thicker cell wall. The effect of free zinc ions released from the nanostructures was also investigated. Gram-negative strains were unaffected by the release of free zinc ions (due to LPS layer), whereas Gram-positive strains were more susceptible to the presence of the ions. Similarly, ZnO NR appeared also more damaging in comparison to ZnO NP in the case of eukaryotes with one exception (A431 due to morphological and mechanical properties of the cells). Again, the importance of mechanical stress in dynamic conditions in comparison to the static experiment was highlighted for tested $HepG_2$ cancer cell line.

To conclude, the shape of nanoparticles is a significant physical factor that should be taken into consideration especially in biological experiments. The presented results may have implications in drug delivery systems, transplantology, implantology and cybernetics where nanoparticles are introduced to the human body or integrated with tissues. But most importantly, follow-up experiments presented in the next section show very intriguing behavior of bacteria.

2.7. Experimental section

Synthesis of ZnO nanorods

The ZnO nanopowder consisting of rounded nanoparticles was purchased from Alfa Aesar Company (USA). ZnO nanorods were prepared using aqueous chemical growth (ACG) method[367] According to this method ZnO crystallizes as the sea urchin-like structure. After 1 hour-synthesis, ZnO NR were flushed with water three times and sonicated for 6 minutes. Sonication was applied to disrupt the crystallites and obtain single, separated needles. The ZnO NP and NR were sterilized and suspended in proper growth medium before addition to cell cultures.

Characterization of ZnO nanostructures

XRD patterns of ZnO NR and NP were recorded using Bruker Discover D8 (USA). Zeta potential was measured using Malvern Zetasizer Nano ZS equipped with a dynamic light scattering (DLS) module (He-Ne laser 633 nm, Max 4 mW). Before measurements, ZnO NP and ZnO NR were dispersed in filtered MiliQ water (concentration of 0.05 mg/mL). 1 mL of each solution was used for measurements. Scanning electron microscopy images were taken with the use of FEI Nova NanoSEM 450 (USA).

Determination of the amount of Zn^{2+} released from ZnO NP and ZnO NR

The amount of Zn^{2+} ions released from ZnO NR and ZnO NP of concentration of 1 mg/mL was in LB medium and MiliQ water was measured. The suspensions were mixed for 24 hours in the same conditions as bacteria cultures (37°C, 200 rpm). Afterward, the suspensions of ZnO NR and ZnO NP were centrifuged at 10 000 rpm for 10 minutes. Supernatants were additionally filtered through filters with a pore size of 0.22 μm and then analyzed by spectrophotometric titration in the presence of eriochrome black T indicator. All interfering ions were complexed by CN^- ions, whereas Zn^{2+} ions were released from such complexes upon the addition of formaldehyde.

Exposure of cells to Zn^{2+} ions

ZnO nanorods and rounded ZnO nanoparticles (25 mg in plastic eppendorfs covered with aluminum foil) were sterilized in a steam autoclave (Varioclav 3000 EP-Z, HP Medizintechnik, Germany) and suspended in growth medium just before adding to the cell culture. *Escherichia coli* BL21 (obtained from the Institute of Biochemistry and Biophysics in Warsaw, Poland) and *Enterobacter aerogenes* PCM 1832 (purchased from Polish Collection of Microorganisms, Wroclaw, Poland) were used in the experiments with ZnO nanostructures as examples of Gram-negative bacteria. Wild type *Staphylococcus epidermidis* (obtained from Faculty of Biology, Warsaw University, Poland) and *Corynebacterium glutamicum* PCM 1954 (purchased from Polish Collection of Microorganisms, Wroclaw, Poland) were Gram-positive representatives used to investigate mechanical stress. *Saccharomyces cerevisiae* (obtained from the Institute of Biochemistry and Biophysics in Warsaw, Poland) was used as an example of fungal cells. Firstly, single colonies of bacteria were inoculated for overnight culturing in order to obtain cell suspensions (37°C for *E. coli*, *E. aerogenes*, *S. epidermidis,* and 30°C for *C. glutamicum*; S. cerevisiae, 200 rpm). In the case of Gram-negative strains, a small amount of overnight culture was added to the LB medium with the proper amount of $ZnCl_2$ (optical density, OD=0.01). In the case of Gram-positive strains, OD at the start of the experiment was higher (OD=0.03-0.05) due to vulnerability to the presence of zinc ions.

For OD=0.01 increase of OD over time was not observed. The influence of Zn^{2+} ions on the cells was determined by optical density measurements over time.

Exposure of cells to ZnO nanostructures

Escherichia coli BL21, *Enterobacter aerogenes* PCM 1832, *Staphylococcus epidermidis, Corynebacterium glutamicum* PCM 1954 were used in the experiments to investigate mechanical stress induced by ZnO nanostructures. The bacteria were cultured according to the standard protocol. First, the single colony from the agar plate was inoculated into LB-medium (Carl-Roth) for overnight culturing (37°C for *E. coli*, *E. aerogenes*, *S. epidermidis,* and 30°C for *C. glutamicum*; 200 rpm). The small amount of the overnight culture was inoculated into a new portion of LB-medium and cultured to obtain suspensions of OD_{600}=0.5. The bacterial suspension was split between three flasks (control and containing ZnO NP and ZnO NR) and ZnO nanoparticles were added into the flasks. Samples of bacterial suspensions were taken at certain time points and the colony count method was used to determine the viability of the bacteria upon exposure to ZnO NP and NR exposure (25 µl of diluted bacterial suspension in PBS buffer was spread on the agar plate). Colony forming units (CFU) were directly correlated with the number of bacteria within the sample.

Yeasts - *Saccharomyces cerevisiae* (obtained from the Institute of Biochemistry and Biophysics in Warsaw, Poland) were cultured according to standard protocol using Yeast Extract-Peptone-Dextrose (YPD) medium (Roth). Firstly, a single colony from YPD agar plate was inoculated into YPD medium growth (30°C, 200 rpm) to obtain suspension of OD_{600}=0.5.

The cell lines and PBMC were obtained from the Section for Infection Medicine, BMC Lund University in Sweden. The human hepatoma $HepG_2$ cells were cultured in RPMI 1640 medium with GlutaMAX medium supplemented with 10% fetal bovine serum (FBS). The human epithelial carcinoma cells A431 were cultured in KGM-Gold medium and the stable line of A594 human lung carcinoma cells in F-12 medium. The immortal human keratinocyte line HaCaT was cultured in MEM medium. All media were purchased from Gibco/Invitrogen (USA). The cells were incubated at 37°C in an atmosphere of 95% air and 5% CO_2. To avoid bacterial and fungal contamination, 100 mg/ml of antibiotics (mix of penicillin and streptomycin) and 100 mg/ml of antimycotics were added to the media. The cells were detached from the stock flasks using trypsin as described elsewhere[396]. At the beginning of experiments, cells were kept at approximately 80-90% confluency.

PMBC were isolated from heparinized whole blood by use of Ficoll density gradient centrifugation. The cells observed under the fluorescence microscope after six hours of incubation with Zn NP and Zn NR were stained using Hoechst 33342 (present in all cells) and propidium iodide (present only in dead cells, denoted as PI) according to the protocol provided by the manufacturer.

Statistics

In the case of bacteria and yeasts, the experiments were repeated at least three times. Presented results are averaged from at least six independent agar plates. Student`s t-test was performed to evaluate the statistical significance. * $P < 0.05$; ** $P < 0.01$; *** $P < 0.001$. In the case of cancer cell lines and PBMCs, experiments were repeated three times. The LDH levels were measured three times for each time point for each experiment. Error bars represent a standard deviation of triplicated LDH measurement multiplied by 4.303, which is Student-Fisher $t_{n,a}$ factor (for n = 3 corresponds to the level of confidence of a = 0.95).

Chapter 3

Phenotypic plasticity of *E. coli* after exposure to ZnO nanorods

Nanomechanical stress induced by sharp ZnO nanorods caused changes in the phenotype of *E. coli*. The bacteria's shape became more spherical, the density of their periplasm and the average thickness of the cell wall was increased. *E. coli* after exposure to sharp nanorods appeared almost as Gram-positive bacteria in the standard Gram staining. The same phenotype changes were observed in *Enterobacter aerogenes* (Gram-negative) but not in *Corynebacterium glutamicum* (Gram-positive). The changes in the phenotype of *E. coli* were stable over time, even after the removal of the stressor.

This chapter has been published as:

Kinga Matuła, Łukasz Richter, Marta Janczuk-Richter, Wojciech Nogala, Mikołaj Grzeszkowiak, Barbara Peplińska, Stefan Jurga, Elżbieta Wyroba, Szymon Suski, Henryk Bilski, Adrian Silesian, Hans A. R. Bluyssen, Natalia Derebecka, Joanna Wesoły, Joanna M. Łoś, Marcin Łoś, Przemyslaw Decewicz, Lukasz Dziewit, Jan Paczesny, Robert Hołyst, Phenotypic plasticity of *Escherichia coli* upon exposure to physical stress induced by ZnO nanorods. *Scientific Reports*, 2019, 12;9(1).

3.1. Introduction

Recently, nanoparticles became promising agents in the fight with multi-drug resistant bacteria[156,291,332–334,397]. Hopes are high, especially regarding nanostructures and their non-chemical mechanisms of bacteria-killing, e.g., mechanical puncturing[269,270,342] or contact killing[291,340,341]. So far, no data have been shown to demonstrate the behavior of bacteria upon exposure to nanoparticles or any other physical stressor from a more broad chemical, physical and biological perspective.

In this chapter, the main focus is on bacteria and examination if ZnO nanostructures can serve as a new sterilization agent utilizing the mechanical killing mechanism. The most pronounced changes in killing bacteria were observed during exposure to ZnO nanorods compared to rounded ZnO nanoparticles. Thus, most of the experiments presented in this chapter are limited to the influence of ZnO nanorods.

3.2. Hertzian theory of collisions: interaction of ZnO nanorods with *E. coli*

The interaction between bacteria and ZnO nanorods (Fig. 3.1A, B) suspended in a medium can be estimated using contact mechanics formalism. Fig. 3.1C shows the mode of action of a ZnO nanorod (NR) on a bacterium, proving that the bacteria can be mechanically pierced by ZnO nanorods. During stirring (200 rpm) of the medium, the characteristic relative velocities of the bacteria and the nanorods are of the order of v~0.2-1.8 m/s ($v = \omega \cdot r$, v is the linear velocity of a medium in a flask in a shaker, ω is the angular viscosity and r is the distance of a moving fluid from the axis of rotation, r~1 cm to 10 cm). Assuming that the size of the bacterium is d_b ~1 μm, its mass is m_b~10^{-12} g, and the viscosity of water is η~1 mPa·s, the calculated Stokes number $Stk = m_b v/(\eta {d_b}^2)$ for the bacterium is 10^{-1}. The Stokes number actually compares the inertia, given by the momentum of the bacterium, to dissipation forces that are proportional to viscosity. Importantly, for Stk<<1 the bacterium follows the streamlines of the water-based medium during stirring in the shaker.

For cylindrical nanorods of length 400 nm, radius 40 nm and density ρ~5.6 g/cm^3 (ZnO) the mass is m_{nr}~10^{-14} g, giving Stk~10^{-4} for the nanorods. Thus, they also follow the streamlines of water. However, the Reynolds number $R_e = \rho v L/\eta$ equals to around 10^4 (for the density of water at 37 °C ρ~10^3 kg/m^3 and dynamic viscosity η~0.7 mPa·s, moving in a flask of L~0.1 m with velocity v~1 m/s). Consequently, the flow of the medium is turbulent and fosters high-velocity collisions of the bacteria with the nanorods. The pressure exerted at the surface of the bacteria was estimated using the Hertzian theory of collisions since eventually, both objects come into mechanical contact. The characteristic time of collision is given by the equation[398]:

$$t = 2.54\rho^{2/5}\left(\frac{1-\mu_{nr}^2}{E_{nr}} + \frac{1-\mu_b^2}{E_b}\right)^{2/5} dV^{-1/5} \qquad (1)$$

where E is the Young modulus of the ZnO nanorods (nr) and the bacteria (b) and μ is the Poisson ratio, d is the size of contact (size of the tip of the nanorod) and V is the velocity upon impact. The Young modulus of the bacteria is E_b~ 25 MPa[399] and is four orders of magnitude smaller than the Young modulus of NR E_{nr}~100 GPa[400]. The Poisson ratio for the bacteria is ~0.4[401]. The size of the tip of the nanorod obtained from SEM measurements is

~10 nm, but the tip is rough and locally may have 1 nm roughness. For d=10 nm, the collision time is around t=1 ns.

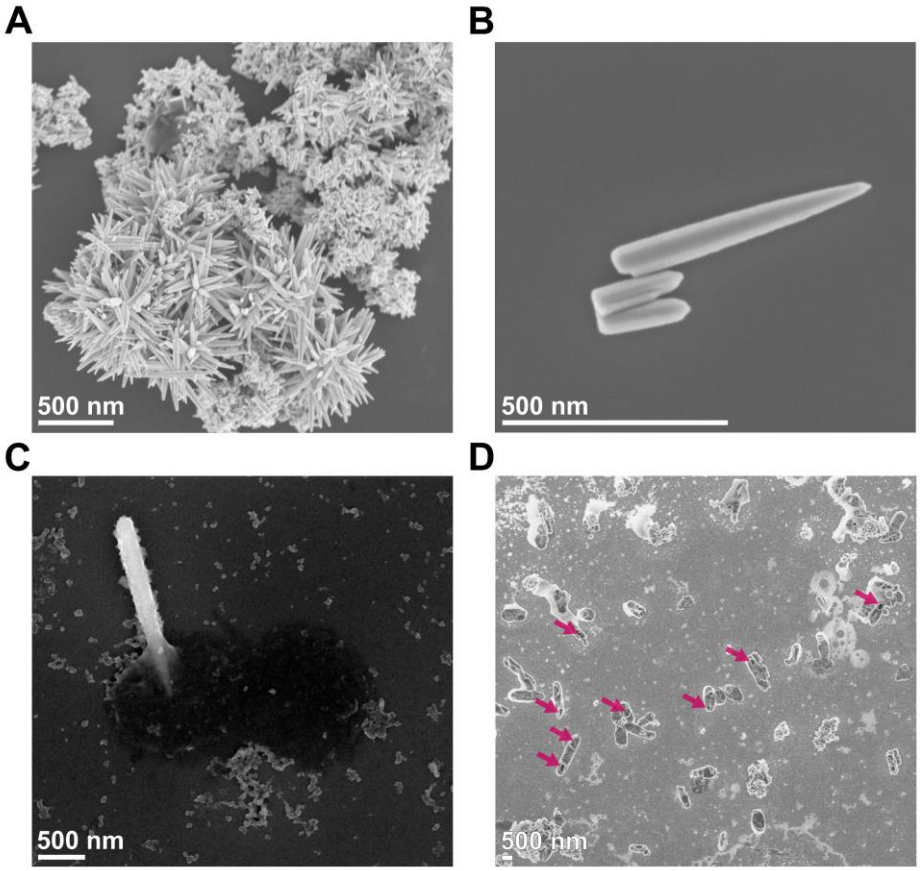

Fig. 3.1. Interaction between *E. coli* bacteria and ZnO nanorods. (A) Sharp, cone-like tips of ZnO NR imaged by SEM. (B) SEM image of single ZnO nanorod. (C) *E. coli* cell pierced by ZnO nanorods. (D) SEM image of a sample with *E. coli* bacteria after exposure to ZnO nanorods. The arrows indicate holes in the cells that were created by ZnO nanorods.

The calculated force exerted by the 10 nm tip on the bacterial cell wall is $F = m_{nr} \cdot V/t$ =1 nN and 10 nN for the 1 nm tip. The pressure exerted at the surface of the bacteria can be described by the Hertz theory[402]. For a cylindrical tip of radius d/2 acting with a force F on the surface of bacteria, from the Hertz theory, $p = 2F/\pi d^2$~0.1 MPa (for collisions with sides of the nanorod) to 10^4 MPa (for direct collisions of the cells with the 1 nm tip of ZnO nanorod). This lowest pressure is comparable to the turgor pressure inside the bacteria (~0.3 MPa[403]) and the larger one is much greater than the Young modulus of bacteria. Moreover, this pressure may be much larger if a cone geometry is considered instead of a cylinder[402] since the pressure theoretically diverges at the tip of the cone. Upon direct collision of the bacteria and nanorods, the pressure is sufficient to pierce a cell as shown in Fig.3.1C.

The estimated value calculated according to Hertzian theory was compared with literature data connected with AFM measurements on *E. coli i*[404]. It was demonstrated

that when the force acting on the cantilever was 10 nN (pressure~3,000 MPa) during the experiments performed using an AFM tip (a radius of 2 nm), the holes created by the tip spontaneously "healed" without losing visible traces on the surface of the *E. coli*[404]. Therefore, during exposure to ZnO nanorods where the similar pressure was exerted on the surface of cells, the bacteria may be hit or punctured many times without losing their viability.

3.3. Viability curves of *E. coli* after exposure to ZnO nanorods

The bacteria that survived the first exposure to the nanorods were exposed once again to mechanical stress. In this experiment, two types of nanoparticles of the same concentration were used: sharp ZnO nanorods (NR) and ZnO rounded nanostructures (NP). However, the shape of the ZnO nanostructures was utilized as a marker indicating changes within the cell envelope of the bacteria.

The difference between the viability curves of *E. coli* exposed to ZnO NR and ZnO NP during the first exposure is presented in Fig. 3.2A. The bacteria that survived the first treatment with ZnO NR were collected and exposed to the nanostructures in the second experiment. The hypothesis was that bacteria would not survive the second exposure to mechanical stress. Surprisingly, the comparison of the viability curves after the second treatment to ZnO NR and ZnO NP (Fig. 3.2B) revealed that *E. coli* became invulnerable to the shape of nanostructures, i.e., no difference between viability after exposure to ZnO NR or ZnO NP was observed. The lack of susceptibility to the shape of the nanostructures was a characteristic feature observed for Gram-positive strains (*Staphylococcus epidermidis*, *Corynebacterium glutamicum*, Fig. 2.8)[391] that are mechanically resistant to the nanostructures due to more peptidoglycan within in the cell wall in comparison to Gram-negative bacteria. This interesting feature observed in the case of *E. coli* exposed to ZnO NR was the first sign suggesting structural changes within the cell wall of the survivals.

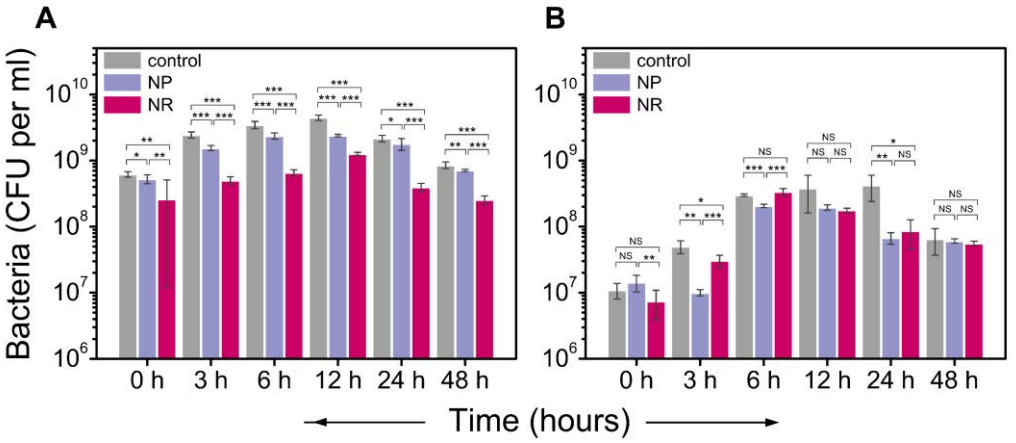

Fig. 3.2. Viability curves of *E. coli* after exposure to ZnO nanorods (NR) and rounded ZnO nanostructures (NP). (A) The first exposure to the nanostructures. (B) The second exposure of *E. coli* that had survived the first exposure to ZnO NR. Error bars show standard error of the mean (s.e.m.), where ** P < 0.05; ** P < 0.01; *** P < 0.001*; NS, not significant.

3.4. Gram staining of *E. coli*

To check whether the lack of susceptibility of survivor *E.coli* to the shape of the nanostructures during exposure is a result of the increased amount of peptidoglycan, Gram staining was performed (see Fig. 3.3). This method is a classical identification procedure used in microbiology, to distinguish Gram-negative from Gram-positive strains, that is based on the thickness of peptidoglycan within the cell wall of bacteria.

In principle, Gram staining is based on the utilization of three dyes are used: crystal violet, Lugol's iodine, and safranine as a counterstain. Firstly, crystal violet dissociates in aqueous solution into CV^+ and Cl^- ions which penetrate cell through the cell wall and the cell membrane. The negatively charged components of the cell interact with CV^- ions.

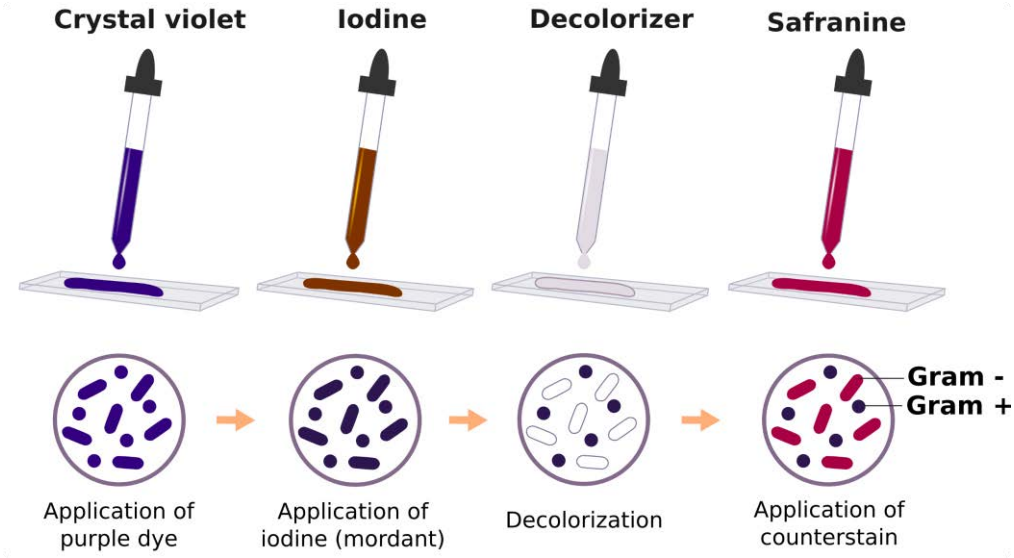

Fig. 3.3. The scheme presents Gram staining step by step. Fixed bacterial smear on the glass slide is firstly flooded with crystal violet, rinsed with water and then Lugol's iodine is poured on the sample. The glass slide is washed by water and next, decolorizer (acetone and ethanol) is added drop by drop on the tilted glass slide and immediately rinsed with water. Finally, the sample is dyed with safranine that is counterstain. The slides are air-dried and visualized by the optical microscope.

In the next step, iodide in the form of I^- or I^{3-} interacts with crystal violet and creates large complexes with CV^- ions within the outer membrane of the cell and cytoplasm. Subsequent washing with a decolorizer, which is usually a mixture of ethanol and acetone, dissolves the lipid layer within the cell wall of Gram-negative cells. The removal of the lipid layer leaves the peptidoglycan layer exposed and enhances the leaching of the formed complexes CV-I. In contrast, the decolorizer dehydrates the thicker cell walls of Gram-positive bacteria, closing the pores and making them resistant to decolorization (all complexes are trapped within the cell wall). Finally, safranine or fuchsin is applied as a counterstain to the smear to give colorless Gram-negative bacteria a pink color[405].

In this experiment, two species of bacteria were used: *E. coli* control and after two exposures to ZnO nanorods, and *S. epidermidis* as control Gram-positive strain.

Performed staining revealed that the survivor *E. coli* started to resemble Gram-positive strain. Fig. 3.4 A shows direct images taken after staining of the bacteria on the glass slides revealing the difference in the color of *E. coli* (control and exposed to ZnO nanorods) and *Staphylococcus epidermidis*. Fig. 3.4 B presents a quantitative, chemical interpretation of Gram staining based on UV-Vis spectra (see also Fig. S4 in the Appendix).

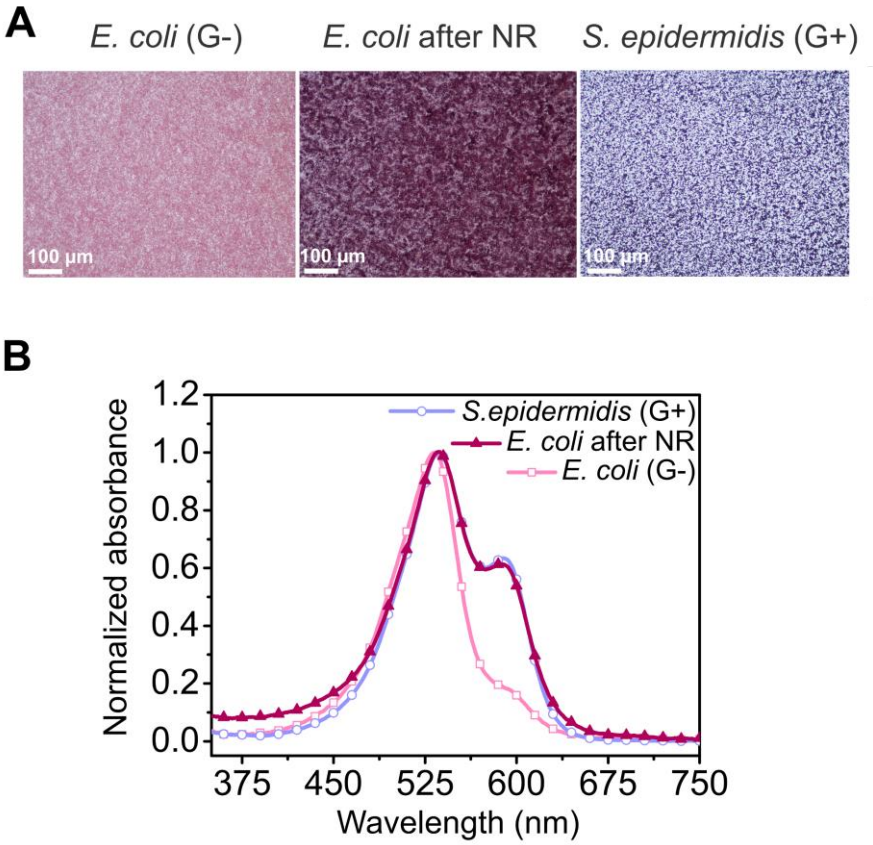

Fig. 3.4. Gram staining of *E. coli* bacteria upon exposure to ZnO nanorods. (A) Microscope images of Gram-stained bacteria marked: *E. coli* control as *E. coli* (G-); *E. coli* exposed to ZnO NR as *E. coli* after NR, and control Gram-positive *S. epidermidis* as *S. epidermidis* (G+). (B) Comparison of UV spectra of the samples after Gram staining. The maximum absorption in the range of about 530 nm corresponds to the presence of safranine. The peak for crystal violet that remains in the layer of peptidoglycan is around 590 nm.

3.5. Shape and thickness of the cell wall of *E. coli*

The next experimental step comprised an examination of phenotypic changes of *E. coli* that survived the second exposure to ZnO NR. SEM and cryo-scanning electron microscopy (cryo-SEM) were used for the morphology characterization. Cryo-SEM is especially recommended in the analysis of biological samples as it allows for the preservation of native morphology of cells. Additionally, transmission electron microscopy analysis coupled with energy dispersion analysis (TEM with EDS)[406] was performed to i) examine the internal cell structure, mainly the thickness of the cell wall, and ii) quantify

changes in the elemental composition within the cell wall (measurements were performed for periplasm - the space between the inner and outer membrane within the cell envelope; and cytoplasm). In the case of SEM imaging performed at the Institute of Physical Chemistry PAS, a new protocol for the sample preparation was successfully established. The aim was to avoid several centrifugation steps required during an exchange of solvents during gradual dehydration (standard sample preparation protocol). In the samples, where the bacteria were suspended with the nanorods, the applied centrifugal force could intensify the piercing of the bacteria by the nanorods, and consequently, that could affect the actual morphology of the cells.

SEM and cryo-SEM analysis revealed that the shape of *E. coli* cells changed after the exposure to ZnO NR. In addition to rod-like cells, elliptical and even spherical bacteria appeared in the samples (Fig. 3.5). In parallel, additional SEM imaging (on a different scanning electron microscope and samples prepared in a similar manner) performed at Nanobiomedical Centre, Adam Mickiewicz University in Poznań revealed similar changes in the morphology of the bacteria exposed to ZnO NR (see Fig.S5).

The length and width of the control bacteria and the cells exposed to the nanorods were evaluated using SEM after three (24-hour each) exposures to ZnO nanorods (Fig. 3.6). The average ratios of the length to the width of the control cells and the bacteria exposed to ZnO NR after each experimental run are presented in Fig. 3.7. The ratio of the length to the width of *E. coli* decreased from 2.44 ± 0.52 before treatment (for native bacteria) to 1.48 ± 0.32 after 72 hours of exposure to ZnO NR (*** $P < 0.001$), more statistical data are provided in Fig. 3.7.

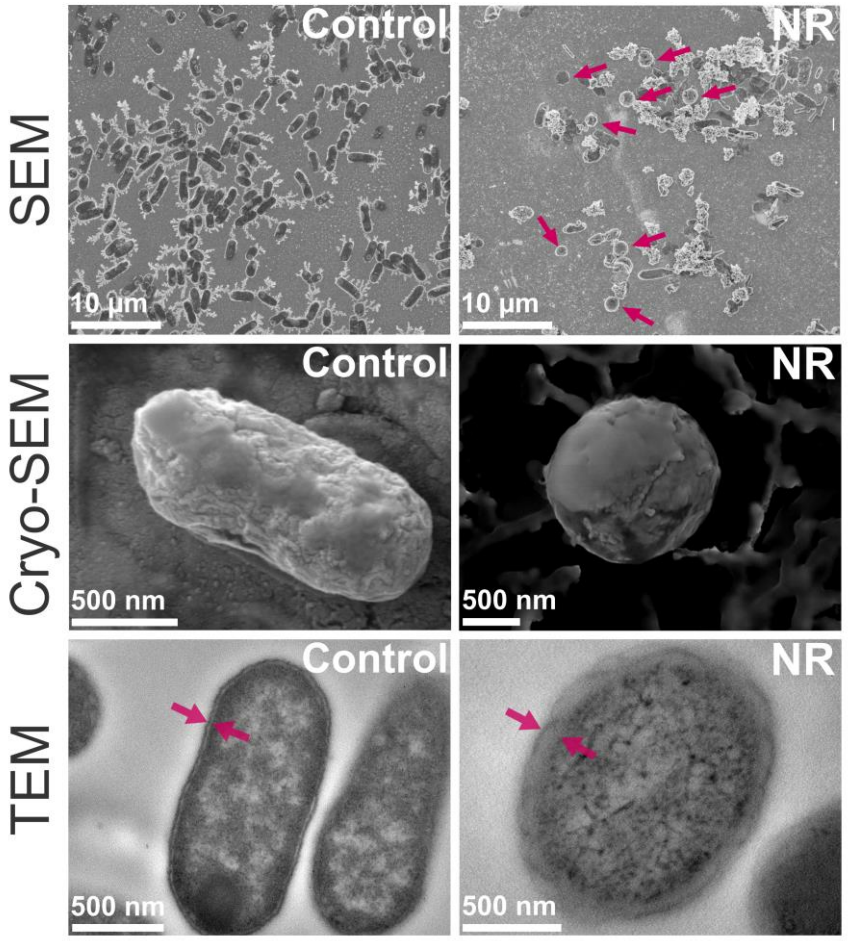

Fig. 3.5. The phenotype of *E. coli* after the exposures to ZnO nanorods. Images of non-treated *E. coli* (marked as Control) and cells exposed to ZnO nanorods (marked as NR) were obtained by scanning electron microscopy (SEM), cryo-scanning electron microscopy (Cryo-SEM) and transmission electron microscopy (TEM). In SEM images, the pink arrows indicate spherical *E. coli* cells, and in TEM images the cell wall thickness after one exposure to ZnO NR was marked.

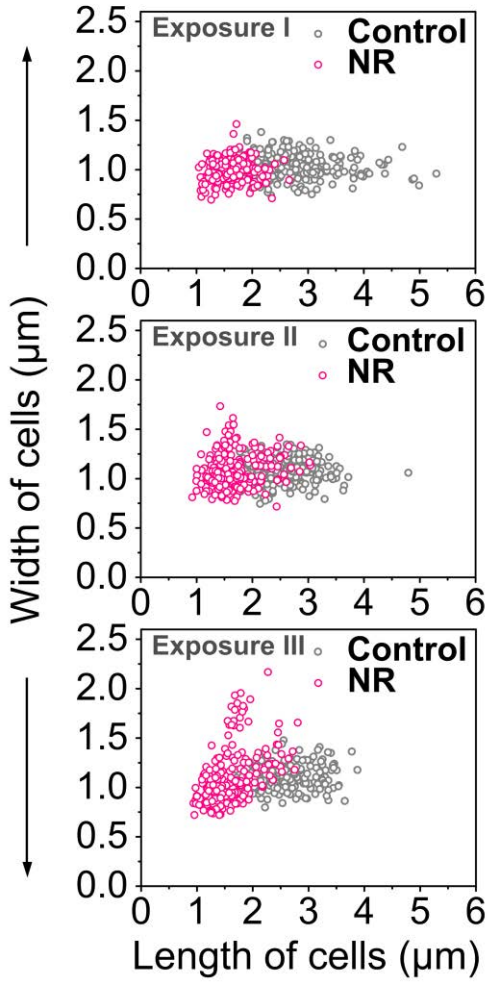

Fig.3.6. Change of the width and the length of *E. coli* after the first, second and third exposure to ZnO nanorods. For each population, at least 200 bacteria were examined. The number of more spherical cells increased with each subsequent exposure to ZnO nanorods.

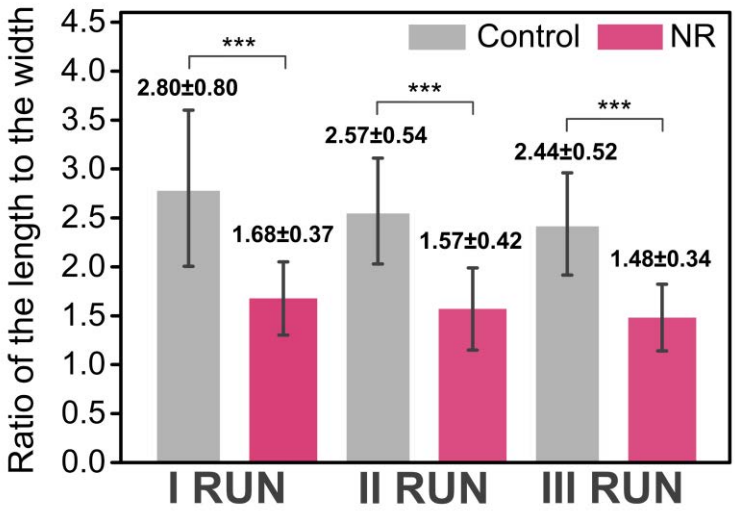

Fig. 3.7. Comparison of the ratios of the length to the width of control *E. coli* (Control) and after exposure to ZnO nanorods (NR). The calculation of ratios was based on SEM images acquired after each of the three exposures to ZnO nanorods (NR). For each experimental run, three biological repeats were performed. In each population (Control and NR) at least 200 cells were measured. Error bars show standard error of the mean (s.e.m.), where *** $P < 0.001$ (Student's t-test).

Transmission electron microscopy was used to examine the thickness of the cell wall of *E. coli* after the exposure to ZnO nanorods. A small portion of the survivor bacteria after one exposure and also control bacteria were cultivated in the nanorods-free medium. The reason for the application of additional cultivation step was connected with the necessity of depletion of ZnO NR from the medium. The presence of the nanostructures could impede the preparation of samples for TEM imaging and further elemental composition analysis. The samples for microscopic imaging were prepared in four different variants: i) on nickel TEM mesh, i) on copper TEM mesh, iii) with osmium tetroxide saturation on nickel TEM mesh, iv) with osmium tetroxide saturation on the copper mesh. Exemplary images of *E. coli* prepared on nickel meshes and nickel meshes with osmium tetroxide saturation are presented in Fig. 3.8. The actual numbers of cells analyzed for all preparation methods were 142 control cells and 171 bacteria after exposure to ZnO nanorods (more details provided in the experimental section). The preparation techniques influenced the obtained thickness for control bacteria and the cells exposed to ZnO NR (Fig. 3.9). Especially, in the case of the samples without post-fixation with osmium tetroxide, the cell wall was swollen compared to the natural size of the cell wall of Gram-negative bacteria. The most similar values in comparison to the native thickness of the cell wall were obtained for the samples with osmium tetroxide saturation on nickel TEM grids. All collected results are compared by an average increase in the thickness of the cell wall of *E. coli* after the exposure to ZnO NR calculated in reference to the average thickness of the control population (Tab. 3.1). The average thickness of the cell wall of *E. coli* after one exposure to nanorods increased by 30-55.9% on average (*** $P < 0.001$). Only in the case of the result acquired for copper meshes, the observed increase in the thickness of the cell wall was by 20%. The highest increase reported for single bacteria in each population was in the range of 53.5-215.1%.

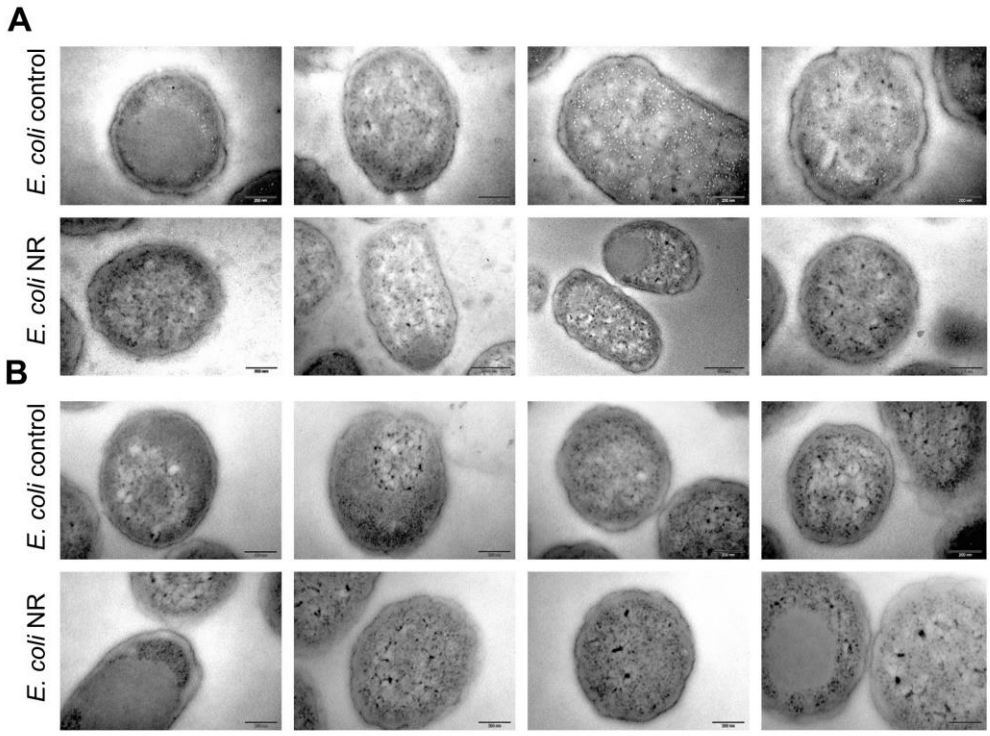

Fig. 3.8. Exemplary TEM images of control *E. coli* (marked as control) and after one exposure to sharp nanorods (*E. coli* NR). (A) TEM images of *E. coli* prepared on nickel grids (B) TEM images of the bacteria prepared on nickel grids with osmium tetroxide saturation.

Table 3.1. Comparison of the measured thickness of the cell wall of *E. coli* obtained by four different sample preparation methods. The thickness was measured as a distance between the middle point of the inner and outer membrane, in three different spots along with the cell envelope. The average increase in thickness is the difference between the average value for *E. coli* after exposure to ZnO nanorods in reference to the average value determined for control bacteria. The highest increase in thickness is the most pronounced difference for single bacteria in reference to the average value for control bacteria, reported for each preparation protocol.

	The average increase in thickness [%]	The highest increase in the thickness of the cell wall in the population [%]
Copper meshes with osmium tetroxide saturation	35.5	**149.4±8.6**
Nickel meshes with osmium tetroxide saturation	30.0	**215.1±5.6**
Copper meshes	20.2	**53.5±7.1**
Nickel meshes	55.9	**195.8±14.6**

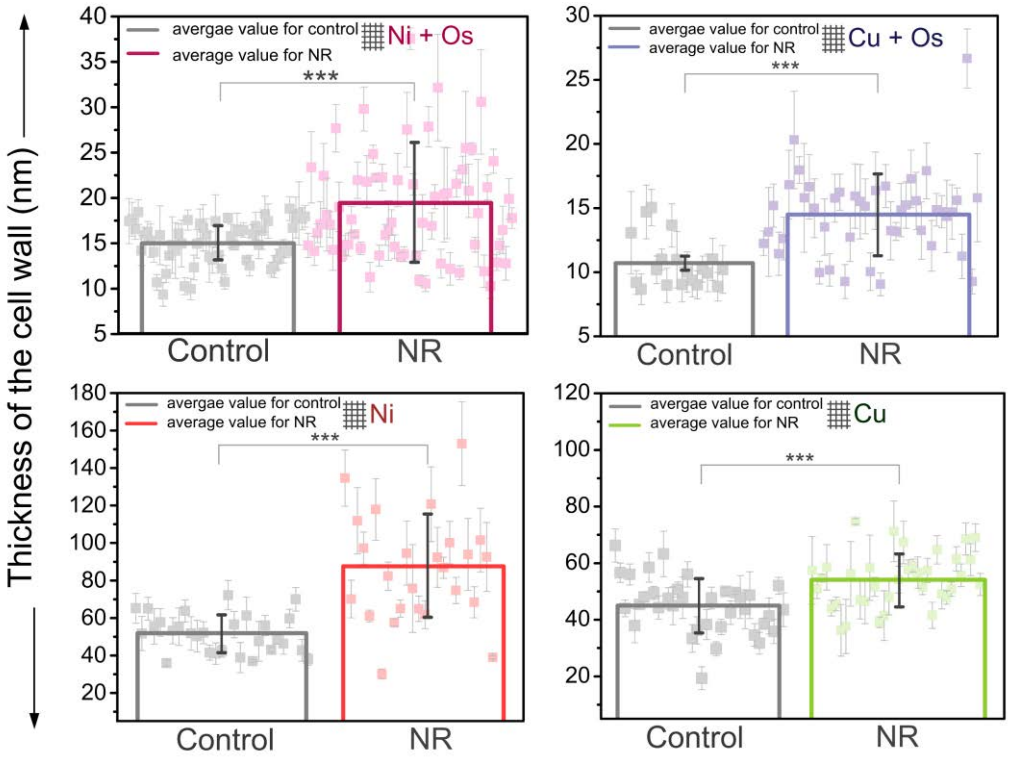

Fig. 3.9. The thickness of the cell wall of control *E. coli* and after one exposure to ZnO nanorods (NR) measured by transmission electron microscopy (TEM). Single points correspond to the mean value determined for single cells, the cell wall of which was measured at three different spots (error bars correspond to the deviation of three values). Histograms show the average thickness of the cell wall measured for the whole population. Error bars for the average value show standard error of the mean for the whole population (s.e.m.), where *** $P < 0.001$.

3.6. Change of shape of bacteria after exposure to ZnO nanorods

Imaging by SEM and Cryo-SEM revealed that the rod-shaped *E. coli* changed the shape into spherical after the exposure to ZnO nanorods (NR).

To check whether similar changes in shape after exposure to physical stress are observed in the case of other bacteria, two bacterial strains were tested. *E. aerogenes* (Gram-negative, rod-shaped bacterium) and *C. glutamicum* (Gram-positive, rod-shaped bacterium) were exposed to ZnO NR, and then the survivor bacteria were subjected to the second treatment with the nanostructures. Again, as in section in 3.4, a new protocol for sample preparation was used to avoid several centrifugations that could affect the morphology of the cells. Thus, the quality of the acquired images was different compared to those obtained after a multi-step protocol comprising fixation, dehydration in a gradient of alcohol and gold deposition onto the specimen.

SEM analysis revealed that *E. aerogenes*, as a bacterium with the thin cell wall, became spherical after exposure to ZnO nanorods (Fig. 3.10A). The shape of *C. glutamicum* did not change due to the higher amount of peptidoglycan that provides sufficient mechanical resistance (Fig. 3.10B). Many experiments (viability tests, Gram

staining) were also performed for Gram-positive *S. epidermidis*. However, this bacterium is coccus-shaped and observation of possible spheronization of the cells was groundless.

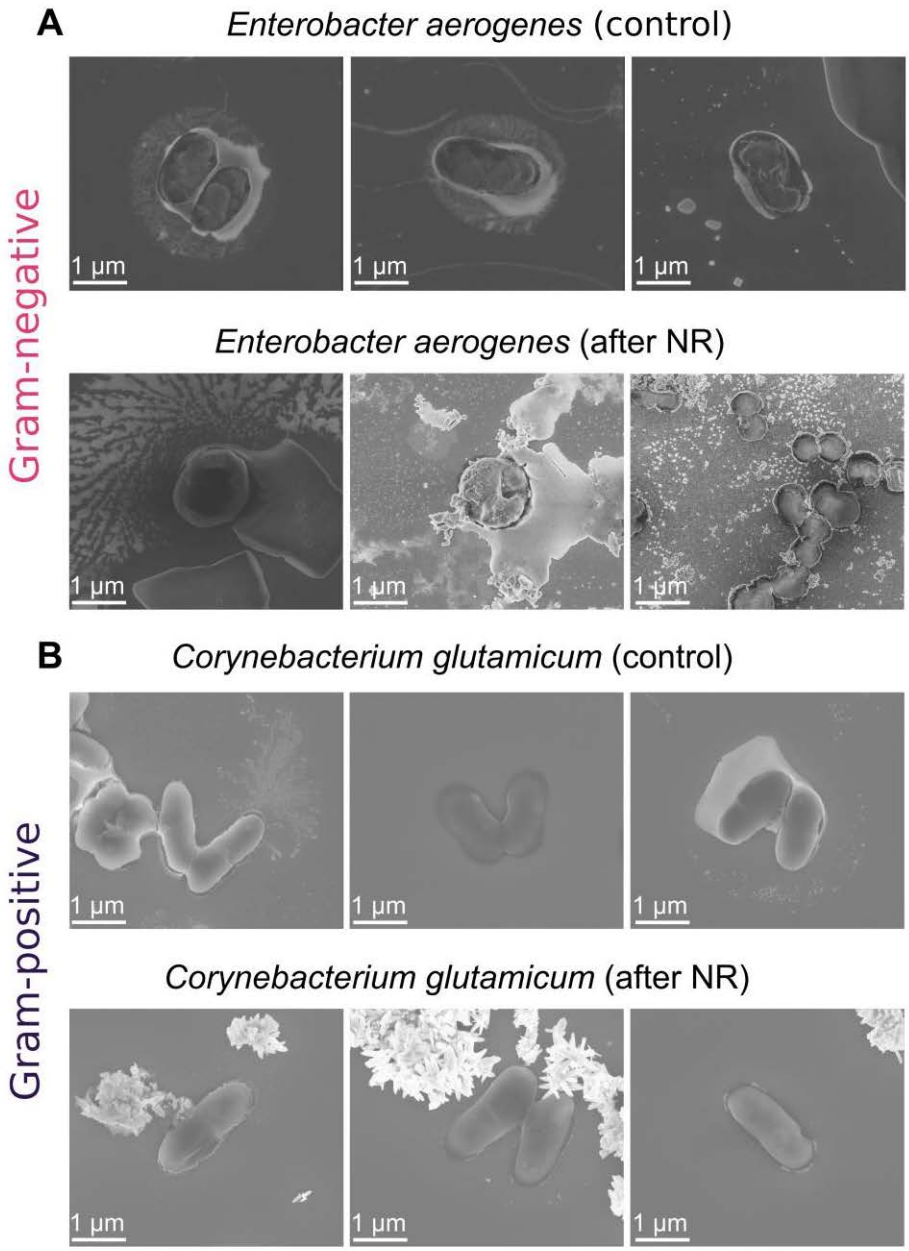

Fig. 3.10. Scanning electron microscopy images of *E. aerogenes* and *C. glutamicum* exposed two times to ZnO nanorods (NR). Images of non-treated bacteria (control) and the cell exposed to ZnO nanorods (after NR) obtained by scanning electron microscopy (SEM). (A) Images of non-treated *E. aerogenes (control) and the bacteria* after exposure to ZnO NR (after NR). (B) Images of non-treated *C. glutamicum (control) and the bacteria* after exposure to ZnO NR (after NR).

In conclusion, the exposure to ZnO nanorods induced changes of shape in the case of Gram-negative bacteria (*E. coli*, *E. aerogenes*) but not in the case of Gram-positive (*C. glutamicum)*.

3.7. Elemental composition of periplasm and cytoplasm of *E. coli*

Coupling of transmission electron microscopy with X-ray spectroscopy (EDS) enabled to analyze changes in the elemental composition of the periplasm and the interior of the bacteria (cytoplasm) before and after exposure to ZnO nanorods. Periplasm is defined as a gel-like matrix space between the inner and outer membrane of the cell wall of Gram-negative bacteria. The same samples that were firstly imaged by means of TEM (four different variants of sample preparation), were subsequently subjected to the analysis of the elemental composition.

Analysis of the composition of periplasm and the interior of *E. coli* revealed clear changes between control *E. coli* and the bacteria subjected to physical stress. Interestingly, in sample variants (on nickel TEM mesh, on copper TEM mesh, with osmium tetroxide saturation on nickel TEM mesh, with osmium tetroxide saturation on copper mesh) the higher amount of carbon was found both, in periplasm and cytoplasm of *E. coli* after exposure to mechanical stress (Fig. 3.11). Based on EDS measurements, it was calculated that the density of periplasm increased by around 15% in the case of ZnO NR-treated bacteria. The estimation was based on carbon content in periplasm before and after exposure to the nanostructures. The beam during EDS measurements collects data from the fixed volume of the specimen. Since the structural building blocks are mainly composed of carbon, a higher amount of this element in a given volume translates to higher density. The increase of carbon content and simultaneous decrease of oxygen could indicate the exchange of water in gel-matrix space for peptidoglycan monomers that were inserted into existing peptidoglycan. A similar increase of carbon content and decrease of oxygen was also observed in the cytoplasm of treated bacteria that could be correlated with a higher concentration of the peptidoglycan monomers that are firstly synthesized in the cytosol and then are transported across the cytoplasmic membrane by bactoprenol. Statistically significant decrease (*** $P < 0.001$) in the case of four sample variants was also observed for phosphorus, iron, and silicon.

Phosphorus (P) is a crucial element that composes different biomolecules (e.g., RNA, DNA, phospholipids, polyphosphates, and ATP). The decrease in P content in cytoplasm might suggest lower transcriptome abundance (RNA content is in fact almost entirely responsible for the changes in P concentration[407]), depletion of triphosphates (ATP, GTP, UTP, CTP), and consequently reduced protein and lipid synthesis, and carbohydrate metabolism.

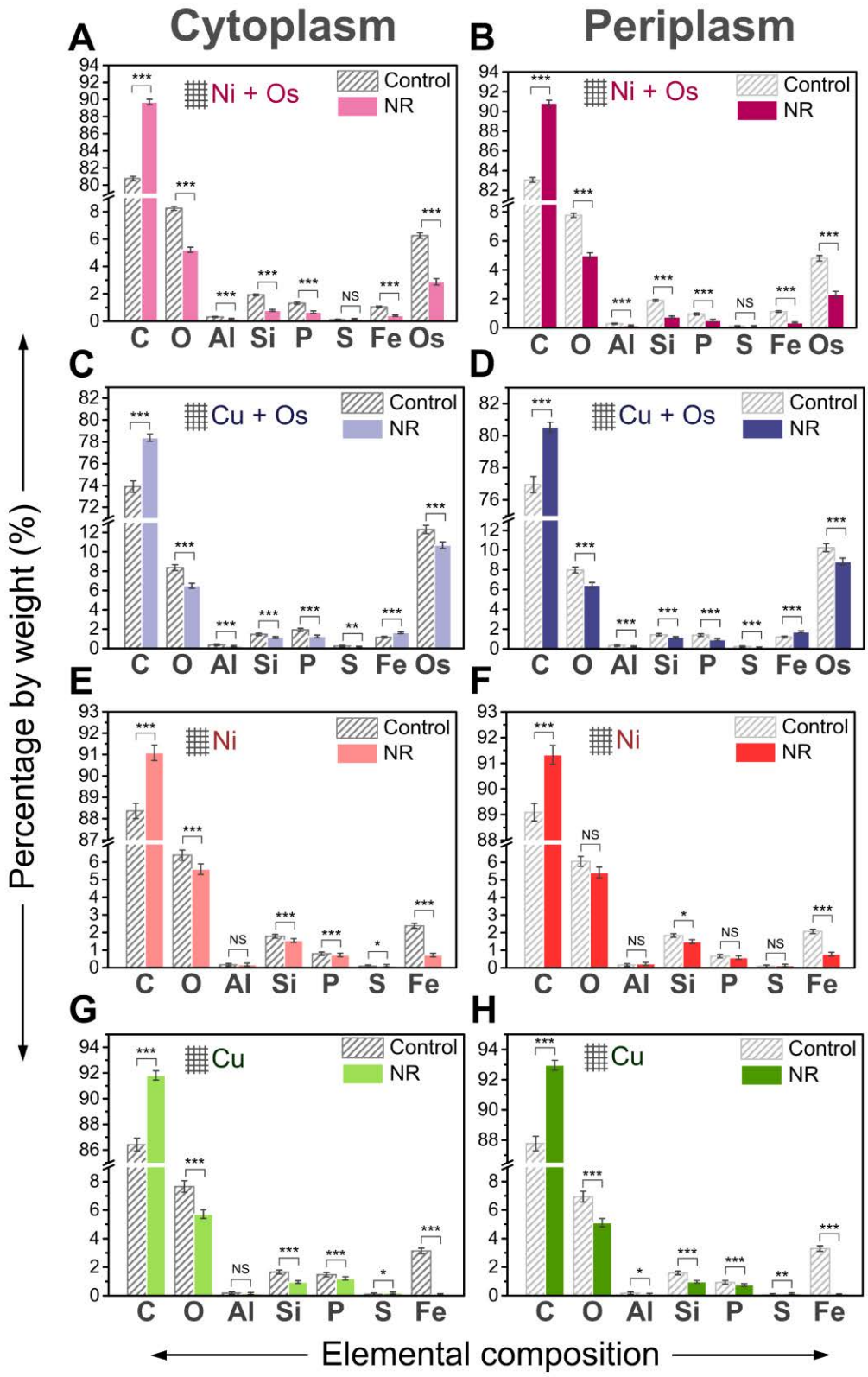

Fig. 3.11. Change of elemental composition of cytoplasm and periplasm of control *E. coli* (Control) and the cells exposed to ZnO nanorods (NR) determined by energy-dispersive X-ray spectroscopy (EDS). Elemental composition was evaluated for the content of carbon (C), oxygen (O), aluminum (Al), silicon(Si), phosphorus (P), S (sulfur), iron (Fe). Elemental composition measured on (A-B) nickel meshes with osmium tetroxide postfixation; (C-D) copper meshes with osmium tetroxide postfixation; (E-F) nickel meshes, (G-H) copper meshes. Error bars show standard error of the mean (s.e.m.), where * *P < 0.05;* ** *P < 0.01;* *** *P < 0.001*; NS, not significant.

Iron (Fe) is an essential versatile component that is incorporated into proteins as a biocatalyst or electron carrier, and its functionality depends upon form in which Fe is incorporated (mono-, binuclear species). Fe participates in many biological processes, such as respiration, H_2 production and consumption, oxygen transport, the trichloroacetic acid (TCA) cycle, DNA biosynthesis and regulation, and gene expression[408,409].
Unfortunately, very little is known about the biochemistry of Si in a bacterial world. It is very difficult to drive conclusions with any references in literature. Recently, it was reported in *Science* magazine that engineered *E. coli* (with introduced mutation) was efficient at producing silicon-organic compounds[410].

To sum up, besides changes in the size of *E. coli* upon exposure to mechanical stress, also increased thickness of the cell wall (by at least 30%) which possessed higher density (increased by around 15%) was observed. Analysis of the elemental composition of the periplasm and the interior of *E. coli* performed by means of EDS revealed clear changes in the elemental composition upon exposure to external stress. Changes in carbon and oxygen content can be correlated with a higher amount of peptidoglycan. Statistically significant changes in the composition of other elements may suggest that the overall rate of cellular metabolism is affected.

3.8. Stiffness of *E. coli* cell wall

Based on the results of Gram staining and TEM measurements (thickness of the cell wall, a difference in the stiffness of the cell wall of the bacteria after exposure to ZnO nanorods was suspected.

Atomic force microscopy (AFM) was used to perform preliminary measurements of the stiffness of the cell wall of the control *E. coli* cells and the bacteria after exposure to ZnO nanorods. Approach curves (amplitude and phase shift of vibrating cantilever versus distance) were recorded (Fig. 3.12C). One can see larger amplitude drop and phase shift when the vibrating tip started to push against the cell wall of bacteria treated with ZnO nanorods. This clearly indicates a more rigid cell wall of NR-treated bacteria in comparison to the control sample. However, measurements were performed in non-contact mode and quantification of the stiffness of the cell wall was not possible.

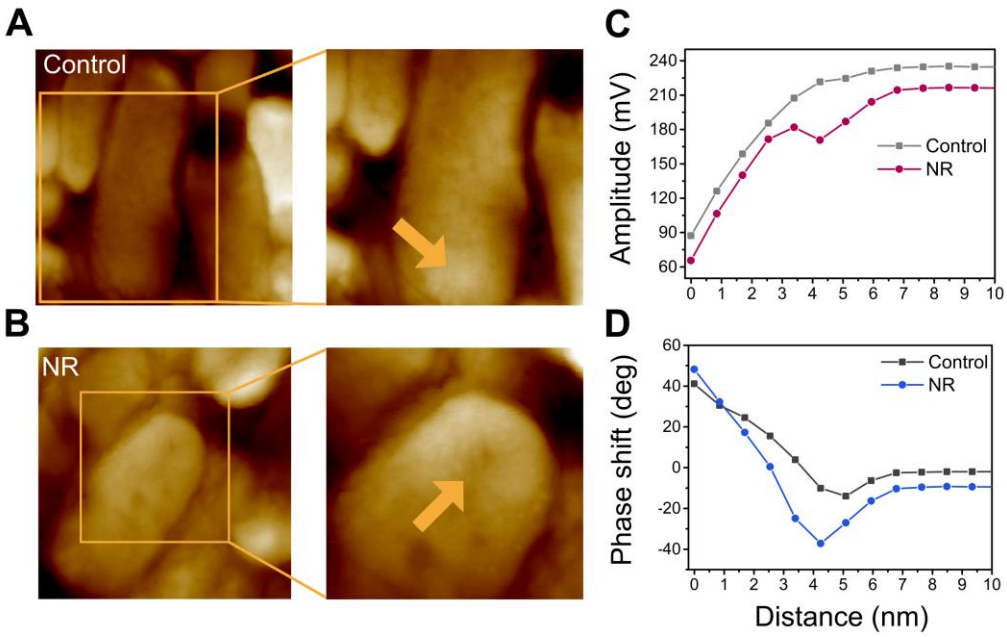

Fig. 3.12. Comparable studies of the bacterial cell wall stiffness by AFM. *E. coli* control is marked as Control and *E. coli* after exposure to ZnO nanorods is marked as NR. Arrows indicate the place where the AFM tip was positioned. (A) Topography images of control bacteria. (B) Topography images of *E. coli* after exposure to ZnO nanorods. (C) Approach curve: amplitude of vibrating cantilever versus distance. (D) Approach curve: phase shift of vibrating cantilever versus distance.

3.9. Evaluation of minimal inhibitory concentration (MIC)

Since the cell wall of bacteria is the first barrier for bacteria protecting from the external environment, its modification upon exposure to physical stress could induce changes in protein and lipid composition. In fact, there is a number of various antibiotics interfering with proteins involved in the cell envelope synthesis or lipids composing the cell memebrane[411].

The goal of the experiment was to check whether the thicker cell wall renders bacteria more resistant or susceptible to specific antibiotics by evaluation of minimum inhibitory concentration (MIC). MIC is defined as the lowest concentration of an antimicrobial agent that inhibits the visible growth of a microorganism after overnight incubation[412]. This is a 'golden standard' used for the determination of the susceptibility of bacteria to antibiotics. MIC was determined using E-tests that are plastic strips with a predefined antibiotic gradient immobilized on one side and a MIC interpretive scale printed on the other side[413]. The MIC value was determined for *Escherichia coli* (Gram-negative strain) upon exposure to nanorods and compared to the value obtained for control *E. coli*. *S. epidermidis* was used as a reference Gram-positive strain to determine MIC values for antibiotics interfering with the cell wall synthesis (Fig. 3.13). However, it should be stressed that susceptibility to antibiotics is a unique characteristic and differences even between strains of bacteria within the same species may occur.

The bacteria were tested for ampicillin, bacitracin, cefaclor, cefazolin, cefpirome, chloramphenicol, ciprofloxacin, colistin, kanamycin, norfloxacin, rifampicin,

imipenem, tetracycline and only results with statistical significance that was obtained in all biological repeats were taken in consideration. Thus, only results for ampicillin, bacitracin, cefazolin, kanamycin, colistin are presented and mechanism of action are discussed.

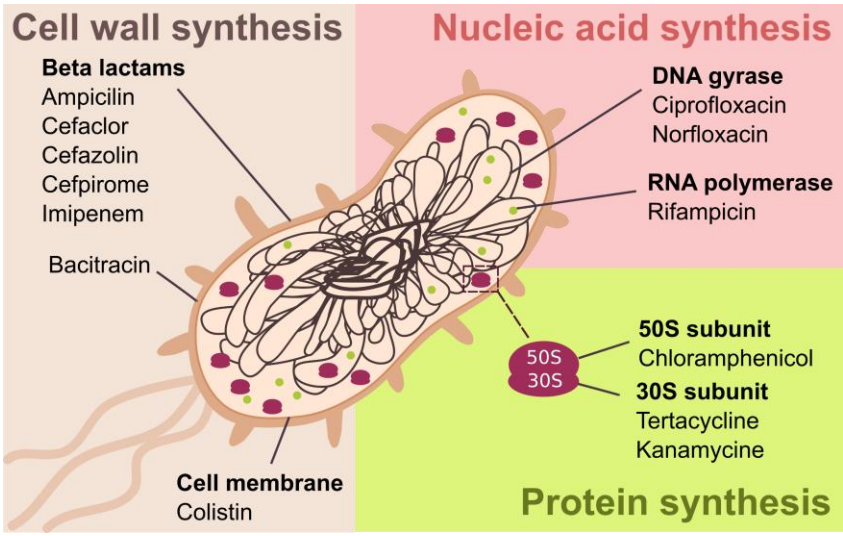

Fig. 3.13. Classification of applied antibiotics based on the mechanism of action.

Ampicillin belongs to the class of organic compounds known as penicillins and inhibits the third (the last stage) of bacterial cell wall synthesis. Ampicillin binds to primary receptors called membrane-bound penicillin-binding proteins (PBPs) that play crucial roles in cell cycle-related formation of peptidoglycan. The inactivation of PBPs by antibiotic has immediate, arresting actions on their function[414,415].

Bacitracin is a mixture of related cyclic polypeptides that interferes with the dephosphorylation of the 55-carbon, biphosphate lipid transport molecule C55-isoprenyl pyrophosphate (undecaprenyl pyrophosphate), which carries the building blocks of the peptidoglycan bacterial cell wall outside the inner membrane for construction. Administration of the antibiotic blocks the formation of the bacterial cell wall[416,417]. In general, bacitracin is not distributed to treat infection caused by Gram-negative bacteria. Bacitracin also binds divalent transition metal ions (Mn(II), Co(II), Ni(II), Cu(II), and Zn(II)), and oxidatively cleaves DNA[416,417].

Cefazolin is a first-generation cephalosporin that is a beta-lactam antibiotic. Cefazolin binds and inactivates PBPs located on the inner membrane of the bacterial cell envelope. Inactivation of PBPs interferes with the cross-linkage of peptidoglycan chains necessary for bacterial cell wall integrity and rigidity. Cell lysis is induced by the weakening of the bacterial cell envelope[418,419].

Kanamycin is an aminoglycoside antibiotic that irreversibly binds to the bacterial 30S ribosomal subunit, causing misreading of t-RNA. Consequently, incorrect amino acids are inserted into the polypeptide chain that leads to the synthesis of nonfunctional or toxic peptides and the breakup of polysomes (a cluster of ribosomes) into nonfunctional monosomes. As a result, the bacterium is not able to synthesize proteins required for further growth[420,421].

Colistin is a polymyxin antibiotic agent, a surface-active agent, which penetrates and disrupts the bacterial cell membrane. This antibiotic is polycationic and has both hydrophobic and lipophilic moieties. It interacts with the bacterial cytoplasmic membrane, changing its permeability[422].

The MIC evaluation revealed that the most pronounced changes in susceptibility between exposed and control *E. coli* were observed in the case of antibiotics affecting the synthesis of peptidoglycan (ampicillin, bacitracin, cefazolin; Fig. 3.14). Interestingly, bacitracin is used exclusively for the treatment of infections caused by Gram-positive bacteria. The susceptibility of treated *E. coli* to kanamycin has decreased which might suggest that exposure to physical stress affected the translational machinery of bacteria. In contrast, tolerance to colistin has increased compared to control bacteria that may indicate that the composition of the lipid membrane within the cell envelope has changed.

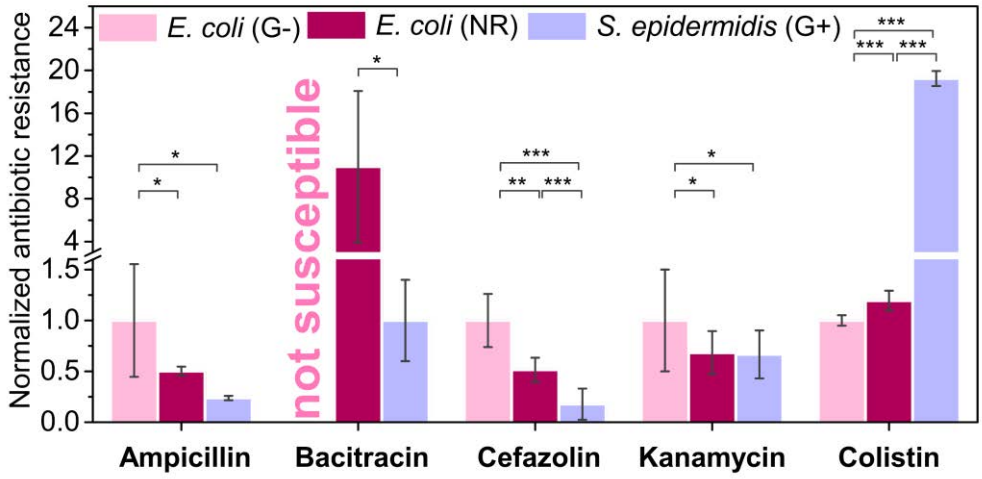

Fig. 3.14. Normalized minimum inhibitory concentration (MIC) for ampicillin, bacitracin, cefazolin, colistin and tetracycline determined for *E. coli* after exposure to ZnO nanorods (*E. coli* NR), control *E. coli* (*E. coli* G-) and *S. epidermidis*. Error bars show standard error of the mean (s.e.m.), where * $P < 0.05$; ** $P < 0.01$; *** $P < 0.001$.

The possible inhibition of the activity of applied antibiotics in the presence of Zn ions, released from ZnO NR, was excluded. First, Mueller Hinton medium used for MIC determination is additionally supplemented with Mg^{2+}, Ca^{2+}, and Zn^{2+} ions that act as cofactors for different enzymes deactivating antibiotics that are synthesized by bacteria. Before plating, the bacterial suspension was diluted according to the general protocol to reach 0.5 McFarland standard (approx. 50-fold dilution), therefore the final concentration of Zn^{2+} was significantly decreased. According to literature data, zinc ions do not inhibit (rather enhance) the activity of ampicillin[423], bacitracin[424], cefazolin[425], kanamycin[426], and colistin[427].

To sum up, the exposure of *E. coli* to ZnO NR resulted in changes in the susceptibility to the studied antibiotics approaching MIC values characteristic for Gram-positive bacteria.

3.10. Interaction of *E. coli* bacteria with bacteriophages

Bacteriophages (phages for short) are viruses that infect and replicate within bacteria[428]. The viral life cycle (Fig. 3.15) is a complex process that consists of many steps like adsorption at the cell surface of bacteria, penetration, biosynthesis of proteins and nucleic acids, assembly of virions and lysis. Therefore, phages can be utilized as "biomarkers" of changes within the bacterial cell envelope or the cell functioning when perturbation connected with the whole life cycle or a certain stage of the virus replication occurs.

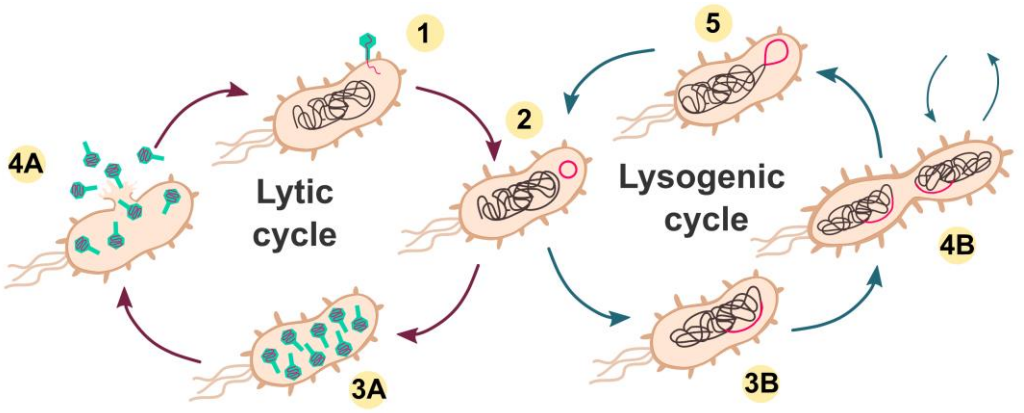

Fig. 3.15. The lytic and lysogenic cycle of bacteriophage. (1) Phage attaches to the host bacterium and injects genetic material. (2) Bacteriophage genetic material circularizes. Certain factors determine whether phage lytic or lysogenic is induced. (3A) New proteins and genetic material are replicated; virions are assembled. (4A) The host lysis and progeny phages are released. (3B) The phage DNA integrates into the bacterial chromosome and becomes prophages ("dormant phage"). (4B) The bacterium with prophage reproduces and viral DNA is passed on to daughter cells through many generations. (5) In rare cases, prophage can excise from bacterial chromosome and enter the lytic cycle.

Firstly, classical plaque method (covers whole lytic cycle) was used to examine whether modification of the cell wall of *E. coli* after the exposure to physical stress induced by ZnO nanorods has an influence on the number of active phages. During the experiment, also a morphology of formed plaques was carefully analyzed. Any changes in size, shape, turbidity, an appearance of the plaque halo or border of the viral colonies can be a proof of handicapped/restricted mechanism of phage activity. Seven different types of bacteriophages with DNA-based genome were used in the experiment (Table 3.2.). The adsorption of phages onto host cells is recognized as a sine qua non condition for the initiation of the infection process, thus in Table 3.1 information about recognized receptor at the surface of bacteria is provided.

Table 3.2. Phage specification. These mutants have been designated "r" for rapid lysis; they differ from the wild type by a failure to cause "lysis inhibition" on strain B.

Phage	Recognized receptor	Plaque morphology	Comments
T7[429]	OmpA and OmpF	3-4 mm in diameter, clear and sharply defined center about 30%	40-kbp dsDNA;

		of diameter constitutes turbid, sharply defined halo	latent period ~17 minutes (100 progeny phages)
T1[430,431]	TonA (FhuA, involved in ferrichrome uptake) and TonB[b]	7-8 mm in diameter, clear central part surrounded by three rings of alternating turbidity and clarity	50.7-kbp dsDNA, the latent period of 13 min (100 progeny phages)
P1[432]	glycolipid	2 mm in diameter, clear and without halo	93-kbp dsDNA, the latent period of 45 min (10 progeny phages)
λ[430,433]	Protein LamB Terminal	3-4 mm in diameter, turbid and without halo	48-kbp, period of 40 min (100 progeny phages)
T4D[434]	presumably LPS and protein B	3 mm in diameter, clear central part, small halo	169-kbp dsDNA,
T4rII[435]	presumably LPS and protein B	4 mm in diameter, clear and sharp	169-kbp dsDNA,
T4rIII[435]	presumably LPS and protein B	4 mm in diameter, clear and sharp	169-kbp dsDNA,

In the case of T1 phage, the formed plaques on *E. coli* bacteria after exposure to ZnO nanorods were ~40% smaller in size compared to plaques formed on control *E. coli*. This result might indicate rather perturbations at the stage of virion formation and release. No significant changes in the morphology of plaques of P1, λ, T7, T4D, T4rII, T4rIII phages were observed. The differences between the number of plaques were not statistically significant in most cases (Fig. 3.16) which suggest that the lytic cycle is not affected.

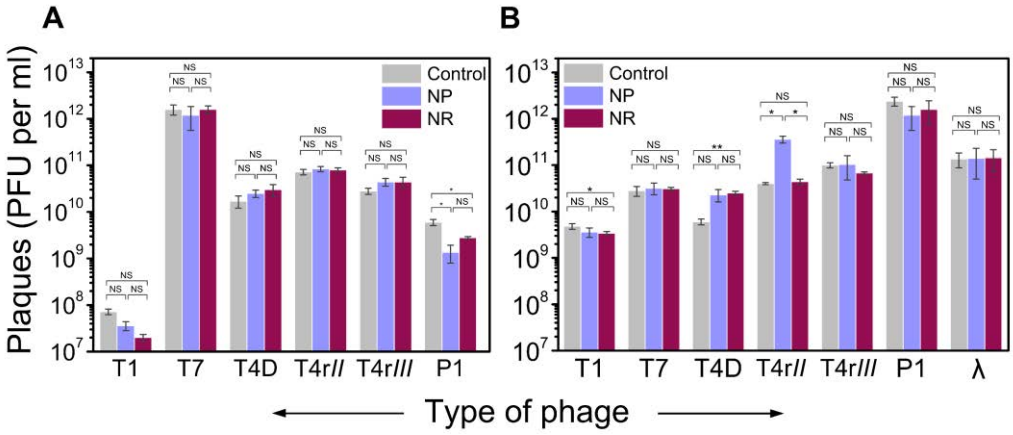

Fig. 3.16. Plaque formation. The differences in the number of plaque forming units (PFU) of T1, T7, T4D, T4rII, T4rIII P1, λ for (A) *E. coli* Bl21(DE3) and (B) *E. coli* Bl21. In the case of BL21(DE3) phage λ was not used because of presence prophage λ in the bacterial genome. Different samples variant were tested: *E. coli* control is marked as control, *E. coli* cells after exposure to ZnO nanorods as NR, *E. coli* cells after exposure to rounded ZnO nanoparticles as NP. Error bars shows standard error of the mean (s.e.m.), where * $P < 0.05$; ** $P < 0.01$; *** $P < 0.001$; NS, not significant.

During the lytic cycle, bacteriophages perform a few consecutive steps. Recognition of specific host cell is followed by the injection of the genetic material. Bacterial intracellular machinery is utilized to produce proteins and replicate nucleic acid.

Finally, assembled virions are released by bacterial lysis[436]. When new progeny phages are released into the environment, where not-yet infected bacteria are present, the whole cascade is repeated, resulting in an increased amount of phages. The cascade is repeated over and over until all bacteria get infected. It should be stressed that the whole process is unsynchronized because diffusion and attachment of phages to the surface can be shifted in time. The synchronized version of this experiment is called "one-step growth" and it requires one additional washing step to remove all unbound phages after the short incubation.

The goal of the next experiment was to check whether differences in growth kinetics of T4 bacteriophage in *E. coli* BL21 after three exposures to ZnO nanorods (ZnO NR) and ZnO nanoparticles (ZnO NP) in comparison to non-treated cells occur. Fig. 3.17 compares the kinetics of growth of T4 phage in control bacteria and after exposure to ZnO nanostructures. Prolongation or handicap of any of step during bacterial infection should result in a decrease of the growth rate. However, no statistically significant differences were observed in growth kinetics between control *E. coli* and the bacteria exposed to ZnO NR or ZnO NP, thus it can be concluded that unsynchronized replication cycle of T4 phage is not affected.

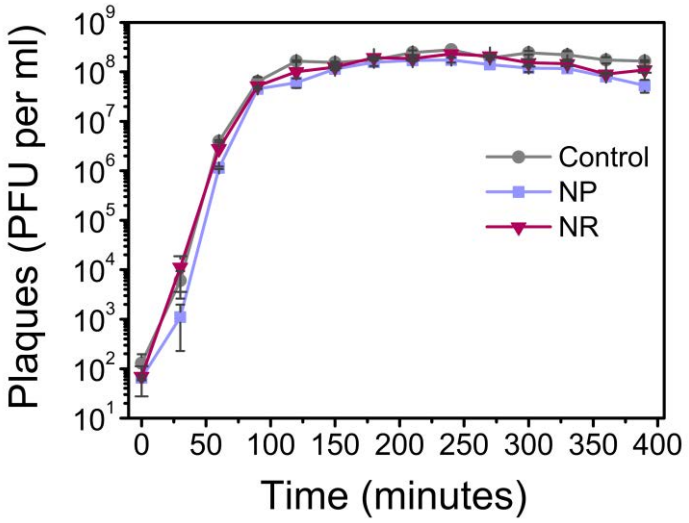

Fig. 3.17. Growth kinetics of T4 bacteriophage. Differences in the number of plaque forming units (PFU) for the population of control *E. coli* are (control), *E. coli* cells after exposure to ZnO NP (NP) and ZnO nanorods (NR).

3.11. Induction of the SOS response

Unfavorable environmental conditions can force bacteria to induce DNA repair system that helps them to survive sudden damages that occur in DNA code[437]. The method that allows investigation of induction of the SOS system involves the utilization of bacteria with prophage (a latent form of bacteriophage that is integrated into bacterial chromosome). Damages of DNA leads to the initiation of the SOS response in the bacteria that triggers the induction of prophages. Induction of prophage means transformation from lysogenic to more aggressive, lytic cycle, during which numerous copies of phages are created

and released from disrupted bacterial cells[438] (Fig. 3.15 3B→4B→5→2→3A→4A→1). The level of DNA damages is reflected in the number of released progeny phages, since the higher the stress, the higher the yield of phages is observed. Importantly, the number of released progeny phages depends on the number of available host bacteria that can be infected.

The aim of the next experiment was to check whether exposure of *E. coli* to ZnO nanorods and rounded ZnO nanoparticles can induce SOS response. It was observed that the number of bacteria decreased during the exposure to ZnO nanorods and ZnO nanoparticles. Therefore, during the experiment, the number of phages and the number of living bacteria were analyzed simultaneously. Figure 3.18 shows normalized changes in the number of phages that are divided by the number of bacteria (PFU/CFU per ml). Mitomycin C was used as a marker that induced high SOS response by crosslinking DNA and inhibition of replication.

The higher induction of the SOS signal in the case of *E. coli* exposed ZnO NR and ZnO NP compared to control can be associated with the higher probability of piercing of the bacteria during collisions. Disintegration or increased permeability of the cell wall can cause the efflux of external solvent to the interior of the cell, inducing stress. Although higher induction of prophage is observed in the case of the samples with ZnO NP and ZnO NR, the maintained level is relatively low in comparison to mitomycin C stimulation. Thus, it can be concluded that DNA damages were not significant.

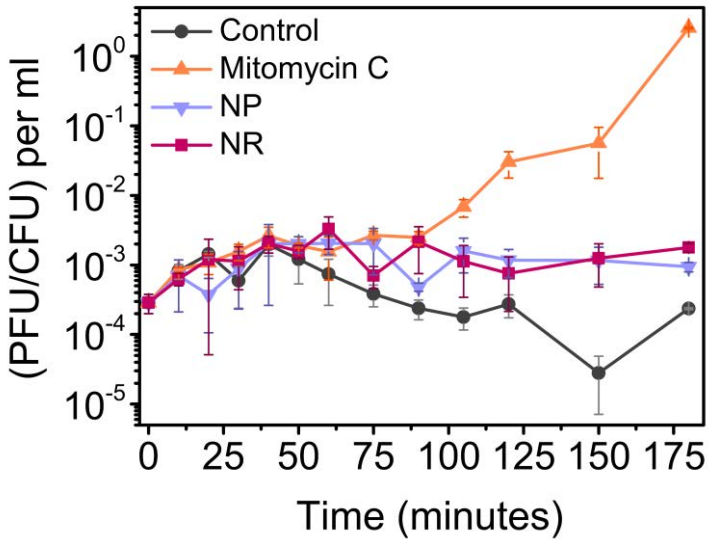

Fig. 3.18. Induction of SOS signal in *E. coli* K12 MG 1655 with prophage **λ** PaPa. The difference in number of plaque forming units (PFU) divided by the number of the bacteria (CFU) for control *E. coli* (control), *E. coli* cells exposed to mitomycin C (mitomycin C), *E. coli* cells after exposure to ZnO nanorods (NR) and *E. coli* cells after exposure to ZnO nanoparticles (NP).

3.12. Conclusions

In this chapter data on phenotype plasticity of *E. coli* upon exposure to mechanical stress induced by sharp ZnO nanorods (size exceeding 300 nm and concentration of 1 mg/mL) were presented.

Phenotype investigation by SEM and Cryo-SEM revealed that *E. coli*, which survived mechanical stress, changed the shape to more spherical. The increased number of experimental runs and exposures to the ZnO NR resulted in the appearance of spherical cells in the population. Jain et al. also reported the change of shape of *E. coli* cells after exposure to ZnO nanorods. The authors explained that the reshaping of bacteria can be a sign of distress since the cells were not able to normally divide[354].

The changes in the shape of *E. coli* upon exposure to physical stress could be a consequence of entering the viable but non-culturable (VBNC) state. This is a survival strategy adopted by bacteria exposed to different types of stressful condition (low temperature, starvation, ionic strength, irradiation, etc.). Although a characteristic feature of *E. coli* entering the VBNC state is a coccus-like shape[439], there is a significant difference between the state obtained through the mechanical stress and the VBNC state. Firstly, bacteria in the VBNC state lose their cultivability in the media in which they normally grow. Thus, it is not possible to recover the cells when they are cultured onto conventional growth media. In appeared that the bacteria exposed to ZnO NR grew normally on lysogeny broth (LB-Miller medium), hence it was possible to determine growth curves by counting bacterial colonies on agar plates. Also bacteria were refreshed for TEM measurements.

Secondly, the bacteria in VBNC state have dramatically lowered metabolic activity[440], thus they are not a target for most bacteriophages that infect cells which have exhibit higher metabolism[441]. Similar susceptibility to bacteriophages was obtained for nanorods-treated cells similar and native bacteria. Plaques of T1, P1, T4D, T4*rII*, TR4*rIII*, T7, λ phages were properly formed without statistical differences in the efficiency of plating. Statistically significant changes in growth kinetics of T4 bacteriophage in control *E. coli* and exposed to ZnO nanorods was not observed. The induction of the SOS response (induction of prophage) was performed to check the level of DNA damages in *E. coli* after the exposure to ZnO nanorods. The number of released progeny phages reflected that the DNA damages were not significant.

Besides changes in the size of bacteria, also increased the thickness of the cell wall that had higher density was observed. Analysis of the elemental composition of the periplasm and the interior of *E. coli* performed using the energy-dispersive X-ray spectroscopy revealed significant changes in the elemental composition in the case of *E. coli* upon exposure to physical stress. Intriguingly, performed Gram staining for *E. coli* after exposure to the mechanical stress shown the higher amount of peptidoglycan within the cell wall in comparison to control *E. coli.* Therefore, it was tested whether a thicker cell wall could render bacteria more resistant or susceptible to antibiotics, especially those interfering with proteins involved in the cell envelope synthesis[411]. The most pronounced changes in susceptibility between exposed and control bacteria were observed in the case of antibiotics interfering with the synthesis of peptidoglycan: i) ampicillin that interferes with the cell cycle-related formation of peptidoglycan[414]; ii) bacitracin which

affects the transport of building blocks for the peptidoglycan synthesis (used to treat infection caused by Gram-positive bacteria)[416], and iii) cefazolin that inactivates penicillin-binding proteins, and consequently interferes with the cross-linkage of peptidoglycan chains required for bacterial cell wall integrity and rigidity[418,419]. Based on the results of Gram staining and TEM measurements (thickness of the cell wall), the difference in the stiffness of the cell wall of the treated bacteria compared to control population was suspected. AFM was used to confirm changes between the Young modulus of the cell wall of the control *E. coli* and the bacteria after exposure to ZnO nanorods. AFM results strongly suggest that the cell wall of nanorod-treated bacteria is stiffer due to the higher amount of peptidoglycan that is the component that contributes to the stiffness of the cell envelope to the greatest extent[442].

To conclude, all the presented results in this chapter support the statement that *E. coli* after exposure to ZnO nanorods acquires different phenotype by changing the thickness, density, and composition of the cell envelope as a result of mechanical stress induced by ZnO nanorods.

3.13. Experimental section

The procedure of *E. coli* exposure to ZnO nanostructures

E. coli BL21 (obtained from the Faculty of Biology, University of Warsaw, Poland), *E. coli* BL21(DE3) (obtained from the Institute of Biochemistry and Biophysics of the Polish Academy of Sciences in Warsaw, Poland) were in the experiments with ZnO nanorods and rounded ZnO nanoparticles. The *E. coli* BL21(DE3) strain had two plasmids and was resistant to chloramphenicol and kanamycin. Thus, the medium was supplemented with chloramphenicol and kanamycin (Sigma-Aldrich) to final concentrations of 50 μg/ml and 25 μg/ml, respectively.

First, a single colony from an agar plate was inoculated into LB medium (Roth) for seven hours (37 °C, 200 rpm). The overnight culture was inoculated into a new portion of the medium (volume ratio 1:100) and cultured to obtain suspensions of OD_{600} = 0.1. The bacterial suspension was split into two sterile flasks (the same starting amount of the bacteria was maintained). ZnO NR and ZnO NP were added to one of the flasks to obtain a concentration of 1 mg/mL. *E. coli* cultured in a shaker (IKA KS 4000 i, Germany) for 24 hours (37 °C, 200 rpm). In the case of a higher number of exposures, after 24 hours, 100 μl of control bacteria were inoculated into a fresh portion of LB medium, and similarly 100 μl of the cells that had survived the first exposure to sharp ZnO nanorods (NR) were inoculated into the fresh portion of LB medium supplemented with the nanorods. Bacteria were cultured for 24 hours in the shaker. To determine the viability of the bacteria upon exposure to ZnO nanorods (NR), we applied the colony count method (at least 6 technical replicates for each dilution) to 50 μl of the bacterial suspension was seeded per agar plate. After 24 hours of incubation on Petri dishes, the bacteria were counted to determine the colony forming units (CFU). The whole experiment was performed in three independent repeats.

UV spectra of Gram-stained bacteria

Gram staining was performed for the *E. coli* BL21(DE3) strain after two exposures to ZnO nanorods (each exposure for 24 hours). Firstly, nanorod-treated bacteria were left for 5 minutes motionless in order to decrease the number of bigger aggregates of nanorods by sedimentation. The supernatant with the bacteria was collected and the same OD~1.0

was adjusted for all samples. Subsequently, the bacteria were centrifuged (5 minutes, 4000 rpm) and the pellet was suspended in sterile physiological saline (0.9% mass/volume). The sodium chloride was purchased from Sigma-Aldrich. A smear of bacterial suspension was made on a clean glass slide by pipetting 250 µl of suspension, left to dry in the air and then heat-fixed by passing it several times through a flame. The glass slides were flooded with crystal violet for 30 seconds; washed with sterile MQ water; treated with Lugol solution for 60 seconds, rinsed with water, gently rinsed with ethanol (96%, POCH, Poland) by pouring over the smear for about 3-4 seconds and washed with MQ water. Finally, the glass slides were flooded with safranine for 60 seconds, rinsed with water and drained. The crystal violet, safranine, and Lugol solution were purchased from Aqua-Med Company (Poland). Samples were imaged using the Nikon Eclipse 50i (Japan) microscope. The smears from the plates (control and upon exposure to NR) were entirely washed using 4 ml of a mixture of ethanol and water (50% volume/volume). UV-Vis spectra were registered using the UV-Visible Spectrophotometer Evolution 201 (Thermo Scientific, USA).

Scanning electron microscopy (SEM) and cryo-scanning electron microscopy (Cryo-SEM)
The shape of *E. coli* BL21 and *E. coli* BL21(DE3) were investigated using SEM microscope. In the case of SEM imaging, a special sample protocol was established to avoid several centrifugation steps that are required during the exchange of solvents. In the samples where the bacteria were suspended together with the nanorods, the centrifugal force could intensify the piercing of the bacteria by the nanorods that could falsify the native pictures of the cells. *E. coli* BL21 (control and after exposure to NR every 24 hours) were centrifuged (4 minutes, 4000 rpm). The pellet was suspended in a sterile, 50-fold diluted solution of physiological saline in MQ water. The bacterial suspension (5 µl) was placed on (prior washed in acetone, ethanol, MQ water) silicon plates. After 60 seconds, half of the liquid was discarded to obtain a thin film on the surface of the plates. Just as the edges of the spot started to dry out, the plates were gently rinsed by a rowing movement in filtered MQ water to remove the excess of salt from the surface. Silicon plates with the samples were attached to the metal holder by silver paste. The samples were imaged using the FEI Nova NanoSEM 450 (USA) scanning electron microscope. In the case of cryo-SEM, *E. coli* BL21(DE3) cells after two exposures to ZnO NR (each exposure for 24 hours) were analyzed. Images were taken using JEOL JSM-7001F TTLS (JEOL Ltd., Japan) scanning electron microscope equipped with the PP3000T cryo-SEM preparation system that enables the preparation, loading, processing, and transfer of cryo-specimens into the SEM chamber. The speciemen wasprepared by pipetting 50 µl of bacterial suspension on the metal holder. The samples were rapidly frozen by plunging the holder into slush nitrogen (-210°C) and transferred under a vacuum to the preparation chamber mounted onto the SEM. Inside the preparation chamber (-185°C), the specimens were fractured to expose a fresh surface, and subsequently sublimated and coated with a thin platinum layer. Finally, the samples were transferred under a vacuum into the SEM cryo stage (-190°C) where the surface was analyzed by applying an accelerating voltage of 10 kV and secondary electron (SEI) detector.

Transmission electron microscopy (TEM) and X-ray microanalysis
The cell wall thickness of *E. coli* BL21(DE3) was measured after 24-hours exposure to ZnO nanorods. 100 µl of the bacteria from the control and the nanorod-treated culture was inoculated into a fresh portion of LB medium in order to remove ZnO nanorods Overnight cultures were centrifuged (5 minutes, 4000 rpm) and the pellet was suspended in 0.9%

physiological saline. The cells were fixed in 1.5% glutaraldehyde (final concentration) in 0.1 M cacodylate buffer (pH=7.2) for 2 hours with mixing (Biosan Mini rocker MR-1; max speed) at room temperature. Next, the bacteria were washed twice in the same buffer followed by gentle centrifugation after each step. The cultures were divided into two parts: post-fixed in 2% osmium tetroxide for 1 h (with gentle shaking) and without fixation. After washing in cacodylate buffer, the samples were gradually dehydrated (50% and 70% ethanol), centrifuged and left O/N in 70% ethanol. After dehydration in graded series of ethanol solutions followed by 3 changes (30 minutes each) of LR-White resin mixture (Polysciences, Inc., Warrington, PA) with 100% ethanol (at 1:1, 2:1, and 3:1 ratio, respectively) on a rotator, the samples were infiltrated with LR-White O/N, and embedded in the resin. After thin-sectioning, the samples were collected on copper or nickel grids, respectively (Agar Scientific Ltd., Stansted, UK). Ultrastructure and X-ray microanalysis of the specimens was performed using the transmission electron microscope JEM 1400 (JEOL Co., Japan), equipped with a digital camera (CCD MORADA, SiS-Olympus, Germany) and an energy-dispersive full range X-ray microanalysis system EDS INCA (The Microanalysis Suite, Issue 18, ver. 4.11, Energy TEM 250, Oxford Instruments, UK). The analysis was performed in an energy range of 1–10 kV at applied accelerating voltage of 80 kV (Livetime 300.0 s) in the Laboratory of Electron Microscopy (Nencki Institute of Experimental Biology, PAS). Thickness of the cell wall (TEM) was measured for the following number of cells: 1) nickel meshes: 29 control cells and 25 cells after exposure to ZnO NR; 2) nickel meshes with osmium tetroxide saturation: 58 control cell and 67 cells after exposure to ZnO NR; 3) copper meshes: 36 control cells and 36 cells after exposure to ZnO NR; 4) copper meshes with osmium tetroxide saturation: 19 control cells and 43 cells after exposure to ZnO NR. X-ray microanalysis analysis of the cytoplasm and the periplasm was performed using the following numbers of the bacteria: 1) nickel meshes: 22 control cells and 22 cells after exposure to ZnO nanorods (NR); 2) nickel meshes with osmium tetroxide saturation: 11 control cell and 8 cells after exposure to NR; 3) copper meshes and copper meshes with osmium tetroxide saturation: 12 control cells and 12 cells after exposure to NR.

Minimum inhibitory concentration (MIC) evaluation

The MIC was determined using the E-test with a predefined antibiotic gradient immobilized on one side of the plastic strip. The E-test with ampicillin, bacitracin, cefazolin, colistin, kanamycin, tetracycline were used on *E. coli* BL21 (Gram-negative strain): control cells and after exposure to ZnO nanorods. *S. epidermidis* was used as the referential Gram-positive strain. E-tests for all antimicrobials were used in a gradient of antibiotic concentrations of 0.016-256 μg/mL. First, the bacteria were exposed to ZnO nanorods (NR) (described above). 250 μl of each bacterial suspension after the first exposure (control *E. coli*; treated *E. coli*, control *S. epidermidis*) was inoculated into a fresh portion of LB medium (25 ml) and LB medium with suspended ZnO NR at a concentration of 1 mg ml^{-1} (in the case of exposed *E. coli*). After the second exposure, the flask with ZnO NR was left for 5 minutes to enable sedimentation of the larger aggregates. Subsequently, suspensions of the bacteria were used to prepare inoculum in 0.9% physiological saline and the turbidity was adjusted to 0.5 McFarland standard. Dedicated standardized Mueller Hinton (MH) agar broth (Biocorp, Poland) was used to evaluate the MIC concentration. The bacterial suspensions were spread on dry MH agar plates using sterile swabs and E-tests were put on agar plates with the bacteria. After 20-hour- incubation,

the MIC values were read. Two biological repeats of the experiment were performed, for each type of sample two technical replicates were done.

Statistical analysis

The unpaired t-test was used to check significant differences between control *E. coli* and upon exposure to ZnO nanorods in the experiments where data from SEM, cryo-SEM, TEM, EDS, and antibiotic susceptibility were obtained.

Chapter 4

Changes in genome and transcriptome of *E. coli* after exposure to ZnO nanorods

Mechanical stress induced by ZnO nanorods induces changes in the genome that are stable over time. Genome sequencing revealed twenty-five single nucleotide polymorphisms mutations (SNPs) in *E. coli* BL21 and sixteen SNP mutations in *E. coli* BL21(DE3). In both cases, the majority of SNPs occurred within intergenic regions. Only two mismatch mutations were observed within coding sequences - one amino acid was changed in the protein from the Rhs family or Rhs-like protein, and the second one in gene encoding the transposase belonging to the IS*4* family. The transcriptomic analysis revealed the down-regulation of expression of sixty-one genes involved in β-oxidation of fatty acids, glycolysis, the citric acid cycle and uptake of amino acids and enzyme cofactors.

This chapter has been published as:

Kinga Matuła, Łukasz Richter, Marta Janczuk-Richter, Wojciech Nogala, Mikołaj Grzeszkowiak, Barbara Peplińska, Stefan Jurga, Elżbieta Wyroba, Szymon Suski, Henryk Bilski, Adrian Silesian, Hans A. R. Bluyssen, Natalia Derebecka, Joanna Wesoły, Joanna M. Łoś, Marcin Łoś, Przemyslaw Decewicz, Lukasz Dziewit, Jan Paczesny, Robert Hołyst, *Phenotypic plasticity of Escherichia coli upon exposure to physical stress induced by ZnO nanorods*. *Scientific Reports*, 2019, 12;9(1).

4.1. Introduction

Although the natural evolution of microorganisms is of great importance since it gives new insight into mutation rate and the correlation between the genomic and phenotypic plasticity, currently it is the evolution of microbes under antibiotic pressure that takes on increased importance. Considering the emergence of drug-resistant bacteria, surprisingly little is known about adaptation or evolution of bacteria under physical stress. It becomes clear that not only the effect of nanoparticles on bacterial cell morphology but also changes emerging at genome and transcriptome level should be deeply investigated.

In this chapter, a step toward a better understanding of the genome and transcriptome changes of bacteria exposed to nanomechanical stress and nanoparticles is presented. The genetic analysis compromises one time-point measurement using DNA-sequencing and RNA-sequencing.

4.2. Genome analysis of *E. coli* after exposure to ZnO nanorods

DNA-sequencing (DNA-seq) gives an opportunity to investigate changes that occur at the genome level. Since the drug-resistance (i.e., chemical stress) is often associated with the emergence of new mutations[443], the next experimental goal was examination whether changes induced by physical stress were also related to modifications in the DNA of bacteria.

The whole-genome sequencing of *E. coli* BL21 and *E. coli* BL21(DE3) exposed to ZnO nanorods was performed to investigate changes in the genome upon the exposure to ZnO nanorods. The DNA material from the control bacteria and after exposure to sharp ZnO nanorods (3 exposures, 72 hours in total) was isolated and processed to obtain libraries suitable for DNA sequencing (MiSeq, Illumina platform). After careful literature review, two programs: HaplotypeCaller and FreeBayes were chosen to analyze the data after sequencing. Only mutations detected by both programs for two bacterial strains were considered (see Fig. 4.1A). Figure 4.1B shows point mutations for two bacterial strains that were identified in all three biological repeats of the experiment (details for SNPs determined for *E.coli* BL21 and *E. coli* BL21DE3 are provided in Table 4.1 and Table 4.2, respectively). Twenty-five single nucleotide polymorphisms (SNPs) were identified in *E. coli* BL21. Interestingly, only one mismatch type SNP changed the protein-coding sequence (SNP in the first position in codon), while other mutations were located within the intergenic regions or were silent mutations. In the case of *E. coli* BL21(DE3), sixteen SNPs were found and two SNPs were located within the protein-coding sequences. Intriguingly, in both strains (each bacterial strain was obtained from a different, independent source) the SNP appeared in the region coding the Rhs protein or Rhs-like protein. Although the role of this gene is not clearly understood yet, its function is associated with the cell surface and it is suggested that the Rhs protein possesses binding properties[444,445]. One additional SNP was identified within the gene encoding the transposase of the IS*4* family which is an enzyme responsible for transposition (transfer of mobile genetic elements within the genome). Importantly, this mechanism is responsible for genome flexibility and triggers the bacterial evolutionary process[446].

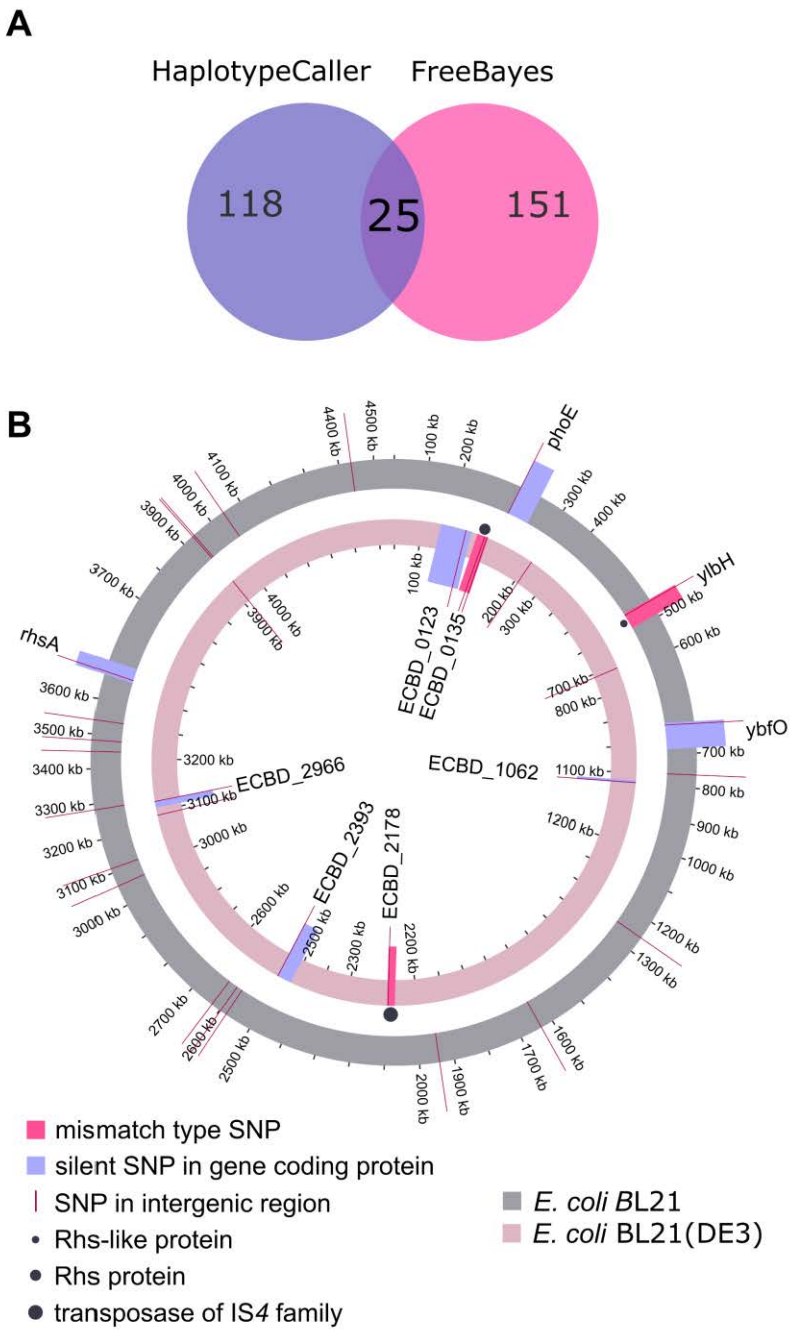

Figure 4.1. Changes in the genome of *E.coli* after exposure to ZnO nanorods. (A) Representative Venn diagram determined for *E. coli* Bl21 shows SNPs detected by HaplotypeCaller and FreeBayes. (B) Single nucleotide polymorphisms (SNPs) identified in genomes of *E. coli* BL21 and BL21(DE3) after three exposure to ZnO nanorods (72 hours in total). The outer ring (grey) depicts mutations found in the genome of *E. coli* BL21 and the inner one (pink) represents SNPs for *E. coli* BL21(DE3). The kilobase-scale (kb) shows the genome position. SNPs located in intergenic regions are indicated with straight red lines, dark-pink areas mark protein-coding sequences (genes) with mismatch type SNPs and

violet regions represent genes with silent mutations that do not change the protein sequence. The length of protein-coding sequences corresponds with the different sizes of dark-pink and violet areas. In the case of *E. coli* BL21 in the region between 1200 and 1300 kb, there are four SNPs marked as one line due to their close location. Similarly, in the region between 3100 and 3200 kb in *E. coli* BL21 two SNPs were identified in close proximity. In the region between 700 kb and 800 kb of *E. coli* BL21(DE3) genome, there are three SNPs marked as one line, and additionally, in the regions between 3000 and 3100 kb and 3900 and 4000 kb there are two SNPs indicated by a single red line. Locus tags and/or gene names with SNPs (both, silent and mismatch type) are indicated. The names of encoded proteins are marked with dots.

Although the majority of identified SNPs was localized within intergenic regions (noncoding DNA located between two genes), it is still possible that they arose within the not yet identified regions encoding ncRNAs that can play crucial regulatory functions. Therefore, in the presence of the growing body of literature related to the characterization of ncRNAs, at least some of those SNPs may have a meaningful effect on the overall gene expression level.

Table 4.1. Details for SNP mutations identified in *E. coli* BL21.

Escherichia coli BL21						
Gene	Genome position	Reference	Variant	Type	Change in amino acid	Description of the gene product
phoE	263558	C	A	synonymous variant	p.Ala344Ala	outer membrane pore protein E
ylbH	497181	C	G	missense variant	p.His31Gln	conserved Rhs-like protein
ybfO	691808	G	A	synonymous variant	p.Thr24Thr	conserved rhs-like protein
Rz/borD	766400	A	C	intergenic region	-	DLP12 prophage; predicted murein endopeptidase/bacteriophage lambda Bor protein homologue
rdlD/ldrB	1257654	G	A	intergenic region	-	RdlD antisense regulatory RNA of the LdrD-RdlD toxin-antitoxin system/ small toxic polypeptide LdrB
rdlD/ldrB	1257661	G	A	intergenic region	-	
rdlD/ldrB	1257670	T	C	intergenic region	-	
rdlD/ldrB	1257686	A	G	intergenic region	-	
ydgA/uidC	1636657	C	T	intergenic region	-	conserved protein with unknown function/membrane-associated protein
hchA_2	1941183	T	A	pseudogene	-	-

srmB/yfiE	2580938	C	T	intergenic region	-	DEAD-box RNA helicase/DNA-binding transcriptional regulator LYSR-type
rrsG/clpB	2597817	C	T	intergenic region	-	16S ribosomal RNA /ClpB chaperone
ybl116/insA-15	2627707	G	T	intergenic region	-	ybl116/IS1 protein InsA
yqiK/SlB_RNA	3060713	A	G	intergenic region	-	inner membrane protein YqiK/Sib RNA
yhaC/RNaseP_bact_a	3136047	C	A	intergenic region	-	uncharacterized protein YhaC/ribonuclease P
yhaC/RNaseP_bact_a	3136086	A	C	intergenic region	-	
yhdZ/rrfF	3284549	C	T	intergenic region	-	component of YhdW/YhdX/YhdY/YhdZ ABC transporter/5S ribosomal RNA
ugpB/livF	3454964	G	A	intergenic region	-	sn-glycerol-3-phosphate-binding periplasmic protein Ugp/subunit of leucine ABC transporter
yrhC/yhhI	3486576	T	C	intergenic region	-	Pseudogene/putative transposase
bcsG/ldrD	3561157	A	G	intergenic region	-	inner membrane protein/LdrD peptide of the LdrD-RdlD toxin-antitoxin system
rhsA	3628692	A	G	synonymous variant	p.Gly42Gly	RhsA protein in rhs element
fre/fadA	3934314	T	C	intergenic region	-	FMN reductase/ 3-ketoacyl-CoA thiolase
hemG/rrsA	3942070	G	C	intergenic region	-	protoporhyrinogen oxidase/16S ribosomal RNA
yijF/gldA	4046396	T	G	intergenic region	-	conserved protein with unknown function/D-aminopropanol dehydrogenase
insAB-26	4432523	A	C	pseudogene	-	-

Table 4.2. Details for SNP mutations identified in *E. coli* BL21(DE3).

Escherichia coli BL21(DE3)						
Gene	Genome position	Reference	Variant	Type	Change in amino acid	Description of the gene product
ECBD_0123	129347	A	G	synonymous variant	p.Asn700An	YadA domain protein
ECBD_0135	142160	C	T	synonymous variant	p.Arg119Ag	Rhs protein
ECBD_0135	142420	T	G	missense variant	p.Lys33Gln	
ECBD_0200/ ECBD_0210	211766	G	T	intergenic region	-	hypothetical protein/cellulose synthase operon protein YhjU
ECBD_0689/ ECBD_0690	713101	T	G	intergenic region	-	D-beta-D-heptose 7-phosphate kinase, D-beta-D-heptose 1-phosphate adenosyltransferas/band 7 protein
	713111	T	C	intergenic region	-	
	713152	T	G	intergenic region	-	
ECBD_1062	1112063	A	G	synonymous variant	p.Thr24Thr	insertion element protein PFAM
ECBD_2178	2293820	G	T	missense variant	p.Ala219Gu	transposase of IS*4* family
ECBD_2393	2510574	G	A	synonymous variant	p.His20His	nitrate reductase subunit beta
ECBD_2958/ ECBD_2959	3090512	C	T	intergenic region	-	pseudogene/hypothetical protein
	3090571	C	T	intergenic region	-	
ECBD_2966	3101368	A	G	synonymous variant	p.Gly197Gly	DNA-binding transcriptional activator KdpE response regulator
ECBD_3744	3910203	A	C	synonymous variant	-	pseudogene
ECBD_3744/ ECBD_3745	3910560	T	C	intergenic region	-	pseudogene/RNA polymerase sigma factor FecI
	3910565	T	A	intergenic region	-	

4.3. Transcriptome analysis of *E. coli* after exposure to physical stress

To get a deeper insight into the response of bacteria to external perturbations (i.e., chemical or physical changes), RNA sequencing was utilized for analysis and quantification of the activity of genes.

Whole RNA-sequencing (RNA-seq) was performed for *E. coli* after three exposures to ZnO nanorods (72 hours in total) and the control *E. coli*. Most of the experiments presented in the previous chapter were performed on the cells harvested at the end of the logarithmic phase or in the stationary phase. To be consistent, *E. coli* was also collected at the stationary phase for the RNA-seq experiment. Importantly, the same samples were used in two experiments: i) the first part was used for library preparation and DNA sequencing (described in the previous section), and ii) the second portion was processed for RNA sequencing. Briefly, total RNA was isolated and purified from lysed control *E. coli* and the bacteria after exposure to mechanical stress. Next, rRNA was depleted, leaving mRNA that was subsequently fragmented, reversibly transcribed to complementary DNA (cDNA), purified and ligated to adapters. Obtained libraries after qualitative and quantitative analysis (chip electrophoresis and fluorometric analysis) were sequenced using Miseq (Illumina).

RNA-seq analysis (Fig. 4.2) revealed 606 differentially expressed genes (DEGs) in all three biological repetitions of the experiment: 363 genes were upregulated and 243 genes were downregulated (see Supplementary Fig. S6-S11).

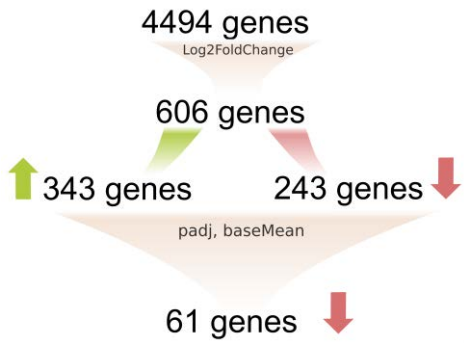

Figure 4.2. Scheme shows the transcriptome data analysis process including criteria taken into consideration. Log2FoldChange is $\log_2$ (logarithm to base 2) from the difference in gene expression control between control and treated sample. Padj corresponds to modified p-value and baseMean refers to the number of reads mapping to a gene in a reference sequence. The green arrow indicates upregulated genes, the red one downregulated genes.

Since the bacteria were harvested in the stationary phase and thus the number of transcripts was relatively low, only genes with i) a high baseMean (the average number of reads mapped to a given gene in treated and control samples) and ii) statistically significant padj <0.05 criterion (modified p-value corrected by multiple testing of the differences in gene expression using the Benjamini-Hochberg procedure[447]) were taken into consideration. These two criteria resulted in 61 DEGs, all of which were down-regulated (more details are provided in Fig. 4.3. and Table 4.3).

There were only 4 upregulated genes that fulfilled the statistical significance conditions (p-value < 1e-5, padj < 0,002). All of them were 4-5 times upregulated on average:

- WP_000502388.1: encoding putative selenate reductase subunit YgfK;
- WP_000953449.1: encoding TonB-dependent siderophore receptor that is the outer membrane receptor for ferric coprogen and ferric-rhodotorulic acid, involved in inorganic ion transport and metabolism;
- WP_000177906.1: encoding beta-galactosidase;
- WP_001026900.1: encoding a hypothetical protein, glycoside hydrolase family 127 protein.

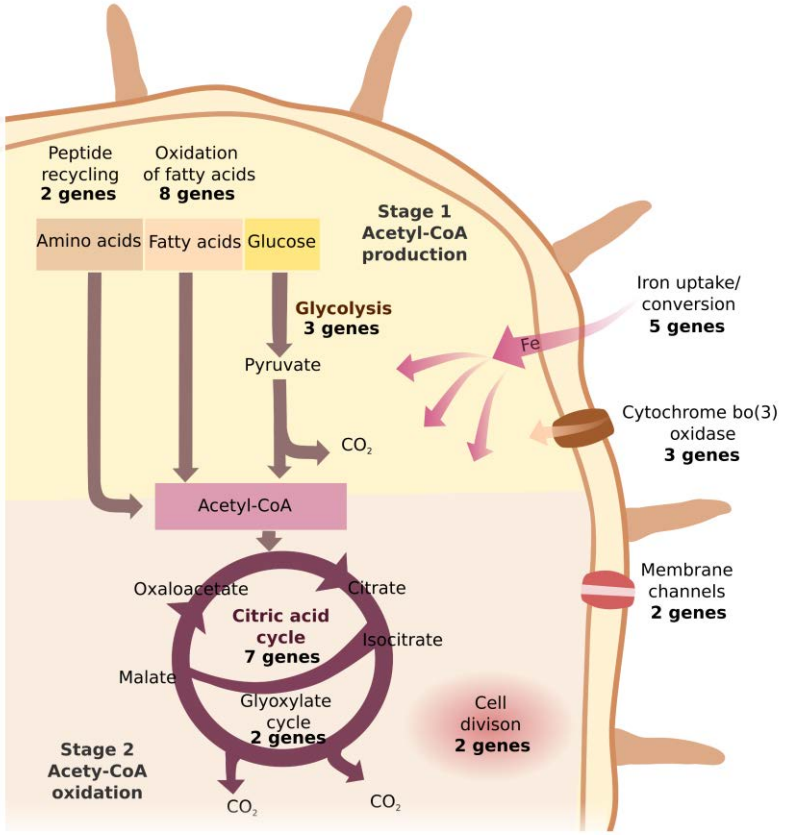

Figure 4.3. Downregulation of genes involved in different pathways in *E. coli* after exposure to mechanical stress. Only half of the downregulated genes is presented in the scheme.

The analysis revealed downregulation of genes related to oxidation and degradation of fatty acids (eight genes in total). Lower expression of these genes may lead to a lower rate of β-oxidative cleavage of fatty acids into acetyl-CoA[448] and consequently i) decrease the overall metabolism of the cell and ii) have an impact on the structure and fluidity of the cell membrane which is composed of lipids[449]. The latter is supported by higher minimum inhibitory concentration determined for colistin that acts as a surface-active agent (see Fig. 3.14). Different lipid composition of the cell membrane, being the result of decreased degradation of fatty acid, may lead to lower susceptibility to colistin.

Inhibited (slowed-down) general metabolism of the bacteria after the exposure to the nanorods is reflected also by lower expression of genes (ten genes in total) related to the tricarboxylic acid cycle (TCA) and genes linking the glycolysis pathway with the citric acid cycle (three genes). This is because lipid metabolism results in the production of acetyl-CoA which is subsequently used in the TCA cycle. Downregulation of the genes involved in: catabolism of galactitol, products of which are converted into intermediates of glycolysis (three genes), the glyoxylate cycle (a carbon metabolic pathway that is an alternative to the TCA cycle; two genes), and the glycolysis process (three genes) support the observation of inhibited metabolism upon exposure of the bacteria to nanorods.

Downregulation of three genes encoding subunits of cytochrome bo(3) ubiquinol oxidase was observed. This enzyme located in the cytoplasmic membrane is a terminal oxidase in the aerobic respiratory chain of *E. coli* [450]. This enzyme has also proton pump activity and translocates protons across the membrane that results in building a potential gradient[451]. Crucially, one of the key cofactors of this enzyme is iron, the lower amount of which was determined by EDS in the case of bacteria after exposure to ZnO nanorods (see Fig. 3.11). Of the particular interest was a lower expression of three other genes, involved in uptake/conversion of iron. This can lead to a lower accumulation of iron inside the cell. Consequently, this may affect many enzymes using iron as a cofactor e.g., cytochromes.

Moreover, transcriptome analysis revealed downregulation of genes involved in: i) transport of amino acids (two genes), ii) metabolism of amino acids (two genes), iii) cell division (two genes) and iv) peptide recycling during carbon starvation (two genes).

Table 4.3. Gene expression results. Log2FoldChange is defined as $\log_2$ from the difference in gene expression between treated and control *E. coli*; gene product is the name of the protein encoded by the gene, a function of which is discussed in the last column. The functions of genes were found in UniProt and BioCyc databases. Only genes with padj from 4.79E-18 to 0.04095 are presented.

Gene	Log2 Fold Change	Gene product	The Function of the gene product
B21_RS03155 (gltL)	-3.93	glutamate/aspartate ABC transporter substrate-binding protein	involved in glutamate and aspartate uptake
B21_RS15760 (mtr)	-2.46	tryptophan-specific transporter	involved in transporting tryptophan across the cytoplasmic membrane
B21_RS01990 (cyoD)	-4.44	cytochrome bo(3) ubiquinol oxidase subunit 4	the component of the aerobic respiratory chain that predominates when cells are grown at high aeration; has proton pump activity across the membrane
B21_RS01995 (cyoC)	-3.21	cytochrome bo(3) ubiquinol oxidase subunit 3	involved in the aerobic respiratory chain of *E. coli* that predominates when cells are grown at high aeration; has proton pump activity across the membrane in addition to electron transfer
B21_RS02000 (cyoB)	-2.27	cytochrome ubiquinol oxidase subunit 1	involved in aerobic respiratory chain that predominates when cells are grown at high aeration; has proton pump activity across the membrane

B21_RS03510 (sdhA)	-3.20	succinate dehydrogenase flavoprotein subunit	involved in step 1 of the subpathway that synthesizes fumarate from succinate
B21_RS03535 (sucC)	-3.14	succinyl-CoA ligase subunit beta	the component of succinyl-CoA synthetase involved in the citric acid cycle (TCA)
B21_RS03530 (sucB)	-3.28	dihydrolipoyllysine-residue succinyltransferase component of 2-oxoglutarate dehydrogenase complex	catalyzes the overall conversion of 2-oxoglutarate to succinyl-CoA and CO_2
B21_RS03525 (sucA)	-2.41	2-oxoglutarate dehydrogenase E1 component	the component of the 2-oxoglutarate dehydrogenase complex that catalyzes the overall conversion of 2-oxoglutarate to succinyl-CoA and CO_2
B21_RS06035 (icdA)	-2.92	isocitrate dehydrogenase (NADP(+))	connected with rapid shifts between TCA and glyoxalate bypass pathways
B21_RS16115 (mdh)	-2.21	malate dehydrogenase	catalyzes the reversible oxidation of malate to oxaloacetate
B21_RS08295 (fumC)	-3.48	class II fumarate hydratase	involved in the TCA cycle. FumC seems to be a backup enzyme for FumA under conditions of iron limitation and oxidative stress
B21_RS19540 (fadA)	-3.80	3-ketoacyl-CoA thiolase	catalyzes the final step of fatty acid oxidation
B21_RS19545 (fadB)	-4.74	multifunctional fatty acid oxidation complex subunit alpha	involved in the aerobic and anaerobic degradation of long-chain fatty acids via beta-oxidation cycle
B21_RS11745 (fadI)	-3.41	3-ketoacyl-CoA thiolase	catalyzes the final step of fatty acid oxidation
B21_RS01140 (fadE)	-4.76	acyl-CoA dehydrogenase	involved in the pathway fatty acid beta-oxidation which is part of lipid metabolism
B21_RS11740 (fadJ)	-3.69	multifunctional fatty acid oxidation complex subunit alpha	catalyzes the formation of a hydroxyacyl-CoA; strongly involved in the anaerobic degradation of long and medium-chain fatty acids
B21_RS15365 (fadH)	-2.89	NADPH-dependent 2.4-dienoyl-CoA reductase	involved in the beta-oxidation of unsaturated fatty acids with double bonds at even carbon positions
B21_RS09320 (fadD)	-3.25	long-chain-fatty-acid-CoA ligase	catalyzes the esterification, connected with transport of exogenous long-chain fatty acids into metabolically active CoA thioesters for subsequent degradation or incorporation into phospholipids
B21_RS00615 (acnB)	-1.57	aconitate hydratase B	involved in the catabolism of short chain fatty acids (SCFA)
B21_RS10515 gatY	-4.03	tagatose-1. 6-bisphosphate aldolase	catalytic subunit of the tagatose-1.6-bisphosphate aldolase GatYZ. which catalyzes reversible aldol condensation
B21_RS10510 (gatY_2)	-2.75	tagatose-bisphosphate aldolase	component of the tagatose-1.6-bisphosphate aldolase GatYZ that is required for full activity and stability of the Y subunit
B21_RS03685 (gpmA)	-3.28	2.3-bisphosphoglycerate-dependent phosphoglycerate mutase	catalyzes the interconversion of 2-phosphoglycerate and 3-phosphoglycerate
B21_RS02785 (fepA)	-2.88	outer membrane receptor FepA	involved in the initial step of iron uptake by binding ferrienterobactin. that allows *E. coli* to extract iron from the environment

B21_RS08660 (sufD)	-2.82	Fe-S cluster assembly protein SufD	the component of SufBCD complex that acts synergistically with SufE to stimulate the cysteine desulfurase activity of SufS; the complex contributes to the assembly or repair of oxygen-labile iron-sulfur clusters under oxidative stress
B21_RS11935 (mntH)	-2.77	divalent metal cation transporter	H+-stimulated. divalent metal cation uptake system; involved in manganese and iron uptake
B21_RS15775 (nlpI)	-2.82	lipoprotein NlpI	probably involved in cell division and play a role in bacterial septation or regulation of cell wall degradation during cell division
B21_RS13530 (nlpD)	-2.78	lipoprotein NlpD	activates the cell wall hydrolase AmiC; required for septal murein cleavage and daughter cell separation during cell division
B21_RS00070 (dnaK)	-4.66	molecular chaperone DnaK	involved in the initiation of phage lambda DNA replication and chromosomal DNA replication
B21_RS12940 (clpB)	-3.20	chaperone protein ClpB	involved in the recovery of the cell from heat-induced damage. part of a stress-induced multi-chaperone system
B21_RS20435 (aceA)	-2.67	isocitrate lyase	involved in the metabolic adaptation in response to environmental changes
B21_RS20430 (aceB)	-1.99	malate synthase A	involved in step 2 of the subpathway that synthesizes (S)-malate from isocitrate
B21_RS04955 (phoE)	-3.77	phosphoporin PhoE	outer membrane phosphoporin PhoE that expression is induced under phosphate limitation
B21_RS05440 (phoH)	-2.92	phosphate starvation protein PhoH	the enzyme that possesses ATP binding activity and similarity to –terminal domain of superfamily I helicases
B21_RS16450 (secY)	-2.63	protein translocase subunit SecY	the central subunit of the protein translocation channel SecYEG on the extracellular side of the membrane which forms a plug
B21_RS12705 (hmp)	-3.10	flavohemoprotein	involved in NO detoxification in anaerobic process. termed nitric oxide dioxygenase (NOD) reaction that utilizes O_2 and NAD(P)H to convert NO to nitrate. which protects the bacterium from various noxious nitrogen compounds
B21_RS01985 (cyoE)	-3.60	protoheme IX farnesyltransferase	converts heme B (protoheme IX) to heme O by substitution
B21_RS00505 (lpxC)	-4.02	UDP-3-O-[3-hydroxymyristoyl] N-acetylglucosamine deacetylase	catalyzes the hydrolysis of UDP-3-O-myristoyl-N-acetylglucosamine to form UDP-3-O-myristoylglucosamine and acetate. the committed step in lipid A biosynthesis
B21_RS00605 (lpdA)	-2.75	dihydrolipoyl dehydrogenase	involved in the glycine cleavage system as well as of the alpha-ketoacid dehydrogenase complexes
B21_RS00600 (aceF)	-2.40	dihydrolipoyllysine-residue acetyltransferase component of pyruvate dehydrogenase complex	the component of pyruvate dehydrogenase complex catalyzes the overall conversion of pyruvate to acetyl-CoA and CO_2
B21_RS00595 (aceE)	-1.84	pyruvate dehydrogenase E1 component	catalyzes the overall conversion of pyruvate to acetyl-CoA and CO_2

B21_RS06220 (dadX)	-2.98	alanine racemase catabolic	isomerizes L-alanine to D-alanine which is then oxidized to pyruvate by DadA
B21_RS06215 (dadA)	-3.66	D-amino acid dehydrogenase small subunit	catalyzes the oxidative deamination of D-amino acids
B21_RS09425 (cspC)	-3.39	cold-shock protein CspC	involved in transcription antitermination and regulation of expression of RpoS and UspA
B21_RS09430 (yobF)	-3.00	DUF2527 domain-containing protein	small protein involved in stress response
B21_RS02860 (cstA)	-1.95	carbon starvation protein A	involved in peptide utilization during carbon starvation
B21_RS22270 (cstA)	-2.42	carbon starvation protein A	utilizes peptide during carbon starvation
B21_RS12825 (rseA)	-3.17	anti-sigma-E factor RseA	inhibits sigma-E factor that is related to stress response
B21_RS21115 (aspA)	-3.93	aspartate ammonia-lyase	carries out the reversible conversion of L-aspartate to fumarate and ammonia
B21_RS16645 (tuf)	-2.93	translation elongation factor EF-Tu 1	promotes the GTP-dependent binding of aminoacyl-tRNA to the A-site of ribosomes during protein biosynthesis
B21_RS06855 (pspA)	-3.67	phage shock protein A	involved in the competition for survival under nutrient- or energy-limited conditions
B21_RS15850 (ftsH)	-2.50	ATP-dependent zinc metalloprotease FtsH	acts as a processive. ATP-dependent zinc metallopeptidase for both cytoplasmic and membrane proteins. plays a role in the quality control of integral membrane proteins
B21_RS16425 (rpoA)	-2.74	DNA-directed RNA polymerase subunit alpha	catalyzes the transcription of DNA into RNA
B21_RS18165 (kbl)	-2.31	glycine C-acetyltransferase	catalyzes the cleavage of 2-amino-3-ketobutyrate to glycine and acetyl-CoA
B21_RS07515	-2.35	hypothetical protein	-
B21_RS08995 (astB)	-2.49	succinylarginine dihydrolase	catalyzes the hydrolysis of N2-succinylarginine into N2-succinylornithine. ammonia and CO_2
B21_RS04930 (ldtD)	-1.83	transpeptidase	removal of the D-alanine residue of an acyl donor peptidoglycan tetrapeptide stem
B21_RS12900 (pka)	-1.32	protein lysine acetyltransferase	acetylates and inactivates the acetyl-CoA synthase (Acs) and also acetylate other central metabolic enzymes in response to environmental changes
B21_RS09010 (argD)	-2.48	aspartate aminotransferase family protein	catalyzes amination steps in arginine and lysine biosynthesis
B21_RS02800 (entF)	-1.55	enterobactin synthase subunit F	activates the carboxylate group of L-serine via ATP-dependent PPi exchange reactions to the aminoacyladenylate
B21_RS20490 (pgi)	-1.44	glucose-6-phosphate isomerase	involved in the pathway gluconeogenesis. which is part of carbohydrate biosynthesis

4.4. Conclusions

Considering the importance of the adaptive response of microbes to nanoparticles, this chapter provided a preliminary overview of changes in the genome and transcriptome level of *E. coli* after exposure to mechanical stress.

DNA-seq performed on the whole population of bacteria (bulk approach), revealed a high number of SNPs detected by HaplotypeCaller and FreeBayes. Crucially, only mutations identified by both programs were considered during DNA-seq analysis. The reason for such pronounced differences in the number of identified mutations could be explained by the fact that physical stress as a selective factor, is not as strong as antibiotic treatment, where a specific genetic mutation in a specific locus is required for survival. Presumably, *E. coli* developed various mutations that could be spread in different loci in the genome. (i.e., different mutants appeared in the population). Therefore, bioinformatic tools that are based on different algorithms for SNP calling give some variations in detected mutations, especially when the whole population with a high number of cells and different mutations is investigated. In this case, DNA-seq at the single-cell level would be recommended since it might reveal cellular heterogeneity. However, currently, there are no available platforms that enable the single-cell RNA-seq for bacteria. Of particular concern can be the performance of follow up experiments to test whether the SNPs identified are relevant in the context of exposure to the nanorods and the observed changes in phenotype.

DNA-seq analysis revealed twenty-five SNPs in the genome of *E. coli BL21* and sixteen in *E. coli* BL21(DE3). This provides additional evidence that phenotype changes of the bacteria after exposure to physical stress is not a consequence of entering the VBNC state that is associated with changes only on a metabolic, proteome and gene expression level and not on genome level (i.e., mutations)[439,440].

RNA-seq analysis shown downregulation of genes mainly involved in metabolic pathways such as β-oxidation of fatty acids, the citric acid cycle, glycolysis, transport of amino acids, enzyme cofactors (e.g., iron) and other compounds used as sources of energy and "building blocks". Thus, it can be concluded that the overall rate of bacterial metabolism is decreased by partial blocking of key metabolic pathways and energy production is inhibited (e.g., by limiting glycolysis and transport of crucial substrates), and bacteria seem to invest energy and substrates in creating stronger barriers, like the thicker cell wall that isolates them from the harsh environment (i.e., mechanical stressors). What is meaningful, decreased expression of genes involved in β-oxidation of the fatty acids may result in changes of the membranes structure, fluidity and in consequence also cell shape. Different lipid composition of the cell membrane of treated *E. coli* that is the result of decreased degradation of fatty acid can lead to lower susceptibility to colistin in comparison to control *E. coli* and control *S. epidermidis* (Gram-positive). In fact, this statement can be supported by higher MIC for colistin (acts as a surface-active agent)[452,453] determined for *E. coli* exposed to ZnO nanorods.

In conclusion, the exposure of *E. coli* to ZnO nanorods leads to adaptation that is observable in a time scale comparable to the time of acquisition of resistance to antibiotics, i.e., hours[330,454]. The effect of exposure of *E. coli*, in a turbulent flow in stirred medium, is fixed in genome and phenotype even when the stressing factor was removed.

The latter was confirmed by TEM and EDS measurements performed after 16 hours, during which a small fraction of the survivor bacteria was inoculated and grown in the nanorods-free medium. It should be stressed that the observed phenotypic plasticity of *E. coli* is a multilevel effect - a combination of changes at transcriptome and genome level. The experiments described in chapter 3 and 4 provide evidence that the adaptation of bacteria to physical stress in a homogeneous environment (without concentration gradient of stressing like in the case of antibiotics) is stable over time in phenotype, even without the presence of the mechanical stressor.

4.5. Experimental section

DNA isolation and whole-genome sequencing

Whole-genome sequencing was performed for *E. coli* BL21 and *E. coli* BL21(DE3). Firstly, bacteria were exposed to ZnO nanorods three times (24 h run each). For each bacterial strain and sample type, three biological replicates were prepared. DNA was isolated using a commercial GeneMATRIX Bacterial & Yeast Genomic DNA Purification Kit (EURx, Poland), according to the manufacturer's protocol for Gram-negative bacteria. Quantitive and qualitative evaluation of DNA was performed spectrophotometrically using NanoDrop (Thermo Fisher Scientific, USA). In addition, the quantity of isolated DNA was also measured fluorometrically on Qubit (Life Technologies, USA) using the dsDNA HS Assay (Life Technologies, USA) reagent kit. Diluted DNA (0.2 ng/µl)was used for library preparation with the Nextera XT DNA Sample Preparation Kit (Illumina, USA). The quality and quantity of the obtained product were determined by chip electrophoresis on the 2100 Bioanalyzer (Agilent, USA) using the Agilent High Sensitivity DNA Kit (Agilent, USA). The quantity was checked fluorometrically on Qubit. DNA sequencing (PE 2x150) was performed on the MiSeq device (Illumina, USA).

Whole-genome analysis and SNP calling

DNA reads were searched for sequencing adapters and contaminations using the FastQ screen with standard settings. Error correction was performed by Blue program. Adapters, low-quality reads, short sequences, and over-represented sequences were removed by Flexbar. Next, purified reads were mapped to reference sequence (for each sample separately) using the Bowtie2 aligner. The best reference sequence for *E. coli* BL21 was acquired from the GeneBank with reference number AM946981 and referred as *E. coli* BL21(DE3) ASM956v1. BL21-Gold(DE3)pLysS AG from the GeneBank was used to map reads for *E. coli* BL21(DE3). Variants were established using the FreeBayes and Haplotype Caller (standard settings for each sample separately). Crucially, all analyzed genomes were filtered out to comprise variants which were common to all three biological replicates and were discovered by both, the FreeBayes and Haplotype Caller. VCFtools was utilized to compare obtained results for all groups. ANNOVAR was used for execution of discovered variants.

RNA isolation and whole-transcriptome analysis

E. coli BL21 bacteria were exposed to ZnO nanorods (1 mg/mL) three times in 24-hour runs to enrich the population with more spherical cells. The total RNA was isolated using the commercial GeneMatrix Universal RNA purification kit (EURx. Poland) according to user guide attached by the manufacturer. The quantity of isolated RNA was determined spectrophotometrically using Nanodrop (Thermo Fisher Scientific. USA) and

fluorometrically on Qubit (Life Technologies, the USA) with the Qubit RNA HS Assay kit (Thermo Fisher Scientific, the USA). The quality was additionally checked by electrophoresis in 1% agarose gel. Depletion of rRNA from samples was performed using the Ribominus™ Transcriptome Isolation Kit (Invitrogen, USA) according to manufacture's instruction. The Maxima H Minus Double-stranded cDNA Synthesis Kit (Thermo Fisher Scientific, USA) was used to obtain double-stranded DNA. Purification of cDNA was carried out with the PCR Purification Kit (Qiagen, The Netherlands, followed by fluorimetric quantification using Qubit (dsDNA HS Assay). Next, library preparation was conducted using the Nextera XT DNA Sample Preparation Kit (Illumina, USA). The quality and quantity of the obtained libraries were evaluated on the 2100 Bioanalyzer (using the Agilent High Sensitivity DNA Kit) and Qubit. Sequencing of obtained libraries was conducted on the MiSeq device (Illumina, USA; v2 kit); PE 2x150 cycles.

The procedure of gene expression analysis

FastQC was used to evaluate the quality of raw RNA-Seq datasets which were subsequently processed with Trimmomatic v0.36 to remove adapters and low-quality nucleotides using the following command ILLUMINACLIP:ADAPTORS:2:30:10 LEADING:5 TRAILING:5 SLIDINGWINDOW:15:20 MINLEN:36[455]. The reads for each sample replicate were mapped against *E. coli* BL21(DE3) genome (accession number: NC_012892.2) with HISAT2 v2.1.0 in unstranded mode using separately paired and unpaired reads[456]. Counts of reads mapping to each gene were extracted with htseq-count v.0.9.0 (paired and single reads) in union mode and combined afterward to obtain the total count for each sequencing sample[457]. The analysis of differentially expressed genes was executed based on acquired count tables and analyzed with DESeq2 v1.16.1[458]. Figure S10-S15 represent rlog transformed count tables of significantly DEGs (padj < 0.05) generated with ggplot2 v.2.2.1 (H. Wickham. ggplot2: Elegant Graphics for Data Analysis. Springer-Verlag New York, 2009).

Chapter 5

Time-course measurement of transcriptome landscape and mutation rate

This chapter provides a general overview of ongoing projects related to whole transcriptome analysis of bacteria during exposure to ZnO nanorods and studies of the mutation rate.

Manuscripts in preparation:

Kinga Matuła, Przemyslaw Decewicz, Lukasz Dziewit, Natalia Derebecka, Joanna Wesoły, Jan Paczesny, Robert Hołyst, *Profiling transcriptome dynamics of Escherichia coli upon exposure to mechanical stress induced by ZnO nanorods*.

Kinga Matuła, Przemyslaw Decewicz, Lukasz Dziewit, Jan Paczesny, Robert Hołyst, *Mother and daughter bacterial cells may have different genomes: a study of the mutation rate of Escherichia coli*.

5.1. Introduction

The RNA-seq presented in section 4.3. was performed to gain a general overview of changes in gene expression after longer exposure (72 hours in total), performed in parallel with DNA-seq. However, in order to understand how bacteria response to mechanical stress (i.e., which genes/cluster of genes are activated one by one), whole transcriptome profiling overtime is required to get a more quantitative grip of the changes within the cell. In this chapter, data from extended RNA (multiple time points) and DNA experiment will be described.

5.2. Transcriptome dynamics during exposure to ZnO nanorods

To date, just a few transcriptome studies were published regarding exposure of bacteria to physical stress. Studies were performed on examination of transcriptome landscape upon exposure to heat stress (osmotic stress was additionally tested)[459,460], low temperature[461], high or low temperature (additionally oxidative stress, exposure to lactose diauxic starvation, hyperosmolarity, pH downshift were examined)[462,463], prolonged cold stress[464]. Most research focused on transcriptome analysis upon exposure to nonoptimal temperature.

It is worth mentioning that up to date, there is a plethora of published research focused on profiling bacterial transcriptome using DNA microarrays and surprisingly, not RNA-sequencing. A microarray consists of a predetermined selection of nucleic acid probes attached to a surface. To assess gene expression, one needs to derive complementary DNA (cDNA) from isolated RNA, label the cDNA with a fluorescent dye, place labeled cDNA over the array, and detect fluorescence to determine how much cDNA bounded to each DNA probe. In practice, microarray technology limits experiments to the detection of transcripts that correspond to known (i.e., existing) genomic sequencing information. In contrast, whole RNA-seq relies on converting RNA into a cDNA library that is directly sequenced. Therefore, RNA-seq is suitable for investigating both, known and novel transcripts and single nucleotide variants or gene fusions[465,466]. Moreover, RNA-seq offers quantification of expression levels across a larger dynamic range (>10^5 for RNA-seq compared to 10^3 for microarrays)[465,466]. In fact, this technology detects a higher percentage of differentially expressed genes (DEGs), in particular genes with low expression. Flexibility in increasing sequencing coverage depth allows for the detection of rare transcripts or even single transcripts per cell, which is not possible in the case of DNA microarrays[467,468,469]. Despite the lower upfront cost and popularity of the microarray-based experiment, undoubtedly RNA-seq is a cutting-edge technology best suited for purposes of the project.

In the whole-transcriptome profiling the mRNA mean lifetime, which is ~5 minutes is particularly important. It was reasonable to cover this period with sampling during the experiment. Interestingly, most of the reported experiments on transcriptome changes were performed in the time range between 20 and 60 minutes. Despite the technical challenge related to rapid sample isolation and processing, the experimental time points included 0, 1, 5, 15, 60 and 180 minutes. Transcriptome dynamics was investigated for *E. coli* Bl21 during dynamic exposure to ZnO nanorods (concentration of 1 mg/mL). Briefly, small aliquots of bacteria suspensions were taken from flasks at specific time points and immediately transferred to falcons with RNAprotect Reagent. This reagent was used to ensure accurate analysis of RNA that truly represents *in vivo* gene expression. This has two major advantages over using conventional methods to harvest bacteria. First, RNA is

enzymatically degraded by RNases, resulting in a reduction or even loss of many transcripts in the case of genes with low expression. Secondly, genes may be induced during the handling and processing of bacterial cells, leading to higher expression of specific genes. Ideally, RNA should be stabilized *in vivo*, since changes in the gene expression landscape occur during or directly after harvesting of cells. RNAprotect Reagent stabilized RNA before cells are lysed, which gives sufficient time for further steps.

First, enzymatic disruption of cells was performed using lysozyme with the addition of proteinase K that digested proteins present in the medium (to avoid protein contamination). Isolation of total RNA was followed by DNA digestion and further purification on silica-membrane spin columns. Purified RNA was depleted of rRNA using magnetic beads, washed and reversely transcribed to cDNA. Libraries preparation using Ultra Directional RNA Library yielded in RNA-strand specific libraries. To achieve maximal strand specificity, actinomycin D was used during sample preparation. During second-strand synthesis, uracil is added to mark one of the strands. Consequently, such strand cannot take part in the further PCR reaction and later degrades. This can make a crucial difference when comparing gene expression levels because one can exclude counting reads from the antisense strand that would otherwise significantly bias the results. The whole experiment was performed in three biological replicates and each time point was run in two technical replicates. Obtained libraries for each sample after qualitative and quantitative analysis (chip electrophoresis and fluorometric analysis) were subjected to sequencing. Before starting six long sequencing runs, one pilot sequencing was conducted to check if obtained libraries are properly clustered on a flow cell, adapters are identified and the whole sequencing run is accomplished. After the successful pilot run. All libraries were subjected to deep sequencing using Miseq (Illumina, PE 600) to provide a sufficient number of reads and saturate the annotated transcriptome[470].

To summarize the experiment, the main improvements compared to the first RNA-seq experiment comprised:

- Increased number of samples: three biological repeats with six time points, where each one had two technical replicates were taken, which gave in total 66 samples compared to three samples analyzed during the first experiment.
- RNaprotect Reagent was used to stabilize RNA and assure good quality of the material that will reflect a real expression profile instead of snap freeze in liquid nitrogen during the first experiment.
- Directional library preparation with high specificity was used to exclude reads from the antisense strand.
- High-depth sequencing was performed: 1.1–1.25 gigabases (Gb) of output per sample compared to 0.3–0.34 Gb planned during the first experiment[470] comprise major improvement.

Obtained reads (after normalization by the median of ratios method incorporated in DESeq2) were mapped to the reference sequence (acquired from NCBI database) and DEGs were determined. The gene was considered as differentially expressed if the expression was changed (i.e., upregulated or downregulated) in at least one-time point. Importantly, statistically significant DEGs for each biological replication were evaluated based on average gene expression from two technical replicates and were determined for padj <1e-5 (a modified p-value). The representative plots are shown in Fig. 5.1.

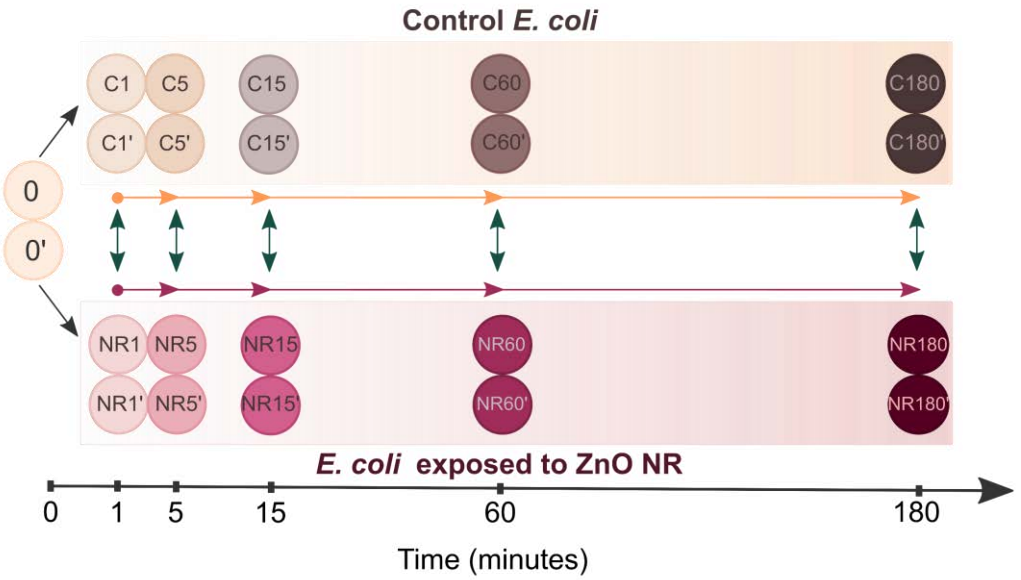

Figure 5.1. Scheme of the experimental design of the RNA-seq experiment. Samples are marked with circles; two circles denote two technical replicates of one-time point. Arrows indicate two types of analysis: i) horizontal - at each time point control samples are compared to samples with bacteria after exposure to ZnO nanorods (greenish arrows); ii) vertical – analysis between time points within the control population and bacteria after exposure to ZnO nanorods. The scheme shows one biological replication. In total, three biological repeats were conducted.

The first part of the RNA-seq analysis revealed:

- 629 DEGs for the first biological replication,
- 1350 DEGs for the second biological replication,
- 1528 DEGs for the third biological replication.

The number of DEGs evaluated for the second and the third biological repetition is similar, in contrast to the first biological replication. The lower number is a result of the lower number of reads saturating the sample (for the Ist biological replicate 76,5 mln were obtained, for the IInd 87,5 mln, and III biol 104,8 mln). This issue will be discussed later in the follow-up analysis. Technical mistakes related to sample preparation (e.g., loss of material) and sequencing can be excluded since the qualitative and quantitative analysis of libraries from the first biological repetition were comparable to libraries from the other runs and the sequencing run proceeded correctly.

Results suggest that exposure to physical stimulus provokes modifications that led to multiple pathway responses with different functional characteristics (Fig. 5.2A). Analysis of transcriptome changes yielded 576 DEGs when all three biological repeats were analyzed together and consequently different DEGs were obtained. Most transcripts encoding proteins were related to i) translation, ribosomal structure, and biogenesis (99 DEGs), ii) amino acid transport and metabolism (46 DEGs), inorganic ion transport and metabolism (40 DEGs), iii) post-translational modifications, protein turnover, and chaperones (35 DEGs), iv) transcription (31 DEGs), v) energy production and conversion (28 DEGs)(Fig. 5.2B). A large number of DEGs fall into a group of transcripts encoding proteins with a missing category (46 DEGs). To sum up, the most significant changes

emerged in genes encoding membrane transporters, membrane proteins, mechanosensitive channels, transcription factors, and protein involved in the DNA repair system. Representative plots showing DEGs are presented in Fig. 5.3. (in total 3507 plots for all biological repeats were generated).

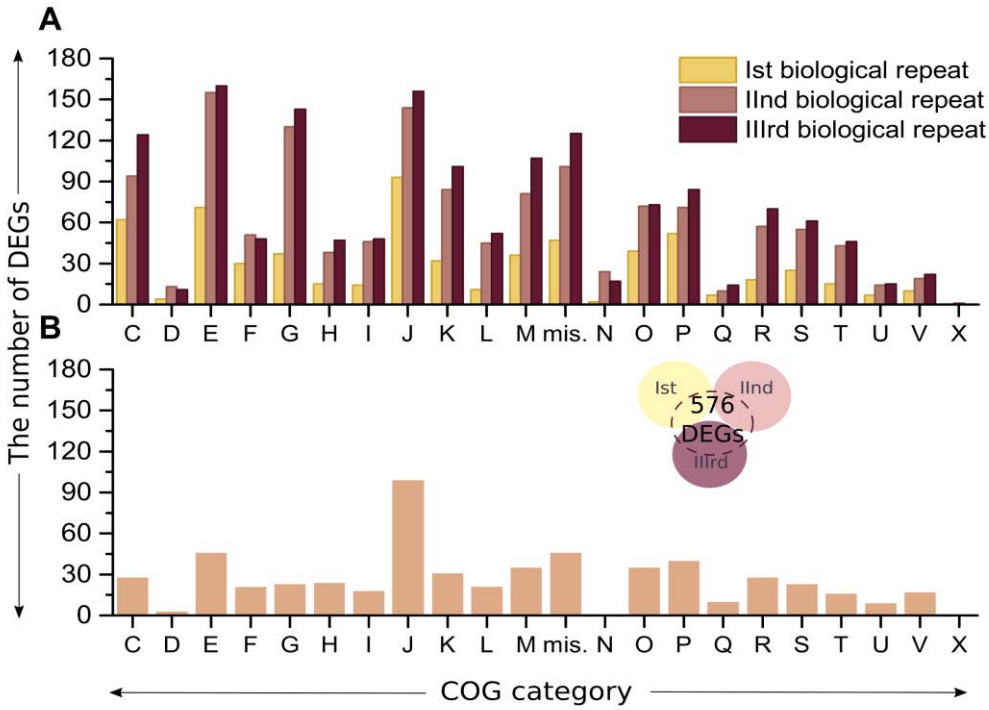

CELLULAR PROCESSES AND SIGNALING
[D] Cell cycle control, cell division, chromosome partitioning
[M] Cell wall/membrane/envelope biogenesis
[N] Cell motility
[O] Post-translational modification, protein turnover, and chaperones
[T] Signal transduction mechanisms
[U] Intracellular trafficking, secretion, and vesicular transport
[V] Defense mechanisms

INFORMATION STORAGE AND PROCESSING
[J] Translation, ribosomal structure and biogenesis
[K] Transcription
[L] Replication, recombination and repair

METABOLISM
[C] Energy production and conversion
[E] Amino acid transport and metabolism
[F] Nucleotide transport and metabolism
[G] Carbohydrate transport and metabolism
[H] Coenzyme transport and metabolism
[I] Lipid transport and metabolism
[P] Inorganic ion transport and metabolism
[Q] Secondary metabolites biosynthesis, transport, and catabolism

POORLY CHARACTERIZED
[R] General function prediction only
[S] Function unknown
[X] Mobilome, prophages, transposons

[mis.] Missed

Figure 5.2. Comparison of differentially expressed genes (DEGs) evaluated by RNA sequencing. The classification was performed according to the database of Clusters of Orthologous Groups of proteins (COGs). (A) Comparison of the number of DEGs for each biological replications (an average from two technical replicates was taken into consideration). (B) DEGs obtained when three biological repeats were analyzed together.

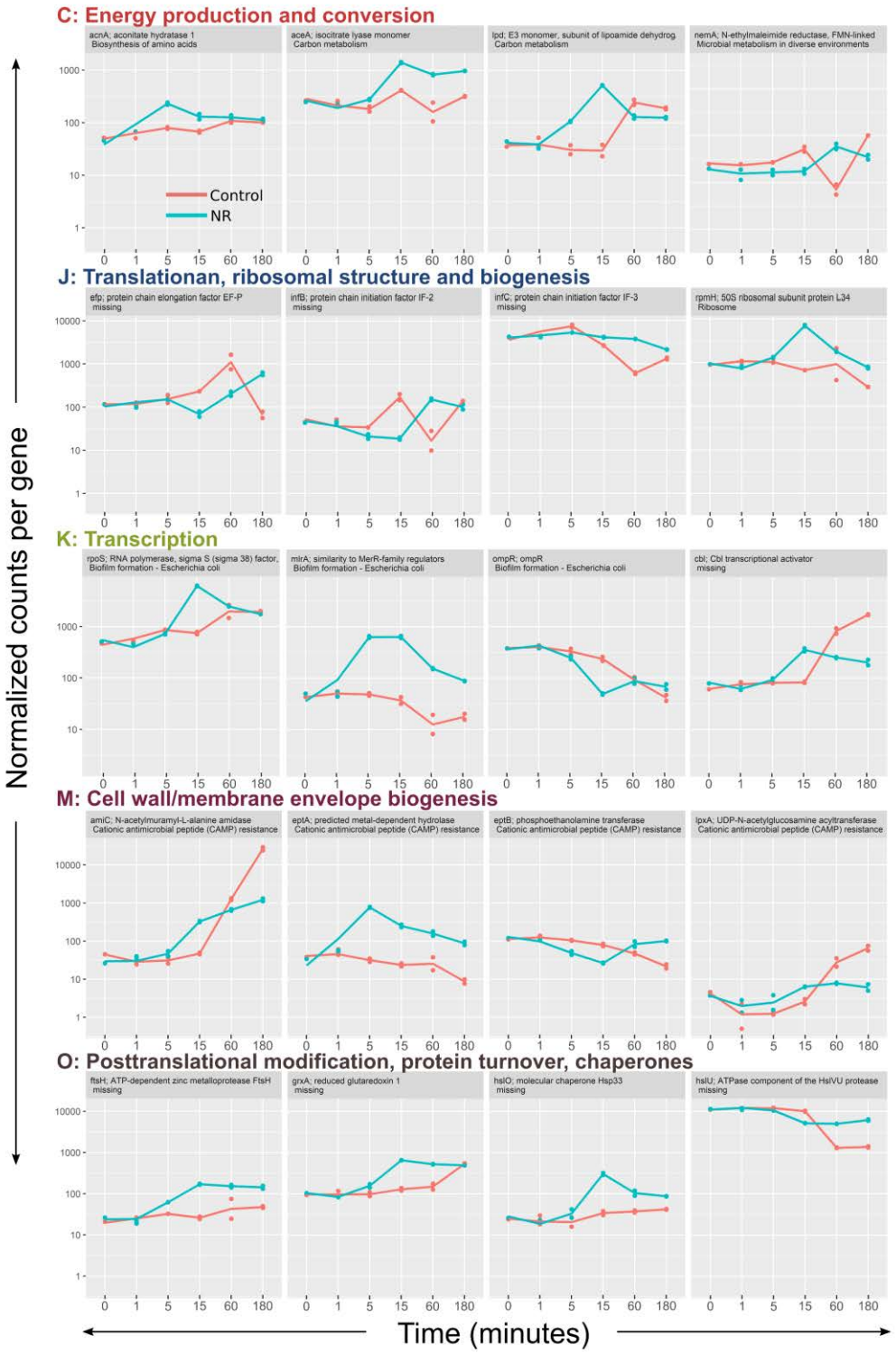

Figure 5.3. Representative plots (from 2nd biological repeat) showing differentially expressed genes (DEGs) over time classified according to Orthologous Groups of proteins (COGs).

Future plans assume a few steps listed in the table below (Table 5.1).

Table 5.1. List of planned bioinformatic analyzes in the RNA-sequencing project.

Tasks	Why?	How?
Mapping reads to a new reference	A few up to over a dozen percent of reads were not mapped to reference.	The first reference sequence was downloaded from the database and used during mapping, however, loss of) reads was noticed. A new approach assumes assembling a new reference based on DNA-seq data presented in section 4.2. All control sequences will be used to obtain consensus sequence and the analysis will be performed again.
Re-analysis of reads which map to two genes	Reads are long (300 bp) and can map to the reference sequence covering partially two genes instead of fully covering one gene.	Two variants of mapping: i) mapping to one gene, ii) mapping to two genes, will be taken into consideration.
Comparison of the expression levels of control bacteria at time point "0"	Initial gene expression level will influence the transcriptome landscape, especially in the case of treated bacteria.	A comparison of the transcriptome profile of bacteria from three biological replication at time point "0" will be performed by checking which genes are upregulated/downregulated (visual check-up of mapped reads along the genome).
Determination of candidate regions for noncoding RNA (ncRNA)	NcRNA are crucial regulators that adjust bacterial physiology as a response to environmental cues (e.g., stress).	Screening of intergenic regions using pipelines/programs available on Omics tools or using published computational methods to identify sRNAs using support vector machine (SVM) classifier (small noncoding RNA)[471] will be performed.
Data representation	Provide a comprehensive and compact overview of changes in the transcriptome landscape.	For each time point and each sample (66 in total, volcano plots will be generated. A volcano plot is a type of scatterplot, which depicts statistical significance (p-value) versus the magnitude of change (fold change). All gens will be taken into consideration. The second type of analysis comprises generation of heat maps - two-dimensional graphical false-color image representations. Only the most interesting genes will be taken into account.
Gene clustering	Determination of genes with a similar expression profiles in order to check which genes or pathways are regulated together.	Vectors reflecting changes between treated and untreated samples will be generated and used for further gene clustering.

5.3. The increased mutation rate in *E. coli* revealed by high depth DNA-seq

Mutations in bacteria arise spontaneously during DNA replication or accidentally as a result of action of mutagens – physical or chemical factors[472,473]. Quantification of the speed of mutations emergence is of high importance, especially in evolutionary dynamics. The mutation rate provides an insight into the adaptation of bacteria in the

natural environment or upon exposure to stressors, e.g., antibiotics[474,475], and is a measure of mutagenesis. Precisely, the mutation rate is defined as a probability of emergence of mutation in DNA of the particular length and in a given time unit (expressed as a number of mutations, either per genome per generation or per base pair per generation)[476,477,478]. In practice, the mutation rate can be determined experimentally by three available techniques: Luria and Delbrück fluctuation analysis[479], mutant accumulation[480] or by comparative genomics[481].

Fluctuation analysis is the most frequently used method that is based on the distribution of a number of mutants in a large number of parallel cultures. At the beginning, each culture is inoculated with a small number of identical cells (e.g., LTEE experiment[482,483]). Bacteria are allowed to grow, usually to saturation phase, and their number is determined by plating the cell suspension in proper dilution on both, selective medium (the number of mutants is determined) and nonselective medium (total number of cells is counted). The number of mutations per culture is used to calculate the distribution of mutants. Calculation of the mean or most likely number of mutations per culture can be performed using one of available estimators[476,477,478]. The mutation rate is calculated as the mean number of mutations divided by some measure of the number of cell-lifetimes at risk of mutation[477,484].

Mutation accumulation (MA) is a less frequently used approach, presumably due to laborious character[480]. The method relies on assumptions, that the number of mutants increases linearly in an exponentially growing population. The mean probability of mutation occurrence in each generation reaches unity, when the culture of bacteria reaches a certain size (i.e., the number of cells). The general protocol is based on the establishment of multiple clonal cultures from a single colony, that are passed through single-cell bottlenecks[474] (reduction of population size that decreases genetic diversity). The process is repeated and mutations accumulate over a longer period of time. After several generations, bacterial genomes are sequenced, and mutations are determined[474,478,485]. This method is used particularly in the evaluation of mutation rates in chemostats[486,487,488], i.e. bioreactors designed for continuous cultivation of bacteria, where mutant accumulation is a function of the growth rate[477].

In contrast to fluctuation analysis and mutant accumulation method, comparative genomics is used for the comparison of DNA sequences of organisms at long evolutionary time scales (long phylogenetic distances), e.g., millions of years from the moment of separation from the common ancestor. It can be also adapted to the studies of the mutation rate of microbes in the experiments meeting the criteria connected, for instance, with the evolutionary time scale or estimation of divergence time[478,489,490]. It is based on the major principle that DNA sequence encoding polypeptides or RNAs responsible for a particular function, is conserved between the species[481].

Importantly, accuracy in the determination of mutation rate using approaches described above is based on how the experiment reflects the assumptions of the used methods, taking into consideration all limitations and optimizations. Crucially, all the above methods assume that a single bacterial colony is genetically homogeneous (i.e. bacteria have the same genome) and consequently, the bacterial suspension derived from the single colony represents a clonal population of one single bacterium.

Interestingly, the mutation rate in bacteria is studied for over 70 years, and thus it is striking that the reported numbers vary even by more than the order of magnitude (0.10×10^{-3} - 3.70×10^{-3}) [485,490,491,492,493,494]. The most recent studies suggest that the mutation rate determined by MA followed by whole-genome sequencing (WGS) is somewhere between 1×10^{-3} and 2×10^{-3} mutations per genome per generation[485]. Robert et al. published interesting results on following directly point mutation arising from replication errors in single cells, visualized by the usage of fluorescently tagged MutL mismatch repair protein, in a "mother machine" microfluidic chip. The estimated mutation rate for *E. coli* wild-type is ~ 0.0022 mutation/hour[495], which, after recalculation, is in line with work by Lee et al. (~1×10^{-3} mutation per genome per generation)[491].

In the previous chapter, the real-time adaptation of *E. coli* upon exposure to physical stress was demonstrated. The mutations in the form of single nucleotide polymorphisms (SNPs) and changes in transcription profile for the whole population of bacteria after 72 hours of exposure to sharp ZnO nanorods were determined (bulk approach). In the following chapter, the main focus is put on determination of spontaneous mutation rate for *E. coli* and mutation rate for the bacteria after exposure to physical (ZnO nanorods) and chemical (Zn^{2+} ions) stressors, estimated directly from the experiment followed by whole genome sequencing (WGS). This experimental approach is based on a completely new, and possibly more accurate protocol.

The aim was to check, whether mutations after a shorter time upon exposure to ZnO nanorods (6 hours) emerge at the single-cell level. Crucially, the determination of the referential mutation rate for control bacteria was required for reliable interpretation of DNA-seq data for *E. coli* after the exposure to ZnO nanorods. The whole procedure with all operations is described below and illustrated in Fig. 5.4 to unveil the difference between developed protocol (will be discussed in the text) and standard approaches used for the determination of the mutation rate.

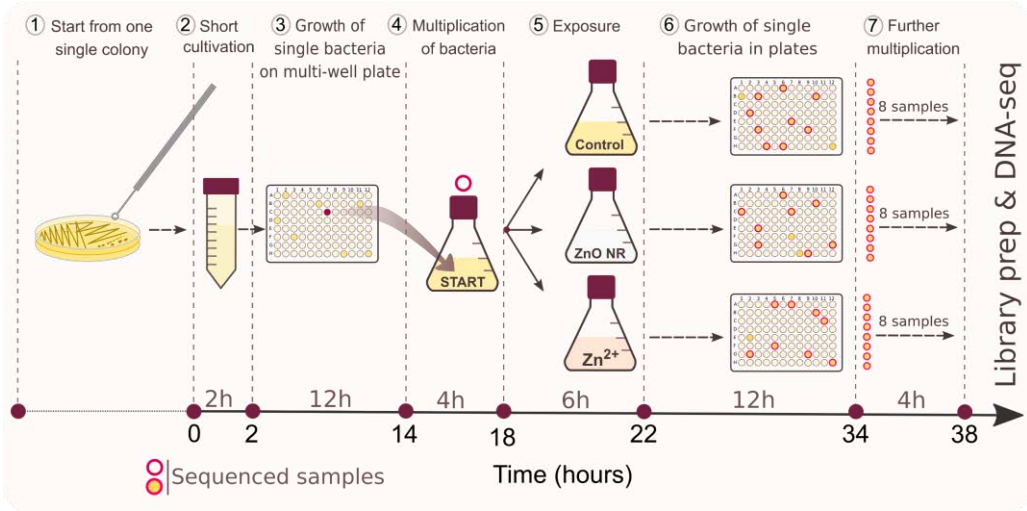

Figure 5.4. The experimental workflow design to study the mutation rate of E.coli. DNA sequencing comprised the following samples: i) control *E. coli* (Control), ii) *E. coli* after exposure to ZnO nanorods (ZnO NR), iii) *E. coli* after exposure to ZnO nanorods Zn^{2+} (Zn^{2+}).

The experiment was started with the preparation of the population of theoretically identical clones (bacteria derived from one colony-forming unit, i.e. one cell) by inoculation of one single colony into LB medium and cultivation for 2 hours (Fig. 5.4, step 1). After the short cultivation, bacteria were diluted and the suspension was pipetted into wells of 96-well plate (Fig. 5.4, step 2). The concentration of bacteria obtained by serial dilution was adjusted in order to capture one cell in a well and avoid doublets. According to Poisson's distribution[496], over 90% of the wells should be empty to ensure that ~10% wells contain single cells. Multi-well plates were incubated for the next 12 hours in order to obtain clones derived from single cell. Subsequently, the content of one chosen well was transferred into the flask for further short multiplication to provide a sufficient number of bacterial clones derived from the single cell (Fig. 5.4, step 3). The obtained bacterial suspension was split into three flasks: i) control *E. coli*, ii) *E. coli* exposed to ZnO nanorods (of final concentration of 1 mg/mL), iii) *E. coli* in LB containing Zn^{2+} (concentration matching this in the sample, c.f. chapter 2 (ii)) (Fig. 5.4, step 4).After 6-hour exposure (growth curves provided in Fig. 5.4, step 5), the bacteria suspension from each flask was diluted through limiting dilution and pipetted into plates in order to obtain single bacteria in wells. (Fig. 5.4, step 6). Instead of using commercially available whole-genome amplification kits, the multi-well plates were incubated for the next 12 hours to obtain clones of single bacteria. Crucially, this approach had three major advantages: i) additional mistakes are not introduced by standard amplification reactions[497] since only natural bacterial replication machinery is utilized to amplify DNA material, ii) emergence of mutations in bacterial population derived from single cells can be tracked in each locus in the genome, meaning that early-acquired mutations should be inherited by progeny bacteria, iii) this approach allows to capture only viable bacteria that survived the treatment with nanostructures (during the exposure to ZnO nanorods, the number of viable bacteria decreased due to mechanical contact). Finally, the content of eight chosen wells was transferred for short multiplication and further sequencing without amplification at any stage of library preparation (Fig. 5.4, step 7). Importantly, during the course of the experiment, the content of wells was validated by means of optical density measurement that supported exclusion of wells with doublets. Deep sequencing with average coverage of ~250X was performed for the samples.

After trimming and quality control of reads, determination of mutations was performed for each sample separately using a computational pipeline. Based on literature data on the mutation rate of *E.coli*, it was assumed that 8 control bacteria after multiplication within each biological replication (Fig. 5.4. steps 6 and 7) should have exactly the same genome. Astonishingly, the data analysis revealed that each multiplied control bacterium had a different set of SNPs spread along the genome, suggesting a large genome variability in the control population. The estimated spontaneous mutation rate for *E. coli* BL21 is ~0.5 mutation per genome per generation, which is at least two orders of magnitude higher in comparison to literature data.

One can ask: what the probability of drawing eight bacteria with different genomes? P defines the probability of single nucleotide polymorphism occurrence during one division. Taking into consideration that the experiment is started from one single bacterium that divides n-time, the final number of bacteria is $2^n >> 1$. The probability that one bacterium has an unchanged genome is $(1-p)^n$. The probability that eight chosen bacteria from 2^n cells have the same genome is equal $(1-p)^{(8*n)}$. If p = 0.001 and there are 10 generations, the probability that eight bacteria have the same genomes is 92,3%, and

that at least one bacterium is genetically different is equal to 7.7%. This number is decreasing when one assumes that two, three or more bacteria are different. Finally, for eight bacteria with different genomes, this probability is extremely low. While p=1, each bacterium is genetically different with probability equal 1. Taking this into account, in each biological replication, eight bacteria with different genomes can be obtained.

Future plans

The presented results provide the first estimation of the mutation rate for control population of *E. coli* that requires further verification. This assumes screening genomes of the bacteria using several different programs/pipelines that utilize various algorithms (can also detect mutations with different sensitivity). Next, the mutation rate will be verified for *E. coli* after exposure to ZnO nanorods and Zn^{2+} ions to check whether mechanical stress can induce faster mutation emergence compared to the control population or exposed to Zn^{2+}.

5.4. Conclusions

The presented projects provide a unique approach to understand the consequences of mechanical stress induced at the genome and transcriptome. Studying different landscapes can give a more detailed picture that aids in the correlation of genetic with phenotype changes. In addition, the experimental approach executed during the design and performance does not represent typical biological concept, thus for discovery purposes of the projects, still a lot exciting results can be obtained.

5.5. Experimental section

Profiling whole-transcriptome upon exposure to ZnO nanorods

The experiment was performed for control *E. coli* BL21 and upon exposure to ZnO nanorods (concentration of 1 mg/mL). Three biological replicates were performed, each comprising six time points (0, 1, 5, 15, 60, 180 minutes). During the experiment RNase free plastic eppendorfs and pipette tips, ad the surface was cleaned with RNase zap. The total RNA was stabilized and purified by with RNAprotect Reagent and RNeasy Protect Bacteria Midi Kit (Qiagen, The Netherlands) according to manufacturer's instruction). On-column DNase digestion during RNA purification was conducted using RNeasy MinElute Cleanup Kit (Qiagen, The Netherlands) with Baseline-ZERO Dnase (1000U, Epicentre, the USA). The quantity of isolated and purified RNA was evaluated spectrophotometrically on Nanodrop and fluorometrically on Qubit (using the Qubit RNA HS Assay kit). Ribo-Zero™ Bacteria Kit (Epicentre, USA) was used for the depletion of rRNA according to the manufacture's instruction. Library preparation was performed using NEBNext Ultra Directional RNA Library Prep Kit (New England Biolabs, USA) with Actinomycin (Sigma-Aldrich, USA) according to provided instruction manual. The quality and quantity of the libraries were evaluated on the Bioanalyzer (the Agilent High Sensitivity DNA Kit) and Qubit (dsDNA HS Assay). Sequencing of DNA was performed on the MiSeq device (Illumina, USA; v3 kit PE 2x300 cycles).

Whole-transcriptome profiling

RNA-seq datasets were viewed in FASTQ and afterward processed with Trimmomatic v0.36 to trim the remaining parts of adapters and low-quality bases. The reads for each sample replicate were mapped against *E. coli* BL21 genome (accession number: NC_012892) with HISAT2 v2.1.0 in unstranded mode. Subsequently, the reads were

counted using htseq-count version 0.11.1. The analysis of differentially expressed genes was executed based on acquired count tables and analyzed with DESeq2 package version 1.24.0.

The mutation rate experiment

The experiment was performed for *E. coli* BL21 strain. First, a single colony was inoculated into 8 ml in LB medium for 2 hours (37°C, 200 rpm) to reach OD_{600} around 0.1 (~5×10^6 CFU ml^{-1}). The inoculum was prepared by limiting dilutions, where 20 µl of bacterial aliquots (~0.2-0.3 cell per aliquot) were pipetted into each well within 96-well plates (Biokom, Poland) filled up with 230 µl of LB medium (Carl Roth, Germany). The microplates were covered with plastic lids, and the edges were additionally sealed with parafilm to prevent evaporation. The plate was incubated in a shaker (37 °C, 170 rpm; IKA KS 4000 i, Germany) for 12 hours. Microplate reader (BioTek Synergy HTX, USA) was used to check the absorbance of the wells within the microplate. The content of one chosen well with the clonal population was transferred into falcon with 10 ml of LB medium and cultivated to reach OD~0.1. Subsequently, bacterial suspension was diluted in order to obtain ~200 CFU ml^{-1} in each of three flasks: i) control, ii) with ZnO nanorods, and iii) LB medium with Zn^{2+}. LB medium with Zn^{2+} was prepared before the experiment by incubation of ZnO nanorods in the medium for 6 hours. Subsequently, ZnO nanorods were removed from the solution by centrifugation (10 000 rpm, 10 minutes, MPW) and filtration (pore size 0.2 µm, VWR, USA). The prepared solution containing Zn^{2+} was used to dilute the stock solution of the bacteria. ZnO nanorods were suspended in 1 mL of LB medium and added to obtain a final concentration of 1 mg/mL. Alignment of bacterial concentrations was achieved by the addition of 1 ml of pure LB into control flask, and 1 ml of LB medium containing Zn^{2+} into the last flask. After 6-hour exposure, limiting dilution was applied for each flask, and 20 µl of bacterial aliquots were pipetted into each well of microplate (for each dilution at least 4 microplates were prepared). The microplates were incubated (37°C, 170 rpm) for 12 hours (control bacteria) and 14 hours (the bacteria exposed to ZnO nanorods). Absorbance analysis conditioned the choice of 8 wells from each type of sample that were used for sequencing.

Genome sequencing

Contents of 8 wells for each sample type were multiplied in 3 ml in LB-medium for 3-4 hours to reached OD around 0.8. This allowed for the isolation of 12 µg of DNA which was required for further sample processing. Genomic DNA isolation was performed using TruSeq DNA PCR-Free Library Preparation Kit (FC-121-3003, Illumina, USA). Focused-ultrasonicator E210 (Covaris, USA) was used for DNA fragmentation. For each sample library was prepared with a short 350 bp insert. The sequencing of DNA was performed on HiSeq4000 (Illumina, USA) (PE150). Cutadapt 1.9.1. was used to trim to remove adapters and ending of reads and filter sequences.

Quality control

Raw reads were viewed in FASTQ and afterward processed with fastp v0.12.5 using default parameters to trim remaining parts of adapters and low-quality bases (<Q30 on average in last 10NT in 3' end of each read). Assemblages obtained with SPAdes were compared and evaluated with QUAST. The quality and efficiency of reads mapping during mutation rate analysis was verified with QualiMap.

SNP calling and data analysis

SNP calling against "mother" cells assembled with SPAdes v3.11 in carefully mode performed with breseq v0.30.1. Hot-spots visualization was obtained with Integrative Genomic Viewer (IGV).

Estimation of the mutation rate

Filtered reads were corrected using BayesHammer (k-mer), Blue (k-mer) and Karect (MSA)[498]. Each uncorrected and corrected pair of reads was assembled with SPAdes v3.11 (without read-error correction) and afterward mapped against obtained contigs with bwa mem. Frequencies of nucleotides in each position were recovered with bamreadcounts and used for calculation of the mutation rate.

Chapter 6

Summary and perspectives

This chapter summarizes the finding presented in this thesis and provides the framework for future research in the field of bacterial adaptation to different, non-obvious factors. Important suggestions on the execution of possible applications are also included.

6.1. Summary

Currently, nanotechnology plays a pivotal role in various fields, allowing to introduce considerable improvement in a relatively short time. In bio- and medical-related branches of science, a lot of effort was devoted to the utilization of nanoparticles as a tool for early diagnosis, innovative drug delivery systems, tissue-engineered scaffolds, antimicrobial agents, etc. The primary focus is on the investigation of the cytotoxic effect of nanoparticles after application *in vivo* or *in vitro* in control studies.

So far, no data have been reported on the behavior of cells upon exposure to nanoparticles or any other physical stressor in a broader (chemical, physical and biological) perspective. The main goal of this thesis is to make a step towards better understanding of the physical interactions between cells and nanoparticles, in particular, repercussions related to the influence of the mechanical stress induced by nanoparticles.

Chapter 1 provides a general overview of nanotechnology and nanoparticles in several aspects. It should be highlighted that comprehensive divisions of approaches used to obtain and characterize nanostructures, modes of interaction of nano-sized objects with cells are reviewed and prepared by the author based on literature. Importantly, interactions between cells and nanoparticles are also discussed.

Chapter 2 follows the detailed characterization of ZnO nanostructures used in the experiments. Results obtained by means of SEM, measurements of zeta potential and X-ray diffraction are shown. The mechanical stress induced by rounded ZnO nanoparticles and ZnO nanorods is investigated for Gram-positive (*S. epidermidis*, *C. glutamicum*) and Gram-negative (*E. coli*, *E. aerogenes*) bacteria, as well as eukaryotic cells of various origin like yeast (*Saccharomyces cerevisiae*), and the human cell lines (liver cancer $HepG_2$-cells, lung cancer A594-cells, skin cancer HaCaT-cells and A431-cells), as well as primary human peripheral blood mononuclear cells (PBMC). Under dynamic conditions, that enabled collisions between ZnO nanostructures and cells, ZnO nanorods appear to be more damaging compared to rounded ZnO nanoparticles. This is explained by the increased probability of mechanical damage caused by ZnO nanorods upon puncturing of the cell wall and/or membranes. Gram-positive bacteria, which have thicker cell walls, appear to be more resistant to mechanical stress induced by nanorods compared to Gram-negative bacteria and eukaryotic cells.

Chapter 3 reveals the phenotype characteristics of *E. coli* that survived the second exposure to a large number of collisions with ZnO nanorods and acquired mechanical resistance. Experimental results were obtained using various chemical and biological techniques: SEM, Cryo-SEM, TEM with EDS, viability measurements, Gram staining, tests with antibiotics and bacteriophages-based tests. Phenotype changes are related to the bacteria's shape (change from elongated towards spherical), the density of the periplasm (increased by 15 %) and the average thickness of the cell wall. Mechanically resistant bacteria appear almost as Gram-positive strain in standard Gram staining. Interestingly, the same phenotype changes are found in *E. aerogenes (*Gram-negative) but not in *C. glutamicum* (Gram-positive strain, that possesses a thick cell wall).

Chapter 4 constitutes the first step towards a better understanding of genome and transcriptome changes in *E. coli* exposed to nanomechanical stress. DNA-

sequencing reveals 25 mutations in the form of SNPs in *E. coli* BL21 and 16 SNPs in *E. coli* BL21(DE3). Only two mismatch mutations are located within protein-coding sequences. Although the majority of identified SNPs are localized within intergenic regions, it is still possible that they emerged within the not yet identified regions of ncRNAs that can play crucial regulatory functions. The transcriptome analysis shows the down-regulation of expression of 61 genes involved in key metabolic pathways like glycolysis, β-oxidation of fatty acids, the citric acid cycle, and transport of amino acids and enzyme cofactors and other compounds used as sources of energy and "building blocks". *E. coli* exposed to ZnO nanorods seem to invest energy and substrates in creating stronger barriers, like the thicker cell wall that protects the cell from the harsh environment.

Chapter 5 provides an overview of ongoing research that is a continuation of the experiments with bacteria exposed to ZnO nanorods. The first project is focused on the investigation of transcriptome dynamics upon exposure to ZnO nanorods. Multiple experimental improvements have been adapted compared to the first RNA-sequencing. Interestingly, preliminary results show that the expression of a large number of genes (membrane transporters and proteins, mechanosensitive channels, transcription factors, proteins involved in the DNA repair system) changes within the first minutes after the addition of ZnO nanorods. Further work assumes data analysis, gene clustering, screening for ncRNA regions. The second project is related to the investigation of the mutation rate upon exposure to mechanical stress. Astonishingly, the preliminary data analysis of the control *E. coli* population revealed a high heterogeneity at the genome level. This project requires establishing and further verification of the mutation rate for the control population, and then estimation for *E. coli* after exposure to ZnO nanorods.

To understand the influence of mechanical stress (and other stressing factors) it is crucial to extract manifold layers of information using various chemical and biological tools. The experimental observations provide evidence that this *savoir-faire* of the adaptation process seems to be rehearsed to perfection by cells and incorporated into this complex molecular machinery, created to sustain life. A better understanding of cellular processes, especially in terms of the acquisition of resistance to stress factors, can prevent unwanted effects. On the other hand, obtained knowledge can be also utilized to improve certain applications (i.e., increase the efficiency of industrial processes by using mutants).

6.2. Perspectives and recommendations

Evolution of bacteria[482,474,499] is no longer considered as a gradual process occurring over a long period of time. Recently Baym *et al.*[500,454] and Zhang *et al.*[330] demonstrated fast (within a few hours) evolution of *Escherichia coli* under antibiotic selective pressure. It should be underlined that such experiments are performed in a concentration gradient, i.e., plates or multi-well plates with increasing concentration of antimicrobial reagent. In this work, it is demonstrated that instantaneous physical stress in a homogeneous environment also induces a fast adaptation of bacteria. The changes in phenotype and genome are stable over time, even when mechanical stress is removed. This is the first example of a real-time experiment, where the bacteria undergo adaptation upon instantaneous and acute mechanical stress without any obviously available time for gradual adaptation.

Certainly, there are various exciting directions to investigate and hopefully, this work will be a catalyst for other scientists to study not only physical factors influencing microbes but also understanding how cells respond to different types of stimuli, and how dynamic and heterogenous is such response between stimulated/stressed cells. As mentioned in Chapter 5, undoubtedly genetic studies are a very promising source of information. Profiling transcriptome dynamics during exposure to ZnO nanorods might provide more details on which genes are differentially expressed, how fast and what is the level of expression. The next (very challenging) step will be to perform transcriptome analysis at the single-cell level to reveal cellular heterogeneity of gene expression profile. Preliminary investigations of the mutation rate showed that cells derived from single bacterium from the control population exhibit high heterogeneity at the genome level. This finding may shed new light on understanding the evolutionary process and emerged heterogeneity between bacteria exposed to the stressing factor. It would be also relevant to perform follow up experiments to examine whether the identified mutations are important in the context of the stress induced by ZnO nanorods and the observed changes in phenotype.

Another interesting aspect could be the investigation of proteome changes within the cell envelope that is a target for many antimicrobial substances. The cell envelope is the first stress-bearing barrier, that protects the internal part of the bacterial cell from the unpredictable and often hostile environment. It provides structural integrity, dictates the shape of bacterium cell, induce the remodeling that is required for bacterial division and growth[387,389,390]. Protein toolkit coordinated by sophisticated regulatory networks evolves to accommodate bacterial survival under stress conditions such as varying temperatures, nutrient availability, etc.[501]. To examine the protein profile of the cell envelope, differential centrifugation in the gradient of sucrose, 2D SDS-PAGE[435], and measurements using MALDI TOF/TOF Analyzer can be recommended. Currently, no tools to profile the proteome at the single-cell level in bacteria are available.

Another alternative to the physical effect of nanoparticles could be the utilization of the electric field as a physical factor. To date, very little is known about the exact mechanism and influence on bacteria exposed to the electric field. Understanding the mechanisms of the influence of the electric field on microorganisms can have two applications. The electric field can be used as a new physical sterilizing agent or as a factor accelerating bacterial growth in industrial branches, where bacteria are used to produce certain molecules.

Many issues regarding the effect of the electric field influencing bacterial survival and behavior remain unknown. In the literature, two types of experiments with bacteria exposed to the electromagnetic field can be distinguished. Bacteria can be subjected to the electromagnetic field of constant frequency and variable intensity of electric strength over time. Typically, a flask with bacterial suspension is placed inside the solenoid and the number of bacteria is measured over time. This type of investigation is primarily characterized by the dominant magnetic component of the electromagnetic field during the exposure of bacteria. The second type of study comprises experiments where bacteria are subjected to the pulsed electric field (used in electroporation of bacteria to introduce plasmids). The bacteria are placed between two metal plates, and then voltage pulses are applied between two electrodes. In consequence, cells are subjected to the pulsed electric field, and the magnetic component is negligible.

The most blatant mistake often found in the literature, is, that in addition to the electric field, the electric current flows through the system. The voltage applied to uninsulated electrodes immersed in the solution induces redox reactions on the electrodes and consequently, the electric current is flowing through the solution with bacteria, significantly contributing to the overall effect.

Therefore, the first conceptual framework of investigation of the influence of the electric field was performed, which might structure further research in this field. After careful research review, the experimental system for testing the effect of the electric field on bacteria was designed to ensure optimal growth conditions and allow exposure of cells to the stressing factor. Special cuvettes with electrodes were prepared from materials that do not exhibit a toxic effect (control experiments were performed). Three frequencies between 10 and 100 kHz were tested at the electric field strength of 1 V/m and 10 V/cm. The most interesting results were obtained for the experiments, where 100 Hz and the electric field strength of 1 V/cm were used. The decrease in the number of bacteria was observed during the first exposure (similarly to the experiments with ZnO nanoparticles). The survivor bacteria were exposed once again to the electric field (the same parameters), and surprisingly, the second exposure resulted in a lack of susceptibility of bacteria to the electric field, i.e., acquisition of resistance to the electric field. Importantly, in this experiment, the applied voltage was 1000 times lower compared to the voltage used in electroporation. It highlights the importance of two parameters that should be taken into consideration when the electric field is applied: electric field strength and frequency. The preliminary results suggest that bacteria adapted to the electric field. Confirmation of this hypothesis requires further experiments, including DNA-sequencing, and RNA-sequencing to check whether changes occurred only on transcriptome level or both, transcriptome and genome levels. The impact of the electric field on bacteria requires further investigation to provide better insight into the mechanism of adaptation. SEM/Cryo-SEM should be performed to investigate changes in the morphology of exposed bacteria. Measurements of the zeta potential can reveal changes in charge distribution of the bacterial cell wall that might support the suppression of the effect of the electric field. It is also worth mentioning that examination of charge distribution of the cell wall of *E. coli* can be performed using SICM (Scanning ion-conductance microscopy), a technique developed at the IPC PAS by Dr. Eng. Wojciech Nogala. The surface is scanned using a nanoelectrode and thus the charge distribution can be measured *in situ* (the first control experiments have been performed in collaboration). The research can also explore other directions – examination of the parameters of the electric field which can effectively kill bacteria, or could lead to the development of a new sterilization method. It would be even more important in the current burning problem of bacteria resistant to antibiotics.

6.3. Contribution

Robert Hołyst and Jan Paczesny supervised the research, helped to design experiments and discuss the results. Jan Paczesny and Bo Åkerström helped to perform the first experiments on eukaryotic cells. Łukasz Richter helped to perform experiments in external laboratories (with bacteriophages, the first DNA-seq and the RNA-seq), and imaged samples using SEM (at the IPC PAS). Marta Janczuk-Richter is acknowledged for help with yeast experiments and Witold Adamkiewicz for help with ZnO nanorods. Wojciech Nogala

helped to conduct AFM measurements (IPC PAS). Mikołaj Grzeszkowiak, Barbara Peplińska, and Stefan Jurga helped to perform SEM and cryo-SEM imaging of samples at the Nanobiomedical Centre, Adam Mickiewicz University in Poznań. Elżbieta Wyroba, Szymon Suski and Henryk Bilski are gratefully acknowledged for help with TEM visualization and X-ray microanalysis at the Nencki Institute of Experimental Biology of the Polish Academy of Sciences in Warsaw. Adrian Silesian and Hans A. R. Bluyssen from Department of Human Molecular Genetics, Institute of Biotechnology and Molecular Biology, Faculty of Biology, Adam Mickiewicz University in Poznań, performed the first DNA-seq data analysis. Natalia Derebecka and Joanna Wesoły helped to conduct the first DNA-seq and RNA-seq experiments. Natalia is also gratefully acknowledged for assistance during the second RNA-seq experiment (library preparation). Joanna M. Łoś and Marcin Łoś helped to carry out experiments with bacteriophages and analyze the results at the Department of Molecular Genetics of Bacteria, Faculty of Biology, University of Gdańsk. Przemysław Decewicz and Łukasz Dziewit conducted the first RNA-seq analysis, and currently they are supporting the DNA-seq (mutation rate) analysis and the RNA-seq analysis (transcriptome landscape after exposure to ZnO nanorods).

6.4. Acknowledgments

I would never have gotten along the scientific journey towards the Ph.D. if it was not for a few special people.

First and foremost, I would like to thank **Robert Hołyst** for giving me an opportunity to work in his group, for his guidance, mentoring on my research, for his support and suggestions on my academic career. Your enthusiasm, physical intuition, obsession for genuine science and ability to approach complex problems with clarity and simplicity (despite "the experimental whole"), are truly inspiring and have very much shaped the type of scientist that I aspire to be. I enjoyed very much our early morning (philosophical) conversations about life, science... and actually about everything. Morning coffee with you will always rouse my recollection of memories. You always believed that this project has the potential to spark new and exciting interdisciplinary directions, and I am very grateful that you have encouraged me to think in this way, even when I had my moments of weakness. Working with you was a great honor, and I will remain forever grateful for these truly inspiring times.

Next, of course, I wish to thank Jan Paczesny. Collaborating* with you was the best thing that could have happened to me before (during my summer internship) and during my Ph.D. You taught me the most important lessons during my scientific adventure and certainly, you shaped my soft skills and encouraged to popularize science. Let me thank you especially for your friendly company, patience, and your care. Without doubts, working with you was my privilege. I have no idea how to express my gratitude to you. Instead, I have put "collaborating" with *, and I think you know better than anyone else what this * represents :)

Furthermore, I would like to express my genuine appreciation to **Łukasz Richter** for his essential help and contribution to the experimental work. I would like to thank you for sharing your creativity, enthusiasm, and company during days, nights, weekends spent in the lab, conferences as well, but mostly for showing me your support when I needed it the most.

Krzysztof Bielec, thank you for your help and support, all the serious and less serious conversations we had during last years, and for being my friend (I will always miss pizza during weekends and gym at 7 am).

I would like to thank Agnieszka Wiśniewska, Krzysztof Sozański, Marta Janczuk-Richter for your kindness, advice, a lot of chats, and a nice time overall.

The working atmosphere was essential for having a nice time during the realization of projects. Therefore, I would like to thank the entire Hołyst and Garstecki group for contributing to this. Tomek, Krzysztof, Monika, Paweł, Karina, Marta, Grzegorz, Patrycja, Airit, Ying, Yirui, Katarzyna, Michał, Artur, Tomek, Natalia, Magdalena, Witold, Adam, Łukasz, Karol, Dominika, Magdalena, Ott, Ladislav, Patryk, Karol, Justyna, Marco, Jan, Piotr, thank you all. You are wonderful.

W szczególności chciałam podziękować swoje rodzinie za wsparcie. Moim Rodzicom, siostrze (Izabeli), moim braciszkom (Kubie i Jasiowi) oraz kochanym Dziadkom. Dziękuję Wam za Waszą cierpliwość i bezgraniczną miłość. Mamo, dziękuję za wszystkie wspaniałe życiowe lekcje, których mi udzieliłaś, za Twoją troskę i wytrwałość. Jesteś dla mnie prawdziwą inspiracją. Mamo i Tato, dziękuję za to, że od najmłodszych lat pielęgnowaliście moją ciekawość świata i za to, że dostałam od Was wolność i odpowiedzialność. Wierze, że ukończenie tego doktoratu w dużej mierze zawdzięczam Wam jako rodzinie. Zawsze wspieraliście mnie w pełni na każdym etapie mojego życia.

Thank you all,
Kinga

About the author

Kinga Matuła graduated from Rzeszow University of Technology, Faculty of Chemistry where she was studying biotechnology. As a part of her master studies, Kinga was on Erasmus exchange and she was studying chemical and process engineering at the Otto-von-Guericke University Magdeburg and worked at the Max Planck Institute for Dynamic and Complex Technical Systems in Magdeburg. She defended her master thesis with distinction in 2013 (*Separation of pharmaceutically active isomers by crystallization*). Her main field of research is the examination of the influence of physical and chemical factors on growth and evolution of living cells. She is mostly focused on the investigation of the effect of nanomechanical stress induced by nanoparticles on various types of cells (bacterial, fungal and eukaryotic). She took part in additional projects concentrated on the study of the effect of electric field on viruses, self-organization of materials on the surface, dielectric properties of bacterial cells, surface charge mapping of cell membranes and antibacterial effects of materials and composites with incorporated nanoparticles.

Kinga Matuła participated in shorter and longer internships, courses and scientific programs, among others two times at Radboud University in Nijmegen (the Netherlands), Lund University Commissioned Education (Sweden), University of Gdańsk (Faculty of Biology), Bio-Tech Media in Warsaw, PicoQuant in Berlin (Germany), Adam Mickiewicz University in Poznań (Faculty of Biology and Nanomedical Center), Coca-Cola HBC (region of Krynica-Zdrój). As a high school student, she took part in two student exchanges and she was learning at Loyola Academy in Chicago (USA) and Jesuit High School in Palermo (Italy). After finishing the experimental part related to Ph.D. thesis, she was working in Cytofind Diagnostics B.V.in the Netherlands on the development of a microfluidic platform for isolation, detection and of circulating tumor cells and circulating stromal cells from metastatic cancer patients. Currently, Kinga is working at the Radboud University in Nijmegen on the droplet-based microfluidic platform for the detection of CTCs and stromal cells, and further characterization using single-cell RNA sequencing. The second project she is working on is related to the development and application of a novel tool to measure reaction rates of cellular enzymatic reaction networks using single-cell transcriptomics and proteomics (droplet-based microfluidics).

She was awarded for best poster presentation and twice for best oral presentation during scientific conferences. Kinga gained also Rector's award for scientific and organizational work, Primus inter pares award for the best graduates of the Rzeszow University of Technology and she was awarded a title Tutor of The Year 2015/2016 by children participating in Children's University. She was also a semifinalist of FameLab competition (2015) and semifinalist of Radboud Talks (2019). Kinga also popularized science as part of the Children's University project and the University of Young Researcher.

The list of publications:

1.**Matuła K,** Richter Ł, Janczuk-Richter M, Nogala W, Grzeszkowiak M, Peplińska B, Jurga S, Wyroba E, Suski S, Bilski H, Silesian S, Bluyssen HAR, Derebecka N, Wesoły J, Łoś JM, Łoś M, Decewicz P, Dziewit L, Paczesny J, Hołyst R. Phenotypic plasticity of Escherichia coli upon exposure to physical stress induced by ZnO nanorods. *Sci. Rep.* 9, 8575 (2019).

2. Paczesny J, Wolska-Pietkiewicz M, Binkiewicz I, Wadowska M, Wróbel Z, **Matuła K,** et al. Photoactive Langmuir–Blodgett, Freely Suspended and Free Standing Films of Carboxylate Ligand-Coated ZnO Nanocrystals. *ACS Appl Mater Interfaces*. American Chemical Society; 2016;8: 13532–13541.

3. **Matuła K***, Richter Ł*, Adamkiewicz W, Åkerström B, Paczesny J, Hołyst R, et al. Influence of nanomechanical stress induced by ZnO nanoparticles of different shapes on the viability of cells. *Soft Matter*. The Royal Society of Chemistry; 2016;12: 4162–4169. *equal contribution

4. Richter Ł*, **Matuła K***, Leśniewski A, Kwaśnicka K, Łoś J, Łoś M, et al. Ordering of bacteriophages in the electric field: Application for bacteria detection. *Sensors Actuators B Chem*. 2016;224: 233–240. *equal contribution

5. Paczesny J, Wolska-Pietkiewicz M, Binkiewicz I, Wrõbel Z, Wadowska M, **Matuła** K, et al. Towards Organized Hybrid Nanomaterials at the Air/Water Interface Based on Liquid-Crystal/ZnO Nanocrystals. *Chem - A Eur J.* Wiley-VCH Verlag; 2015;21: 16941–16947.

6. Olbrycht M, Balawejder M, **Matuła K,** Piatkowski W, Antos D. Multistage Cross-Current and Countercurrent Flow Crystallization for Separation of Racemic 2-Methylbutanoic Acid. *Ind Eng Chem Res*. American Chemical Society; 2014;53: 15990–15999.

Patents

1. Paczesny J,Wadowska M, Wróbel Z, Dzięcielewski I, **Matuła K**, Lewiński J, Hołyst R. "Method for preparation of nanorods at the air/water interface", P- 401054, 04.10.2012.

2. Paczesny J, Wadowska M, Wróbel Z, **Matuła K**, Lewiński J, Hołyst R. "Method for preparation of free standing thin films of quantum dots at the air/water interface and such films", P-401055, 04.10.2012.

3. Dolińska J, Opałło M, **Matuła K**, Richter Ł. "The pectin matrix. A method of preparation and application in the synthesis of gold nanoparticles, electrochemistry and microbiology", P-418299, 11.08.2016.

Manuscript submitted

1. Rivello F*, **Matuła K***, Piruska A, Smits M, Mehra N, Huck W, *Detection and isolation of highly metabolically active circulating stromal cells from metastatic prostate cancer patients using blood-based biopsies*, review submitted to *Science Advances*, *equal contribution

2. **Matuła K***, Rivello R*, Huck W, *Single-cell Analysis Using Droplet-based Microfluidics*, under revision in *Advanced Biosystems*, *equal contribution

3. Wisniewska A, Kalwarczyk T, Szymanski J, Kryszczuk K, **Matuła K**, Hołyst R, *Cell extract gels as example of active matter*, submitted to *Journal of Rheology*

Manuscripts in preparation

Kinga Matuła, Przemyslaw Decewicz, Lukasz Dziewit, Natalia Derebecka, Joanna Wesoły, Jan Paczesny, Robert Hołyst, Profiling transcriptome dynamics of Escherichia coli upon exposure to mechanical stress induced by ZnO nanorods

Kinga **Matuła**, Przemyslaw Decewicz, Lukasz Dziewit, Jan Paczesny, Robert Hołyst, Mother and daughter bacterial cells may have different genomes: a study of the mutation rate of Escherichia coli

Appendix

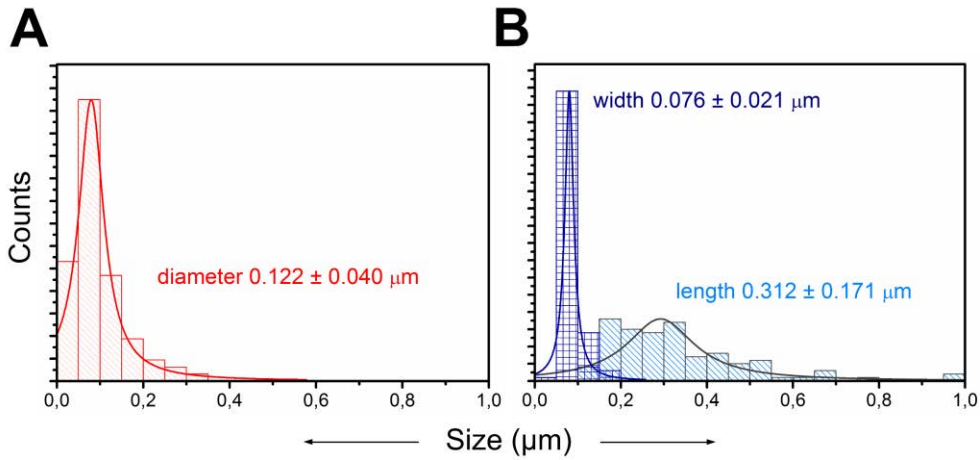

Fig. S1. Comparison of size distributions measured by SEM for(A) ZnO NP and (B) ZnO NR.

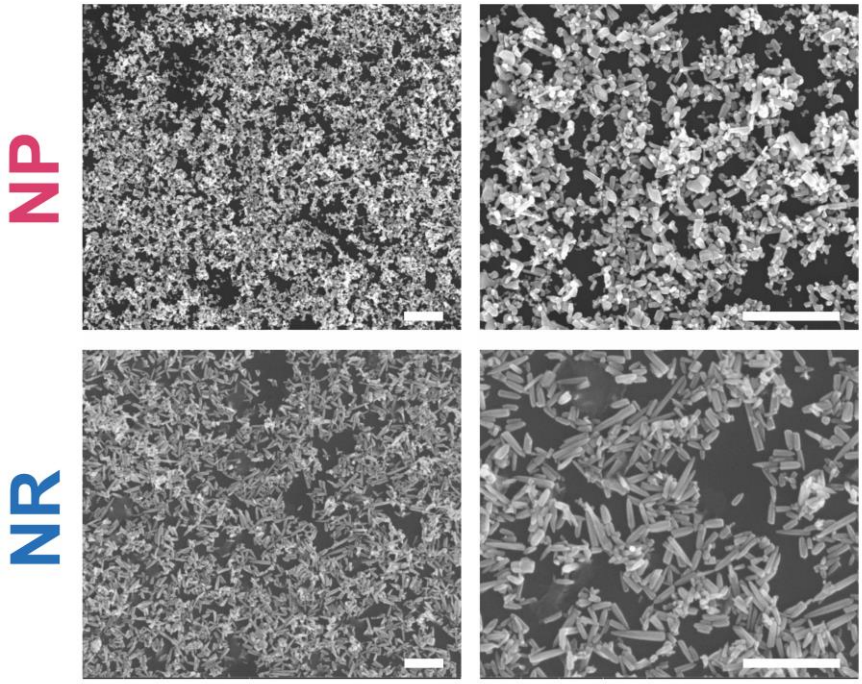

Fig. S2. SEM images of rounded ZnO nanoparticles (NP) and ZnO nanorods (NR). Scale bars correspond to 1 μm.

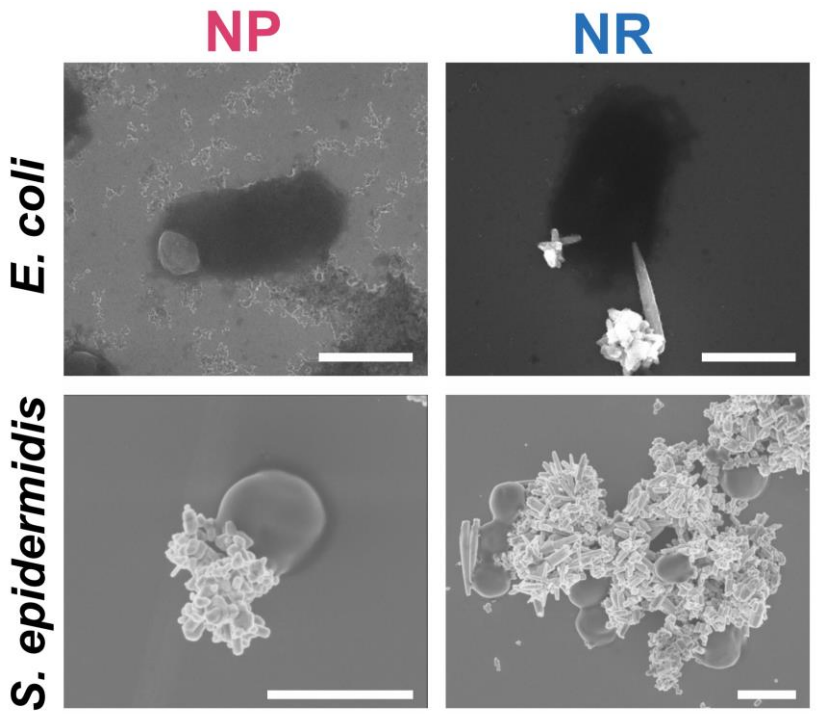

Fig. S3. SEM images of *E. coli* and *S. epidermidis* exposed to rounded ZnO nanoparticles (NP) and ZnO nanorods (NR). Scale bars correspond to 1 μm.

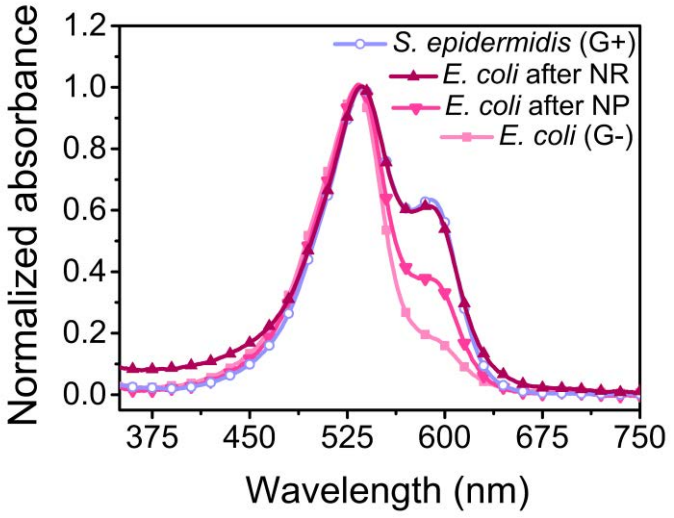

Fig. S4. Comparison of UV-Vis spectra of the bacteria after Gram staining. Control *E. coli* and *S. epidermidis* are marked *E. coli* (G-) and *S. epidermidis* (G+), respectively. *E. coli* after exposure to ZnO nanorods is marked as *E. coli* after NR and *E. coli* after exposure to the more spherical ZnO nanoparticles is marked as *E. coli* after NP. The peak in the range about 530 nm corresponds to the presence of safranine and for crystal violet is around 590.

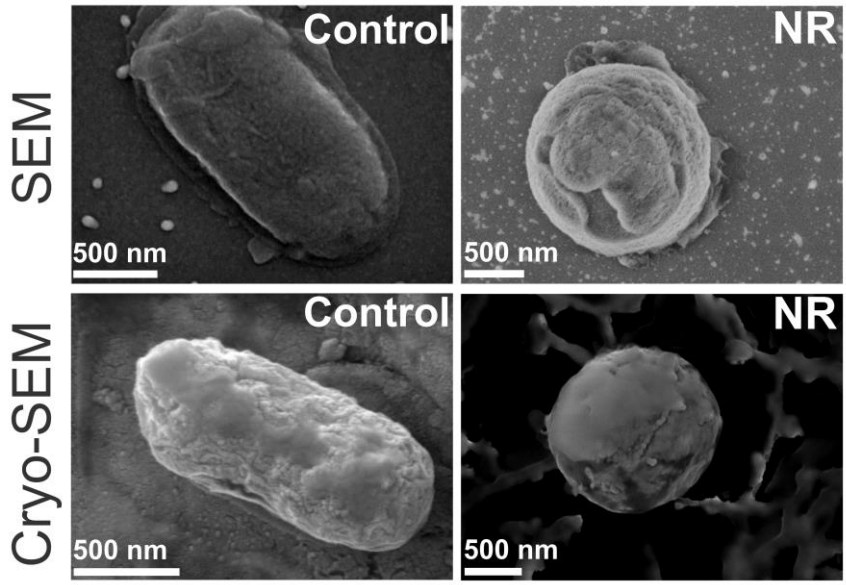

Fig. S5. Scanning electron microscope (SEM) and cryo-scanning electron (Cryo-SEM) images of control *E. coli* (Control) and upon exposure to ZnO NR (NR).

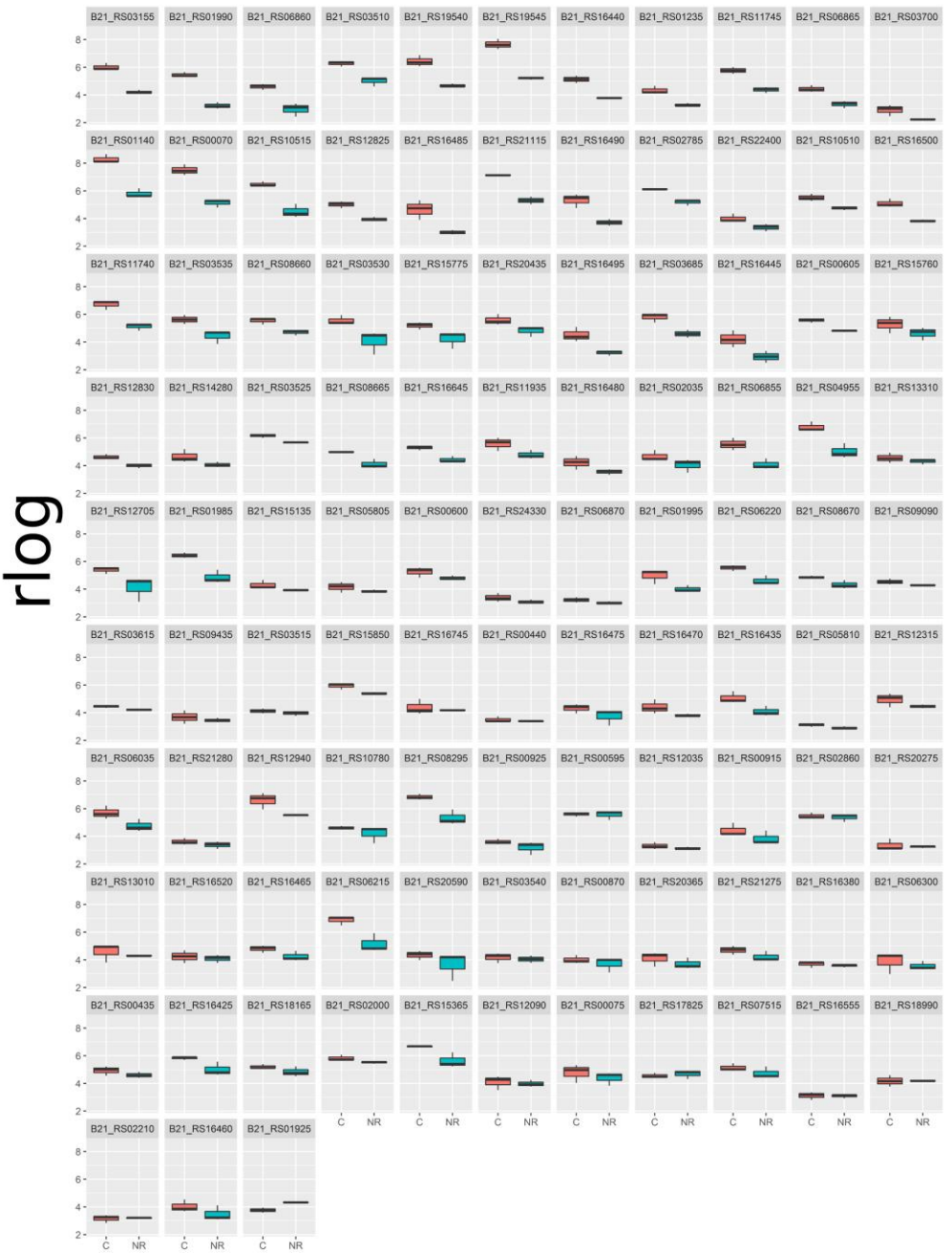

Fig. S6. Comparison of gene expression profile of *E. coli* exposed to ZnO nanorods (marked as NR) and control *E. coli* (marked as C). Expression of genes with 4.78E-18 ≤padj≤ 0.000286991.

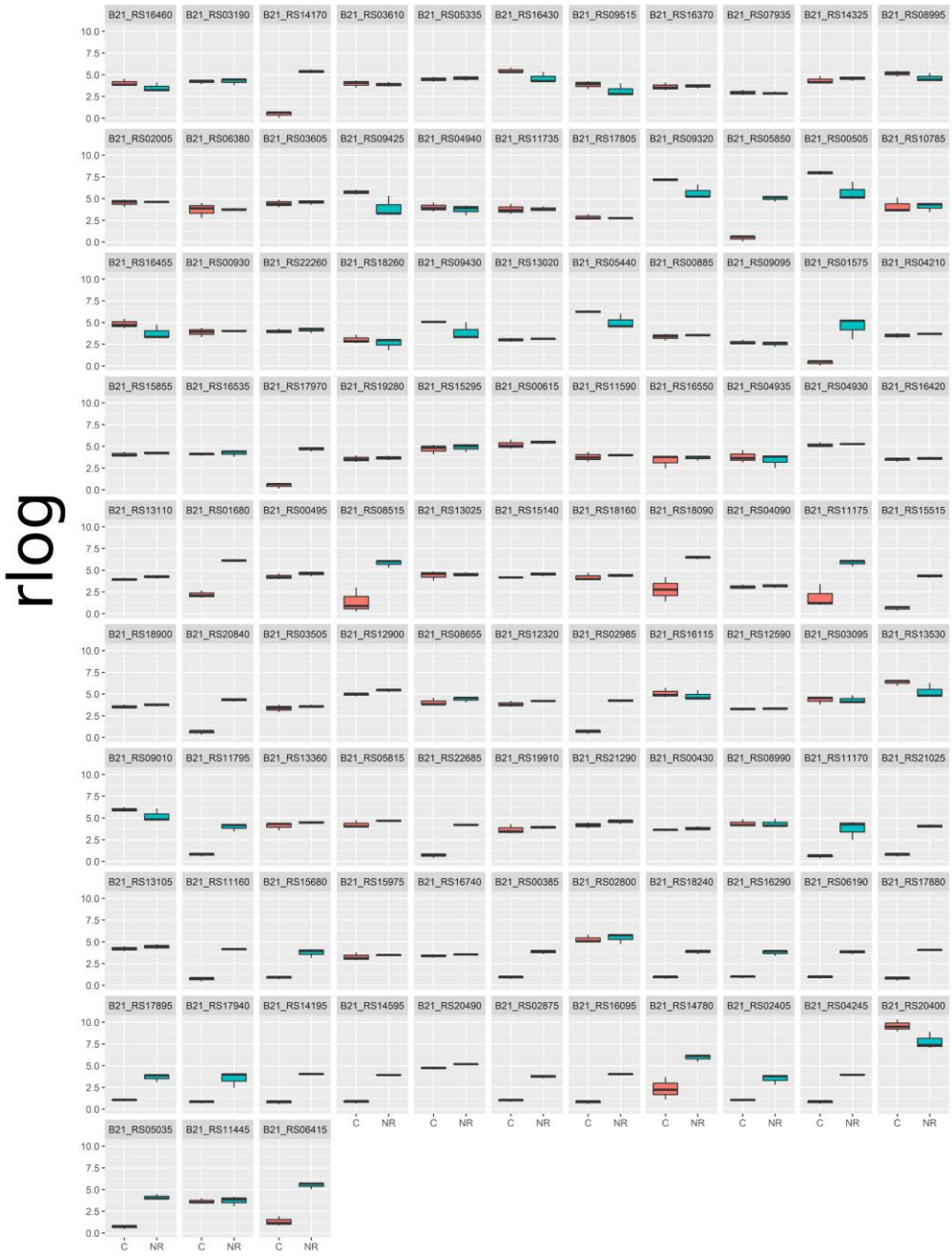

Fig. S7. Comparison of gene expression profile of *E. coli* exposed to ZnO nanorods (marked as NR) and control *E. coli* (marked as C). Expression of genes with 0.000286991≤padj≤0.011253454

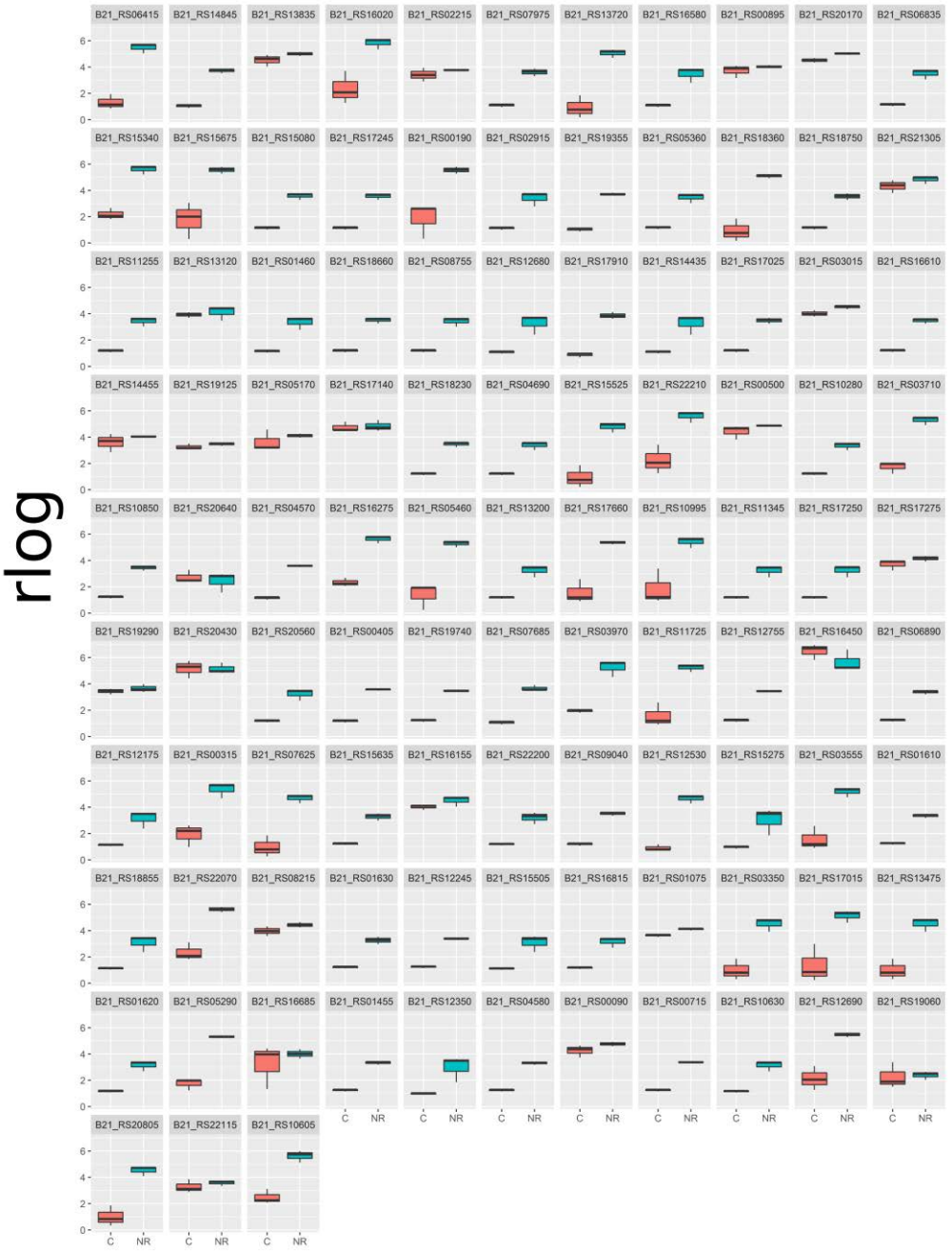

Fig. S8. Comparison of gene expression profile of *E. coli* exposed to ZnO nanorods (marked as NR) and control *E. coli* (marked as C). Expression of genes with 0.011253454≤padj≤0.023850404.

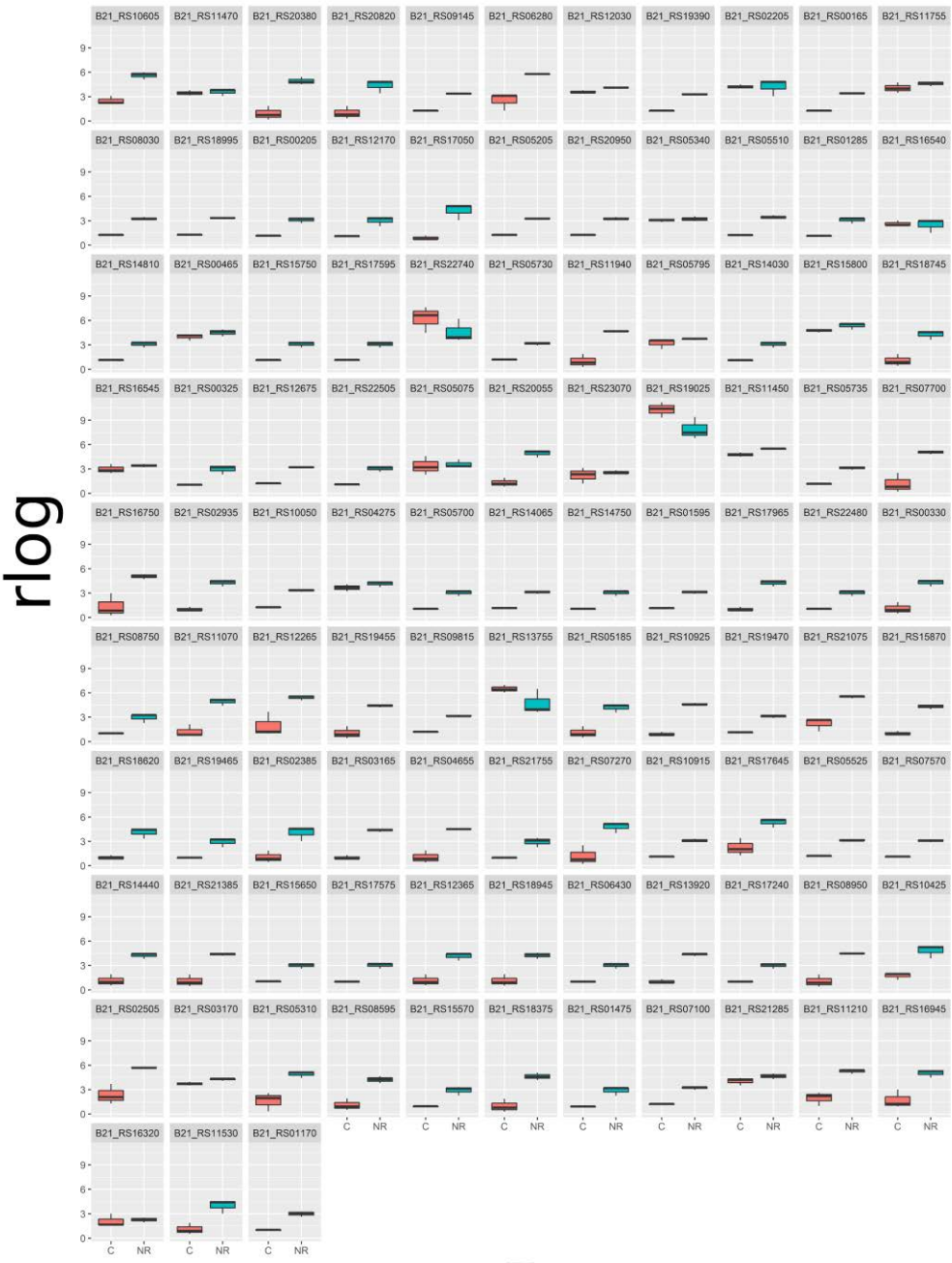

Fig. S9. Comparison of gene expression profile of *E. coli* exposed to ZnO nanorods (marked as NR) and control *E. coli* (marked as C). Expression of genes with 0.023850404≤padj≤0.035008568.

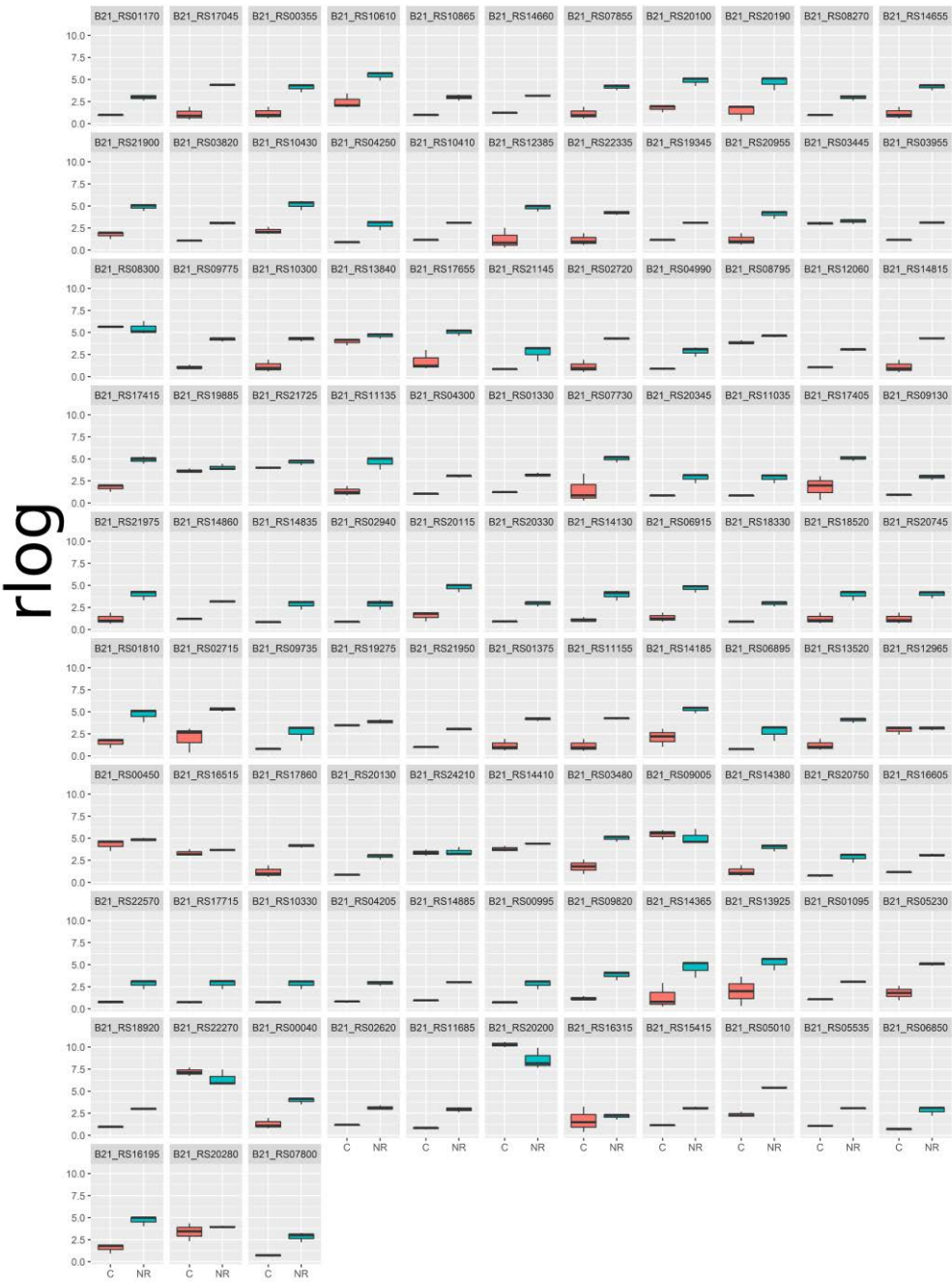

Fig. S10. Comparison of gene expression profile of *E. coli* exposed to ZnO nanorods (marked as NR) and control *E. coli* (marked as C). Expression of genes with 0.035008568≤padj≤0.041854951.

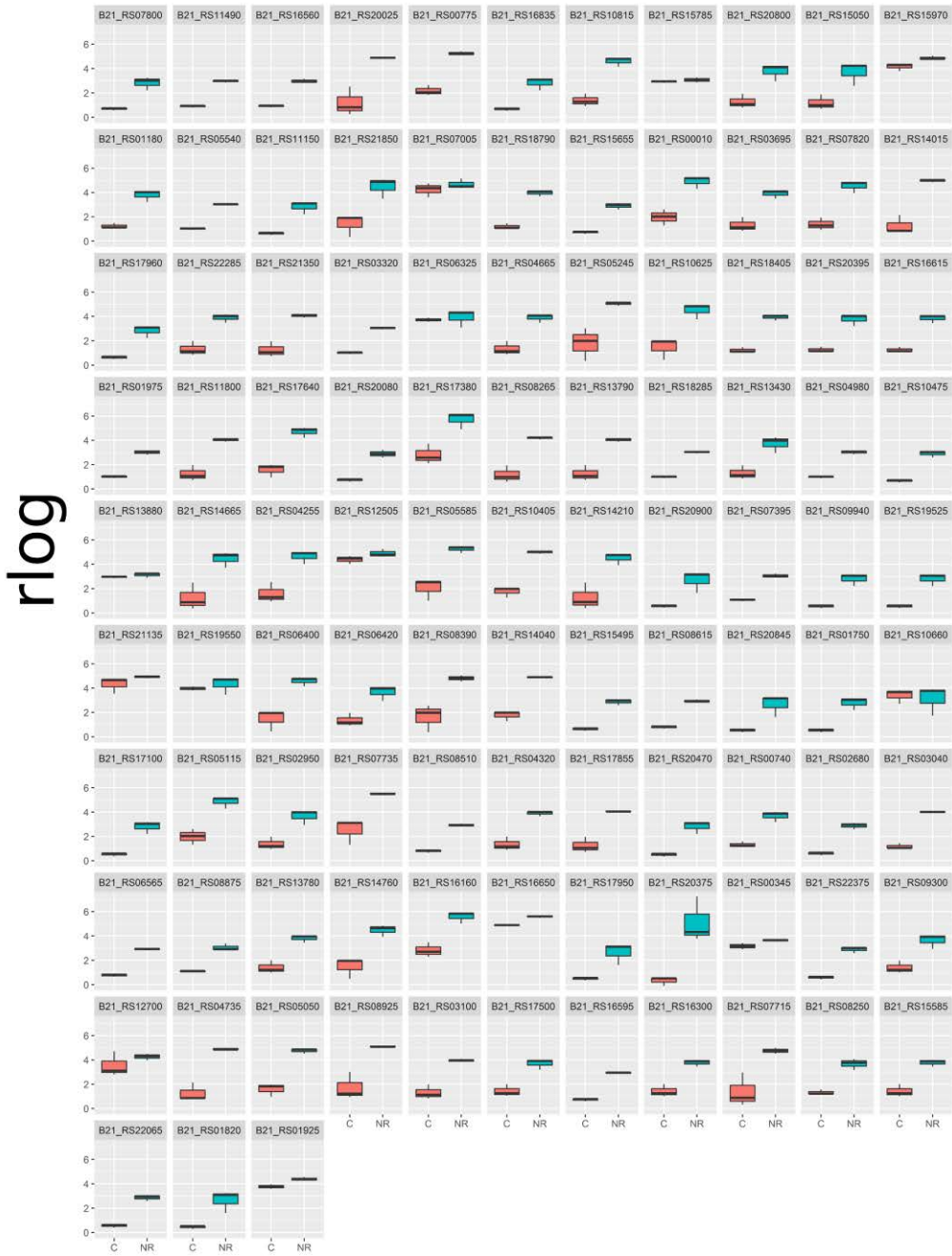

Fig. S11. Comparison of gene expression profile of *E. coli* exposed to ZnO nanorods (marked as NR) and control *E. coli* (marked as C). Expression of genes with 0.041854951≤padj≤0.049983382.

List of references

1. *Handbook of nanoscience, engineering, and technology, Third edition*. (CRC PRESS, 2017).
2. Cao, G. & Wang, Y. *Nanostructures and nanomaterials: synthesis, properties, and applications*. (World Scientific, 2011).
3. Size-comparison-Bio-nanoparticles nanometer scale comparison nanoparticle size comparison nanotechnology chart ruler. Available at: http://www.wichlab.com/nanometer-scale-comparison-nanoparticle-size-comparison-nanotechnology-chart-ruler-2/. (Accessed: 19th April 2018)
4. Nowack, B. & Bucheli, T. D. Occurrence, behavior and effects of nanoparticles in the environment. *Environ. Pollut.* 150, 5–22 (2007).
5. Kajander, E. O. & Çiftçioglu, N. Nanobacteria: An alternative mechanism for pathogenic intra- and extracellular calcification and stone formation. *Proc. Natl. Acad. Sci.* 95, (1998).
6. Luef, B. *et al.* Diverse uncultivated ultra-small bacterial cells in groundwater. *Nat. Commun.* 6, 6372 (2015).
7. Horikoshi, S. & Serpone, N. *Microwaves in nanoparticle synthesis : fundamentals and applications*. (Wiley-VCH, 2013).
8. Needham, J., Wang, L., Mét́ailie, G. & Huang, H. T. *Science and civilisation in China*.
9. Barber, D. J. & C., F. I. An ivestigation of the origin of the colour of the Lycurgus cup by analytical transmission electron microscopy. *Archaeometry* 32, 33–45 (1990).
10. Arvizo, R. R. *et al.* Intrinsic therapeutic applications of noble metal nanoparticles: past, present and future. *Chem. Soc. Rev.* 41, 2943–70 (2012).
11. Martin, M. N., Basham, J. I., Chando, P. & Eah, S.-K. Charged Gold Nanoparticles in Non-Polar Solvents: 10-min Synthesis and 2D Self-Assembly. *Langmuir* 26, 7410–7417 (2010).
12. Cobley, C. M., Skrabalak, S. E., Campbell, D. J. & Xia, Y. Shape-Controlled Synthesis of Silver Nanoparticles for Plasmonic and Sensing Applications. *Plasmonics* 4, 171–179 (2009).
13. González, A. L., Noguez, C., Beránek, J. & Barnard, A. S. Size, Shape, Stability, and Color of Plasmonic Silver Nanoparticles. *J. Phys. Chem. C* 118, 9128–9136 (2014).
14. Hutter, E. & Fendler, J. H. Exploitation of Localized Surface Plasmon Resonance. *Adv. Mater.* 16, 1685–1706 (2004).
15. Polman, A. Applied physics. Plasmonics applied. *Science* 322, 868–9 (2008).
16. Luther, J. M., Jain, P. K., Ewers, T. & Alivisatos, A. P. Localized surface plasmon resonances arising from free carriers in doped quantum dots. *Nat. Mater.* 10, 361–366 (2011).
17. Jain, P. K., Huang, X., El-Sayed, I. H. & El-Sayed, M. A. Noble Metals on the Nanoscale: Optical and Photothermal Properties and Some Applications in Imaging, Sensing, Biology, and Medicine. *Acc. Chem. Res.* 41, 1578–1586 (2008).
18. Heiligtag, F. J. & Niederberger, M. The fascinating world of nanoparticle research. *Mater. Today* 16, 262–271 (2013).
19. Annabelle Hett. *Nanotechnology: Small Matter, Many Unknowns - Annabelle Hett - Google Books*. (Swiss Reinsurance Company, 2004).
20. Nouailhat, A. *An Introduction to Nanoscience and Nanotechnology*. (ISTE, 2008). doi:10.1002/9780470610954
21. Wang, W. *et al.* Predicting Nano-Bio Interactions by Integrating Nanoparticle Libraries and Quantitative Nanostructure Activity Relationship Modeling. *ACS Nano* 11, 12641–12649 (2017).
22. Helma, C., Rautenberg, M. & Gebele, D. Nano-Lazar: Read across Predictions for Nanoparticle Toxicities with Calculated and Measured Properties. *Front. Pharmacol.* 8, 377 (2017).
23. Rasulev, B., Leszczynska, D. & Leszczynski, J. Nanoparticles. in *Advanced Methods and Applications in Chemoinformatics* 92–110 (IGI Global). doi:10.4018/978-1-60960-860-6.ch003
24. de Mello Donegá, C. The Nanoscience Paradigm: "Size Matters!" in *Nanoparticles* 1–12 (Springer Berlin Heidelberg, 2014). doi:10.1007/978-3-662-44823-6_1
25. Annabelle Hett. *Nanotechnology: Small Matter, Many Unknowns - Annabelle Hett - Google Books*. (Swiss Reinsurance Company, 2004).
26. Losert, S. *et al.* Human Exposure to Conventional and Nanoparticle-Containing Sprays - Critical Review. doi:10.1021/es5001819
27. Ray, P. C., Yu, H. & Fu, P. P. Toxicity and environmental risks of nanomaterials: challenges and future needs. *J. Environ. Sci. Health. C. Environ. Carcinog. Ecotoxicol. Rev.* 27, 1–35 (2009).
28. Sajid, M. *et al.* Impact of nanoparticles on human and environment: review of toxicity factors, exposures, control strategies, and future prospects. *Environ. Sci. Pollut. Res.* 22, 4122–4143 (2015).
29. *Nanocharacterisation*. (Royal Society of Chemistry, 2015). doi:10.1039/9781782621867
30. Ersen, O., Florea, I., Hirlimann, C. & Pham-Huu, C. Exploring nanomaterials with 3D electron microscopy. *Mater. Today* 18, 395–408 (2015).
31. Liu, J. & Wöll, C. Surface-supported metal–organic framework thin films: fabrication methods, applications, and challenges. *Chem. Soc. Rev.* 46, 5730–5770 (2017).
32. Krishnan, V., Sakakibara, K., Mori, T., Hill, J. P. & Ariga, K. Manipulation of thin film assemblies: Recent progress and novel concepts. *Curr. Opin. Colloid Interface Sci.* 16, 459–469 (2011).
33. Ariga, K., Ji, Q., Nakanishi, W. & Hill, J. P. Thin Film Nanoarchitectonics. *J. Inorg. Organomet. Polym. Mater.* 25, 466–479 (2015).
34. Paczesny, J. *et al.* Photoactive Langmuir–Blodgett, Freely Suspended and Free Standing Films of Carboxylate Ligand-Coated ZnO Nanocrystals. *ACS Appl. Mater. Interfaces* 8, 13532–13541 (2016).
35. Paczesny, J. *et al.* Towards Organized Hybrid Nanomaterials at the Air/Water Interface Based on Liquid-Crystal/ZnO Nanocrystals. *Chem. - A Eur. J.* 21, 16941–16947 (2015).

36. Thiruvengadathan, R. *et al.* Nanomaterial processing using self-assembly-bottom-up chemical and biological approaches. *Reports Prog. Phys.* 76, 066501 (2013).
37. Moving bottom-up science closer to the top. *Nat. Methods* 9, 847–847 (2012).
38. Pitorre, M. *et al.* Recent advances in nanocarrier-loaded gels: Which drug delivery technologies against which diseases? *J. Control. Release* 266, 140–155 (2017).
39. Mura, S., Nicolas, J. & Couvreur, P. Stimuli-responsive nanocarriers for drug delivery. *Nat. Mater.* 12, 991–1003 (2013).
40. Letchford, K. A review of the formation and classification of amphiphilic block copolymer nanoparticulate structures: micelles, nanospheres, nanocapsules and polymersomes. *Eur. J. Pharm. Biopharm.* 65, 259–269 (2007).
41. *Nanocharacterisation*. (Royal Society of Chemistry, 2015). doi:10.1039/9781782621867
42. Medina-Sánchez, M., Miserere, S. & Merkoçi, A. Nanomaterials and lab-on-a-chip technologies. *Lab Chip* 12, 1932 (2012).
43. Segerink, L. I. & Eijkel, J. C. T. Nanofluidics in point of care applications. *Lab Chip* 14, 3201–3205 (2014).
44. Kovarik, M. L. & Jacobson, S. C. Nanofluidics in Lab-on-a-Chip Devices. *Anal. Chem.* 81, 7133–7140 (2009).
45. Fischer, A. C. *et al.* Integrating MEMS and ICs. *Microsystems Nanoeng.* 1, 15005 (2015).
46. Seymour, J. P., Wu, F., Wise, K. D. & Yoon, E. State-of-the-art MEMS and microsystem tools for brain research. *Microsystems Nanoeng.* 3, 16066 (2017).
47. Zhao, X., Duan, G., Li, A., Chen, C. & Zhang, X. Integrating microsystems with metamaterials towards metadevices. *Microsystems Nanoeng. 2019 51* 5, 5 (2019).
48. Mishra, R., Pramanick, B., Maiti, T. K. & Bhattacharyya, T. K. Glassy carbon microneedles—new transdermal drug delivery device derived from a scalable C-MEMS process. *Microsystems Nanoeng.* 4, 38 (2018).
49. Li, S. *et al.* A DNA nanorobot functions as a cancer therapeutic in response to a molecular trigger in vivo. *Nat. Biotechnol.* 36, 258–264 (2018).
50. Kim, J., Lee, J., Hamada, S., Murata, S. & Ha Park, S. Self-replication of DNA rings. *Nat. Nanotechnol.* 10, 528–533 (2015).
51. Li, J., Esteban-Fernández de Ávila, B., Gao, W., Zhang, L. & Wang, J. Micro/nanorobots for biomedicine: Delivery, surgery, sensing, and detoxification. *Sci. Robot.* 2, eaam6431 (2017).
52. Kwon, E. J., Lo, J. H. & Bhatia, S. N. Smart nanosystems: Bio-inspired technologies that interact with the host environment. *Proc. Natl. Acad. Sci. U. S. A.* 112, 14460–6 (2015).
53. Jang, B. *et al.* Undulatory Locomotion of Magnetic Multilink Nanoswimmers. *Nano Lett.* 15, 4829–4833 (2015).
54. Ding, T. *et al.* Light-induced actuating nanotransducers. *Proc. Natl. Acad. Sci. U. S. A.* 113, 5503–7 (2016).
55. Delgado-Ramos, G. C. Nano-Conceptions: A Sociological Insight of Nanotechnology Conceptions. *J. Philos. Sci. Law* 6, 25–57 (2006).
56. European Commission & Research DG. *Nanosciences and nanotechnologies: An action plan for Europe 2005-2009 | Nanowerk*. (2005).
57. Kjølberg, K., Delgado-Ramos, G. C., Wickson, F. & Strand, R. Models of governance for converging technologies. *Technol. Anal. Strateg. Manag.* 20, 83–97 (2008).
58. Subbenaik, S. C. Physical and Chemical Nature of Nanoparticles. in *Plant Nanotechnology* 15–27 (Springer International Publishing, 2016). doi:10.1007/978-3-319-42154-4_2
59. Bhatia, S. Nanoparticles Types, Classification, Characterization, Fabrication Methods and Drug Delivery Applications. in *Natural Polymer Drug Delivery Systems* 33–93 (Springer International Publishing, 2016). doi:10.1007/978-3-319-41129-3_2
60. Pattni, B. S., Chupin, V. V. & Torchilin, V. P. New Developments in Liposomal Drug Delivery. *Chem. Rev.* 115, 10938–10966 (2015).
61. Boas, U. & Heegaard, P. M. H. Dendrimers in drug research. *Chem. Soc. Rev.* 33, 43 (2004).
62. Tiwari, G., Tiwari, R. & Rai, A. K. Cyclodextrins in delivery systems: Applications. *J. Pharm. Bioallied Sci.* 2, 72–9 (2010).
63. Zhang, Z., Li, J., Wang, Z., He, C. & Wang, Y. Polymeric nanospheres with tunable sizes, water dispersibility, and thermostability from heating-enabled micellization of polysulfone- *block* -polyethylene glycol. *J. Polym. Sci. Part B Polym. Phys.* 56, 769–777 (2018).
64. Brinkhuis, R. P., J T Rutjes, F. P. & M van Hest, J. C. Polymeric vesicles in biomedical applications. doi:10.1039/c1py00061f
65. Kakkar, A., Traverso, G., Farokhzad, O. C., Weissleder, R. & Langer, R. Evolution of macromolecular complexity in drug delivery systems. *Nat. Rev. Chem.* 1, 0063 (2017).
66. Ishihara, K., Chen, W., Liu, Y., Tsukamoto, Y. & Inoue, Y. Cytocompatible and multifunctional polymeric nanoparticles for transportation of bioactive molecules into and within cells. *Sci. Technol. Adv. Mater.* 17, 300–312 (2016).
67. Miao, Q. *et al.* Molecular afterglow imaging with bright, biodegradable polymer nanoparticles. *Nat. Biotechnol.* 35, 1102 (2017).
68. Pu, K., Chattopadhyay, N. & Rao, J. Recent advances of semiconducting polymer nanoparticles in in vivo molecular imaging. *J. Control. Release* 240, 312–322 (2016).
69. Kairdolf, B. A., Qian, X. & Nie, S. Bioconjugated Nanoparticles for Biosensing, in Vivo Imaging, and Medical Diagnostics. *Anal. Chem.* 89, 1015–1031 (2017).
70. van Rijt, S. & Habibovic, P. Enhancing regenerative approaches with nanoparticles. *J. R. Soc. Interface* 14, (2017).
71. Lam, S. J., Wong, E. H. H., Boyer, C. & Qiao, G. G. Antimicrobial polymeric nanoparticles. *Prog. Polym. Sci.* 76, 40–64 (2018).

72. Allen, T. M. & Cullis, P. R. Drug delivery systems: entering the mainstream. *Science* 303, 1818–22 (2004).
73. Duncan, R. & Vicent, M. J. Polymer therapeutics-prospects for 21st century: The end of the beginning. *Adv. Drug Deliv. Rev.* 65, 60–70 (2013).
74. Cho, E. C., Glaus, C., Chen, J., Welch, M. J. & Xia, Y. Inorganic nanoparticle-based contrast agents for molecular imaging. *Trends Mol. Med.* 16, 561–573 (2010).
75. Tong, L., Wei, Q., Wei, A. & Cheng, J.-X. Gold nanorods as contrast agents for biological imaging: optical properties, surface conjugation and photothermal effects. *Photochem. Photobiol.* 85, 21–32 (2009).
76. Tong, L., Cobley, C. M., Chen, J., Xia, Y. & Cheng, J.-X. Bright Three-Photon Luminescence from Gold/Silver Alloyed Nanostructures for Bioimaging with Negligible Photothermal Toxicity. *Angew. Chemie Int. Ed.* 49, 3485–3488 (2010).
77. Sharma, B., Frontiera, R. R., Henry, A.-I., Ringe, E. & Van Duyne, R. P. SERS: Materials, applications, and the future. *Mater. Today* 15, 16–25 (2012).
78. Kumar, A., Zhang, X. & Liang, X.-J. Gold nanoparticles: Emerging paradigm for targeted drug delivery system. *Biotechnol. Adv.* 31, 593–606 (2013).
79. Giner-Casares, J. J., Henriksen-Lacey, M., Coronado-Puchau, M. & Liz-Marzán, L. M. Inorganic nanoparticles for biomedicine: where materials scientists meet medical research. *Mater. Today* 19, 19–28 (2016).
80. *Metal Nanoparticles for Catalysis*. (Royal Society of Chemistry, 2014). doi:10.1039/9781782621034
81. Mistry, H., Sofia Varela, A., Kühl, S., Strasser, P. & Roldan Cuenya, B. Nanostructured electrocatalysts with tunable activity and selectivity. *Nat. Publ. Gr.* (2016). doi:10.1038/natrevmats.2016.9
82. Pal, J. & Pal, T. Faceted metal and metal oxide nanoparticles: design, fabrication and catalysis. *Nanoscale* 7, 14159–14190 (2015).
83. Shipway, A. N., Katz, E. & Willner, I. Nanoparticle Arrays on Surfaces for Electronic, Optical, and Sensor Applications. *ChemPhysChem* 1, 18–52 (2000).
84. Watanabe, K., Menzel, D., Niklas Nilius, A. & Freund, H.-J. Photochemistry on Metal Nanoparticles. (2006). doi:10.1021/CR050167G
85. Bhushan, B. *Springer handbook of nanotechnology*. (2017).
86. Andreescu, S., Ornatska, M., Erlichman, J. S., Estevez, A. & Leiter, J. C. Biomedical Applications of Metal Oxide Nanoparticles. in *Fine Particles in Medicine and Pharmacy* 57–100 (Springer US, 2012). doi:10.1007/978-1-4614-0379-1_3
87. Pal, J. & Pal, T. Faceted metal and metal oxide nanoparticles: design, fabrication and catalysis. *Nanoscale* 7, 14159–14190 (2015).
88. Andreescu, S., Ornatska, M., Erlichman, J. S., Estevez, A. & Leiter, J. C. Biomedical Applications of Metal Oxide Nanoparticles. in *Fine Particles in Medicine and Pharmacy* 57–100 (Springer US, 2012). doi:10.1007/978-1-4614-0379-1_3
89. Mohammed, L., Gomaa, H. G., Ragab, D. & Zhu, J. Magnetic nanoparticles for environmental and biomedical applications: A review. *Particuology* 30, 1–14 (2017).
90. Reddy, L. H., Arias, J. L., Nicolas, J. & Couvreur, P. Magnetic Nanoparticles: Design and Characterization, Toxicity and Biocompatibility, Pharmaceutical and Biomedical Applications. *Chem. Rev.* 112, 5818–5878 (2012).
91. Xu, G. *et al.* New Generation Cadmium-Free Quantum Dots for Biophotonics and Nanomedicine. *Chem. Rev.* 116, 12234–12327 (2016).
92. Xu, G. *et al.* New Generation Cadmium-Free Quantum Dots for Biophotonics and Nanomedicine. *Chem. Rev.* 116, 12234–12327 (2016).
93. Jing, L. *et al.* Aqueous Based Semiconductor Nanocrystals. *Chem. Rev.* 116, 10623–10730 (2016).
94. Jamieson, T. *et al.* Biological applications of quantum dots. *Biomaterials* 28, 4717–4732 (2007).
95. Choi, M. K., Yang, J., Hyeon, T. & Kim, D.-H. Flexible quantum dot light-emitting diodes for next-generation displays. *npj Flex. Electron.* 2, 10 (2018).
96. Pietryga, J. M. *et al.* Spectroscopic and Device Aspects of Nanocrystal Quantum Dots. *Chem. Rev.* 116, 10513–10622 (2016).
97. Pietryga, J. M. *et al.* Spectroscopic and Device Aspects of Nanocrystal Quantum Dots. *Chem. Rev.* 116, 10513–10622 (2016).
98. Cha, C., Shin, S. R., Annabi, N., Dokmeci, M. R. & Khademhosseini, A. Carbon-Based Nanomaterials: Multifunctional Materials for Biomedical Engineering. *ACS Nano* 7, 2891–2897 (2013).
99. Hong, G., Diao, S., Antaris, A. L. & Dai, H. Carbon Nanomaterials for Biological Imaging and Nanomedicinal Therapy. *Chem. Rev.* 115, 10816–10906 (2015).
100. Yan, Q.-L., Gozin, M., Zhao, F.-Q., Cohen, A. & Pang, S.-P. Highly energetic compositions based on functionalized carbon nanomaterials. *Nanoscale* 8, 4799–4851 (2016).
101. Novoselov, K. S. *et al.* Electric Field Effect in Atomically Thin Carbon Films. *Science (80-.).* 306, 666–669 (2004).
102. Hong, G., Diao, S., Antaris, A. L. & Dai, H. Carbon Nanomaterials for Biological Imaging and Nanomedicinal Therapy. *Chem. Rev.* 115, 10816–10906 (2015).
103. Cha, C., Shin, S. R., Annabi, N., Dokmeci, M. R. & Khademhosseini, A. Carbon-Based Nanomaterials: Multifunctional Materials for Biomedical Engineering. *ACS Nano* 7, 2891–2897 (2013).
104. Kroto, H. W., Heath, J. R., O'Brien, S. C., Curl, R. F. & Smalley, R. E. C60: Buckminsterfullerene. *Nature* 318, 162–163 (1985).
105. Poveda, R. L. & Gupta, N. Carbon Nanofibers: Structure and Fabrication. in 11–26 (Springer, 2016). doi:10.1007/978-3-319-23787-9_2
106. Al-Saleh, M. H. & Sundararaj, U. Review of the mechanical properties of carbon nanofiber/polymer composites. *Compos. Part A Appl. Sci. Manuf.* 42, 2126–2142 (2011).
107. Zeiger, M., Jäckel, N., Mochalin, V. N. & Presser, V. Review: carbon onions for electrochemical energy

storage. *J. Mater. Chem. A* 4, 3172–3196 (2016).
108. Sano, N., Wang, H., Chhowalla, M., Alexandrou, I. & Amaratunga, G. A. J. Synthesis of carbon "onions" in water. *Nature* 414, 506–507 (2001).
109. Mochalin, V. N., Shenderova, O., Ho, D. & Gogotsi, Y. The properties and applications of nanodiamonds. *Nat. Nanotechnol.* 7, 11–23 (2012).
110. Baker, S. N. & Baker, G. A. Luminescent Carbon Nanodots: Emergent Nanolights. *Angew. Chemie Int. Ed.* 49, 6726–6744 (2010).
111. Goryacheva, I. Y., Sapelkin, A. V. & Sukhorukov, G. B. Carbon nanodots: Mechanisms of photoluminescence and principles of application. *TrAC Trends Anal. Chem.* 90, 27–37 (2017).
112. Antunes, M. & Velasco, J. I. Multifunctional polymer foams with carbon nanoparticles. *Prog. Polym. Sci.* 39, 486–509 (2014).
113. Kaiser, K. *et al.* An sp-hybridized molecular carbon allotrope, cyclo[18]carbon. *Science* eaay1914 (2019). doi:10.1126/science.aay1914
114. Goryacheva, I. Y., Sapelkin, A. V. & Sukhorukov, G. B. Carbon nanodots: Mechanisms of photoluminescence and principles of application. *TrAC Trends Anal. Chem.* 90, 27–37 (2017).
115. Harrison, B. S. & Atala, A. Carbon nanotube applications for tissue engineering. *Biomaterials* 28, 344–353 (2007).
116. Angione, M. D. *et al.* Carbon based materials for electronic bio-sensing. *Mater. Today* 14, 424–433 (2011).
117. Liao, M. & Koide, Y. Carbon-Based Materials: Growth, Properties, MEMS/NEMS Technologies, and MEM/NEM Switches. *Crit. Rev. Solid State Mater. Sci.* 36, 66–101 (2011).
118. Coro, J., Suárez, M., Silva, L. S. R., Eguiluz, K. I. B. & Salazar-Banda, G. R. Fullerene applications in fuel cells: A review. *Int. J. Hydrogen Energy* 41, 17944–17959 (2016).
119. Tiwari, J. N., Tiwari, R. N. & Kim, K. S. Zero-dimensional, one-dimensional, two-dimensional and three-dimensional nanostructured materials for advanced electrochemical energy devices. *Prog. Mater. Sci.* 57, 724–803 (2012).
120. Huang, Z., Gong, J. & Nie, Z. Symmetry-Breaking Synthesis of Multicomponent Nanoparticles. *Acc. Chem. Res.* 52, 1125–1133 (2019).
121. Ghosh Chaudhuri, R. & Paria, S. Core/Shell Nanoparticles: Classes, Properties, Synthesis Mechanisms, Characterization, and Applications. *Chem. Rev.* 112, 2373–2433 (2012).
122. Wu, B. *et al.* Anisotropic Growth of TiO_2 onto Gold Nanorods for Plasmon-Enhanced Hydrogen Production from Water Reduction. *J. Am. Chem. Soc.* 138, 1114–1117 (2016).
123. Zheng, Z., Tachikawa, T. & Majima, T. Plasmon-Enhanced Formic Acid Dehydrogenation Using Anisotropic Pd–Au Nanorods Studied at the Single-Particle Level. *J. Am. Chem. Soc.* 137, 948–957 (2015).
124. Liang, S. *et al.* Symmetric and Asymmetric Au–AgCdSe Hybrid Nanorods. *Nano Lett.* 12, 5281–5286 (2012).
125. Fuente, J. M. de la. & Grazu, V. *Nanobiotechnology : inorganic nanoparticles vs organic nanoparticles*. (Elsevier, 2012).
126. Nguyen, K. T. & Zhao, Y. Engineered Hybrid Nanoparticles for On-Demand Diagnostics and Therapeutics. *Acc. Chem. Res.* 48, 3016–3025 (2015).
127. Sailor, M. J. & Park, J.-H. Hybrid nanoparticles for detection and treatment of cancer. *Adv. Mater.* 24, 3779–802 (2012).
128. Sierra-Martin, B. & Fernandez-Barbero, A. Inorganic/polymer hybrid nanoparticles for sensing applications. *Adv. Colloid Interface Sci.* 233, 25–37 (2016).
129. Gawande, M. B. *et al.* Cu and Cu-Based Nanoparticles: Synthesis and Applications in Catalysis. *Chem. Rev.* 116, 3722–3811 (2016).
130. Song, H. Metal Hybrid Nanoparticles for Catalytic Organic and Photochemical Transformations. *Acc. Chem. Res.* 48, 491–499 (2015).
131. Banin, U., Ben-Shahar, Y. & Vinokurov, K. Hybrid Semiconductor–Metal Nanoparticles: From Architecture to Function. *Chem. Mater.* 26, 97–110 (2014).
132. Banin, U., Ben-Shahar, Y. & Vinokurov, K. Hybrid Semiconductor–Metal Nanoparticles: From Architecture to Function. *Chem. Mater.* 26, 97–110 (2014).
133. What is the difference between one, two, three, and zero dimensional nanomaterials? - Quora. Available at: https://www.quora.com/What-is-the-difference-between-one-two-three-and-zero-dimensional-nanomaterials.
134. Benelmekki, M. *Designing Hybrid Nanoparticles*. (Morgan & Claypool Publishers, 2015). doi:10.1088/978-1-6270-5469-0
135. Jo, D. H., Kim, J. H., Lee, T. G. & Kim, J. H. Size, surface charge, and shape determine therapeutic effects of nanoparticles on brain and retinal diseases. *Nanomedicine Nanotechnology, Biol. Med.* 11, 1603–1611 (2015).
136. Dreaden, E. C., Alkilany, A. M., Huang, X., Murphy, C. J. & El-Sayed, M. A. The golden age: gold nanoparticles for biomedicine. *Chem. Soc. Rev.* 41, 2740–79 (2012).
137. Wu, Z., Yang, S. & Wu, W. Shape control of inorganic nanoparticles from solution. *Nanoscale* 8, 1237–59 (2016).
138. Luttge, R. & Luttge, R. Nanotechnology. *Microfabr. Ind. Appl.* 91–146 (2011). doi:10.1016/B978-0-8155-1582-1.00004-6
139. Vigneswaran, N., Samsuri, F., Ranganathan, B. & Padmapriya. Recent Advances in Nano Patterning and Nano Imprint Lithography for Biological Applications. *Procedia Eng.* 97, 1387–1398 (2014).
140. Edelstein, A. S. Nanomaterials. *Encycl. Mater. Sci. Technol.* 5916–5927 (2001). doi:10.1016/B0-08-043152-6/01031-7
141. Gibson, D. G. *et al.* Creation of a Bacterial Cell Controlled by a Chemically Synthesized Genome.

Science (80-.). 329, 52–56 (2010).
142. Grzybowski, B. A., Fitzner, K., Paczesny, J. & Granick, S. From dynamic self-assembly to networked chemical systems. *Chem. Soc. Rev.* 46, 5647–5678 (2017).
143. Singh, P., Kim, Y.-J., Zhang, D. & Yang, D.-C. Biological Synthesis of Nanoparticles from Plants and Microorganisms. *Trends Biotechnol.* 34, 588–599 (2016).
144. Li, X., Xu, H., Chen, Z.-S. & Chen, G. Biosynthesis of Nanoparticles by Microorganisms and Their Applications. *J. Nanomater.* 2011, 1–16 (2011).
145. Bottero, I., Huck, J., Kosikova, T. & Philp, D. A Synthetic Replicator Drives a Propagating Reaction–Diffusion Front. *J. Am. Chem. Soc.* 138, 6723–6726 (2016).
146. Sadownik, J. W., Mattia, E., Nowak, P. & Otto, S. Diversification of self-replicating molecules. *Nat. Chem.* 8, 264–269 (2016).
147. Pogodaev, A. A., Wong, A. S. Y. & Huck, W. T. S. Photochemical Control over Oscillations in Chemical Reaction Networks. *J. Am. Chem. Soc.* 139, 15296–15299 (2017).
148. Grzybowski, B. A. & Huck, W. T. S. The nanotechnology of life-inspired systems. *Nat. Nanotechnol.* 11, 585–592 (2016).
149. Mann, S. Systems of Creation: The Emergence of Life from Nonliving Matter. *Acc. Chem. Res.* 45, 2131–2141 (2012).
150. Xu, C., Hu, S. & Chen, X. Artificial cells: from basic science to applications. *Mater. Today* 19, 516–532 (2016).
151. Buzea, C., Pacheco, I. I. & Robbie, K. Nanomaterials and nanoparticles: Sources and toxicity. *Biointerphases* 2, MR17–MR71 (2007).
152. Navalón, S. & García, H. Nanoparticles for Catalysis. *Nanomater. (Basel, Switzerland)* 6, (2016).
153. Ghosh, S. Surface functionalized hybrid nanomaterials. in *Surface Chemistry of Nanobiomaterials* 1–32 (Elsevier, 2016). doi:10.1016/B978-0-323-42861-3.00001-7
154. Sun, J. *et al.* Effect of particle size on solubility, dissolution rate, and oral bioavailability: evaluation using coenzyme Q_{10} as naked nanocrystals. *Int. J. Nanomedicine* 7, 5733–44 (2012).
155. Bzdek, B. R., Zordan, C. A., Luther, G. W. & Johnston, M. V. Nanoparticle Chemical Composition During New Particle Formation. *Aerosol Sci. Technol.* 45, 1041–1048 (2011).
156. Pillai, P. P., Kowalczyk, B., Kandere-Grzybowska, K., Borkowska, M. & Grzybowski, B. A. Engineering Gram Selectivity of Mixed-Charge Gold Nanoparticles by Tuning the Balance of Surface Charges. *Angew. Chemie* 128, 8752–8756 (2016).
157. Pillai, P. P., Huda, S., Kowalczyk, B. & Grzybowski, B. A. Controlled pH Stability and Adjustable Cellular Uptake of Mixed-Charge Nanoparticles. *J. Am. Chem. Soc.* 135, 6392–6395 (2013).
158. Clogston, J. D. & Patri, A. K. Zeta Potential Measurement. in 63–70 (Humana Press, 2011). doi:10.1007/978-1-60327-198-1_6
159. Liu, Y. *et al.* A Novel Method to Improve Crystallinity of Supported Nanoparticles Using Low Melting Point Metals. *J. Phys. Chem. C* 115, 14591–14597 (2011).
160. Toropov, N. A., Leonov, N. B. & Vartanyan, T. A. Influence of Silver Nanoparticles Crystallinity on Localized Surface Plasmons Dephasing Times. *Phys. status solidi* 255, 1700174 (2018).
161. Shang, J. & Gao, X. Nanoparticle counting: towards accurate determination of the molar concentration. *Chem. Soc. Rev.* 43, 7267–78 (2014).
162. de Assumpção Pereira-da-Silva, M. & Ferri, F. A. Scanning Electron Microscopy. *Nanocharacterization Tech.* 1–35 (2017). doi:10.1016/B978-0-323-49778-7.00001-1
163. Goldstein, J. *et al. Scanning electron microscopy and x-ray microanalysis*. (Springer, 2017).
164. Winey, M., Meehl, J. B., O'Toole, E. T., Giddings, T. H. & Jr. Conventional transmission electron microscopy. *Mol. Biol. Cell* 25, 319–23 (2014).
165. Su, D. Advanced electron microscopy characterization of nanomaterials for catalysis. *Green Energy Environ.* 2, 70–83 (2017).
166. Ercius, P., Alaidi, O., Rames, M. J. & Ren, G. Electron Tomography: A Three-Dimensional Analytic Tool for Hard and Soft Materials Research. *Adv. Mater.* 27, 5638–63 (2015).
167. Kuntsche, J., Horst, J. C. & Bunjes, H. Cryogenic transmission electron microscopy (cryo-TEM) for studying the morphology of colloidal drug delivery systems. *Int. J. Pharm.* 417, 120–137 (2011).
168. Nagamanasa, K. H., Wang, H. & Granick, S. Liquid-Cell Electron Microscopy of Adsorbed Polymers. *Adv. Mater.* 29, 1703555 (2017).
169. Bhushan, B. & Marti, O. Scanning Probe Microscopy — Principle of Operation, Instrumentation, and Probes. in *Nanotribology and Nanomechanics* 41–115 (Springer-Verlag, 2005). doi:10.1007/3-540-28248-3_2
170. Raigoza, A. F., Dugger, J. W. & Webb, L. J. Review: Recent Advances and Current Challenges in Scanning Probe Microscopy of Biomolecular Surfaces and Interfaces. *ACS Appl. Mater. Interfaces* 5, 9249–9261 (2013).
171. Gross, L. Recent advances in submolecular resolution with scanning probe microscopy. *Nat. Chem.* 3, 273–278 (2011).
172. Dufrêne, Y. F. *et al.* Imaging modes of atomic force microscopy for application in molecular and cell biology. *Nat. Nanotechnol. www.nature.com/naturenanotechnology* 12, (2017).
173. Bhushan, B. & Marti, O. Scanning Probe Microscopy — Principle of Operation, Instrumentation, and Probes. in *Nanotribology and Nanomechanics* 41–115 (Springer-Verlag, 2005). doi:10.1007/3-540-28248-3_2
174. Raigoza, A. F., Dugger, J. W. & Webb, L. J. Review: Recent Advances and Current Challenges in Scanning Probe Microscopy of Biomolecular Surfaces and Interfaces. *ACS Appl. Mater. Interfaces* 5, 9249–9261 (2013).
175. Gross, L. Recent advances in submolecular resolution with scanning probe microscopy. *Nat. Chem.* 3,

273–278 (2011).
176. Stetefeld, J., McKenna, S. A. & Patel, T. R. Dynamic light scattering: a practical guide and applications in biomedical sciences. *Biophys. Rev.* 8, 409–427 (2016).
177. Yin, L. Dynamic Light Scattering. in *Nanotechnology Research Methods for Foods and Bioproducts* 145–161 (Wiley-Blackwell, 2012). doi:10.1002/9781118229347.ch8
178. Patravale, V. *et al.* Characterization techniques for nanoparticulate carriers. in *Nanoparticulate Drug Delivery* 87–121 (Elsevier, 2012). doi:10.1533/9781908818195.87
179. Lakowicz, J. R. *Principles of fluorescence spectroscopy*. (Springer, 2006).
180. Deptuła, T., Buitenhuis, J., Jarzębski, M., Patkowski, A. & Gapinski, J. Size of Submicrometer Particles Measured by FCS: Correction of the Confocal Volume. *Langmuir* 31, 6681–6687 (2015).
181. Wajih Al-Soufi, *,† *et al.* Fluorescence Correlation Spectroscopy, a Tool to Investigate Supramolecular Dynamics: Inclusion Complexes of Pyronines with Cyclodextrin. (2005). doi:10.1021/JA0508976
182. Elson, E. L. Fluorescence Correlation Spectroscopy: Past, Present, Future. *Biophys. J.* 101, 2855–2870 (2011).
183. Kolin, D. L. & Wiseman, P. W. Advances in Image Correlation Spectroscopy: Measuring Number Densities, Aggregation States, and Dynamics of Fluorescently labeled Macromolecules in Cells. *Cell Biochem. Biophys.* 49, 141–164 (2007).
184. Brown, C. M. *et al.* Raster image correlation spectroscopy (RICS) for measuring fast protein dynamics and concentrations with a commercial laser scanning confocal microscope. *J. Microsc.* 229, 78–91 (2008).
185. Digman, M. A. *et al.* Fluctuation Correlation Spectroscopy with a Laser-Scanning Microscope: Exploiting the Hidden Time Structure. *Biophys. J.* 88, L33–L36 (2005).
186. Scipioni, L., Di Bona, M., Vicidomini, G., Diaspro, A. & Lanzanò, L. Local raster image correlation spectroscopy generates high-resolution intracellular diffusion maps. *Commun. Biol.* 1, 10 (2018).
187. Shen, H. *et al.* Single Particle Tracking: From Theory to Biophysical Applications. *Chem. Rev.* 117, 7331–7376 (2017).
188. Butler, C., Galland, R., Studer, V. & Sibarita, J.-B. Multicolor 3D Single Particle Tracking using Spectrally Displaced Localization. *Biophys. J.* 112, 296a (2017).
189. Jin, S., Haggie, P. M. & Verkman, A. S. Single-Particle Tracking of Membrane Protein Diffusion in a Potential: Simulation, Detection, and Application to Confined Diffusion of CFTR Cl− Channels. *Biophys. J.* 93, 1079–1088 (2007).
190. Mehrabi, K., Nowack, B., Arroyo Rojas Dasilva, Y. & Mitrano, D. M. Improvements in Nanoparticle Tracking Analysis To Measure Particle Aggregation and Mass Distribution: A Case Study on Engineered Nanomaterial Stability in Incineration Landfill Leachates. *Environ. Sci. Technol.* 51, 5611–5621 (2017).
191. Ribeiro, L. N. de M., Couto, V. M., Fraceto, L. F. & de Paula, E. Use of nanoparticle concentration as a tool to understand the structural properties of colloids. *Sci. Rep.* 8, 982 (2018).
192. Filipe, V., Hawe, A. & Jiskoot, W. Critical evaluation of Nanoparticle Tracking Analysis (NTA) by NanoSight for the measurement of nanoparticles and protein aggregates. *Pharm. Res.* 27, 796–810 (2010).
193. Amendola, V., Pilot, R., Frasconi, M., Maragò, O. M. & Iatì, M. A. Surface plasmon resonance in gold nanoparticles: a review. *J. Phys. Condens. Matter* 29, 203002 (2017).
194. Petryayeva, E. & Krull, U. J. Localized surface plasmon resonance: Nanostructures, bioassays and biosensing—A review. *Anal. Chim. Acta* 706, 8–24 (2011).
195. Stafford, W. Analytical Ultracentrifugation: Sedimentation Velocity Analysis. in *Current Protocols in Protein Science* Chapter 20, 20.7.1-20.7.11 (John Wiley & Sons, Inc., 2003).
196. Planken, K. L. & Cölfen, H. Analytical ultracentrifugation of colloids. *Nanoscale* 2, 1849 (2010).
197. Liu, J. & Shire, S. J. Analytical ultracentrifugation in the pharmaceutical industry. *J. Pharm. Sci.* 88, 1237–1241 (1999).
198. Wiedensohler, A. *et al.* Mobility particle size spectrometers: Calibration procedures and measurement uncertainties. *Aerosol Sci. Technol.* 52, 146–164 (2018).
199. Wiedensohler, A. *et al.* Mobility particle size spectrometers: harmonization of technical standards and data structure to facilitate high quality long-term observations of atmospheric particle number size distributions. *Atmos. Meas. Tech* 5, 657–685 (2012).
200. Roberts, G. S. *et al.* Tunable Nano/Micropores for Particle Detection and Discrimination: Scanning Ion Occlusion Spectroscopy. *Small* 6, 2653–2658 (2010).
201. de Vrij, J. *et al.* Quantification of nanosized extracellular membrane vesicles with scanning ion occlusion sensing. *Nanomedicine* 8, 1443–1458 (2013).
202. Yang, L., Broom, M. F. & Tucker, I. G. Characterization of a Nanoparticulate Drug Delivery System Using Scanning Ion Occlusion Sensing. *Pharm. Res.* 29, 2578–2586 (2012).
203. Pitkänen, L. & Striegel, A. M. Size-exclusion chromatography of metal nanoparticles and quantum dots. *TrAC Trends Anal. Chem.* 80, 311–320 (2016).
204. Karl M. Krueger, Ali M. Al-Somali, Joshua C. Falkner, and & Colvin*, V. L. Characterization of Nanocrystalline CdSe by Size Exclusion Chromatography. (2005). doi:10.1021/AC0481912
205. Hong, P., Koza, S. & Bouvier, E. S. P. Size-Exclusion Chromatography for the Analysis of Protein Biotherapeutics and their Aggregates. *J. Liq. Chromatogr. Relat. Technol.* 35, 2923–2950 (2012).
206. Li, T., Senesi, A. J. & Lee, B. Small Angle X-ray Scattering for Nanoparticle Research. *Chem. Rev.* 116, 11128–11180 (2016).
207. Pauw, B. R., Kästner, C. & Thünemann, A. F. Nanoparticle size distribution quantification: results of a small-angle X-ray scattering inter-laboratory comparison. *J. Appl. Crystallogr.* 50, 1280–1288 (2017).
208. Pau Bernadó, *,†,‡, Efstratios Mylonas, †, Maxim V. Petoukhov, †,§, Martin Blackledge, ⊥ and & Dmitri I. Svergun*, †,§. Structural Characterization of Flexible Proteins Using Small-Angle X-ray Scattering. (2007). doi:10.1021/JA069124N

209. Putnam, C. D., Hammel, M., Hura, G. L. & Tainer, J. A. X-ray solution scattering (SAXS) combined with crystallography and computation: defining accurate macromolecular structures, conformations and assemblies in solution. *Q. Rev. Biophys.* 40, 191–285 (2007).
210. Xiang, Y., Zhang, J. & Liu, C. Verification for Particle Size Distribution of Ultrafine Powders by the SAXS Method. *Mater. Charact.* 44, 435–439 (2000).
211. Walton, K. S. & Snurr, R. Q. Applicability of the BET Method for Determining Surface Areas of Microporous Metal−Organic Frameworks. *J. Am. Chem. Soc.* 129, 8552–8556 (2007).
212. Sing, K. S. W. *et al.* Assessment of Surface Area by Gas Adsorption. in *Adsorption by Powders and Porous Solids* 237–268 (Elsevier, 2014). doi:10.1016/B978-0-08-097035-6.00007-3
213. Fagerlund, G. Determination of specific surface by the BET method. *Matériaux Constr.* 6, 239–245 (1973).
214. Zhang, L. W. *et al.* New insights provided by solvent relaxation NMR-measured surface area in liquids to explain phenolics sorption on silica nanoparticles. *Environ. Sci. Nano* 4, 577–584 (2017).
215. Cooper, C. L., Cosgrove, T., van Duijneveldt, J. S., Murray, M. & Prescott, S. W. The use of solvent relaxation NMR to study colloidal suspensions. *Soft Matter* 9, 7211 (2013).
216. Chen, J. J. *et al.* NMR relaxation and exchange in metal–organic frameworks for surface area screening. *Microporous Mesoporous Mater.* 205, 65–69 (2015).
217. Schladitz, A. *et al.* A concept of an automated function control for ambient aerosol measurements using mobility particle size spectrometers. *Atmos. Meas. Tech.* 7, 1065–1073 (2014).
218. Garratt-Reed, A. J. (Anthony J. . & Bell, D. C. (David C. . *Energy-dispersive X-ray analysis in the electron microscope*. (BIOS, 2003).
219. Goldstein, J. *et al. Scanning electron microscopy and x-ray microanalysis*. (Springer, 2017).
220. Rades, S. *et al.* High-resolution imaging with SEM/T-SEM, EDX and SAM as a combined methodical approach for morphological and elemental analyses of single engineered nanoparticles. *RSC Adv.* 4, 49577–49587 (2014).
221. van Hoek, C. & Koolwijk, M. Conventional wavelength dispersive spectroscopy versus parallel beam spectroscopy – a basic overview. *Microchim. Acta* 161, 287–293 (2008).
222. Hart, J. L. *et al.* Direct Detection Electron Energy-Loss Spectroscopy: A Method to Push the Limits of Resolution and Sensitivity. *Sci. Rep.* 7, 8243 (2017).
223. Raza, S. *et al.* Electron energy-loss spectroscopy of branched gap plasmon resonators. *Nat. Commun.* 7, 13790 (2016).
224. Mattox, D. M. *Handbook of physical vapor deposition (PVD) processing : film formation, adhesion, surface preparation and contamination control*. (Noyes Publications, 1998).
225. Singh, A. K. & Singh, A. K. Experimental Methodologies for the Characterization of Nanoparticles. *Eng. Nanoparticles* 125–170 (2016). doi:10.1016/B978-0-12-801406-6.00004-2
226. Hollander, J. M. & Jolly, W. L. X-ray photoelectron spectroscopy. *Acc. Chem. Res.* 3, 193–200 (1970).
227. Fransson, T. *et al.* X-ray and Electron Spectroscopy of Water. *Chem. Rev.* 116, 7551–7569 (2016).
228. Oswald, S. X-Ray Photoelectron Spectroscopy in Analysis of Surfaces. in *Encyclopedia of Analytical Chemistry* (John Wiley & Sons, Ltd, 2013). doi:10.1002/9780470027318.a2517.pub2
229. 3D electron microscopy in the physical sciences: the development of Z-contrast and EFTEM tomography. *Ultramicroscopy* 96, 413–431 (2003).
230. Kurata, H. Advantages of elemental mapping by high-voltage EFTEM. *Ultramicroscopy* 78, 233–240 (1999).
231. Leapman, R. D. & Aronova, M. A. Localizing Specific Elements Bound to Macromolecules by EFTEM. *Methods Cell Biol.* 79, 593–613 (2007).
232. Pitt, J. J. Principles and applications of liquid chromatography-mass spectrometry in clinical biochemistry. *Clin. Biochem. Rev.* 30, 19–34 (2009).
233. Eigenheer, R. *et al.* Silver nanoparticle protein corona composition compared across engineered particle properties and environmentally relevant reaction conditions. *Environ. Sci. Nano* 1, 238–247 (2014).
234. Büyükköroğlu, G., Dora, D. D., Özdemir, F. & Hızel, C. Techniques for Protein Analysis. *Omi. Technol. Bio-Engineering* 317–351 (2018). doi:10.1016/B978-0-12-804659-3.00015-4
235. Doane, T. L., Chuang, C.-H., Hill, R. J. & Burda, C. Nanoparticle ζ -Potentials. *Acc. Chem. Res.* 45, 317–326 (2012).
236. Bhattacharjee, S. DLS and zeta potential – What they are and what they are not? *J. Control. Release* 235, 337–351 (2016).
237. Kuo, Y.-C. & Chen, I.-C. Evaluation of Surface Charge Density and Surface Potential by Electrophoretic Mobility for Solid Lipid Nanoparticles and Human Brain−Microvascular Endothelial Cells. *J. Phys. Chem. B* 111, 11228–11236 (2007).
238. Dhar, S., Sood, V., Lohiya, G., Devenderan, H. & Katti, D. Role of Physicochemical Properties of Protein in Modulating the Nanoparticle-Bio interface. *bioRxiv* 484972 (2018). doi:10.1101/484972
239. Sakamoto, K. *et al.* Structural Analysis of Formulations. *Cosmet. Sci. Technol.* 635–655 (2017). doi:10.1016/B978-0-12-802005-0.00038-0
240. Gergely, A. *et al.* Hybrid Zinc-Rich Paint Coatings: The Impact of Incorporation of Nano-Size Inhibitor and Electrical Conducting Particles. *Intell. Coatings Corros. Control* 195–249 (2015). doi:10.1016/B978-0-12-411467-8.00006-4
241. Kim, S. H., Woo, K. S., Liu, B. Y. H. & Zachariah, M. R. Method of measuring charge distribution of nanosized aerosols. *J. Colloid Interface Sci.* 282, 46–57 (2005).
242. Flagan, R. C. Continuous-Flow Differential Mobility Analysis of Nanoparticles and Biomolecules. *Annu. Rev. Chem. Biomol. Eng.* 5, 255–279 (2014).
243. Leppä, J., Mui, W., Grantz, A. M. & Flagan, R. C. Charge distribution uncertainty in differential mobility analysis of aerosols. *Aerosol Sci. Technol.* 51, 1168–1189 (2017).

244. McKelvey, K., Kinnear, S. L., Perry, D., Momotenko, D. & Unwin, P. R. Surface Charge Mapping with a Nanopipette. *J. Am. Chem. Soc.* 136, 13735–13744 (2014).
245. Perry, D., Al Botros, R., Momotenko, D., Kinnear, S. L. & Unwin, P. R. Simultaneous Nanoscale Surface Charge and Topographical Mapping. *ACS Nano* 9, 7266–7276 (2015).
246. Shevchuk, A. I. *et al.* Imaging Proteins in Membranes of Living Cells by High-Resolution Scanning Ion Conductance Microscopy. *Angew. Chemie Int. Ed.* 45, 2212–2216 (2006).
247. Zhao, C., Ebeling, D., Siretanu, I., van den Ende, D. & Mugele, F. Extracting local surface charges and charge regulation behavior from atomic force microscopy measurements at heterogeneous solid-electrolyte interfaces. *Nanoscale* 7, 16298–16311 (2015).
248. Butt, H.-J., Cappella, B. & Kappl, M. Force measurements with the atomic force microscope: Technique, interpretation and applications. *Surf. Sci. Rep.* 59, 1–152 (2005).
249. Heinz, W. F. & Hoh, J. H. Relative Surface Charge Density Mapping with the Atomic Force Microscope. *Biophys. J.* 76, 528–538 (1999).
250. Moreau, L. M. *et al.* Defining Crystalline/Amorphous Phases of Nanoparticles through X-ray Absorption Spectroscopy and X-ray Diffraction: The Case of Nickel Phosphide. *Chem. Mater.* 25, 2394–2403 (2013).
251. Vorontsov, A. V. & Tsybulya, S. V. Influence of Nanoparticles Size on XRD Patterns for Small Monodisperse Nanoparticles of Cu^0 and TiO_2 Anatase. *Ind. Eng. Chem. Res.* 57, 2526–2536 (2018).
252. Small, J. A., Michael, J. R. & Bright, D. S. Improving the quality of electron backscatter diffraction (EBSD) patterns from nanoparticles. *J. Microsc.* 206, 170–8 (2002).
253. Inkson, B. J. Scanning electron microscopy (SEM) and transmission electron microscopy (TEM) for materials characterization. *Mater. Charact. Using Nondestruct. Eval. Methods* 17–43 (2016). doi:10.1016/B978-0-08-100040-3.00002-X
254. Zaefferer, S., Elhami, N.-N. & Konijnenberg, P. Electron backscatter diffraction (EBSD) techniques for studying phase transformations in steels. *Phase Transform. Steels* 557–587 (2012). doi:10.1533/9780857096111.4.557
255. Welker, R. W. Size Analysis and Identification of Particles. *Dev. Surf. Contam. Clean.* 179–213 (2012). doi:10.1016/B978-1-4377-7883-0.00004-3
256. Njuguna, J. & Sachse, S. Measurement and sampling techniques for characterization of airborne nanoparticles released from nano-enhanced products. *Heal. Environ. Saf. Nanomater.* 78–111 (2014). doi:10.1533/9780857096678.2.78
257. Peters, T. M., Park, J. Y. & Raynor, P. C. Assessing and Managing Exposures to Nanomaterials in the Workplace. *Assess. Nanoparticle Risks to Hum. Heal.* 21–44 (2016). doi:10.1016/B978-0-323-35323-6.00002-5
258. Doane, T. & Burda, C. Nanoparticle mediated non-covalent drug delivery. *Adv. Drug Deliv. Rev.* 65, 607–21 (2013).
259. Walkey, C. D. & Chan, W. C. W. Understanding and controlling the interaction of nanomaterials with proteins in a physiological environment. *Chem. Soc. Rev.* 41, 2780–99 (2012).
260. Zhang, X.-Q. *et al.* Interactions of nanomaterials and biological systems: Implications to personalized nanomedicine. *Adv. Drug Deliv. Rev.* 64, 1363–1384 (2012).
261. Sharifi, S. *et al.* Toxicity of nanomaterials. *Chem. Soc. Rev.* 41, 2323–43 (2012).
262. Behzadi, S. *et al.* Cellular uptake of nanoparticles: journey inside the cell. *Chem. Soc. Rev.* 46, 4218–4244 (2017).
263. Stark, W. J. Nanoparticles in Biological Systems. *Angew. Chemie Int. Ed.* 50, 1242–1258 (2011).
264. Limbach, L. K. *et al.* Oxide nanoparticle uptake in human lung fibroblasts: effects of particle size, agglomeration, and diffusion at low concentrations. *Environ. Sci. Technol.* 39, 9370–9376 (2005).
265. Studer, A. M. *et al.* Nanoparticle cytotoxicity depends on intracellular solubility: comparison of stabilized copper metal and degradable copper oxide nanoparticles. *Toxicol. Lett.* 197, 169–174 (2010).
266. Treuel, L., Jiang, X. & Nienhaus, G. U. New views on cellular uptake and trafficking of manufactured nanoparticles. *J. R. Soc. Interface* 10, 20120939 (2013).
267. Ji, Z. *et al.* Designed synthesis of CeO2 nanorods and nanowires for studying toxicological effects of high aspect ratio nanomaterials. *ACS Nano* 6, 5366–5380 (2012).
268. Jacob, S. J. P., Mohammed, H., Murali, K. & Kamarudeen, M. Synthesis of silver nanorods using Coscinium fenestratum extracts and its cytotoxic activity against Hep-2 cell line. *Colloids Surf. B. Biointerfaces* 98, 7–11 (2012).
269. Ivanova, E. P. *et al.* Natural bactericidal surfaces: mechanical rupture of Pseudomonas aeruginosa cells by cicada wings. *Small* 8, 2489–2494 (2012).
270. Pogodin, S. *et al.* Biophysical Model of Bacterial Cell Interactions with Nanopatterned Cicada Wing Surfaces. *Biophys. J.* 104, 835–840 (2013).
271. Rosenblum, D., Joshi, N., Tao, W., Karp, J. M. & Peer, D. Progress and challenges towards targeted delivery of cancer therapeutics. *Nat. Commun.* 9, 1410 (2018).
272. Senapati, S., Mahanta, A. K., Kumar, S. & Maiti, P. Controlled drug delivery vehicles for cancer treatment and their performance. *Signal Transduct. Target. Ther.* 3, 7 (2018).
273. Tran, S., DeGiovanni, P.-J., Piel, B. & Rai, P. Cancer nanomedicine: a review of recent success in drug delivery. *Clin. Transl. Med.* 6, 44 (2017).
274. Demchick, P. & Koch, A. L. The permeability of the wall fabric of Escherichia coli and Bacillus subtilis. *J. Bacteriol.* 178, 768–73 (1996).
275. Fuerst, J. A. & Sagulenko, E. Protein uptake by bacteria. *Commun. Integr. Biol.* 3, 572–575 (2010).
276. Brunner, T. J. *et al.* In vitro cytotoxicity of oxide nanoparticles: comparison to asbestos, silica, and the effect of particle solubility. *Environ. Sci. Technol.* 40, 4374–81 (2006).
277. Contini, C., Schneemilch, M., Gaisford, S. & Quirke, N. Nanoparticle–membrane interactions. *J. Exp. Nanosci.* 13, 62–81 (2018).

278. Geiser, M. *et al.* Ultrafine Particles Cross Cellular Membranes by Nonphagocytic Mechanisms in Lungs and in Cultured Cells. *Environ. Health Perspect.* 113, 1555–1560 (2005).
279. Barbara M. Rothen-Rutishauser, *,‡, Samuel Schürch, §, Beat Haenni, ‡, Nadine Kapp, ⊥ and & Gehr‡, P. Interaction of Fine Particles and Nanoparticles with Red Blood Cells Visualized with Advanced Microscopic Techniques†. (2006). doi:10.1021/ES0522635
280. Wang, T., Bai, J., Jiang, X. & Nienhaus, G. U. Cellular Uptake of Nanoparticles by Membrane Penetration: A Study Combining Confocal Microscopy with FTIR Spectroelectrochemistry. *ACS Nano* 6, 1251–1259 (2012).
281. Vincent, M., Duval, R. E., Hartemann, P. & Engels-Deutsch, M. Contact killing and antimicrobial properties of copper. *J. Appl. Microbiol.* 124, 1032–1046 (2018).
282. Mathews, S., Hans, M., Mücklich, F. & Solioz, M. Contact killing of bacteria on copper is suppressed if bacterial-metal contact is prevented and is induced on iron by copper ions. *Appl. Environ. Microbiol.* 79, 2605–11 (2013).
283. Sondi, I. & Salopek-Sondi, B. Silver nanoparticles as antimicrobial agent: a case study on E. coli as a model for Gram-negative bacteria. *J. Colloid Interface Sci.* 275, 177–182 (2004).
284. Hans, M., Mathews, S., Mücklich, F. & Solioz, M. Physicochemical properties of copper important for its antibacterial activity and development of a unified model. *Biointerphases* 11, 018902 (2016).
285. Vincent, M., Hartemann, P. & Engels-Deutsch, M. Antimicrobial applications of copper. *Int. J. Hyg. Environ. Health* 219, 585–591 (2016).
286. Slavin, Y. N., Asnis, J., Häfeli, U. O. & Bach, H. Metal nanoparticles: understanding the mechanisms behind antibacterial activity. *J. Nanobiotechnology* 15, 65 (2017).
287. Tao, B. *et al.* Copper-nanoparticle-embedded hydrogel for killing bacteria and promoting wound healing with photothermal therapy. *J. Mater. Chem. B* 7, 2534–2548 (2019).
288. Agnihotri, S., Mukherji, S. & Mukherji, S. Immobilized silver nanoparticles enhance contact killing and show highest efficacy: elucidation of the mechanism of bactericidal action of silver. *Nanoscale* 5, 7328 (2013).
289. Zhi Li, †, Daeyeon Lee, ‡, Xiaoxia Sheng, †, Robert E. Cohen, *,‡ and & Michael F. Rubner*, †. Two-Level Antibacterial Coating with Both Release-Killing and Contact-Killing Capabilities. (2006). doi:10.1021/LA0622166
290. Li, Y. *et al.* Rational Design of Silver Gradient for Studying Size Effect of Silver Nanoparticles on Contact Killing. *ACS Biomater. Sci. Eng.* 5, 425–431 (2019).
291. Wybrańska, K. *et al.* Gold–Oxoborate Nanocomposites and Their Biomedical Applications. *ACS Appl. Mater. Interfaces* 7, 3931–3939 (2015).
292. Hajipour, M. J. *et al.* Antibacterial properties of nanoparticles. *Trends Biotechnol.* 30, 499–511 (2012).
293. Nel, A., Xia, T., Mädler, L. & Li, N. Toxic potential of materials at the nanolevel. *Science* 311, 622–627 (2006).
294. Xia, Q., Hwang, H.-M., Ray, P. C. & Yu, H. Mechanisms of nanotoxicity: Generation of reactive oxygen species. *J. Food Drug Anal.* 22, 64–75 (2014).
295. Walters, C., Pool, E. & Somerset, V. Nanotoxicology: A Review. in *Toxicology - New Aspects to This Scientific Conundrum* (InTech, 2016). doi:10.5772/64754
296. Lewinski, N., Colvin, V. & Drezek, R. Cytotoxicity of Nanoparticles. *Small* 4, 26–49 (2008).
297. Oberdörster, G., Oberdörster, E. & Oberdörster, J. Nanotoxicology: An Emerging Discipline Evolving from Studies of Ultrafine Particles. *Environ. Health Perspect.* 113, 823–839 (2005).
298. Eyckmans, J., Boudou, T., Yu, X. & Chen, C. S. A Hitchhiker's Guide to Mechanobiology. *Dev. Cell* 21, 35–47 (2011).
299. Perez, R. A. *et al.* Biomaterials control of pluripotent stem cell fate for regenerative therapy. *Prog. Mater. Sci.* 82, 234–293 (2016).
300. Discher, D. E., Janmey, P. & Wang, Y.-L. Tissue cells feel and respond to the stiffness of their substrate. *Science* 310, 1139–1143 (2005).
301. Kurniawan, N. A., Chaudhuri, P. K. & Lim, C. T. Mechanobiology of cell migration in the context of dynamic two-way cell–matrix interactions. *J. Biomech.* 49, 1355–1368 (2016).
302. Spill, F., Reynolds, D. S., Kamm, R. D. & Zaman, M. H. Impact of the physical microenvironment on tumor progression and metastasis. *Curr. Opin. Biotechnol.* 40, 41–48 (2016).
303. Wang, N., Butler, J. P. & Ingber, D. E. Mechanotransduction across the cell surface and through the cytoskeleton. *Science* 260, 1124–7 (1993).
304. Pelham, R. J. & Wang, Y. l. Cell locomotion and focal adhesions are regulated by substrate flexibility. *Proc. Natl. Acad. Sci. U. S. A.* 94, 13661–5 (1997).
305. Engler, A. J., Sen, S., Sweeney, H. L. & Discher, D. E. Matrix Elasticity Directs Stem Cell Lineage Specification. *Cell* 126, 677–689 (2006).
306. Janmey, P. A. & McCulloch, C. A. Cell mechanics: integrating cell responses to mechanical stimuli. *Annu. Rev. Biomed. Eng.* 9, 1–34 (2007).
307. Johannes, L. & Mayor, S. Induced domain formation in endocytic invagination, lipid sorting, and scission. *Cell* 142, 507–10 (2010).
308. Alber, F. *et al.* Determining the architectures of macromolecular assemblies. *Nature* 450, 683–694 (2007).
309. Aruguete, D. M. & Hochella, M. F. Bacteria - nanoparticle interactions and their environmental implications. *Environ. Chem.* 7, 3 (2010).
310. Meng, H. *et al.* Aspect Ratio Determines the Quantity of Mesoporous Silica Nanoparticle Uptake by a Small GTPase-Dependent Macropinocytosis Mechanism. *ACS Nano* 5, 4434–4447 (2011).
311. Chithrani, B. D. & Chan, W. C. W. Elucidating the Mechanism of Cellular Uptake and Removal of Protein-Coated Gold Nanoparticles of Different Sizes and Shapes. *Nano Lett.* 7, 1542–1550 (2007).
312. Champion, J. A. & Mitragotri, S. Shape Induced Inhibition of Phagocytosis of Polymer Particles. *Pharm.*

Res. 26, 244–249 (2009).
313. Chithrani, B. D., Ghazani, A. A. & Chan, W. C. W. Determining the Size and Shape Dependence of Gold Nanoparticle Uptake into Mammalian Cells. *Nano Lett.* 6, 662–668 (2006).
314. Qiu, Y. *et al.* Surface chemistry and aspect ratio mediated cellular uptake of Au nanorods. *Biomaterials* 31, 7606–7619 (2010).
315. Oberdörster, G., Stone, V. & Donaldson, K. Toxicology of nanoparticles: A historical perspective. *Nanotoxicology* 1, 2–25 (2007).
316. Wang, X. *et al.* Dispersal State of Multiwalled Carbon Nanotubes Elicits Profibrogenic Cellular Responses That Correlate with Fibrogenesis Biomarkers and Fibrosis in the Murine Lung. *ACS Nano* 5, 9772–9787 (2011).
317. Nel, A. E. *et al.* Understanding biophysicochemical interactions at the nano–bio interface. *Nat. Mater.* 8, 543–557 (2009).
318. Kostarelos, K. *et al.* Cellular uptake of functionalized carbon nanotubes is independent of functional group and cell type. *Nat. Nanotechnol.* 2, 108–113 (2007).
319. Velzeboer, I., Hendriks, A. J., Ragas, A. M. J. & van de Meent, D. Aquatic ecotoxicity tests of some nanomaterials. *Environ. Toxicol. Chem.* 27, 1942 (2008).
320. Brown, D. M., Wilson, M. R., MacNee, W., Stone, V. & Donaldson, K. Size-Dependent Proinflammatory Effects of Ultrafine Polystyrene Particles: A Role for Surface Area and Oxidative Stress in the Enhanced Activity of Ultrafines. *Toxicol. Appl. Pharmacol.* 175, 191–199 (2001).
321. C. L. Tran, D. Buchanan, R. T. Cull, C. L. *et al.* Inhalation of poorly soluble particles. II. Influence Of particle surface area on inflammation and clearance. *Inhal. Toxicol.* 12, 1113–1126 (2000).
322. Oberdörster, G., Ferin, J., Gelein, R., Soderholm, S. C. & Finkelstein, J. Role of the alveolar macrophage in lung injury: studies with ultrafine particles. *Environ. Health Perspect.* 97, 193–9 (1992).
323. Powers, K. W. *et al.* Research Strategies for Safety Evaluation of Nanomaterials. Part VI. Characterization of Nanoscale Particles for Toxicological Evaluation. *Toxicol. Sci.* 90, 296–303 (2006).
324. Zhu, M. *et al.* Physicochemical Properties Determine Nanomaterial Cellular Uptake, Transport, and Fate. *Acc. Chem. Res.* 46, 622–631 (2013).
325. MENG, H. *et al.* Ultrahigh reactivity provokes nanotoxicity: Explanation of oral toxicity of nano-copper particles. *Toxicol. Lett.* 175, 102–110 (2007).
326. Wang, L. *et al.* Selective Targeting of Gold Nanorods at the Mitochondria of Cancer Cells: Implications for Cancer Therapy. *Nano Lett.* 11, 772–780 (2011).
327. Kim, J. A., Åberg, C., Salvati, A. & Dawson, K. A. Role of cell cycle on the cellular uptake and dilution of nanoparticles in a cell population. *Nat. Nanotechnol.* 7, 62–68 (2012).
328. Summers, H. D. *et al.* Statistical analysis of nanoparticle dosing in a dynamic cellular system. *Nat. Nanotechnol.* 6, 170–174 (2011).
329. Liu, Y.-Y. *et al.* Emergence of plasmid-mediated colistin resistance mechanism MCR-1 in animals and human beings in China: a microbiological and molecular biological study. *Lancet Infect. Dis.* (2015). doi:10.1016/S1473-3099(15)00424-7
330. Zhang, Q. *et al.* Acceleration of Emergence of Bacterial Antibiotic Resistance in Connected Microenvironments. *Science (80-.).* 333, 1764–1767 (2011).
331. Ventola, C. L. The antibiotic resistance crisis: part 1: causes and threats. *P T* 40, 277–83 (2015).
332. Rai, M. K., Deshmukh, S. D., Ingle, A. P. & Gade, A. K. Silver nanoparticles: the powerful nanoweapon against multidrug-resistant bacteria. *J. Appl. Microbiol.* 112, 841–852 (2012).
333. Haider, A., Kang, I.-K., Haider, A. & Kang, I.-K. Preparation of Silver Nanoparticles and Their Industrial and Biomedical Applications: A Comprehensive Review, Preparation of Silver Nanoparticles and Their Industrial and Biomedical Applications: A Comprehensive Review. *Adv. Mater. Sci. Eng. Adv. Mater. Sci. Eng.* 2015, 2015, e165257 (2015).
334. Rauwel, P. *et al.* Silver Nanoparticles: Synthesis, Properties, and Applications, Silver Nanoparticles: Synthesis, Properties, and Applications. *Adv. Mater. Sci. Eng. Adv. Mater. Sci. Eng.* 2015, 2015, e624394 (2015).
335. de Lima, R., Seabra, A. B. & Durán, N. Silver nanoparticles: a brief review of cytotoxicity and genotoxicity of chemically and biogenically synthesized nanoparticles. *J. Appl. Toxicol. JAT* 32, 867–879 (2012).
336. Hendry, A. T. & Stewart, I. O. Silver-resistant Enterobacteriaceae from hospital patients. *Can. J. Microbiol.* 25, 915–921 (1979).
337. Li, X. Z., Nikaido, H. & Williams, K. E. Silver-resistant mutants of Escherichia coli display active efflux of Ag+ and are deficient in porins. *J. Bacteriol.* 179, 6127–6132 (1997).
338. Gupta, A. & Silver, S. Silver as a biocide: will resistance become a problem? *Nat. Biotechnol.* 16, 888 (1998).
339. Hajipour, M. J. *et al.* Antibacterial properties of nanoparticles. *Trends Biotechnol.* 30, 499–511 (2012).
340. Cady, N. C., Behnke, J. L. & Strickland, A. D. Copper-Based Nanostructured Coatings on Natural Cellulose: Nanocomposites Exhibiting Rapid and Efficient Inhibition of a Multi-Drug Resistant Wound Pathogen, A. baumannii, and Mammalian Cell Biocompatibility In Vitro. *Adv. Funct. Mater.* 21, 2506–2514 (2011).
341. Lichter, J. A. & Rubner, M. F. Polyelectrolyte Multilayers with Intrinsic Antimicrobial Functionality: The Importance of Mobile Polycations. *Langmuir* 25, 7686–7694 (2009).
342. Tripathy, A., Sen, P., Su, B. & Briscoe, W. H. Natural and bioinspired nanostructured bactericidal surfaces. *Adv. Colloid Interface Sci.* 248, 85–104 (2017).
343. Yamamoto, O. Influence of particle size on the antibacterial activity of zinc oxide. *Int. J. Inorg. Mater.* 3, 643–646 (2001).
344. Pan, Y. *et al.* Size-dependent cytotoxicity of gold nanoparticles. *Small* 3, 1941–1949 (2007).
345. Raghupathi, K. R., Koodali, R. T. & Manna, A. C. Size-dependent bacterial growth inhibition and

mechanism of antibacterial activity of zinc oxide nanoparticles. *Langmuir ACS J. surfaces colloids* 27, 4020–4028 (2011).
346. Vijayakumar, S. & Ganesan, S. Size-dependent in vitro cytotoxicity assay of gold nanoparticles. *Toxicol. Environ. Chem.* 95, 277–287 (2013).
347. He, C., Hu, Y., Yin, L., Tang, C. & Yin, C. Effects of particle size and surface charge on cellular uptake and biodistribution of polymeric nanoparticles. *Biomaterials* 31, 3657–3666 (2010).
348. Smitha, S. L., Gopchandran, K. G., Nair, N. R., Nampoothiri, K. M. & Ravindran, T. R. SERS and Antibacterial Active Green Synthesized Gold Nanoparticles. *Plasmonics* 7, 515–524 (2012).
349. Zhang, Y., Xu, D., Li, W., Yu, J. & Chen, Y. Effect of Size, Shape, and Surface Modification on Cytotoxicity of Gold Nanoparticles to Human HEp-2 and Canine MDCK Cells. *J. Nanomater.* 2012, 7:7–7:7 (2012).
350. Fan, Z. *et al.* Deciphering an Underlying Mechanism of Differential Cellular Effects of Nanoparticles: An Example of Bach-1 Dependent Induction of HO-1 Expression by Gold Nanorod. *Biointerphases* 7, 1–8 (2012).
351. Rago, I. *et al.* Zinc oxide microrods and nanorods: different antibacterial activity and their mode of action against Gram-positive bacteria. *RSC Adv.* 4, 56031–56040 (2014).
352. Schaeublin, N. M. *et al.* Does shape matter? Bioeffects of gold nanomaterials in a human skin cell model. *Langmuir ACS J. surfaces colloids* 28, 3248–3258 (2012).
353. Bhattacharya, D., Santra, C. R., Ghosh, A. N. & Karmakar, P. Differential toxicity of rod and spherical zinc oxide nanoparticles on human peripheral blood mononuclear cells. *J. Biomed. Nanotechnol.* 10, 707–716 (2014).
354. Jain, A., Bhargava, R. & Poddar, P. Probing interaction of Gram-positive and Gram-negative bacterial cells with ZnO nanorods. *Mater. Sci. Eng. C* 33, 1247–1253 (2013).
355. Reddy, K. M. *et al.* Selective toxicity of zinc oxide nanoparticles to prokaryotic and eukaryotic systems. *Appl. Phys. Lett.* 90, 2139021–2139023 (2007).
356. Wahab, R., Mishra, A., Yun, S.-I., Kim, Y.-S. & Shin, H.-S. Antibacterial activity of ZnO nanoparticles prepared via non-hydrolytic solution route. *Appl. Microbiol. Biotechnol.* 87, 1917–1925 (2010).
357. Xiong, H.-M. *et al.* Bonding Polyether onto ZnO Nanoparticles: An Effective Method for Preparing Polymer Nanocomposites with Tunable Luminescence and Stable Conductivity. *Adv. Funct. Mater.* 15, 1751–1756 (2005).
358. Xiong, H.-M., Xu, Y., Ren, Q.-G. & Xia, Y.-Y. Stable aqueous ZnO@polymer core-shell nanoparticles with tunable photoluminescence and their application in cell imaging. *J. Am. Chem. Soc.* 130, 7522–7523 (2008).
359. Rosi, N. L. & Mirkin, C. A. Nanostructures in biodiagnostics. *Chem. Rev.* 105, 1547–1562 (2005).
360. Bagnall, D. M. *et al.* High temperature excitonic stimulated emission from ZnO epitaxial layers. *Appl. Phys. Lett.* 73, 1038–1040 (1998).
361. Reynolds, D. C., Look, D. C. & Jogai, B. Optically pumped ultraviolet lasing from ZnO. *Solid State Commun.* 99, 873–875 (1996).
362. Kaneko, M. & Okura, I. *Photocatalysis: Science and Technology*. (Springer Berlin Heidelberg, 2002).
363. Szabó, T., Németh, J. & Dékány, I. Zinc oxide nanoparticles incorporated in ultrathin layer silicate films and their photocatalytic properties. *Colloids Surfaces A Physicochem. Eng. Asp.* 230, 23–35 (2003).
364. Gordillo, G. & Calderón, C. Properties of ZnO thin films prepared by reactive evaporation. *Sol. Energy Mater. Sol. Cells* 69, 251–260 (2001).
365. Ryu, H.-W. *et al.* ZnO sol–gel derived porous film for CO gas sensing. *Sensors Actuators B Chem.* 96, 717–722 (2003).
366. Zhao, L.-H., Zhang, R., Zhang, J. & Sun, S.-Q. Synthesis and characterization of biocompatible ZnO nanoparticles. *CrystEngComm* 14, 945–950 (2012).
367. and, Y. C. C. & Chen*, L. J. ZnO Nanoneedles with Enhanced and Sharp Ultraviolet Cathodoluminescence Peak. (2006). doi:10.1021/JP066786Q
368. Sirelkhatim, A. *et al.* Review on Zinc Oxide Nanoparticles: Antibacterial Activity and Toxicity Mechanism. *Nano-Micro Lett.* 7, 219–242 (2015).
369. Arakha, M., Saleem, M., Mallick, B. C. & Jha, S. The effects of interfacial potential on antimicrobial propensity of ZnO nanoparticle. *Sci. Rep.* 5, 9578 (2015).
370. Yamamoto, O., Komatsu, M., Sawai, J. & Nakagawa, Z. Effect of lattice constant of zinc oxide on antibacterial characteristics. *J. Mater. Sci. Mater. Med.* 15, 847–851 (2004).
371. Scherrer, P. Bestimmung der größe und der inneren struktur von kolloidteilchen mittels röntgenstrahlen. *Nachrichten von der Gesellschaft der Wissenschaften zu Göttingen, Math. Klasse* 1918, 98–100
372. Patterson, A. L. The Scherrer formula for X-Ray particle size determination. *Phys. Rev.* 56, 978–982 (1939).
373. Reed, R. B., Ladner, D. A., Higgins, C. P., Westerhoff, P. & Ranville, J. F. Solubility of nano-zinc oxide in environmentally and biologically important matrices. *Environ. Toxicol. Chem.* 31, 93–9 (2012).
374. Wong, S. W. Y., Leung, P. T. Y., Djurišić, A. B. & Leung, K. M. Y. Toxicities of nano zinc oxide to five marine organisms: influences of aggregate size and ion solubility. *Anal. Bioanal. Chem.* 396, 609–618 (2010).
375. Franklin, N. M. *et al.* Comparative Toxicity of Nanoparticulate ZnO, Bulk ZnO, and $ZnCl_2$ to a Freshwater Microalga (Pseudokirchneriella subcapitata): The Importance of Particle Solubility. *Environ. Sci. Technol.* 41, 8484–8490 (2007).
376. David, C. A. *et al.* Dissolution Kinetics and Solubility of ZnO Nanoparticles Followed by AGNES. *J. Phys. Chem. C* 116, 11758–11767 (2012).
377. Mudunkotuwa, I. A., Rupasinghe, T., Wu, C.-M. & Grassian, V. H. Dissolution of ZnO Nanoparticles at Circumneutral pH: A Study of Size Effects in the Presence and Absence of Citric Acid. *Langmuir* 28, 396–403 (2012).
378. Bian, S.-W., Mudunkotuwa, I. A., Rupasinghe, T. & Grassian, V. H. Aggregation and Dissolution of 4 nm ZnO Nanoparticles in Aqueous Environments: Influence of pH, Ionic Strength, Size, and Adsorption of

Humic Acid. *Langmuir* 27, 6059–6068 (2011).
379. Li, Z., Lee, D., Sheng, X., Cohen, R. E. & Rubner, M. F. Two-Level Antibacterial Coating with Both Release-Killing and Contact-Killing Capabilities. *Langmuir* 22, 9820–9823 (2006).
380. Blindauer, C. A. Advances in the molecular understanding of biological zinc transport. *Chem. Commun.* 51, 4544–4563 (2015).
381. Mikhaylina, A., Ksibe, A. Z., Scanlan, D. J. & Blindauer, C. A. Bacterial zinc uptake regulator proteins and their regulons. *Biochem. Soc. Trans.* 46, 983–1001 (2018).
382. Botstein, D., Chervitz, S. A. & Cherry, J. M. Yeast as a model organism. *Science* 277, 1259–60 (1997).
383. Lesage, G. & Bussey, H. Cell wall assembly in Saccharomyces cerevisiae. *Microbiol. Mol. Biol. Rev.* 70, 317–43 (2006).
384. Nicola, R. De & Walker, G. Interaction Between Yeasts and Zinc. in *Yeast Biotechnology: Diversity and Applications* 237–257 (Springer Netherlands, 2009). doi:10.1007/978-1-4020-8292-4_12
385. Roberta Brayner, *,† *et al.* Toxicological Impact Studies Based on Escherichia coli Bacteria in Ultrafine ZnO Nanoparticles Colloidal Medium. (2006). doi:10.1021/NL052326H
386. Waldemar, V. Murein Peptide Amidase MpaA. *Handb. Proteolytic Enzym.* 1383–1385 (2013). doi:10.1016/B978-0-12-382219-2.00310-0
387. Silhavy, T. J., Kahne, D. & Walker, S. The Bacterial Cell Envelope. *Cold Spring Harb. Perspect. Biol.* 2, (2010).
388. Schumann, P. Peptidoglycan Structure. *Methods Microbiol.* 38, 101–129 (2011).
389. Huang, K. C., Mukhopadhyay, R., Wen, B., Gitai, Z. & Wingreen, N. S. Cell shape and cell-wall organization in Gram-negative bacteria. *Proc. Natl. Acad. Sci.* pnas.0805309105 (2008). doi:10.1073/pnas.0805309105
390. Díaz-Mejía, J. J., Babu, M. & Emili, A. Computational and experimental approaches to chart the Escherichia coli cell-envelope-associated proteome and interactome. *FEMS Microbiol. Rev.* 33, 66–97 (2009).
391. Matuła, K. *et al.* Influence of nanomechanical stress induced by ZnO nanoparticles of different shapes on the viability of cells. *Soft Matter* 12, 4162–9 (2016).
392. Pelling, A. E., Veraitch, F. S., Chu, C. P.-K., Mason, C. & Horton, M. A. Mechanical dynamics of single cells during early apoptosis. *Cell Motil. Cytoskeleton* 66, 409–422 (2009).
393. Stankic, S., Suman, S., Haque, F. & Vidic, J. Pure and multi metal oxide nanoparticles: synthesis, antibacterial and cytotoxic properties. *J. Nanobiotechnology* 14, 73 (2016).
394. Stanković, A., Dimitrijević, S. & Uskoković, D. Influence of size scale and morphology on antibacterial properties of ZnO powders hydrothemally synthesized using different surface stabilizing agents. *Colloids Surfaces B Biointerfaces* 102, 21–28 (2013).
395. Ramani, M., Ponnusamy, S. & Muthamizhchelvan, C. From zinc oxide nanoparticles to microflowers: A study of growth kinetics and biocidal activity. *Mater. Sci. Eng. C* 32, 2381–2389 (2012).
396. Åkerström, B., Bratt, T. & Enghild, J. J. Formation of the α1-microglobulin chromophore in mammalian and insect cells: a novel post-translational mechanism? *FEBS Lett.* 362, 50–54 (1995).
397. Lam, S. J. *et al.* Combating multidrug-resistant Gram-negative bacteria with structurally nanoengineered antimicrobial peptide polymers. *Nat. Microbiol.* 1, 16162 (2016).
398. Legendre, D., Zenit, R., Daniel, C. & Guiraud, P. A note on the modelling of the bouncing of spherical drops or solid spheres on a wall in viscous fluid. *Chem. Eng. Sci.* 61, 3543–3549 (2006).
399. Lan, G., Wolgemuth, C. W. & Sun, S. X. Z-ring force and cell shape during division in rod-like bacteria. *Proc. Natl. Acad. Sci. U. S. A.* 104, 16110–5 (2007).
400. Yoshimura, H. N., Molisani, A. L., Narita, N. E., Manholetti, J. L. A. & Cavenagho, J. M. Mechanical properties and microstructure of zinc oxide varistor ceramics. *Mater. Sci. forum* 530–31, 408–413
401. Gumbart, J. C., Beeby, M., Jensen, G. J. & Roux, B. Escherichia coli peptidoglycan structure and mechanics as predicted by atomic-scale simulations. *PLoS Comput. Biol.* 10, e1003475 (2014).
402. Sneddon, I. N. The relation between load and penetration in the axisymmetric boussinesq problem for a punch of arbitrary profile. *Int. J. Eng. Sci.* 3, 47–57 (1965).
403. Cayley, D. S., Guttman, H. J. & Record, Jr., M. T. Biophysical characterization of changes in amounts and activity of Escherichia coli cell and compartment water and turgor pressure in response to osmotic stress. *Biophys. J.* 78, 1748–1764 (2000).
404. Liu, S. *et al.* Antibacterial action of dispersed single-walled carbon nanotubes on Escherichia coli and Bacillus subtilis investigated by atomic force microscopy. *Nanoscale* 2, 2744 (2010).
405. Coico, R. Gram Staining. in *Current Protocols in Microbiology* Appendix 3, Appendix 3C (John Wiley & Sons, Inc., 2005).
406. Eltsov, M. & Zuber, B. Transmission electron microscopy of the bacterial nucleoid. *J. Struct. Biol.* 156, 246–254 (2006).
407. Wade, H. E. Variation in the Phosphorus Content of Escherichia coli during Cultivation. *J. Gen. Microbiol.* 7, 24–30 (1952).
408. Braun, V. Iron uptake by Escherichia coli. *Front. Biosci.* 8, s1409-21 (2003).
409. Andrews, S. C., Robinson, A. K. & Rodríguez-Quiñones, F. Bacterial iron homeostasis. *FEMS Microbiol. Rev.* 27, 215–237 (2003).
410. Kan, S. B. J., Lewis, R. D., Chen, K. & Arnold, F. H. Directed evolution of cytochrome c for carbon-silicon bond formation: Bringing silicon to life. *Science* 354, 1048–1051 (2016).
411. Kohanski, M. A., Dwyer, D. J. & Collins, J. J. How antibiotics kill bacteria: from targets to networks. *Nat. Rev. Microbiol.* 8, 423–35 (2010).
412. Andrews, J. M. Determination of minimum inhibitory concentrations. *J. Antimicrob. Chemother.* 48, 5–16 (2001).
413. Citron, D. M., Ostovari, M. I., Karlsson, A. & Goldstein, E. J. Evaluation of the E test for susceptibility testing

of anaerobic bacteria. *J. Clin. Microbiol.* 29, 2197–2203 (1991).
414. Tipper, D. J. Mode of action of beta-lactam antibiotics. *Pharmacol. Ther.* 27, 1–35 (1985).
415. Ampicillin. *DrugBank*
416. Stone, K. J. & Strominger, J. L. Mechanism of action of bacitracin: complexation with metal ion and C 55 -isoprenyl pyrophosphate. *Proc. Natl. Acad. Sci. U. S. A.* 68, 3223–7 (1971).
417. Bacitracin. *DrugBank*
418. Truesdell, S. E., Zurenko, G. E. & Laborde, A. L. Interaction of cephalosporins with penicillin-binding proteins of methicillin-resistant Staphylococcus aureus. *J. Antimicrob. Chemother.* 23 Suppl D, 13–9 (1989).
419. Yotsuji, A. *et al.* Mechanism of action of cephalosporins and resistance caused by decreased affinity for penicillin-binding proteins in Bacteroides fragilis. *Antimicrob. Agents Chemother.* 32, 1848–53 (1988).
420. Hoerr, V. *et al.* Characterization and prediction of the mechanism of action of antibiotics through NMR metabolomics. *BMC Microbiol.* 16, 82 (2016).
421. Misumi, M. & Tanaka, N. Mechanism of inhibition of translocation by kanamycin and viomycin: a comparative study with fusidic acid. *Biochem. Biophys. Res. Commun.* 92, 647–54 (1980).
422. Colistin. *DrugBank*
423. Alekseev, V. G., Larin, S. V., Shigina, O. Y. & Shcherbakova, E. E. Interaction of ampicillin with zinc and cadmium ions in aqueous solutions. *Russ. J. Gen. Chem.* 76, 317–320 (2006).
424. Engberg, R. M., Hedemann, M. S., Leser, T. D. & Jensen, B. B. Effect of zinc bacitracin and salinomycin on intestinal microflora and performance of broilers. *Poult. Sci.* 79, 1311–9 (2000).
425. Sohnle, P. G. & Hahn, B. L. Effect of zinc-reversible growth-inhibitory activity in human empyema fluid on antibiotic microbicidal activity. *Antimicrob. Agents Chemother.* 44, 139–42 (2000).
426. Sha, S. H., Zajic, G., Epstein, C. J. & Schacht, J. Overexpression of copper/zinc-superoxide dismutase protects from kanamycin-induced hearing loss. *Audiol. Neurootol.* 6, 117–23
427. Stojanoski, V. *et al.* Structure of the catalytic domain of the colistin resistance enzyme MCR-1. *BMC Biol.* 14, 81 (2016).
428. Cuervo, A. & Carrascosa, J. L. Bacteriophages: Structure. in *eLS* (John Wiley & Sons, Ltd, 2012). doi:10.1002/9780470015902.a0024053
429. González-García, V. A. *et al.* Characterization of the initial steps in the T7 DNA ejection process. *Bacteriophage* 5, e1056904 (2015).
430. Bertozzi Silva, J., Storms, Z. & Sauvageau, D. Host receptors for bacteriophage adsorption. *FEMS Microbiol. Lett.* 363, fnw002 (2016).
431. Roberts, M. D., Martin, N. L. & Kropinski, A. M. The genome and proteome of coliphage T1. *Virology* 318, 245–266 (2004).
432. Kuroda, A. *et al.* Polyphosphate kinase as a nucleoside diphosphate kinase in Escherichia coli and Pseudomonas aeruginosa. *Proc. Natl. Acad. Sci.* 94, 439–442 (1997).
433. Szybalski, W. Bacteriophage Lambda. in *Bacteria, Bacteriophages, and Fungi* 309–322 (Springer US, 1974). doi:10.1007/978-1-4899-1710-2_19
434. Zorzopulos, J., Kozloff, L. M., Chapman, V. & DeLong, S. Bacteriophage T4D receptors and the Escherichia coli cell wall structure: role of spherical particles and protein b of the cell wall in bacteriophage infection. *J. Bacteriol.* 137, 545–55 (1979).
435. Golec, P. *et al.* Proteomic profiles and kinetics of development of bacteriophage T4 and its rI and rIII mutants in slowly growing Escherichia coli. *J. Gen. Virol.* 94, 896–905 (2013).
436. Feiner, R. *et al.* A new perspective on lysogeny: prophages as active regulatory switches of bacteria. *Nat. Rev. Microbiol.* 13, 641–650 (2015).
437. Michel, B. After 30 years of study, the bacterial SOS response still surprises us. *PLoS Biol.* 3, e255 (2005).
438. Janion, C. Inducible SOS response system of DNA repair and mutagenesis in Escherichia coli. *Int. J. Biol. Sci.* 4, 338–44 (2008).
439. Signoretto, C., Lleò, M. M. & Canepari, P. Modification of the peptidoglycan of Escherichia coli in the viable but nonculturable state. *Curr. Microbiol.* 44, 125–31 (2002).
440. Oliver, J. D. The viable but nonculturable state in bacteria. *J. Microbiol.* 43 Spec No, 93–100 (2005).
441. Chibani-Chennoufi, S., Bruttin, A., Dillmann, M.-L. & Brüssow, H. Phage-host interaction: an ecological perspective. *J. Bacteriol.* 186, 3677–86 (2004).
442. Auer, G. K. & Weibel, D. B. Bacterial Cell Mechanics. *Biochemistry* 56, 3710–3724 (2017).
443. Didelot, X., Bowden, R., Wilson, D. J., Peto, T. E. A. & Crook, D. W. Transforming clinical microbiology with bacterial genome sequencing. *Nat. Rev. Genet.* 13, 601–612 (2012).
444. Hill, C. W., Sandt, C. H. & Vlazny, D. A. Rhs elements of Escherichia coli: a family of genetic composites each encoding a large mosaic protein. *Mol. Microbiol.* 12, 865–71 (1994).
445. Wang, Y. D., Zhao, S. & Hill, C. W. Rhs elements comprise three subfamilies which diverged prior to acquisition by Escherichia coli. *J. Bacteriol.* 180, 4102–10 (1998).
446. De Palmenaer, D., Siguier, P. & Mahillon, J. IS4 family goes genomic. *BMC Evol. Biol.* 8, 18 (2008).
447. McDonald, J. H. *Handbook of biological statistics, Second edition*. (2009).
448. Fujita, Y., Matsuoka, H. & Hirooka, K. Regulation of fatty acid metabolism in bacteria. *Mol. Microbiol.* 66, 829–839 (2007).
449. Polyak, S. W., Abell, A. D., Wilce, M. C. J., Zhang, L. & Booker, G. W. Structure, function and selective inhibition of bacterial acetyl-coa carboxylase. *Appl. Microbiol. Biotechnol.* 93, 983–992 (2012).
450. Iwata, S. *et al.* The structure of the ubiquinol oxidase from Escherichia coli and its ubiquinone binding site. *Nat. Struct. Biol.* 7, 910–917 (2000).
451. Yap, L. L. *et al.* The quinone-binding sites of the cytochrome bo3 ubiquinol oxidase from Escherichia coli. *Biochim. Biophys. Acta* 1797, 1924–32 (2010).
452. Deane, J. *et al.* Long-Term Implications of Antibiotic Use on Gut Health and Microbiota in Populations

Including Patients With Cystic Fibrosis. *Gut-Brain Axis* 223–259 (2016). doi:10.1016/B978-0-12-802304-4.00011-6
453. Bradley, J. S. & Sauberan, J. B. Antimicrobial Agents. *Princ. Pract. Pediatr. Infect. Dis.* 1453-1484.e5 (2012). doi:10.1016/B978-1-4377-2702-9.00294-4
454. Baym, M. *et al.* Spatiotemporal microbial evolution on antibiotic landscapes. *Science (80-.).* 353, (2016).
455. Bolger, A. M., Lohse, M. & Usadel, B. Trimmomatic: a flexible trimmer for Illumina sequence data. *Bioinformatics* 30, 2114–20 (2014).
456. Pertea, M., Kim, D., Pertea, G. M., Leek, J. T. & Salzberg, S. L. Transcript-level expression analysis of RNA-seq experiments with HISAT, StringTie and Ballgown. *Nat. Protoc.* 11, 1650–1667 (2016).
457. Anders, S., Pyl, P. T. & Huber, W. HTSeq--a Python framework to work with high-throughput sequencing data. *Bioinformatics* 31, 166–169 (2015).
458. Love, M. I., Huber, W. & Anders, S. Moderated estimation of fold change and dispersion for RNA-seq data with DESeq2. *Genome Biol.* 15, 550 (2014).
459. Gunasekera, T. S., Csonka, L. N. & Paliy, O. Genome-wide transcriptional responses of Escherichia coli K-12 to continuous osmotic and heat stresses. *J. Bacteriol.* 190, 3712–20 (2008).
460. Bartholomäus, A. *et al.* Bacteria differently regulate mRNA abundance to specifically respond to various stresses. *Philos. Trans. R. Soc. A Math. Phys. Eng. Sci.* 374, 20150069 (2016).
461. Polissi, A. *et al.* Changes in Escherichia coli transcriptome during acclimatization at low temperature. *Res. Microbiol.* 154, 573–580 (2003).
462. Jozefczuk, S. *et al.* Metabolomic and transcriptomic stress response of Escherichia coli. *Mol. Syst. Biol.* 6, 364 (2010).
463. Weber, H., Polen, T., Heuveling, J., Wendisch, V. F. & Hengge, R. Genome-Wide Analysis of the General Stress Response Network in Escherichia coli: S-Dependent Genes, Promoters, and Sigma Factor Selectivity. *J. Bacteriol.* 187, 1591–1603 (2005).
464. Li, Y. *et al.* Transcriptomic analysis by RNA-seq of Escherichia coli O157:H7 response to prolonged cold stress. *LWT* 97, 17–24 (2018).
465. Wang, Z., Gerstein, M. & Snyder, M. RNA-Seq: a revolutionary tool for transcriptomics. *Nat. Rev. Genet.* 10, 57–63 (2009).
466. Wilhelm, B. T. & Landry, J.-R. RNA-Seq—quantitative measurement of expression through massively parallel RNA-sequencing. *Methods* 48, 249–257 (2009).
467. Wang, C. *et al.* The concordance between RNA-seq and microarray data depends on chemical treatment and transcript abundance. *Nat. Biotechnol.* 32, 926–932 (2014).
468. Li, J. *et al.* Comparison of microarray and RNA-Seq analysis of mRNA expression in dermal mesenchymal stem cells. *Biotechnol. Lett.* 38, 33–41 (2016).
469. Liu, Y. *et al.* RNA-Seq identifies novel myocardial gene expression signatures of heart failure. *Genomics* 105, 83–89 (2015).
470. Haas, B. J., Chin, M., Nusbaum, C., Birren, B. W. & Livny, J. How deep is deep enough for RNA-Seq profiling of bacterial transcriptomes? *BMC Genomics* 13, 734 (2012).
471. Barman, R. K., Mukhopadhyay, A. & Das, S. An improved method for identification of small non-coding RNAs in bacteria using support vector machine. *Sci. Rep.* 7, 46070 (2017).
472. Matic, I. Stress-Induced Mutagenesis in Bacteria. in *Stress-Induced Mutagenesis* 1–19 (Springer New York, 2013). doi:10.1007/978-1-4614-6280-4_1
473. Foster, P. L. Stress-induced mutagenesis in bacteria. *Crit. Rev. Biochem. Mol. Biol.* 42, 373–97 (2007).
474. Barrick, J. E. *et al.* Genome evolution and adaptation in a long-term experiment with Escherichia coli. *Nature* 461, 1243–1247 (2009).
475. Barrick, J. E. & Lenski, R. E. Genome dynamics during experimental evolution. *Nat. Rev. Genet.* 14, 827–839 (2013).
476. Rosche, W. A. & Foster, P. L. Determining Mutation Rates in Bacterial Populations. doi:10.1006/meth.1999.0901
477. Foster, P. L. Methods for Determining Spontaneous Mutation Rates. in *Methods in enzymology* 409, 195–213 (2006).
478. Williams, A. B. Spontaneous mutation rates come into focus in Escherichia coli. *DNA Repair (Amst).* 24, 73–79 (2014).
479. Luria, S. E. & Delbrück, M. Mutations of Bacteria from Virus Sensitivity to Virus Resistance. *Genetics* 28, 491–511 (1943).
480. Halligan, D. L. & Keightley, P. D. Spontaneous Mutation Accumulation Studies in Evolutionary Genetics. *Annu. Rev. Ecol. Evol. Syst.* 40, 151–172 (2009).
481. Hardison, R. C. Comparative genomics. *PLoS Biol.* 1, E58 (2003).
482. Lenski, R. E., Rose, M. R., Simpson, S. C. & Tadler, S. C. Long-Term Experimental Evolution in Escherichia coli. I. Adaptation and Divergence During 2,000 Generations. *Am. Nat.* 138, 1315–1341 (1991).
483. Good, B. H., McDonald, M. J., Barrick, J. E., Lenski, R. E. & Desai, M. M. The dynamics of molecular evolution over 60,000 generations. *Nature* 551, 45–50 (2017).
484. Rosche, W. A. & Foster, P. L. Determining Mutation Rates in Bacterial Populations. doi:10.1006/meth.1999.0901
485. Foster, P. L., Lee, H., Popodi, E., Townes, J. P. & Tang, H. Determinants of spontaneous mutation in the bacterium Escherichia coli as revealed by whole-genome sequencing. *Proc. Natl. Acad. Sci. U. S. A.* 112, E5990-9 (2015).
486. Gresham, D. & Hong, J. The functional basis of adaptive evolution in chemostats. *FEMS Microbiol. Rev.* 39, n/a-n/a (2014).
487. Kubitschek, H. E. & Bendigkeit, H. E. Mutation in continuous cultures. I. Dependence of mutational response upon growth-limiting factors. *Mutat. Res. Mol. Mech. Mutagen.* 1, 113–120 (1964).

488. Novick, A. & Szilard, L. Experiments with the Chemostat on spontaneous mutations of bacteria. *Proc. Natl. Acad. Sci. U. S. A.* **36**, 708–19 (1950).
489. Ochman, H. Neutral Mutations and Neutral Substitutions in Bacterial Genomes. *Mol. Biol. Evol.* **20**, 2091–2096 (2003).
490. Ochman, H., Elwyn, S. & Moran, N. A. Calibrating bacterial evolution. *Proc. Natl. Acad. Sci. U. S. A.* **96**, 12638–43 (1999).
491. Lee, H., Popodi, E., Tang, H. & Foster, P. L. Rate and molecular spectrum of spontaneous mutations in the bacterium Escherichia coli as determined by whole-genome sequencing. *Proc. Natl. Acad. Sci.* **109**, E2774–E2783 (2012).
492. Wielgoss, S. *et al.* Mutation Rate Inferred From Synonymous Substitutions in a Long-Term Evolution Experiment With Escherichia coli. *G3 (Bethesda).* **1**, 183–186 (2011).
493. Drake, J. W. A constant rate of spontaneous mutation in DNA-based microbes. *Proc. Natl. Acad. Sci. U. S. A.* **88**, 7160–4 (1991).
494. Drake, J. W. Avoiding Dangerous Missense: Thermophiles Display Especially Low Mutation Rates. *PLoS Genet.* **5**, e1000520 (2009).
495. Robert, L. *et al.* Mutation dynamics and fitness effects followed in single cells. *Science* **359**, 1283–1286 (2018).
496. Staszewski, R. Cloning by limiting dilution: an improved estimate that an interesting culture is monoclonal. *Yale J. Biol. Med.* **57**, 865–8
497. Blainey, P. C. The future is now: single-cell genomics of bacteria and archaea. *FEMS Microbiol. Rev.* **37**, 407–27 (2013).
498. Heydari, M., Miclotte, G., Demeester, P., Van de Peer, Y. & Fostier, J. Evaluation of the impact of Illumina error correction tools on de novo genome assembly. *BMC Bioinformatics* **18**, 374 (2017).
499. Tenaillon, O. *et al.* Tempo and mode of genome evolution in a 50,000-generation experiment. *Nature* **536**, 165–170 (2016).
500. The Evolution of Bacteria on a "Mega-Plate" Petri Dish (Kishony Lab) - YouTube. Available at: https://www.youtube.com/watch?v=plVk4NVIUh8. (Accessed: 29th March 2017)
501. Brötz-Oesterhelt, H., Bandow, J. E. & Labischinski, H. Bacterial proteomics and its role in antibacterial drug discovery. *Mass Spectrom. Rev.* **24**, 549–565 (2005).

Per aspera ad astra